

University of Alabama in Huntsville

LOUIS

Dissertations

UAH Electronic Theses and Dissertations

2016

Stochastic theory and direct numerical simulations of the relative motion of high-stokes number particles in isotropic turbulence

Rohit Dhariwal

Follow this and additional works at: <https://louis.uah.edu/uah-dissertations>

Recommended Citation

Dhariwal, Rohit, "Stochastic theory and direct numerical simulations of the relative motion of high-stokes number particles in isotropic turbulence" (2016). *Dissertations*. 111.
<https://louis.uah.edu/uah-dissertations/111>

This Dissertation is brought to you for free and open access by the UAH Electronic Theses and Dissertations at LOUIS. It has been accepted for inclusion in Dissertations by an authorized administrator of LOUIS.

STOCHASTIC THEORY AND DIRECT NUMERICAL
SIMULATIONS OF THE RELATIVE MOTION OF
HIGH-STOKES-NUMBER PARTICLES IN ISOTROPIC
TURBULENCE

by

ROHIT DHARIWAL

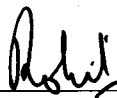
A DISSERTATION

Submitted in partial fulfillment of the requirements
for the degree of Doctor of Philosophy
in
The Department of Mechanical and Aerospace Engineering
to
The School of Graduate Studies
of
The University of Alabama in Huntsville

HUNTSVILLE, ALABAMA

2016

In presenting this Dissertation in partial fulfillment of the requirements for a doctoral degree from The University of Alabama in Huntsville, I agree that the Library of this University shall make it freely available for inspection. I further agree that permission for extensive copying for scholarly purposes may be granted by my advisor or, in his/her absence, by the Chair of the Department or the Dean of the School of Graduate Studies. It is also understood that due recognition shall be given to me and to The University of Alabama in Huntsville in any scholarly use which may be made of any material in this Dissertation.



Rohit Dhariwal

11/03/2016
(date)

ABSTRACT

School of Graduate Studies
The University of Alabama in Huntsville

Degree: Doctor of Philosophy College/Dept.: Engineering/Mechanical and
Aerospace Engineering

Name of Candidate: Rohit Dhariwal

Title: Stochastic Theory and Direct Numerical Simulations of the Relative Motion of
High-Stokes-number Particles in Isotropic Turbulence

This dissertation presents an analytical and computational investigation of the relative motion of monodisperse, non-settling, inertial particle pairs in stationary, homogeneous isotropic turbulence. The research objectives of this dissertation were to: (1) develop a stochastic theory describing the relative velocities and separations of highly inertial particle pairs in isotropic turbulence; (2) analyze and validate the developed theory through comparisons with prior theories, and with data from direct numerical simulations; and (3) investigate the effects of stochastic and deterministic forcing schemes on the relative motion of particle pairs in direct numerical simulations (DNS) of isotropic turbulence.

The PDF kinetic equation describing the relative motion of inertial particle pairs in a turbulent flow requires the closure of the phase-space diffusion current. A novel analytical closure for the diffusion current is presented that is applicable to high-inertia particle pairs with Stokes numbers $St_r \gg 1$, where St_r is a Stokes number based on the time-scale τ_r of eddies whose size scales with pair separation r . In the asymptotic limit of $St_r \gg 1$, the pair PDF kinetic equation reduces to an equation of the Fokker-Planck form. Closure of the diffusivity tensor in the Fokker-Planck

equation is achieved by converting the Lagrangian correlations of fluid relative velocities “seen” by pairs into Eulerian fluid velocity correlations at pair separations that remain essentially constant during timescales of $O(\tau_r)$. A detailed quantitative analysis of the stochastic theory was performed by solving the Langevin equations that are statistically equivalent to the closed Fokker-Planck equation. The pair relative-motion statistics obtained from the Langevin simulations (LS) for $Re_\lambda = 76, 131$ and $St_\eta = 10, 20, 40, 80$ are compared with the results obtained in prior theoretical analyses, as well as with the data from DNS. Excellent comparison between LS and DNS results was found for the radial distribution functions, while a reasonable agreement was seen for the relative velocity statistics.

Finally, the effects of deterministic and stochastic forcing schemes on the relative motion of heavy inertial particles in DNS of isotropic turbulence were studied. The effects of forcing time scale T_f , a key parameter in stochastic forcing, on the relative motion statistics of particle pairs were assessed by considering five T_f 's, ranging from $4T_E$ to $T_E/4$, where T_E is the Eulerian integral time scale obtained from the DNS with deterministic forcing. Six DNS runs (one deterministic and five stochastic) are performed for each of the three grid resolutions $128^3, 256^3, 512^3$. Data from the runs with deterministic forcing and stochastic forcing (with five time scales) were compared, and their effects on particle statistics quantified.

Abstract Approval: Committee Chair



Dr. Sarma Rani

Department Chair



Dr. D. Keith Hollingsworth

Graduate Dean



Dr. David Berkowitz

ACKNOWLEDGMENTS

First of all, I would like to express my sincerest gratitude to my advisor Dr. Sarma L. Rani for his guidance. I would also like to thank him for introducing me to the world of multiphase flows and high performance computing (HPC), and teaching me the virtues of hard work, sincerity and being patient during tough situations. I could not have asked for a better advisor than him.

I would also like to thank my dissertation committee, Dr. Kader Frendi, Dr. Shankar Mahalingam, Dr. Babak Shotorban and Dr. Sivaguru Ravindran for their valuable comments. I would also to thank my friends Sumit Dhankhar, Vijaya Krishna Rani, Shreyas Bidadi, Madhu Sridhar, Rahul Kumar, Satyajeet Padhi, Bangalore Yashwanth, Ambarish Dahale, Kiruthika Sundararajan and Chandana Anand for their help and making my stay in Huntsville fun.

I am also grateful to Alabama Experimental Program to Stimulate Competitive Research (ALEPSCoR) Graduate Research Scholars Program (GRSP) for supporting my graduate studies. I would also like to thank the UAH staff especially Claudia Meyering, Melissa Brown and Euan Holton for their help. I also acknowledge the computational resources provided by Alabama Supercomputing Authority, Extreme Science and Engineering Discovery Environment (XSEDE) and NSF Blue Waters supercomputer.

Finally, none of this would have been possible without the love and support of my parents—Dr. Ompal Singh and Smt. Saroj Bala, and my younger brother Rahul.

To my parents and brother

TABLE OF CONTENTS

	PAGE
List of Figures	xii
List of Tables	xx
Chapter	
1 Introduction	1
1.1 Modeling and Simulation of Particle-laden Turbulent Flows	3
1.2 Dissertation outline	7
2 A Stochastic Model for the Relative Motion of High Stokes Number	
Particles in Isotropic Turbulence	8
2.1 Abstract	8
2.2 Introduction	10
2.3 Theory	24
2.3.1 Phase-Space Density Equation	25
2.3.2 Perturbation Analysis	26
2.3.2.1 Derivation of $\hat{D}_{UU,\perp}$ and $\hat{D}_{UU,\parallel}$	39
2.3.3 Derivation of an expression for W_{rms}	42
2.3.4 Consistency check of the pair diffusion coefficient	44
2.4 Simulations	47

2.5	Results and discussion	50
2.5.1	Transverse and longitudinal components of the diffusion coefficient tensor	50
2.5.2	RDF and relative velocity PDF statistics	52
2.6	Summary and conclusions	62
2.7	Appendix: PDF notation used in the current study	64
3	Stochastic Theory and Direct Numerical Simulations of the Relative Motion of High-Inertia Particle Pairs in Isotropic Turbulence	67
3.1	Abstract	67
3.2	Introduction	69
3.3	Theory	78
3.3.1	Three closure forms for diffusivity D_{UU}	82
3.3.2	CF2 and CF3	84
3.3.3	Expression for W_{rms}	86
3.4	Computational Details	88
3.4.1	DNS	88
3.4.2	Langevin simulations	94
3.5	Results and discussion	98
3.5.1	Diffusivity tensor	99
3.5.2	Radial distribution function	110
3.5.3	Pair relative velocity statistics	120
3.5.4	Collision kernel	135
3.6	Conclusions	138

3.7	Appendix: Comparison with Renormalized Perturbation Expansion of LHDl	144
4	Effects of deterministic and stochastic forcing schemes on the relative motion of inertial particles in DNS of isotropic turbulence	150
4.1	Abstract	150
4.2	Introduction	153
4.3	Computational Method	160
4.3.1	Fluid Phase	160
4.3.1.1	Deterministic Forcing Scheme	162
4.3.1.2	Stochastic Forcing Scheme	162
4.3.2	Particle Phase	164
4.4	Results	165
4.4.1	Particle Clustering	170
4.4.2	Variance of Radial Relative Velocities	187
4.4.3	PDF of Radial Relative Velocities	205
4.4.4	Collision Kernel	210
4.5	Concluding Remarks	215
5	Conclusions	219
5.1	Summary	219
5.2	Future work	223
APPENDIX A: Stochastic Theory for Monodisperse Settling Particle Pairs		226

A.1	$ Sv_I \sim St_I \gg 1$ Regime	228
A.2	$ Sv_I \sim 1$ Regime	232
A.3	Derivation of diffusion coefficient tensor in the settling particle pair relative velocity space	233

LIST OF FIGURES

FIGURE	PAGE
1.1	Examples of particle-laden turbulent flow 2
1.2	Clustering of inertial particles. Figure taken from [69] 4
2.1	Transverse component, $D_{UU,\perp}(r)$, and longitudinal component, $D_{UU,\parallel}(r)$, of the particle-pair diffusion coefficient tensor as a function of dimensionless pair separation r/L for $St_\eta = 20$. Solid and dashed curves represent transverse and longitudinal components, respectively. At small r , transverse and longitudinal components asymptote to the lower and upper dashed lines represented by $4.77(r/L)^2$ and $9.54(r/L)^2$, respectively. At large r , transverse and longitudinal components asymptote to the value of 0.74. 51
2.2	RDFs from our stochastic simulations for the various Stokes numbers as a function of dimensionless pair separation r/η . The radial location at which $r/L = 1$ is also indicated, where L is the integral length scale. 54
2.3	$\langle U^2 \rangle / u_{\text{rms}}^2$ as a function of dimensionless pair separation r/L and particle Stokes number St_η 55
2.4	RDF versus St_η at specific radial separations: (a) $r/\eta = 6$, (b) $r/\eta = 12$, (c) $r/\eta = 18$, and (d) $r/\eta = 24$. In each plot, circles represent data from current stochastic simulations at $Re_\lambda = 75$; squares and triangles represent DNS data at $Re_\lambda = 53$ and $Re_\lambda = 69$, respectively, taken from Février et al. [29]. Solid line represents Zaichik and Alipchenkov [100] data for $Re_\lambda = 69$ 56
2.5	Kurtosis for various Stokes number pairs as a function of dimensionless pair separation r/L 58
2.6	$\langle U^2 \rangle / u_{\text{rms}}^2$ as a function of dimensionless pair separation r/L and particle Stokes number St_η 59
2.7	Relative velocity PDFs ($\Omega(U)$) for the various Stokes numbers at specific separations: (a) $r/L = 3$, (b) $r/L = 1$, (c) $r/L = 1/10$, (d) $r/L = 1/20$ 61

2.8	Comparison of relative velocity PDFs at various pair separations for $St_\eta = 20$	62
2.9	PDF of the radial component of the relative velocity U_r for the various Stokes numbers at $r/L = 1/20$	63
3.1	The Eulerian two-time correlation of fluid relative velocities $R(r, \tau) = \langle \Delta \mathbf{u}(\mathbf{r}, t) \Delta \mathbf{u}(\mathbf{r}, t + \tau) \rangle$. The longitudinal and transverse components of $R(r, \tau)$, i.e. $R_{ }(r, \tau)$ and $R_{\perp}(r, \tau)$, are shown as a function of time at separations $r/L = 0.2, 0.5, 1$. Figures (a,b) $Re_\lambda = 76$, and (c,d) $Re_\lambda = 131$. The integral length scale $L = \pi/(2u'^2) \int_0^{\kappa_{\max}} E(\kappa)/\kappa d\kappa$, and time scale $T_{\text{eddy}} = L/u_{\text{rms}}$	92
3.2	Comparison of the DNS and model energy spectra at $Re_\lambda = 76$ and $Re_\lambda = 131$. The model spectrum is used to compute the CF1 and CF2 diffusivities.	97
3.3	The transverse component, $D_{UU,\perp}(r)$, and the longitudinal component, $D_{UU, }(r)$, of the diffusivity tensor for $St_\eta = 10$ as a function of dimensionless pair separation r/L . Diffusivity tensor components for CF1, CF2 and CF3 are shown. <i>Upper black solid line denotes CF3 transverse component, and lower grey solid line denotes CF2 transverse component.</i> (a) $Re_\lambda = 76$, and (b) $Re_\lambda = 131$. Transverse and longitudinal components of D_{UU} for CF1, CF2 and CF3 in the viscous range at $Re_\lambda = 76$ and 131 are shown in Table 3.3.	100
3.4	Transverse component, $D_{UU,\perp}(r)$, and longitudinal component, $D_{UU, }(r)$, of the diffusion coefficient tensor for $St_\eta = 80$ as a function of dimensionless pair separation r/L at: (a) $Re_\lambda = 76$, and (b) $Re_\lambda = 131$. CF2 and CF3 diffusivities are compared.	101
3.5	Comparison of Closure Form 1 (CF1) of \mathbf{D}_{UU} with the diffusivity of Zaichik and Alipchenkov [100, 103] in the limit $St_r \gg 1$. $\mathbf{D}_{UU, }(r)$ and $\mathbf{D}_{UU,\perp}(r)$ are the longitudinal and transverse components of \mathbf{D}_{UU} , respectively. ‘‘Zaichik’’ refers to the diffusivity calculated from Equation 3.51-Equation 3.53. Diffusion coefficient is plotted as a function of dimensionless pair separation r/L at: (a) $Re_\lambda = 76$, and (b) $Re_\lambda = 131$. Also shown in figure (a) are the diffusivities obtained using the two scaling expressions for the viscous time scale: Equation 3.44 and Equation 3.47, and Equation 3.44 and Equation 3.48. In (b) we show diffusivities obtained from the scaling expressions in the inertial subrange: Equation 3.45 and Equation 3.49. For the viscous range, two forms of scaling expressions are plotted: one in which strain-rate and rotation-rate have identical time scales ($\tau_\sigma = \tau_\omega$), and the second in which they are different ($\tau_\sigma \neq \tau_\omega$).	102

3.6	Radial distribution function (RDF) as a function of St_η at specific separations: (a) $r/\eta = 6$, (b) $r/\eta = 12$, (c) $r/\eta = 18$, and (d) $r/\eta = 24$. In each plot, squares and circles represent data from CF1 and current DNS at $Re_\lambda = 76$; triangles represent DNS data of [29] at $Re_\lambda = 69$. Solid line represents data from Zaichik et al. [105] theory for $Re_\lambda = 69$.	109
3.7	Radial distribution function (RDF) versus St_η at separation $r/\eta = 1$. Squares and circles represent data from CF1 and current DNS at $Re_\lambda = 76$. Curve 1 represents Zaichik et al. [105] theory for $Re_\lambda = 69$; and Curve 2 represents Zaichik and Alipchenkov [104] theory for $Re_\lambda = 75$.	110
3.8	RDFs from Langevin simulations (CF1, CF2, and CF3) and from DNS as a function of dimensionless pair separation r/η for the indicated values of $St_\eta = 10, 80$. (a,b) $Re_\lambda = 76$, and (c,d) $Re_\lambda = 131$.	114
3.9	$\langle U^2 \rangle / u_{\text{rms}}^2$ as a function of r/L for all Stokes numbers. (a) $Re_\lambda = 76$, and (b) $Re_\lambda = 131$. Lines denote CF1 and symbols denote CF2.	115
3.10	RDF versus St_η at $Re_\lambda = 76$ and at specific pair separations: (a) $r/\eta = 1$, (b) $r/\eta = 11$, (c) $r/\eta = 22$, and (d) $r/\eta = 44 (\approx L)$. CF1, CF2, CF3, and DNS are compared.	118
3.11	RDF versus St_η at $Re_\lambda = 131$ and at specific pair separations: (a) $r/\eta = 1$, (b) $r/\eta = 23$, (c) $r/\eta = 46$, and (d) $r/\eta = 92 (\approx L)$. CF1, CF2, CF3, and DNS are compared.	119
3.12	RDF versus pair separation r/η for (a) $St_\eta = 10$, and (b) $St_\eta = 20$. Black curves are for $Re_\lambda = 131$, and green curves are for $Re_\lambda = 76$. CF1, CF3 and DNS are compared.	120
3.13	$\langle U^2 \rangle / u_\eta^2$ versus St_η at $Re_\lambda = 76$ for various separations. (a) $r/L = 1/20$, (b) $r/L = 1/10$, (c) $r/L = 1/2$, and (d) $r/L = 1$. Dashed line in (d) corresponds to the analytical expression for the variance of uncorrelated pairs, $\langle U^2 \rangle = 2u_{\text{rms}}^2 \frac{T_L}{T_L + \tau_v}$, where T_L is the Lagrangian integral time scale. T_L is obtained using $T_L = T_E/1.1$ [58].	121
3.14	$\langle U^2 \rangle / u_\eta^2$ versus St_η at $Re_\lambda = 131$ for various separations. (a) $r/L = 1/20$, (b) $r/L = 1/10$, (c) $r/L = 1/2$, and (d) $r/L = 1$. Dashed line in (d) corresponds to $\langle U^2 \rangle = 2u_{\text{rms}}^2 \frac{T_L}{T_L + \tau_v}$, where T_L is the Lagrangian integral time scale. T_L is obtained using $T_L = T_E/1.1$ [58].	123
3.15	$\langle U^2 \rangle / u_{\text{rms}}^2$ versus St_η . (a) $r/L = 1/20$, and (b) $r/L = 1$. Open symbols denote $Re_\lambda = 131$, and filled symbols $Re_\lambda = 76$.	124

3.16	Dimensionless $D_{UU} \times St_\eta^2$ is plotted as a function of r/η for $Re_\lambda = 76, 131$. Effects of Re_λ on the CF1 closure are shown. The longitudinal and transverse components of $D_{UU}^{[1]}$ are compared at the two Re_λ . D_{UU} is made dimensionless with the Kolmogorov-scale quantities, and then multiplied with St_η^2	127
3.17	Relative velocity PDF $\Omega(U r)$ normalized by $\langle U^2 \rangle^{1/2}$ for $Re_\lambda = 76$ and at $r/L = 1/20$. (a) $St_\eta = 10$, and (b) $St_\eta = 80$. Grey line represents the normal distribution.	129
3.18	Relative velocity PDF $\Omega(U r)$ scaled by u_{rms} for $Re_\lambda = 76$ and at $r/L = 1/20$. (a) $St_\eta = 10$, and (b) $St_\eta = 80$	130
3.19	Relative velocity PDF $\Omega(U r)$ normalized by $\langle U^2 \rangle^{1/2}$ for $Re_\lambda = 131$ and at $r/L = 1/20$. (a) $St_\eta = 10$, and (b) $St_\eta = 80$. Grey line represents the normal distribution.	131
3.20	Relative velocity PDF $\Omega(U r)$ scaled by u_{rms} for $Re_\lambda = 131$ and at $r/L = 1/20$. (a) $St_\eta = 10$, and (b) $St_\eta = 80$	132
3.21	PDF of radial relative velocity $\Omega(U_r r)$ scaled by u_{rms} for $St_\eta = 10, 80$ at $Re_\lambda = 76$ and at specific separations: (a) $r/L = 1/20$, and (b) $r/L = 1$.	134
3.22	Kurtosis as a function of dimensionless pair separation r/L at: (a) $Re_\lambda = 76$, and (b) $Re_\lambda = 131$. CF1, CF3 and DNS are compared for $St_\eta = 10$ and 80	136
3.23	Collision kernel as a function of Stokes number at $Re_\lambda = 76$. CF1, CF3 and DNS are compared. Curve 1 shows the collision kernel when the RDF $g(r) = 1$ and the PDF $P(U_r r)$ is Gaussian. Curve 2 represents the collision kernel computed using the Zaichik and Alipchenkov [104] theory. Curve 3 represents the collision kernel computed using the Abrahamson theory [1, 104]. Curve 4 represents the collision kernel from the Mehlig et al. [53] theory. Curve 5 represents the collision kernel computed using eq. (56) of Zaichik and Alipchenkov [104]. Curves 2 through 4 are at $r/\eta = 1$ and $Re_\lambda = 75$. Curve 5 is at $r/\eta = 2.3$ and $Re_\lambda = 76$	139
3.24	Collision kernel as a function of Stokes number at $Re_\lambda = 131$. CF1, CF3 and DNS are compared.	140

3.25	Effects of Reynolds number on the PDF of radial relative velocity $\Omega(U_r r)$ for $St_\eta = 10, 80$. (a) CF1 closure, and (b) CF3 closure. The PDFs for $Re_\lambda = 76$ are shown for $r = 2.3\eta$, and those for $Re_\lambda = 131$ are for $r = 4.7\eta$	140
4.1	Energy Spectra at (a) 256^3 and (b) 512^3 grid resolutions, and for DF, SF1, SF2, SF3, SF4, and SF5 forcings. Normalized energy Spectra at (c) 256^3 and (d) 512^3 grid resolutions, and for DF, DF2, SF1, SF2, SF3, SF4, and SF5 forcings.	169
4.2	RDFs from stochastic (SF1-SF5) and deterministic (DF and DF2) forcing schemes as a function of dimensionless pair separation r/η for the indicated values of St_η at $Re_\lambda = 80$	172
4.3	RDFs from stochastic (SF1-SF5) and deterministic (DF and DF2) forcing schemes as a function of dimensionless pair separation r/η for the indicated values of St_η at $Re_\lambda = 131$	173
4.4	RDFs from stochastic (SF1-SF5) and deterministic (DF and DF2) forcing schemes as a function of dimensionless pair separation r/η for the indicated values of St_η at $Re_\lambda = 210$	174
4.5	RDFs from stochastic (SF1-SF5) and deterministic (DF and DF2) forcing schemes as a function of dimensionless pair separation r/η for the indicated values of St_η at $Re_\lambda = 80$. DF2 data is not available for $St_\eta = 4$ in (c).	177
4.6	RDFs from stochastic (SF1-SF5) and deterministic (DF and DF2) forcing schemes as a function of dimensionless pair separation r/η for the indicated values of St_η at $Re_\lambda = 131$. DF2 data is not available for $St_\eta = 4$ in (c).	178
4.7	RDFs from stochastic (SF1-SF5) and deterministic (DF and DF2) forcing schemes as a function of dimensionless pair separation r/η for the indicated values of St_η at $Re_\lambda = 210$. DF2 data is not available for $St_\eta = 4$ in (c).	179
4.8	RDFs as a function of dimensionless pair separation r/η for the indicated values of St_η . DF, SF3, and SF4 are compared. Curves without symbols correspond to $Re_\lambda = 80$ data, filled and open symbols correspond to $Re_\lambda = 131$ and 210 data, respectively.	182

4.9	RDFs as a function of dimensionless pair separation r/η for the indicated values of St_η . DF, SF3, and SF4 are compared. Curves without symbols correspond to $Re_\lambda = 80$, filled and open symbols correspond to $Re_\lambda = 131$ and 210 data respectively.	183
4.10	RDFs versus St_η at the indicated pair separations. DF, SF3, and SF4 are compared. Curves without symbols correspond to $Re_\lambda = 80$ data, filled and open symbols correspond to $Re_\lambda = 131$ and 210 data, respectively.	185
4.11	RDF versus St_η at $Re_\lambda = 210$. DF, SF1, SF2, SF3, SF4, and SF5 results are compared. Red, green, blue and black curves correspond to separation of $r = 0.25\eta$, $r = 4\eta$, $r = 10\eta$ and $r = 20\eta$, respectively. . .	186
4.12	$\langle U_r^2 \rangle / u_\eta^2$ from stochastic (SF1-SF5) and deterministic (DF and DF2) forcing schemes as a function of r/η for the indicated values of St_η at $Re_\lambda = 80$	188
4.13	$\langle U_r^2 \rangle / u_\eta^2$ from stochastic (SF1-SF5) and deterministic (DF and DF2) forcing schemes as a function of r/η for the indicated values of St_η at $Re_\lambda = 131$	189
4.14	$\langle U_r^2 \rangle / u_\eta^2$ from stochastic (SF1-SF5) and deterministic (DF and DF2) forcing schemes as a function of r/η for the indicated values of St_η at $Re_\lambda = 210$	190
4.15	$\langle U_r^2 \rangle / u_\eta^2$ from stochastic (SF1-SF5) and deterministic (DF and DF2) forcing schemes as a function of r/η for the indicated values of St_η at $Re_\lambda = 80$. DF2 data is not available for $St_\eta = 4$ in (c).	192
4.16	$\langle U_r^2 \rangle / u_\eta^2$ from stochastic (SF1-SF5) and deterministic (DF and DF2) forcing schemes as a function of r/η for the indicated values of St_η at $Re_\lambda = 131$. DF2 data is not available for $St_\eta = 4$ in (c).	193
4.17	$\langle U_r^2 \rangle / u_\eta^2$ from stochastic (SF1-SF5) and deterministic (DF and DF2) forcing schemes as a function of r/η for the indicated values of St_η at $Re_\lambda = 210$. DF2 data is not available for $St_\eta = 4$ in (c).	194
4.18	$\langle U_r^2 \rangle / u_\eta^2$ as a function of r/η for the indicated values of St_η . DF, SF3, and SF4 are compared. Curves without symbols correspond to $Re_\lambda = 80$ data, filled and open symbols correspond to $Re_\lambda = 131$ and 210 data, respectively.	196

4.19	$\langle U_r^2 \rangle / u_\eta^2$ as a function of r/η for the indicated values of St_η . DF, SF3, and SF4 are compared. Curves without symbols correspond to $Re_\lambda = 80$ data, filled and open symbols correspond to $Re_\lambda = 131$ and 210 data, respectively.	197
4.20	$\langle U_r^2 \rangle / u_\eta^2$ versus St_η at $Re_\lambda = 80$ and at the indicated pair separations. DF, SF1, SF2, SF3, SF4, and SF5 results are compared.	200
4.21	$\langle U_r^2 \rangle / u_\eta^2$ versus St_η at $Re_\lambda = 131$ simulations and at the indicated pair separations. DF, SF1, SF2, SF3, SF4, and SF5 results are compared.	201
4.22	$\langle U_r^2 \rangle / u_\eta^2$ versus St_η at $Re_\lambda = 210$ simulations and at the indicated pair separations. DF, SF1, SF2, SF3, SF4, and SF5 results are compared.	202
4.23	$\langle U_r^2 \rangle / u_\eta^2$ versus St_η at the indicated pair separations. DF, SF3, and SF4 are compared. Curves without symbols correspond to $Re_\lambda = 80$ data, filled and open symbols correspond to $Re_\lambda = 131$ and 210 data, respectively.	204
4.24	PDF of radial relative velocity $\Omega(U_r r)$ normalized by $\langle U_r^2 \rangle^{1/2}$ at $Re_\lambda = 210$, and at the indicated values of St_η . DF, SF3, and SF4 are compared. Blue and green curves correspond to PDF at pair separation of $r = 2\eta$ and $r = L/2$ respectively. Black curve represents the normal distribution.	206
4.25	PDF of radial relative velocity $\Omega(U_r r)$ normalized by $\langle U_r^2 \rangle^{1/2}$ at $Re_\lambda = 210$, and at the indicated values of St_η and pair separations. PDFs shown correspond to DF forcing scheme. Black curve represents the normal distribution.	207
4.26	PDF of radial relative velocity $\Omega(U_r r)$ normalized by $\langle U_r^2 \rangle^{1/2}$ at $Re_\lambda = 210$ and DF forcing scheme. PDFs shown are at $r = 2\eta$. Solid and dashed curves correspond to $St_\eta = 0.4$ and 2, respectively. Blue, green, and red curves represent $Re_\lambda = 80, 131,$ and 210 data, respectively. Normal distribution is shown by black curve.	208
4.27	Collision Kernel a function of St_η at (a) $Re_\lambda = 80$, (b) $Re_\lambda = 131$, and (c) $Re_\lambda = 210$. DF, SF1, SF2, SF3, SF4, and SF5 are compared in (a)-(c). DF, SF3, and SF4 are compared in (d). Curves without symbols represent data for $Re_\lambda = 80$, filled and open symbols correspond to data for $Re_\lambda = 131$ and 210, respectively in (c).	211

- 4.28 Collision Kernel a function of St_η at (a) $Re_\lambda = 80$, (b) $Re_\lambda = 131$, and (c) $Re_\lambda = 210$. DF, SF1, SF2, SF3, SF4, and SF5 are compared. Black circles represent the collision kernel when RDF $g(r) = 1$ and the PDF $P(U_r|r)$ is Gaussian. 212
- 4.29 Collision Kernel a function of St_η is shown. DF, SF3, and SF4 are compared. Curves without symbols represent data at $Re_\lambda = 80$, filled and open symbols correspond to data at $Re_\lambda = 131$ and 210 , respectively. 213

LIST OF TABLES

TABLE		PAGE
3.1	Flow parameters in DNS of isotropic turbulence (arbitrary units). N is the number of grid points in each direction, $Re_\lambda \equiv u_{\text{rms}}\lambda/\nu$ is the Taylor micro-scale Reynolds number, $u_{\text{rms}} \equiv \sqrt{(2k/3)}$ is the fluid RMS fluctuating velocity, k is the turbulent kinetic energy, ν is the fluid kinematic viscosity, $\epsilon \equiv 2\nu \int_0^{\kappa_{\text{max}}} \kappa^2 E(\kappa) d\kappa$ is the turbulent energy dissipation rate, $L \equiv 3\pi/(2k) \int_0^{\kappa_{\text{max}}} E(\kappa)/\kappa d\kappa$ is the integral length scale, $\lambda \equiv u_{\text{rms}}\sqrt{(15\nu/\epsilon)}$ is the Taylor microscale, $\eta \equiv \nu^{3/4}/\epsilon^{1/4}$ is the Kolmogorov length scale, $T_{\text{eddy}} \equiv L/u'$ is the large-eddy turnover time, $\tau_\eta \equiv \sqrt{(\nu/\epsilon)}$ is the Kolmogorov time scale, κ_{max} is the maximum resolved wavenumber, Δt is the time step, and N_p is the number of particles per Stokes number.	90
3.2	Parameters for the model energy spectrum. After determining c_L and c_η , the parameter C was adjusted to match the DNS energy spectrum. [64] suggested $C = 1.5$	96
3.3	Transverse and longitudinal components of D_{UU} for CF1, CF2 and CF3 in the viscous range at $Re_\lambda = 76$ and 131. The values shown are for $St_\eta = 10$. The following notation is used: $D_{UU, }^{[1,2,3],*} = \left[D_{UU, }^{[1,2,3]} \times \tau_v^2 / (u_{\text{rms}}^2 \times T_{\text{eddy}}) \right] / (r/L)^2$	101
4.1	Flow parameters in 128^3 DNS of isotropic turbulence (arbitrary units). $Re_\lambda \equiv u_{\text{rms}}\lambda/\nu$ is the Taylor micro-scale Reynolds number, $u_{\text{rms}} \equiv \sqrt{(2k/3)}$ is the fluid RMS fluctuating velocity, ν is the fluid kinematic viscosity, $\epsilon \equiv 2\nu \int_0^{\kappa_{\text{max}}} \kappa^2 E(\kappa) d\kappa$ is the turbulent energy dissipation rate, $L \equiv 3\pi/(2k) \int_0^{\kappa_{\text{max}}} E(\kappa)/\kappa d\kappa$ is the integral length scale, $\lambda \equiv u_{\text{rms}}\sqrt{(15\nu/\epsilon)}$ is the Taylor microscale, $\eta \equiv \nu^{3/4}/\epsilon^{1/4}$ is the Kolmogorov length scale, $T_E \equiv L/u'$ is the large-eddy turnover time, $\tau_\eta \equiv \sqrt{(\nu/\epsilon)}$ is the Kolmogorov time scale, κ_{max} is the maximum resolved wavenumber, Δt is the time step, and N_p is the number of particles per Stokes number. 167	
4.2	Flow parameters in 256^3 DNS of isotropic turbulence (arbitrary units). Definitions of parameters is provide in the caption of Table 4.1. . . .	167

4.3	Flow parameters in 512^3 DNS of isotropic turbulence (arbitrary units). Definitions of parameters is provide in the caption of Table 4.1. . . .	168
4.4	DF2 flow parameters in DNS of isotropic turbulence (arbitrary units) study of Ireland et al. [39]. N is the number of grid points in each direction, and definitions of other parameters is provide in the caption of Table 4.1.	168

CHAPTER 1

INTRODUCTION

Particle-laden turbulent flows are encountered in a variety of natural and engineering systems such as dispersion of pollutants in the atmosphere, sediment transport in rivers, cloud precipitation, planetesimal formation, spray combustion in engines, and fluidized bed reactors. In these types of two-phase flows, the phase consisting of solid particle or liquid droplets or gas bubbles (commonly referred as particles) is called dispersed phase, whereas the continuous fluid phase (liquid or gas) in which particles are immersed is referred to as the carrier phase. Particle-laden turbulent flows can be broadly categorized into dilute and dense regimes, depending on the dispersed phase volume fraction [19]. In dilute flows, the particle motion is primarily dominated by the fluid drag and lift forces, and inter-particle collisions are negligible. On the other hand, in dense flows the particle motion is controlled by collisions or continuous contact. In dilute regime, the fluid and dispersed phase can have “one-way” or “two-way coupling”. One-way coupling implies that the fluid turbulence is unaffected by the presence of particles and this approach is valid for particle volume fractions $\phi_v < 10^{-6}$ [24]. Whereas, for $10^{-6} < \phi_v < 10^{-3}$, the momentum source/sink provided to carrier phase by the particles is not negligible and their inclusion is called

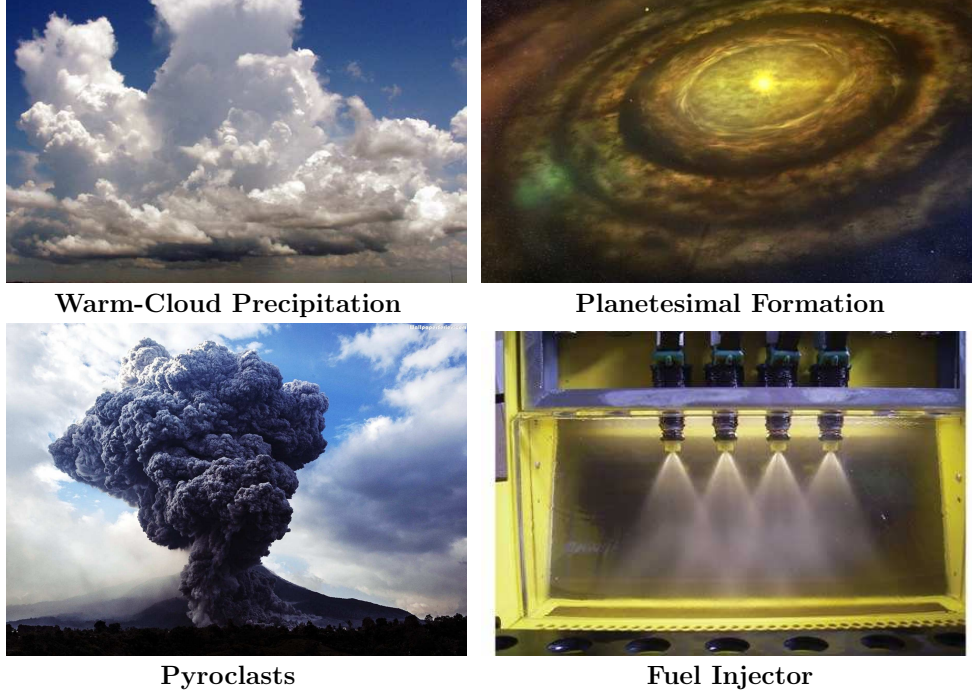


Figure 1.1: Examples of particle-laden turbulent flow

two-way coupling. In this dissertation, dilute one-way coupled particle dispersion in turbulence is considered.

Disperse multiphase flows exhibit a variety of interesting phenomena that become important in the context of a turbulent carrier-phase flow. A comprehensive discussion of dispersed multiphase turbulence can be found in reviews by [4, 80, 82]. One of the important phenomenon in particle dispersion is preferential accumulation or clustering. The preferential concentration of particles refers to the phenomenon of accumulation of particles in certain regions of the flow. This clustering is caused due to the difference between particle and fluid inertia, as the particles due to their inertia are not able to follow the fluid streamlines closely. The particle inertia can be characterized in terms of Stokes number St , which is the defined as a ratio of particle

response time to the flow time scale of interest. In one of the early studies on particle clustering [52, 23] found that the inertial particles are centrifuged out of the high vorticity regions and preferentially accumulate in the high strain regions. Since then, numerous experimental [23, 76, 78, 6, 79] and numerical [52, 89, 23, 91] studies have been devoted to the study of particle clustering, and it is found that the particles having $St \sim O(1)$ show maximum clustering. An important statistical measure of particle clustering is the radial distribution function (RDF)[77]. RDF is defined as the ratio of the number of particle pairs at a given separation to the expected number of particle pairs in a perfectly randomly distributed particle field. RDF of unity denotes uniform distribution of the particles, whereas, RDF more than one means preferential concentration of particles. Reade and Collins [69] performed DNS of isotropic turbulence laden with inertial particles and Shotorban and Balachandar [83] studied dispersion of small Stokes numbers using LES to show clustering of inertial particles. The study of Sengupta et al. [81] describes the application of spectral-based methods to simulate particle-laden turbulent flows. Figure 1.2 shows the effect of clustering for various Stokes numbers.

1.1 Modeling and Simulation of Particle-laden Turbulent Flows

There are two methods to simulate particle-laden turbulent flows, namely Lagrangian-Eulerian (LE) and Eulerian-Eulerian (EE). In both these methods, the fluid phase is solved in Eulerian framework, whereas, the dispersed phase is solved using Lagrangian (in LE) or Eulerian (in EE) framework.

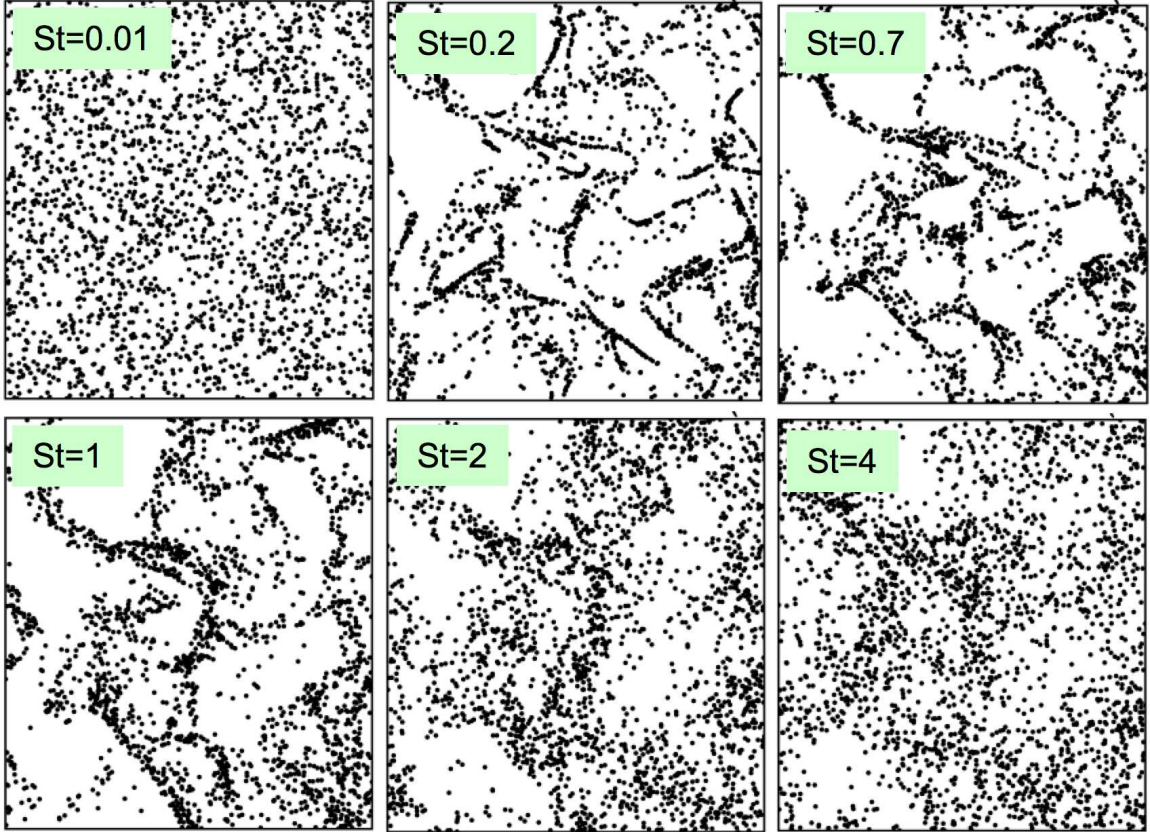


Figure 1.2: Clustering of inertial particles. Figure taken from [69]

In both LE and EE methods, the fluid phase can be modeled using any of the standard techniques to solve the Navier-Stokes equations, namely Reynolds-averaged Navier-Stokes equations (RANS), large-eddy simulation (LES), and direct numerical simulation (DNS). The individual particle trajectories and velocities are computed by integrating the particles equations of motion in LE approach. [48, 93, 50, 88, 78, 31, 94, 26, 41, 84, 85] are few notable studies of DNS and LES of particle-laden turbulent flows. Kuerten [46] provides a recent review on DNS and LES of particle-laden turbulent flows. While in EE approach, the particulate phase is treated as a continuum much like the fluid phase. Hence, in EE approach, mass and momentum

conservation equations are developed for the particle phase, which are then solved for the particle concentration and velocity fields.

In general, the LE approach is preferred when the number of particles to be tracked is “small” so that the CPU time for the Lagrangian tracking of particle positions and velocities does not overwhelm the CPU time for solving the fluid equations. But, when the number of particles to be tracked becomes very large, the LE approach may become computationally unviable. In such scenarios, EE is the preferred method. The EE approach, while being computationally economical compared to LE, also presents a substantial conundrum due to the form of the particulate phase continuum equations. The equations for the conservation of particle mass and momentum are typically obtained through an appropriate averaging process.

An alternative approach to the averaging process to derive and close the particle continuum equations is that motivated by the Boltzmann equation describing the statistical behavior of a thermodynamic system. This method is commonly referred to as the probability density function (PDF) kinetic equation approach. Since the turbulence-driven particle motion is inherently stochastic, the kinetic equation method presents a natural avenue to develop the desired closures for the particle continuum equations. The advantage of this method is that one is able to derive closures for not only the mean particle quantities, but also the second- and third-order moments.

The first step in the kinetic equation method is to derive the transport equation for the PDF of particle velocity and position, $P(\mathbf{x}, \mathbf{v})$, where \mathbf{x} and \mathbf{v} represent the particle position and velocity phase space. It is seen that the equation for P

contains a turbulence-particle interaction term of the form $\langle \mathbf{u} \tilde{f}' \rangle$ that requires closure, where \mathbf{u} is the gas-phase velocity and $\langle \cdot \rangle$ represents ensemble averaging over flow realizations. The quantity \tilde{f}' can be interpreted as the fluctuating particle number density, thereby the term $\langle \mathbf{u} \tilde{f}' \rangle$ is analogous to the Reynolds stress terms that arise when deriving the averaged Navier-Stokes equations. Three methods have been used to close this unknown term; [71, 73, 70] used the Lagrangian History Direct Interaction, [92, 37, 106, 100] used the Furutsu-Novikov correlation splitting technique and [65] used Van Kampen's method. Mashayek and Pandya [49] provides a comprehensive review on various methods for modeling two-phase flows. A detailed description of pdf methods for particle-laden turbulent flows can be found in [55, 54].

In this dissertation, particle dispersion in turbulent flows is studied using both LE and EE approaches. In LE approach, Lagrangian particle tracking is used in conjunction with DNS of fluid velocity field. In EE approach, particle position and velocity PDF is solved using Langevin simulations in combination with an analytically derived diffusion coefficient that describes fluid flow statistics.

1.2 Dissertation outline

In Chapter 2, an analytical model for the pair diffusion coefficient in the limit of high Stokes number is presented. In Chapter 3, a quantitative analysis of the stochastic theory is performed through a comparison of the pair statistics obtained using Langevin simulations with those from DNS. In Chapter 4, the effects of large scale forcing schemes on the relative motion of inertial particle pairs in DNS of isotropic

turbulence is studied. And finally in Chapter 5, key results from this work are summarized.

CHAPTER 2

A STOCHASTIC MODEL FOR THE RELATIVE MOTION OF HIGH STOKES NUMBER PARTICLES IN ISOTROPIC TURBULENCE

2.1 Abstract

The probability density function (PDF) kinetic equation describing the relative motion of inertial particle pairs in a turbulent flow requires closure of phase-space diffusion current. In the current study, a novel analytical closure for the diffusion current is presented that is applicable to high-inertia particle pairs with Stokes numbers $St_r \gg 1$. Here St_r is a Stokes number based on the time-scale τ_r of eddies whose size scales with pair separation r . In the asymptotic limit of $St_r \gg 1$, the pair PDF kinetic equation reduces to an equation of the Fokker-Planck form. The diffusion tensor characterizing the diffusion current in the Fokker-Planck equation is equal to $1/\tau_v^2$ multiplied by the time-integral of the Lagrangian correlation of fluid relative velocities along particle pair trajectories. Here, τ_v is the particle viscous relaxation time. Closure of the diffusion tensor is achieved by converting the Lagrangian correlations of fluid relative velocities “seen” by pairs into Eulerian fluid velocity correlations at pair separations that remain essentially constant during timescales of $O(\tau_r)$; the pair center-of-mass, however, is not stationary and responds to eddies with timescales

comparable to or smaller than τ_v . For isotropic turbulence, Eulerian fluid-velocity correlations may be expressed as Fourier transforms of the velocity spectrum tensor, enabling us to derive a closed-form expression for the diffusion tensor. A salient feature of this closure is that it has a single, unique form for pair separations spanning the entire spectrum of turbulence scales, as opposed to prior closures that involve velocity structure functions with different forms for the integral, inertial subrange, and Kolmogorov-scale separations. Using this closure, Langevin equations—which are statistically equivalent to the Fokker-Planck equation—were solved to evolve particle-pair relative velocities and separations in stationary isotropic turbulence. The Langevin equation approach enables the simulation of the full PDF of pair relative motion, instead of only the first few moments of the PDF as is the case in a moments-based approach. Accordingly, PDFs $\Omega(U|r)$ and $\Omega(U_r|r)$ are computed and presented for various separations r , where the former is the PDF of relative velocity U and the latter is the PDF of the radial component of relative velocity U_r , both conditioned upon the separation r . Consistent with the direct numerical simulation (DNS) study of Sundaram and Collins [91], the Langevin simulations capture the transition of $\Omega(U|r)$ from being Gaussian at integral-scale separations to an exponential PDF at Kolmogorov-scale separations. The radial distribution functions (RDFs) computed from these simulations also show reasonable quantitative agreement with those from the DNS study of Février et al. [29].

2.2 Introduction

The two principal quantities describing particle-pair relative motion in a turbulent flow are: (1) the radial distribution function (RDF) which is a measure of the number density of particles that are located at a separation r from a reference particle, and (2) the probability density function (PDF) of the relative velocities of particle pairs conditioned upon separation r . Both can be determined through direct numerical simulation (DNS) of particle-laden turbulent flows. However, DNS suffers from the well-known computational limitation on the Reynolds numbers that can be achieved. This drawback of DNS is one of the motivating factors for developing PDF equation-based stochastic models for particle-laden turbulent flows. The transport equation for the PDF of pair separation and relative velocity vectors, \mathbf{r} and \mathbf{U} respectively, contains an unclosed phase-space diffusion current. In this study, a novel closure is derived for the diffusion current in the limit of Stokes number $St_r \gg 1$ when the pair PDF equation reduces to the Fokker-Planck form. Here St_r is the Stokes number based on the time-scale τ_r of eddies whose size is of the order of pair separation r . Predictions of RDF and relative velocity PDF obtained from the current closure show good agreement with prior DNS results.

Numerous computational and theoretical studies of inertial particle motion in isotropic turbulence have established that dense particles with response time (τ_v) of the order of the Kolmogorov time-scale (τ_η) preferentially accumulate in regions of excess strain over vorticity [52, 89, 22, 21, 28, 27, 66, 18, 68]. When $\tau_v \lesssim \tau_\eta$, particle accumulation occurs at separations smaller than the Kolmogorov length scale

(η). Preferential concentration at separations of $O(\eta)$ is maximized for particles with Stokes number $St_\eta \sim O(1)$, and is attenuated when $St_\eta > 1$, where $St_\eta = \tau_v/\tau_\eta$. Février et al. [29] found that particles with $St_\eta > 1$ also exhibit preferential concentration, as quantified by RDF values greater than unity, but the peak in the RDF shifts towards separations larger than η for higher St_η .

Turbulence-induced clustering of high-inertia particles has potential applications in many astrophysical environments, such as the interstellar medium, protoplanetary disks, and the atmospheres of planets and dwarf stars [16, 63]. A phenomenon of significant interest in Astrophysics is the formation of planetesimals from dust particles in protoplanetary disks. An intriguing possibility that astrophysicists are investigating is whether gas-turbulence-driven dispersion, sedimentation, collisional coalescence and fragmentation of dust particles play an important role in the formation of planetesimals. Particle preferential concentration at separations in the inertial subrange is of particular interest to the problem of planetesimal formation, where the Stokes numbers of relevance are estimated to be $St_\eta \sim 10$ -100 [63]. The proposed high-Stokes-number theory would be directly applicable in this scenario.

In a DNS study of inertial particle dynamics in isotropic turbulence by Sundaram and Collins [91], it was observed that the PDF of particle-pair relative velocity was Gaussian at pair separations of the order of the turbulent integral length scale, and that this PDF became increasingly non-Gaussian (exponential) as the separation decreased. Particle motion at smaller separations (compared to, say, the integral length scale) will be strongly correlated due to the influence of the fluid, giving rise to the non-Gaussian relative velocity PDF. At larger separations, particles will be

less correlated because turbulent fluctuations effectively behave like Gaussian white noise, leading to a Gaussian relative velocity PDF.

The motion of disperse particles in turbulent flows is inherently stochastic due to the turbulence-driven random fluctuating forces acting on the particles. Hence, a PDF equation-based approach presents a natural avenue to study particle-laden turbulent flows. However, this approach poses a closure problem in the form of a diffusion current term that arises when one averages the phase-space density equation over an ensemble of particle initial conditions and flow realizations. Reeks [71, 73, 70, 72], and Hyland et al. [37] are among the seminal fundamental studies on the PDF kinetic equation approach to model particle transport in turbulent flows.

The PDF kinetic equation approach of Reeks and coworkers considered the single-particle PDF $\langle P(\mathbf{v}, \mathbf{x}; t) \rangle$ whose phase space consists of particle velocity and position vectors \mathbf{v} and \mathbf{x} , respectively. In Reeks [71], the Eulerian Direct Interaction (EDI) approximation [43] was used to close the diffusion current term. In a subsequent study, Reeks [73] showed that in order to preserve invariance to a random Galilean transformation (RGT), the diffusion current should be of following form:

$$\mathbf{j} = - \left(\frac{\partial}{\partial \mathbf{v}} \cdot \boldsymbol{\mu} + \frac{\partial}{\partial \mathbf{x}} \cdot \boldsymbol{\lambda} + \boldsymbol{\gamma} \right) \langle P(\mathbf{v}, \mathbf{x}; t) \rangle \quad (2.1)$$

where \mathbf{j} represents the phase-space diffusion current, $\boldsymbol{\mu}$ and $\boldsymbol{\lambda}$ are diffusion tensors, and $\boldsymbol{\gamma}$ is a drift vector. In an improvement over Reeks [71], Reeks derived a closure for the diffusion current in the particle PDF equation by using Kraichnan's Lagrangian-history direct interaction (LHDI) approximation [44] in conjunction with

a renormalized perturbation theory. One of the important advantages of LHDI is that it preserves RGT invariance. Subsequently, Hyland et al. [37] adopted the Furutsu-Novikov-Donsker (FND) formula to derive closed-form expressions for the two diffusion terms in (2.1).

In an important theoretical study, Pozorski and Minier [65] discussed the significance of the choice of state variables in the PDF equation-based modeling of two-phase flows. They presented two broad formulations depending upon the choice of the state vector. The first formulation considered a state space that included only the particle position and velocity, \mathbf{x} and \mathbf{v} respectively. This is a traditional approach that is used in [73, 37], as well as in the current study (although we consider relative quantities and not single-particle quantities). The first approach gives rise to a diffusion current closure of the form in (2.1). In the second approach, the state vector also includes the fluid velocity “seen” by the particles, \mathbf{u} . Inclusion of \mathbf{u} in the state vector necessitates a Langevin evolution equation of the form $d\mathbf{u}/dt = \mathbf{A}$. The PDF equation for the enlarged state space, $(\mathbf{x}, \mathbf{v}, \mathbf{u})$, now has a new unknown term $\langle \mathbf{A} | \mathbf{x}, \mathbf{v}, \mathbf{u} \rangle$. To achieve closure, Pozorski and Minier [65] proposed a Langevin model for the time evolution of the “seen” fluid velocity.

Gardiner [30], and subsequently Pozorski and Minier [65], observed that one retains the temporally slowly-varying quantities in the state vector, while removing the quickly-varying ones. Gardiner (1990) demonstrated that in dynamical systems characterized by widely separated timescales, one is typically not interested in system variations occurring on very short timescales, and refers to such variables as “fast variables.” He further says that fast variables are effectively slaved by slow variables,

meaning that by the time the latter have relaxed to a steady-state, the fast variable values can simply be determined using the steady-state values of the slow variables. Pozorski & Minier (1999) discuss the replacement of removed fast variables with models containing their equilibrium values along with white-noise terms.

The preceding discussion is directly applicable to the current study, where the reference time-scale is the particle viscous relaxation time, τ_v . This means that the particle variables of interest such as the pair separation and relative velocity vary over times $\sim \tau_v$. In the asymptotic limit of Stokes number $St_r = \tau_v/\tau_r \gg 1$, where τ_r is the time-scale of an eddy whose size scales with separation r , the fluid timescales impacting the pair relative motion are much smaller than τ_v , and hence the seen fluid relative velocity is a fast variable. This justifies the elimination of the seen fluid relative velocity $\Delta \mathbf{u}$ from the state vector. In this context, it is also relevant to discuss the study by Reeks [72]. In that study, Reeks rigorously examined the purported differences between the above two approaches to stochastic modeling of particle-laden flows: the kinetic PDF model (KM) pioneered by Reeks, and the generalized Langevin model (GLM) pioneered by Simonin et al. [87] and Pozorski and Minier [65]. The principal differences between KM and GLM are with regard to the non-inclusion or inclusion, respectively, of \mathbf{u} in the state vector, and the different closure requirements this entails (note that Reeks was considering single particle dynamics). Reeks asserted that KM and GLM will, in principle, give identical results provided the modeling inputs to both approaches are the same. For instance, integrating the GLM PDF equation over all the fluid velocities local to the particles will yield an equation that is identical to the KM PDF equation. However, if the closures for the unknown terms

in the two approaches are fundamentally different, then the closed PDF equations for the two approaches, and thereby their predictions, will differ. Reeks demonstrated that the differences between the two approaches can be attributed to the neglect of the inertial convection term in the GLM equation for the mean carrier flow velocity seen by the particle.

[65] elucidate the implications of the choice of the state vector in the KM approach, and more importantly, the properties of the PDF kinetic equation resulting from such a choice. This equation has a form that is apparently analogous to the Fokker-Planck equation. [73], however, shows that the PDF equation becomes the classical Fokker-Planck equation only for asymptotically large particle Stokes numbers when one may represent the underlying turbulence as white noise. [65] bring out a more crucial difference between the PDF kinetic equation and the Fokker-Planck equation. This difference relates to the fact that in the kinetic equation, the diffusion block matrix \mathbf{B} formed from the diffusion tensors $\boldsymbol{\lambda}$ and $\boldsymbol{\mu}$ (see (1.1)) is not positive definite, whereas for the classical Fokker-Planck equation \mathbf{B} is positive definite. This would mean that \mathbf{B} for the kinetic equation has at least one negative eigenvalue so the effects of turbulence on particles for that eigenvalue are manifested as “antidiffusion” behavior in the phase space. Since the current study specifically considers the asymptotic limit of $St_r \gg 1$, the PDF equation reduces to the classical Fokker-Planck equation for the PDF of pair separation and relative velocity.

In their encyclopedic monograph, [55] provide an overview of the PDF methods for studying particle-laden turbulent flows. For instance, the principle of the elimination of fast variables from the state vector was illustrated in detail, and provides the

basis for the removal of the the “seen” fluid relative velocity $\Delta \mathbf{u}$ from the state vector in the current study. They also show that the effects of the eliminated fast variable may be modeled as a white noise term represented using a Wiener increment in the stochastic differential equation or the Langevin equation governing the slow variable. The relevant slow variable in the present study is the pair relative velocity \mathbf{U} , whose Langevin evolution equation contains a white noise term modeling the effects of the underlying fluid turbulence on pair relative velocity. The consequence of the white noise representation is that this term is manifested as a phase-space diffusion current characterized by a diffusion tensor in the Fokker-Planck equation governing the PDF of pair relative motion.

In a precursor study to the current one, Zaichik and Alipchenkov [100] developed a stochastic model based on the kinetic equation for the joint PDF of pair separation and relative velocity. Although the current study and Zaichik and Alipchenkov [100] are similar in this respect, i.e. a stochastic investigation of particle-pair relative motion, there are important fundamental distinctions between the two studies. The principal difference lies in the approach adopted to close the diffusion current in the PDF equation. Zaichik and Alipchenkov [100] achieved closure by using the Furutsu-Novikov-Donsker (FND) formula wherein the diffusion current was expressed in terms of the second-order cumulants (or moments) of the fluid relative velocities “seen” by the inertial particle pairs. Swailes and Darbyshire [92] showed that the diffusion current, in principle, can be written as an infinite series expansion comprising fluid velocity cumulants of all integral orders. The FND formula is a special case of this generalized expansion, where only the first- and second-order cumulants are

non-zero, and all others are exactly zero (due to the Gaussian random function assumption inherent to FND). For isotropic turbulence, the first-order cumulant is also zero. Therefore, the assumption implicit in Zaichik and Alipchenkov [100] is that the fluid relative velocities are Gaussian. This assumption is reasonable for large-scale eddies driving the relative motion of pairs at integral-scale separations [5]. But, it is questionable at separations in the inertial and dissipative subranges. The increasing non-Gaussianity of the relative velocities of fluid particles as their separations approached the Kolmogorov scale was discussed by Minier and Peirano [55]. This was also confirmed by the DNS of Gualtieri et al. [34] who showed that the PDF of fluid relative velocity at a separation $r/\eta = 8$ is Gaussian only for small values of relative velocity, and that the PDF quickly deviates away from being Gaussian at larger values. The current study does not use the FND formula to achieve closure, but is based on a perturbation analysis of the pair PDF equation.

Using the FND formula, Zaichik and Alipchenkov [100] expressed the particle-eddy interaction (diffusion current) term in the PDF equation as a combination of: (i) a diffusion term in the relative velocity space, and (ii) a cross diffusion term in the separation-relative-velocity space. Both the diffusion terms contain the time-integral of the two-point, two-time Lagrangian correlation of fluid relative velocities along pair trajectories. In order to close these correlations, they further assumed that the correlation of fluid relative velocities along inertial pair trajectories is the same as that along fluid pair trajectories. It is evident that this assumption is appropriate only for Stokes number $St < 1$ when one may assume that the deviation in the trajectories of inertial and fluid particles is not significant. Therefore, the Zaichik and Alipchenkov

[100] theory is most appropriate for small Stokes number particles. In the current study, we consider high St particles, which enables us to develop an alternative closure for the Lagrangian correlations. This is the second major difference between the two studies.

Another important difference concerns the simulation approach adopted in the two studies. In order to predict pair dispersion and particle preferential accumulation in isotropic turbulence, Zaichik and Alipchenkov [100] solved the governing equations for the zeroeth, first and second relative-velocity moments of the pair PDF. These moments equations were derived from the fully closed pair PDF equation, but they all contain unclosed higher order moment terms. In the current study, we simulate the Langevin equations, which are equivalent to the Fokker-Planck equation in a weak sense, to evolve the relative velocity and separation vectors of a large number of particle pairs. When compared to solving a finite number of PDF moments equations, the Langevin approach is higher order accurate in the sense that the Langevin simulations inherently include all moments of the pair PDF. Another advantage of this approach is that it allows us to explicitly compute the PDFs of pair relative velocity at various separations, thereby enabling us to track the transition in the nature of the PDF as the separations are reduced from the order of integral scale to Kolmogorov scale. The moments equations-based approach also presents the conundrum of additional closure problems since an equation for a given moment contains the next higher order moment. This leads to a chain of an infinite number of equations, which is typically broken by assuming that the moments of a certain order or higher are zero. For example, in Zaichik and Alipchenkov [100], fourth and higher order mo-

ments are set to zero, and the third order moments are closed in terms of the second moments using the gradient transport approximation which is likely to be quite poor when the relative velocity PDF is far from Gaussian as we find it is. This problem is completely obviated through the Langevin equations approach since there are no additional closure issues.

Finally, the two studies also differ in the state vectors that they consider in order to derive the final form of the pair PDF equation. Zaichik and Alipchenkov [100] considered a state vector comprising only the pair separation and relative velocity, \mathbf{r} and \mathbf{U} , respectively. The current study begins with the high-dimensional PDF $P(\mathbf{r}, \mathbf{U}, \mathbf{x}, \mathbf{V}; t)$, where the state vector includes the particle-pair center of mass position and velocity \mathbf{x} and \mathbf{V} , respectively, in addition to \mathbf{r} and \mathbf{U} . The need to include \mathbf{x} and \mathbf{V} arises naturally since we do not approximate inertial pair trajectories to be the same as fluid pair trajectories. The state vector $(\mathbf{r}, \mathbf{U}, \mathbf{x}, \mathbf{V})$ allows one to account for not only the relative motion of a particle pair, but also the dynamics of the pair center-of-mass. The inclusion of \mathbf{x} and \mathbf{V} in the state space has an important benefit in that it enables us to determine the orders of magnitude of the various terms representing the dynamics of the center-of-mass in the P equation. The order-of-magnitude information will help us identify the conditions under which certain terms may be neglected when performing a perturbation analysis of the PDF equation. For instance, we incorporate into the diffusion coefficient tensor the effects of change in \mathbf{x} during integral timescales due to the velocity \mathbf{V} through the relative velocity vector $\mathbf{W} = \mathbf{u}_I - \mathbf{V}$. Here \mathbf{u}_I is the velocity with which eddies of size

r are passively advected past the center-of-mass by the large-scale eddies (cf. eqs. (2.23-2.26) and eqs. (2.46-2.53)).

Using the radial distribution functions (RDFs), Zaichik and Alipchenkov [100] demonstrated that high St_η particles show preferential concentration at length scales that are much larger than η , and are scaled by the integral length scale (L). Their study also predicts that for $St_\eta \geq 4$, the RDF plateaus (i.e. nearly zero slope in a log-log plot) for separations smaller than some multiples of the Kolmogorov length scale. For $St_\eta = 10$, Zaichik and Alipchenkov [100] show a plateauing of the RDF for separations $r \lesssim 10\eta$. In contrast, our theory predicts the plateauing of the RDF to begin at smaller separations $r \sim \eta$ for $St_\eta = 10$, which is consistent with the DNS of Pan et al. [63].

In a stochastic and computational study, Chun et al. [18] studied particle relative motion in the limit of $St_\eta \ll 1$. This study was concerned with particle-pair separations smaller than the Kolmogorov length scale, where the pair relative motion is principally determined by the dissipation range of the turbulent energy spectrum. They also assumed a locally linear flow for the fluid velocity difference along the pair trajectory. Using a state space comprising only the pair separation vector \mathbf{r} , they derived the PDF equation consisting of drift and diffusion terms. The closure of the two terms involved expanding the pair relative velocity, \mathbf{w} , as a perturbation expansion in Stokes number (St_η), and retaining only the zeroth- and first-order terms in St_η . This results in a drift velocity $\sim St_\eta^2$, and a diffusion coefficient $\sim r^2$, where r is the particle separation.

Pan and Padoan [57] derived an analytical model for the relative velocity of both monodisperse and bidisperse inertial particles in turbulent flows. Their objective was to derive a model that captures particle relative motion for all particle response times, i.e., $\tau_v \ll \tau_\eta$, $\tau_v \gg \tau_I$, as well as $\tau_\eta \lesssim \tau_v \lesssim \tau_I$. Here τ_I is the integral time-scale. Their model is conceptually based on the approach of Ayala et al. [3]. However, Ayala et al. [3] only considered particle separation due to gravity for sedimenting droplets in turbulent flows, and neglected particle relative motion due to turbulent dispersion. When developing an analytical model for particle relative velocity that includes turbulent dispersion, one invariably encounters two-point two-time correlations of fluid relative velocities along pair trajectories. As was done in earlier studies [37, 100, 102, 20], Pan and Padoan [57] approximated these correlations as being those along fluid particle-pair trajectories. In this respect, our study differs from these studies in that fluid relative-velocity correlations along inertial pair trajectories are converted, in the limit of high Stokes number, into Eulerian two-point fluid velocity correlations.

Recently, Goswami and Kumaran [32, 33] performed both DNS and Langevin stochastic simulations of high Stokes number particle dynamics in a turbulent Couette flow. In their stochastic model, they began by considering the Boltzmann equation for the particle fluctuating velocity PDF, which is reduced to a Fokker-Planck equation. However, the derivation behind modeling particle-eddy interactions as a Fokker-Planck-type diffusion term was not provided. It is important to note that the assumption that allows one to derive the Fokker-Planck equation is that the particle response time is much greater than the decay time for the fluid velocity

fluctuations. In their Langevin simulations, the stochastic forcing term, $\mathbf{F}(t)$, is modelled as Gaussian white noise with zero mean and a second moment given by $\langle F_i(t)F_j(t') \rangle = 2D_{ij}\delta(t-t')$, where D_{ij} is the diffusion coefficient tensor in the particle velocity space (in the current study, diffusion coefficient is in the pair relative velocity space). Diffusion coefficient, D_{ij} , is expressed in terms of a time-integral of the Lagrangian fluid velocity correlation tensor. They, however, do not derive an explicit expression for the diffusion coefficient, and instead compute it using the fluid velocity autocorrelation data obtained from their DNS.

In a notable recent study, [8] performed a first-principles-based comparison of three well-known approaches for closing the diffusion current in the particle PDF kinetic equation. They are the Furutsu-Novikov-Donsker (FND) method, LHDI of Reeks [71], and van Kampen’s operator representation technique [65]. Specifically, they investigated whether the closures obtained from these approaches are all equivalent, as is commonly accepted. Through a remarkably fundamental analysis of the implications of these approaches, they prove that the equivalence breaks down in two scenarios: (1) when the underlying turbulence is inhomogeneous, and (2) when the particles are inertialess, i.e. fluid particles, in which case the zero-drift or the fully mixed condition should be recovered. It is seen that only the FND method provides a closure that satisfies the zero-drift condition in both homogeneous and inhomogeneous incompressible systems.

In the current study, starting with the high-dimensional PDF equation governing the relative and correlated motion of particle pairs, we derive the transport equation for the PDF $\Omega(\mathbf{r}, \mathbf{U})$ of pair separation (\mathbf{r}) and relative velocity (\mathbf{U}) of

high Stokes number particles. The transport equation for $\Omega(\mathbf{r}, \mathbf{U})$, which is of the Fokker-Planck type, contains a diffusion coefficient tensor that can be expressed as $1/\tau_v^2$ times the time-integral of the Lagrangian correlation of fluid relative velocities along the pair trajectory. These Lagrangian correlations also need to be closed. One way to overcome this closure problem is to perform DNS of particle-laden turbulence and collect the correlation statistics. A different approach would be to develop a theoretical closure, which would necessitate certain assumptions. For example, in Zaichik and Alipchenkov [100], the Lagrangian correlations are assumed to be correlations along fluid particle trajectories. This assumption, however, is most appropriate in the limit of small particle Stokes number. In the current study, we begin by developing an alternative closure in the the limit of $St_I \gg 1$ and $St_r \gg 1$. Here St_I and St_r are the Stokes numbers based on the integral time-scale τ_I and the time-scale τ_r of an eddy of size r , respectively. Subsequently, the closure is extended to $St_I \lesssim 1$ particles by accounting for the motion of the pair center-of-mass. It is to be noted that the $St_r \gg 1$ requirement is much less stringent when compared to $St_I \gg 1$. Finally, in the limit of $St_r \gg 1$ but $St_I \lesssim 1$, the Lagrangian two-point, two-time correlation is systematically converted first into an Eulerian two-time correlation, and subsequently into an Eulerian two-point correlation. For isotropic turbulence, these Eulerian velocity correlations can be conveniently expressed as Fourier transforms of the velocity spectrum tensor.

After deriving the closure for the diffusion tensor, the Fokker-Planck equation is solved in a weak sense by solving the corresponding Langevin equations to evolve the relative velocity and separation vectors of a large number of particle pairs. The

Langevin simulations, also referred to as Monte-Carlo simulations, may be contrasted with an approach in which the governing equations for the first few moments of the PDF are derived and solved. The latter approach was adopted in Zaichik and Alipchenkov [100].

The chapter is organized as follows: Section 2.3 presents the complete theoretical basis of this study. Section 2.4 discusses the Langevin-equation-based simulations used to compute the relative velocity PDFs, and the RDFs. Results from the Langevin equation simulations are presented and their implications discussed in Section 2.5.

2.3 Theory

In Section 2.3.1, the particle-pair phase-space density equation along with the pair Lagrangian governing equations are presented. In Section 2.3.2, the phase-space density equation is shown to reduce to the Fokker-Planck equation in the limit of $St_r \gg 1$. Closure is developed for the diffusion tensor, which is then extended to $St_I \lesssim 1$ particles through a finite St_I model for the relative velocity \mathbf{W} between the fluid eddies (that are advected past the particle-pair by integral-scale eddies) and the pair center of mass; the expression for W_{rms} , the r.m.s. of \mathbf{W} , needed for this extension is derived in Section 2.3.3.

2.3.1 Phase-Space Density Equation

For a dispersion of high-Stokes-number particles in stationary homogeneous isotropic turbulence, we consider the phase-space density (PSD), $P(\mathbf{R}_1, \mathbf{R}_2, \mathbf{U}_1, \mathbf{U}_2; t)$, that two particles take phase-space positions and velocities \mathbf{R}_1 and \mathbf{R}_2 , and \mathbf{U}_1 and

\mathbf{U}_2 , respectively. The two-particle PSD is equivalent to $P(\mathbf{r}, \mathbf{U}, \mathbf{x}, \mathbf{V}; t)$, which is the PSD of a particle pair with separation \mathbf{r} , relative velocity \mathbf{U} , center-of-mass position \mathbf{x} , and center of mass velocity \mathbf{V} . The current notation, definition, and significance of the PSD are discussed in Section 2.7. The relative motion of particle pairs will depend not only on their separation and relative velocity vectors, but also on the dynamics of the pair center-of-mass that can influence the way the pair samples the fluid velocity field. Conservation of PSD P yields:

$$\frac{\partial P}{\partial t} + \nabla_{\mathbf{r}} \cdot (\dot{\mathbf{r}}P) + \nabla_{\mathbf{U}} \cdot (\dot{\mathbf{U}}P) + \nabla_{\mathbf{x}} \cdot (\dot{\mathbf{x}}P) + \nabla_{\mathbf{V}} \cdot (\dot{\mathbf{V}}P) = 0 \quad (2.2)$$

where $\nabla_{\mathbf{r}}$, $\nabla_{\mathbf{x}}$, $\nabla_{\mathbf{U}}$, and $\nabla_{\mathbf{V}}$ represent gradients with respect to the corresponding variables.

The governing equations for \mathbf{r} , \mathbf{U} , \mathbf{x} , and \mathbf{V} are:

$$\frac{d\mathbf{r}}{dt} = \mathbf{U} \quad (2.3)$$

$$\frac{d\mathbf{U}}{dt} = -\frac{1}{\tau_v} [\mathbf{U}(t) - \Delta\mathbf{u}(\mathbf{r}, \mathbf{x}, t)] \quad (2.4)$$

$$\frac{d\mathbf{x}}{dt} = \mathbf{V} \quad (2.5)$$

$$\frac{d\mathbf{V}}{dt} = -\frac{1}{\tau_v} \left[\mathbf{V}(t) - \frac{\mathbf{u}(\mathbf{R}_1(t), t) + \mathbf{u}(\mathbf{R}_2(t), t)}{2} \right] = -\frac{1}{\tau_v} [\mathbf{V}(t) - \mathbf{u}_{\text{cm}}(\mathbf{R}_1(t), \mathbf{R}_2(t), t)] \quad (2.6)$$

where τ_v is the particle response time, $\Delta\mathbf{u}(\mathbf{r}, \mathbf{x}, t) = [\mathbf{u}(\mathbf{R}_2(t), t) - \mathbf{u}(\mathbf{R}_1(t), t)]$ is the fluid relative velocity along the pair trajectory, and $\mathbf{u}_{\text{cm}}(\mathbf{R}_1(t), \mathbf{R}_2(t), t) = [\mathbf{u}(\mathbf{R}_1(t), t) +$

$\mathbf{u}(\mathbf{R}_2(t), t)]/2$. Here \mathbf{u}_{cm} may be interpreted as the fluid velocity influencing the dynamics of the pair center-of-mass, but is *not* the fluid velocity at the center-of-mass location. The velocity \mathbf{u}_{cm} can be determined from \mathbf{x} and \mathbf{r} since $\mathbf{R}_2 = \mathbf{x} + \frac{\mathbf{r}}{2}$ and $\mathbf{R}_1 = \mathbf{x} - \frac{\mathbf{r}}{2}$. In (2.4) and (2.6), we assume that the fluid drag force is the predominant force acting on the particles and that the Stokes drag law is valid. Accordingly, the particle response time is defined as $\tau_v = \rho_p d_p^2 / 18\mu$, where ρ_p is the particle density, d_p is the particle diameter, and μ is the dynamic viscosity of the fluid.

Substituting (2.3)-(2.6) into (2.2) yields

$$\begin{aligned} \frac{\partial P}{\partial t} + \nabla_{\mathbf{r}} \cdot (\mathbf{U}P) + \nabla_{\mathbf{x}} \cdot (\mathbf{V}P) - \frac{1}{\tau_v} \nabla_{\mathbf{U}} \cdot (\mathbf{U}P) - \frac{1}{\tau_v} \nabla_{\mathbf{V}} \cdot (\mathbf{V}P) \\ + \frac{1}{\tau_v} \nabla_{\mathbf{U}} \cdot (\Delta \mathbf{u}P) + \frac{1}{\tau_v} \nabla_{\mathbf{V}} \cdot (\mathbf{u}_{\text{cm}}P) = 0 \end{aligned} \quad (2.7)$$

2.3.2 Perturbation Analysis

In this section, the PSD equation (2.7) is transformed into a Fokker-Planck equation under the condition that the changes in pair relative velocity during the correlation times of eddies impacting their relative motion are small compared to the pair relative velocity itself. To model pair-eddy interactions as a Fokker-Planck-type diffusion term, we begin by averaging (2.7) over an ensemble of flow realizations, giving us:

$$\begin{aligned} \frac{\partial \langle P \rangle}{\partial t} + \nabla_{\mathbf{r}} \cdot (\mathbf{U} \langle P \rangle) + \nabla_{\mathbf{x}} \cdot (\mathbf{V} \langle P \rangle) - \frac{1}{\tau_v} \nabla_{\mathbf{U}} \cdot (\mathbf{U} \langle P \rangle) - \frac{1}{\tau_v} \nabla_{\mathbf{V}} \cdot (\mathbf{V} \langle P \rangle) \\ + \frac{1}{\tau_v} \nabla_{\mathbf{U}} \cdot \langle \Delta \mathbf{u}P \rangle + \frac{1}{\tau_v} \nabla_{\mathbf{V}} \cdot \langle \mathbf{u}_{\text{cm}}P \rangle = 0 \end{aligned} \quad (2.8)$$

where $\langle \cdot \rangle$ represents ensemble averaging, and the terms $\langle \Delta \mathbf{u} P \rangle$ and $\langle \mathbf{u}_{\text{cm}} P \rangle$ represent turbulence-particle interactions. Since \mathbf{U} and \mathbf{V} are independent variables (like time t), $\langle \mathbf{U} P \rangle = \mathbf{U} \langle P \rangle$ and $\langle \mathbf{V} P \rangle = \mathbf{V} \langle P \rangle$.

As a first step toward modelling $\langle \Delta \mathbf{u} P \rangle$ and $\langle \mathbf{u} P \rangle$, consider

$$\langle \Delta \mathbf{u} P \rangle = \langle \Delta \mathbf{u} (\langle P \rangle + P') \rangle = \langle \Delta \mathbf{u} P' \rangle$$

where we have used the relations: $P = \langle P \rangle + P'$, and $\langle \Delta \mathbf{u} \rangle = 0$ for isotropic turbulence. Here, P' is a fluctuation in P from the PDF $\langle P \rangle$. Similarly, $\langle \mathbf{u}_{\text{cm}} P \rangle = \langle \mathbf{u}_{\text{cm}} P' \rangle$.

We will show that in the limit of high Stokes number, we can express the last two terms of (2.8) as Fokker-Planck-type diffusion terms. Substituting $P = \langle P \rangle + P'$ into (2.7), and moving terms containing $\langle P \rangle$ to the RHS, we get:

$$\begin{aligned} & \frac{\partial P'}{\partial t} + \nabla_{\mathbf{r}} \cdot (\mathbf{U} P') + \nabla_{\mathbf{x}} \cdot (\mathbf{V} P') - \frac{1}{\tau_v} \nabla_{\mathbf{U}} \cdot (\mathbf{U} P') - \frac{1}{\tau_v} \nabla_{\mathbf{V}} \cdot (\mathbf{V} P') \\ & + \frac{1}{\tau_v} \nabla_{\mathbf{U}} \cdot (\Delta \mathbf{u} P') + \frac{1}{\tau_v} \nabla_{\mathbf{V}} \cdot (\mathbf{u}_{\text{cm}} P') = \\ & - \left[\frac{\partial \langle P \rangle}{\partial t} + \nabla_{\mathbf{r}} \cdot (\mathbf{U} \langle P \rangle) + \nabla_{\mathbf{x}} \cdot (\mathbf{V} \langle P \rangle) - \frac{1}{\tau_v} \nabla_{\mathbf{U}} \cdot (\mathbf{U} \langle P \rangle) - \frac{1}{\tau_v} \nabla_{\mathbf{V}} \cdot (\mathbf{V} \langle P \rangle) \right. \\ & \left. + \frac{1}{\tau_v} \nabla_{\mathbf{U}} \cdot (\Delta \mathbf{u} \langle P \rangle) + \frac{1}{\tau_v} \nabla_{\mathbf{V}} \cdot (\mathbf{u}_{\text{cm}} \langle P \rangle) \right] \end{aligned} \quad (2.9)$$

Subtracting (2.8) from (2.9), and making terms dimensionless with the integral length scale (L), integral time scale (τ_I), and isotropic turbulence r.m.s. fluctuating velocity

(u_{rms}) , yields:

$$\begin{aligned}
& \frac{\partial P'}{\partial t} + \nabla_{\mathbf{r}} \cdot (\mathbf{U}P') + \nabla_{\mathbf{x}} \cdot (\mathbf{V}P') - \frac{1}{St_I} \nabla_{\mathbf{U}} \cdot (\mathbf{U}P') - \frac{1}{St_I} \nabla_{\mathbf{V}} \cdot (\mathbf{V}P') \\
& + \frac{1}{St_I} \nabla_{\mathbf{U}} \cdot (\Delta \mathbf{u}P') + \frac{1}{St_I} \nabla_{\mathbf{V}} \cdot (\mathbf{u}_{\text{cm}}P') = -\frac{1}{St_I} \nabla_{\mathbf{U}} \cdot (\Delta \mathbf{u}\langle P \rangle) \\
& - \frac{1}{St_I} \nabla_{\mathbf{V}} \cdot (\mathbf{u}_{\text{cm}}\langle P \rangle) + \frac{1}{St_I} \nabla_{\mathbf{U}} \cdot \langle \Delta \mathbf{u}P' \rangle + \frac{1}{St_I} \nabla_{\mathbf{V}} \cdot \langle \mathbf{u}_{\text{cm}}P' \rangle \quad (2.10)
\end{aligned}$$

Since $\langle P \rangle$ accounts for averaging over fluid time scales, but particles relax over longer timescales $\sim \tau_v$, one can expect a perturbation of P with respect to $\langle P \rangle$.

Writing P as a perturbation expansion in terms of $\frac{1}{St_I}$,

$$P = P_0 + \frac{1}{St_I} P_1 + O\left(\frac{1}{St_I^2}\right) \quad (2.11)$$

where $St_I = \tau_v/\tau_I$ is the particle Stokes number defined with respect to the turbulence integral time-scale τ_I . Comparing $P = \langle P \rangle + P'$ with (2.11), we can see that $\langle P \rangle = P_0$, and that to leading order $P' \sim \frac{1}{St_I} P_1$. We can now see from (2.10) that the last four terms on the LHS and the last two terms on the RHS are $O(1/St_I^2)$, while the remaining terms are all $O(1/St_I)$.

Considering the $O(1/St_I)$ terms in (2.10), we get:

$$\frac{\partial P_1}{\partial t} + \nabla_{\mathbf{r}} \cdot (\mathbf{U}P_1) + \nabla_{\mathbf{x}} \cdot (\mathbf{V}P_1) = -\nabla_{\mathbf{U}} \cdot (\Delta \mathbf{u}\langle P \rangle) - \nabla_{\mathbf{V}} \cdot (\mathbf{u}_{\text{cm}}\langle P \rangle) \quad (2.12)$$

Equation (2.12) is a Lagrangian evolution equation of P_1 in the $(\mathbf{r}, \mathbf{x}, t)$ space, with \mathbf{U} and \mathbf{V} held fixed; (2.12) may then be written as

$$\left. \frac{dP_1}{dt} \right|_{\mathbf{U}, \mathbf{V}} = -\nabla_{\mathbf{U}} \cdot (\Delta \mathbf{u} \langle P \rangle) - \nabla_{\mathbf{V}} \cdot (\mathbf{u}_{\text{cm}} \langle P \rangle) \quad (2.13)$$

From (2.13), we can write:

$$\begin{aligned} P_1 &= - \int_{-\infty}^s dt' \{ \nabla_{\mathbf{U}} \cdot [\Delta \mathbf{u}(\mathbf{r}(t'), \mathbf{x}(t'), t') \langle P \rangle(\mathbf{r}', \mathbf{U}, \mathbf{x}', \mathbf{V}; t')] + \\ &\quad \nabla_{\mathbf{V}} \cdot [\mathbf{u}_{\text{cm}}(\mathbf{R}_1(t'), \mathbf{R}_2(t'), t') \langle P \rangle(\mathbf{r}', \mathbf{U}, \mathbf{x}', \mathbf{V}; t')] \} \\ &= - \int_{-\infty}^s dt' \{ \Delta \mathbf{u}(\mathbf{r}(t'), \mathbf{x}(t'), t') \cdot \nabla_{\mathbf{U}} \langle P \rangle(t') + \\ &\quad \mathbf{u}_{\text{cm}}(\mathbf{R}_1(t'), \mathbf{R}_2(t'), t') \cdot \nabla_{\mathbf{V}} \langle P \rangle(t') \} \end{aligned} \quad (2.14)$$

where $\mathbf{r}' = \mathbf{r}(t')$, $\mathbf{x}' = \mathbf{x}(t')$, and s is a characteristic variable along the Lagrangian trajectory such that $\frac{dt}{ds} = 1$, and $\frac{d\mathbf{x}'}{dt'}|_{t'=s} = \mathbf{V}$ and $\frac{d\mathbf{r}'}{dt'}|_{t'=s} = \mathbf{U}$. At the upper integration limit s , we have $\mathbf{r}(s) = \mathbf{r}(t) = \mathbf{r}$. We have also used the shorthand notation $\langle P \rangle(t') = \langle P \rangle(\mathbf{r}', \mathbf{U}, \mathbf{x}', \mathbf{V}; t')$. The integral in (2.14) can be reduced to a time integral at fixed positions if the two convective terms on the LHS of (2.12) can be neglected compared to $\frac{\partial P_1}{\partial t}$, which would yield

$$\begin{aligned} \langle \Delta \mathbf{u} P' \rangle &= -\frac{1}{St_I^2} \int_{-\infty}^t dt' \{ \langle \Delta \mathbf{u}(\mathbf{r}, \mathbf{x}, t) \Delta \mathbf{u}(\mathbf{r}, \mathbf{x}, t') \rangle \cdot \nabla_{\mathbf{U}} \langle P \rangle(t') + \\ &\quad \langle \Delta \mathbf{u}(\mathbf{r}, \mathbf{x}, t) \mathbf{u}_{\text{cm}}(\mathbf{R}_1(t), \mathbf{R}_2(t), t') \rangle \cdot \nabla_{\mathbf{V}} \langle P \rangle(t') \} \end{aligned} \quad (2.15)$$

$$\begin{aligned} \langle \mathbf{u}_{\text{cm}} P' \rangle = & -\frac{1}{St_I^2} \int_{-\infty}^t dt' \{ \langle \mathbf{u}_{\text{cm}}(\mathbf{R}_1(t), \mathbf{R}_2(t), t) \Delta \mathbf{u}(\mathbf{r}, \mathbf{x}, t') \rangle \cdot \nabla_{\mathbf{U}} \langle P \rangle(t') + \\ & \langle \mathbf{u}_{\text{cm}}(\mathbf{R}_1(t), \mathbf{R}_2(t), t) \mathbf{u}_{\text{cm}}(\mathbf{R}_1(t), \mathbf{R}_2(t), t') \rangle \cdot \nabla_{\mathbf{V}} \langle P \rangle(t') \} \end{aligned} \quad (2.16)$$

In (2.15) and (2.16), \mathbf{r} and \mathbf{x} are essentially constant during flow timescales. The conditions under which the two convective terms on the LHS of (2.12) can be neglected are derived after (2.22). In (2.15) and (2.16), the PDF $\langle P \rangle$ is evaluated at time t' . The two-time fluid velocity correlations in (2.15) and (2.16) are significant only in the time interval $t - t'$ for which the fluid eddies are correlated. Therefore, we can write $\langle P \rangle(t') \approx \langle P \rangle(t)$, since the timescales over which $\langle P \rangle$ changes are much greater than the fluid correlation timescales. Pulling $\langle P \rangle$ out of the time integrals, and substituting (2.15) and (2.16) into the dimensionless form of (2.8), the Fokker-Planck equation can be written as:

$$\begin{aligned} & \frac{\partial \langle P \rangle}{\partial t} + \nabla_{\mathbf{r}} \cdot (\mathbf{U} \langle P \rangle) + \nabla_{\mathbf{x}} \cdot (\mathbf{V} \langle P \rangle) - \frac{1}{St_I} \nabla_{\mathbf{U}} \cdot (\mathbf{U} \langle P \rangle) - \frac{1}{St_I} \nabla_{\mathbf{V}} \cdot (\mathbf{V} \langle P \rangle) \\ & - \nabla_{\mathbf{U}} \cdot (D_{UU} \cdot \nabla_{\mathbf{U}} \langle P \rangle + D_{UV} \cdot \nabla_{\mathbf{V}} \langle P \rangle) \\ & - \nabla_{\mathbf{V}} \cdot (D_{VU} \cdot \nabla_{\mathbf{U}} \langle P \rangle + D_{VV} \cdot \nabla_{\mathbf{V}} \langle P \rangle) = 0 \end{aligned} \quad (2.17)$$

where

$$D_{UU} = \frac{1}{St_I^2} \tilde{D}_{UU} = \frac{1}{St_I^2} \int_{-\infty}^t dt' \langle \Delta \mathbf{u}(\mathbf{r}, \mathbf{x}, t) \Delta \mathbf{u}(\mathbf{r}, \mathbf{x}, t') \rangle \quad (2.18)$$

$$D_{UV} = \frac{1}{St_I^2} \tilde{D}_{UV} = \frac{1}{St_I^2} \int_{-\infty}^t dt' \langle \Delta \mathbf{u}(\mathbf{r}, \mathbf{x}, t) \mathbf{u}_{\text{cm}}(\mathbf{R}_1(t), \mathbf{R}_2(t), t') \rangle \quad (2.19)$$

$$D_{VU} = \frac{1}{St_I^2} \tilde{D}_{VU} = \frac{1}{St_I^2} \int_{-\infty}^t dt' \langle \mathbf{u}_{\text{cm}}(\mathbf{R}_1(t), \mathbf{R}_2(t), t) \Delta \mathbf{u}(\mathbf{r}, \mathbf{x}, t') \rangle \quad (2.20)$$

$$D_{VV} = \frac{1}{St_I^2} \tilde{D}_{VV} = \frac{1}{St_I^2} \int_{-\infty}^t dt' \langle \mathbf{u}_{\text{cm}}(\mathbf{R}_1(t), \mathbf{R}_2(t), t) \mathbf{u}_{\text{cm}}(\mathbf{R}_1(t), \mathbf{R}_2(t), t') \rangle \quad (2.21)$$

In (2.18)-(2.21), D_{UU} and D_{VV} are the diffusion coefficient tensors in the \mathbf{U} -space and \mathbf{V} -space, respectively; D_{UV} and D_{VU} are the cross-diffusion coefficient tensors in the mixed \mathbf{UV} and \mathbf{VU} spaces, respectively. These diffusion tensors (particularly D_{VV}) are analogous to the formulation of [73], who showed that the single-particle diffusion tensor contains Lagrangian correlations of fluid velocities “seen”. Subsequently, [55] demonstrated that the diffusion coefficient of the slow variable may be expressed as a time-integral of the temporal correlation of the fast variable, which is indeed what we observe in (2.18)-(2.21) as well. The diffusion coefficient tensors can also be interpreted as the time integrals of the two-time correlations of the accelerations of the pair relative and/or center-of-mass velocities caused by fluid velocity fluctuations. For example,

$$D_{UU} = \int_{-\infty}^t \langle \dot{\mathbf{U}}(t) \dot{\mathbf{U}}(t') \rangle dt' \quad (2.22)$$

where $\dot{\mathbf{U}}(t) = \frac{1}{St_I} \Delta \mathbf{u}(t) + O\left(\frac{1}{St_I^2}\right)$.

We will now derive, using an order-of-magnitude analysis, the conditions to be satisfied for neglecting the two convective terms in (2.12) so that the fluid velocity correlations seen by the particles can be approximated as those at fixed positions in space. The neglect of $\nabla_{\mathbf{x}} \cdot (\mathbf{V}P')$ compared with $\frac{\partial P'}{\partial t}$ requires that the change in the position of the pair center of mass during the integral-scale fluid correlation time be small compared with the integral length scale, i.e., $\langle V^2 \rangle^{1/2} \ll 1$. Since it is well known that $\langle V^2 \rangle \sim O\left(\frac{1}{St_I}\right)$ [73], this condition is satisfied for $St_I \gg 1$.

Neglecting $\nabla_r \cdot (\mathbf{U}P')$ compared to $\frac{\partial P'}{\partial t}$ requires that the change in pair separation (r) during the fluid correlation time τ_r of an eddy of size r to be small compared with the eddy size, i.e., $U\tau_r \ll r$. While this condition is not satisfied for all particle pairs, we will see that it is satisfied for those pairs that are significantly influenced by the fluid eddies of size r .

The relative velocity PDFs from Sundaram and Collins [91] indicate that at separations smaller than the integral length scale ($r/L < 1$) the high inertia ($St_\eta > 1$) particle pairs can be divided into two broad classes: “lingerers” and “flyers”. Lingerers are low-relative-velocity pairs that are highly correlated and remain correlated far longer than the timescales of fluid that influence their relative motion. Flyers are uncorrelated pairs with large relative velocities, whose relative motion is unaffected by the fluid eddies with length scales comparable with their separation. For a flyer pair with separation r , the change in relative velocity ΔU due to their interaction with a fluid eddy of size r is small compared with the pair relative velocity, i.e. $\Delta U \ll U$. For lingerers, $\Delta U \sim U$.

The change in the relative velocity of a pair while they interact at separation r is given by the square root of the velocity-space diffusivity times their interaction time, i.e., $\Delta U \sim (D_{UU}\tau_r)^{1/2}$, where τ_r is the time-scale of the fluid eddy of size r . For a “lingerer” pair, using $\Delta U \sim U$, we find that such pairs have a relative velocity $U \sim (D_{UU}r)^{1/3}$. In dimensional form, the relative-velocity-space diffusion coefficient is the product of the square of the acceleration due to the eddy $(u_{\text{eddy}}/\tau_v)^2$ and the correlation time of the eddy τ_r . Since $u_{\text{eddy}} \sim r/\tau_r$, $D_{UU} \sim r^2/(\tau_v^2\tau_r)$. Thus, the relative velocity for the lingerers is $U \sim r/(\tau_r\tau_v^2)^{1/3}$, and the change of the relative position during the fluid time-scale is $U\tau_r = rSt_r^{-2/3}$, where $St_r = \tau_v/\tau_r$ is the Stokes number defined based on the eddies of size r . We see then that the convective term in \mathbf{r} -space on the LHS of (2.12) can be neglected as long as the Stokes number based on eddies of size r is large, i.e. $St_r = \tau_v/\tau_r \gg 1$.

In the previous discussion, we derived a conservation equation for the high dimensional PDF, $\langle P \rangle(\mathbf{r}, \mathbf{U}, \mathbf{x}, \mathbf{V}; t)$. The dependence of $\langle P \rangle$ on \mathbf{x} can be dropped owing to the spatial homogeneity of the flow. Since we are primarily interested in the statistics of the pair relative velocity and relative position, we will consider a more convenient, lower dimensional PDF defined as: $\Omega(\mathbf{r}, \mathbf{U}) = \int \langle P \rangle(\mathbf{r}, \mathbf{U}, \mathbf{V}; t) d\mathbf{V}$. (The effects of \mathbf{x} and \mathbf{V} are included in the diffusion coefficient closure.)

Integrating (2.17) over the \mathbf{V} space, we get:

$$\frac{\partial \Omega}{\partial t} + \nabla_{\mathbf{r}} \cdot (\mathbf{U}\Omega) - \frac{1}{St_I} \nabla_{\mathbf{U}} \cdot (\mathbf{U}\Omega) - \frac{1}{St^2} \nabla_{\mathbf{U}} \cdot (\tilde{D}_{UU} \cdot \nabla_{\mathbf{U}}\Omega) = 0 \quad (2.23)$$

As discussed in [55] and [73], the Fokker-Planck equation governing the PDF $\Omega(\mathbf{r}, \mathbf{U})$ is a consequence of the Stokes numbers of interest, $St_r \gg 1$. For these Stokes numbers, one may represent the effects of the underlying turbulence on the relative velocity \mathbf{U} as a white noise term that is manifested as a phase-space diffusion tensor D_{UU} .

In arriving at (2.23), we have used the divergence theorem in the center-of-mass velocity space:

$$\begin{aligned} & \int_{\mathbf{V}} \nabla_{\mathbf{V}} \cdot (\tilde{D}_{VU} \cdot \nabla_{\mathbf{U}} \langle P \rangle + \tilde{D}_{VV} \cdot \nabla_{\mathbf{V}} \langle P \rangle) d\mathbf{V} \\ &= \int_{\partial\mathbf{V}} (\tilde{D}_{VU} \cdot \nabla_{\mathbf{U}} \langle P \rangle + \tilde{D}_{VV} \cdot \nabla_{\mathbf{V}} \langle P \rangle) \cdot \mathbf{n} dS_{\mathbf{V}} = 0 \end{aligned}$$

where $\int_{\partial\mathbf{V}}$ represents integration over a boundary in the \mathbf{V} -space, and \mathbf{n} is the normal to this boundary. We take the boundary to be at a large velocity so that $|\mathbf{V}| \gg \langle V^2 \rangle^{\frac{1}{2}}$, thereby $\langle P \rangle$ is essentially zero on the boundary. Hence, the integration $\int_{\partial\mathbf{V}}$ is zero.

Also, note that

$$\begin{aligned} \nabla_{\mathbf{U}} \cdot (\tilde{D}_{UV} \cdot \nabla_{\mathbf{V}} \langle P \rangle) &= \nabla_{\mathbf{U}} \cdot [\nabla_{\mathbf{V}} \cdot (\tilde{D}_{UV} \langle P \rangle) - \langle P \rangle \nabla_{\mathbf{V}} \cdot \tilde{D}_{UV}] \\ &= \nabla_{\mathbf{V}} \cdot [\nabla_{\mathbf{U}} \cdot (\tilde{D}_{UV} \langle P \rangle)] \end{aligned} \tag{2.24}$$

Hence, this term also vanishes when integrated over the \mathbf{V} -space, where we have used $\nabla_{\mathbf{V}} \cdot \tilde{D}_{UV} = 0$, as \tilde{D}_{UV} is not a function of \mathbf{V} .

Equation (2.23) is similar to equation (34) in Zaichik and Alipchenkov [100]. However, as discussed in Section 2.2, their formulation consists of two diffusion terms,

one of which is the same as D_{UU} in the limit of $St_I \gg 1$. The next part of our theory deals with the derivation of an analytical formulation for predicting D_{UU} .

Derivation of diffusion coefficient tensor in the pair relative velocity space

We have already seen that the diffusion coefficient tensor D_{UU} can be written as:

$$\begin{aligned}
D_{UU} &= \frac{1}{St_I^2} \tilde{D}_{UU} \\
&= \frac{1}{St_I^2} \int_{-\infty}^t \langle \Delta \mathbf{u}(\mathbf{r}, \mathbf{x}, t) \Delta \mathbf{u}(\mathbf{r}, \mathbf{x}, t') \rangle dt' \\
&= \frac{1}{St_I^2} \int_{-\infty}^0 \langle \Delta \mathbf{u}(\mathbf{r}, \mathbf{x}, 0) \Delta \mathbf{u}(\mathbf{r}, \mathbf{x}, t) \rangle dt
\end{aligned} \tag{2.25}$$

where $\Delta \mathbf{u}(\mathbf{r}, \mathbf{x}, t) = \mathbf{u}[\mathbf{x} + \frac{1}{2}\mathbf{r}, t] - \mathbf{u}[\mathbf{x} - \frac{1}{2}\mathbf{r}, t]$, and $\mathbf{x} + \frac{1}{2}\mathbf{r}$ and $\mathbf{x} - \frac{1}{2}\mathbf{r}$ represent the positions of a pair of particles with separation \mathbf{r} .

The Eulerian two-time fluid velocity correlations contained in $\langle \Delta \mathbf{u}(\mathbf{r}, \mathbf{x}, 0) \Delta \mathbf{u}(\mathbf{r}, \mathbf{x}, t) \rangle$ can be evaluated using DNS. The objective of this study, however, is to derive an analytical, closed-form expression for D_{UU} . To this end, the process of converting the two-time correlations into two-point spatial correlations is discussed next.

Recall that in arriving at (2.25), we have assumed that $St_I \gg 1$ and $St_r \gg 1$. With these assumptions, the particles are nearly stationary so that the temporal evolution of the relative velocity of a particle pair is controlled primarily by the evolution of the fluid velocity field at the particle positions. Moreover, the temporal change in $\Delta \mathbf{u}$ experienced by the particle pair is primarily due to the evolution of the turbulence scales and not due to pair motion itself. We will represent the temporal

evolution of $\Delta \mathbf{u}$ at two positions separated by \mathbf{r} based on an approximation in which a frozen turbulent velocity field associated with the eddies of size r is advected by larger, integral scale eddies. Hence, one may replace the above Eulerian two-time correlation by a two-point spatial correlation between two pairs with the same \mathbf{r} , but with the centers of mass separated by $\mathbf{u}_I t$, where \mathbf{u}_I is the large-scale velocity. This would give us:

$$D_{UU} = \frac{1}{St_I^2} \int_{-\infty}^0 \langle \Delta \mathbf{u}(\mathbf{r}, \mathbf{x}, t) \Delta \mathbf{u}(\mathbf{r}, \mathbf{x} + \mathbf{u}_I t, t) \rangle dt \quad (2.26)$$

In writing (2.26) from (2.25), it is assumed that the large-scale velocity \mathbf{u}_I remains essentially constant during $[t, 0]$. This is reasonable because \mathbf{u}_I does not evolve significantly during the time τ_r of interaction between an eddy of size r and a pair at separation r , as the turnover time τ_r of eddies of size r is much smaller than the turnover time of large-scale eddies. Though this approach is similar to Taylor's frozen turbulence hypothesis, the principal difference is that in Taylor's hypothesis, frozen turbulence is advected by the mean flow, whereas in the current approach, eddies of size r (r is the pair separation) are advected by the integral-scale eddies.

One may relax the requirement of $St_I \gg 1$ so that for particles with $St_I \lesssim 1$, the pair center-of-mass is not stationary. When $St_r \gg 1$ and $St_I \lesssim 1$, the difference is that while the separation \mathbf{r} does not change significantly, the center-of-mass position may change due to interactions with eddies of timescales $\sim \tau_v$, the center-of-mass response time. Therefore, one will have to account for the relative motion between the large-scale eddies that are passively advecting eddies of size r and the center-

of-mass position. This is done by replacing \mathbf{u}_I with the relative velocity \mathbf{W} . This change makes the theory applicable for large-inertia particles that satisfy $St_r \gg 1$ and not necessarily $St_I \gg 1$. Since \mathbf{W} is principally influenced by the large-scale fluid eddies, its PDF $\Phi(\mathbf{W})$, can be considered Gaussian [5]:

$$\Phi(\mathbf{W}) = \frac{1}{\sqrt{(2\pi W_{\text{rms}}^2)^3}} e^{-\frac{W^2}{2W_{\text{rms}}^2}} \quad (2.27)$$

where W_{rms} is the r.m.s. fluctuating velocity of \mathbf{W} and needs to be determined. The diffusivity can then be expressed as an average over all values of the large scale velocity \mathbf{W} as:

$$D_{UU}(\mathbf{r}) = \int \hat{D}_{UU}(\mathbf{r}, W) \Phi(\mathbf{W}) d\mathbf{W} \quad (2.28)$$

where

$$\begin{aligned} \hat{D}_{UU} &= \frac{1}{St_I^2} \int_{-\infty}^0 \langle \Delta \mathbf{u}(\mathbf{r}, \mathbf{x}, t) \Delta \mathbf{u}(\mathbf{r}, \mathbf{x} + \mathbf{W}t, t) \rangle dt \\ &= \frac{1}{St_I^2} \int_{-\infty}^0 \left\langle \left[\mathbf{u}\left(\mathbf{x} + \frac{1}{2}\mathbf{r}, t\right) - \mathbf{u}\left(\mathbf{x} - \frac{1}{2}\mathbf{r}, t\right) \right] \right. \\ &\quad \times \left. \left[\mathbf{u}\left(\mathbf{x} + \mathbf{W}t + \frac{1}{2}\mathbf{r}, t\right) - \mathbf{u}\left(\mathbf{x} + \mathbf{W}t - \frac{1}{2}\mathbf{r}, t\right) \right] \right\rangle dt \\ &= \frac{1}{St_I^2} \int_{-\infty}^0 \left\langle \mathbf{u}\left(\mathbf{x} + \frac{1}{2}\mathbf{r}, t\right) \mathbf{u}\left(\mathbf{x} + \mathbf{W}t + \frac{1}{2}\mathbf{r}, t\right) - \mathbf{u}\left(\mathbf{x} + \frac{1}{2}\mathbf{r}, t\right) \mathbf{u}\left(\mathbf{x} + \mathbf{W}t - \frac{1}{2}\mathbf{r}, t\right) \right. \\ &\quad \left. - \mathbf{u}\left(\mathbf{x} - \frac{1}{2}\mathbf{r}, t\right) \mathbf{u}\left(\mathbf{x} + \mathbf{W}t + \frac{1}{2}\mathbf{r}, t\right) + \mathbf{u}\left(\mathbf{x} - \frac{1}{2}\mathbf{r}, t\right) \mathbf{u}\left(\mathbf{x} + \mathbf{W}t - \frac{1}{2}\mathbf{r}, t\right) \right\rangle dt \end{aligned} \quad (2.29)$$

In (2.29), there are four Eulerian two-point velocity correlation terms. Writing the two-point velocity correlation tensors in terms of the velocity spectrum tensor,

$R(\mathbf{k})$, we get:

$$\widehat{D}_{UU} = \frac{1}{St_I^2} \int R(\mathbf{k}) (2 - e^{-i\mathbf{k}\cdot\mathbf{r}} - e^{i\mathbf{k}\cdot\mathbf{r}}) d\mathbf{k} \int_{-\infty}^0 e^{i\mathbf{k}\cdot\mathbf{W}t} dt \quad (2.30)$$

where \mathbf{k} is the wavenumber vector. The second (time) integral in (2.30) can be conveniently evaluated using the standard Fourier transforms, giving us:

$$\widehat{D}_{UU} = \frac{1}{St_I^2} \int R(\mathbf{k}) [1 - \cos(\mathbf{k}\cdot\mathbf{r})] \delta\left(\frac{\mathbf{k}\cdot\mathbf{W}}{2\pi}\right) d\mathbf{k} \quad (2.31)$$

Note that $\delta\left(\frac{\mathbf{k}\cdot\mathbf{W}}{2\pi}\right)$ is non-zero only when $\mathbf{k}\cdot\mathbf{W} = 0$, i.e. when $\mathbf{k} \perp \mathbf{W}$. Let $\boldsymbol{\xi} = (\xi, \phi)$ represent, in polar coordinates, the plane perpendicular to \mathbf{W} . We can now write:

$$d\mathbf{k} = \frac{1}{W} \xi d\xi d\phi d(\mathbf{k}\cdot\mathbf{W}) \quad (2.32)$$

where $W = |\mathbf{W}|$. This gives us:

$$\widehat{D}_{UU}(\mathbf{r}, W) = \frac{2\pi}{St_I^2} \frac{1}{W} \int_0^\infty \xi d\xi \int_0^{2\pi} \frac{E(\xi)}{4\pi\xi^2} \left(\delta_{ij} - \frac{\xi_i \xi_j}{\xi^2} \right) [1 - \cos(\xi\rho\cos\phi)] d\phi \quad (2.33)$$

where, $\boldsymbol{\rho}$ is the projection of \mathbf{r} into the $\boldsymbol{\xi}$ -plane, $\rho = |\boldsymbol{\rho}|$, and we have written $R(\xi)$ in terms of the energy spectrum $E(\xi)$.

For isotropic turbulence, we can write \widehat{D}_{UU} as:

$$\widehat{D}_{UU,ij} = \widehat{D}_{UU,\perp} \left(\delta_{ij} - \frac{r_i r_j}{r^2} \right) + \widehat{D}_{UU,\parallel} \frac{r_i r_j}{r^2} \quad (2.34)$$

Using (2.33), we will develop expressions for $\widehat{D}_{UU,\perp}$ and $\widehat{D}_{UU,\parallel}$.

2.3.2.1 Derivation of $\widehat{D}_{UU,\perp}$ and $\widehat{D}_{UU,\parallel}$

Since $\boldsymbol{\rho}$ is the projection of \boldsymbol{r} into the $\boldsymbol{\xi}$ -plane, we can write:

$$\rho_i = \left(\delta_{ij} - \frac{W_i W_j}{W^2} \right) r_j \quad (2.35)$$

$$\cos\phi = \frac{\rho_i \xi_i}{\rho \xi} = \frac{r_i \xi_i}{r \xi} \quad (2.36)$$

It can be shown that $\widehat{D}_{UU,ij}$ can be expressed as follows:

$$\widehat{D}_{UU,ij} = \frac{2\pi}{St_I^2} \frac{1}{W} \left[A \left(\frac{W_i W_j}{W^2} + \frac{\rho_i \rho_j}{\rho^2} \right) + D \left(\delta_{ij} - \frac{W_i W_j}{W^2} - 2 \frac{\rho_i \rho_j}{\rho^2} \right) \right] \quad (2.37)$$

where

$$A = \int_0^\infty \xi \, d\xi \int_0^{2\pi} \frac{E(\xi)}{4\pi\xi^2} [1 - \cos(\xi\rho\cos\phi)] \, d\phi \quad (2.38)$$

$$D = \int_0^\infty \xi \, d\xi \int_0^{2\pi} \frac{E(\xi)}{4\pi\xi^2} [1 - \cos(\xi\rho\cos\phi)] \cos^2\phi \, d\phi \quad (2.39)$$

Using (2.34) and (2.37), we can derive expressions for $\widehat{D}_{UU,\perp}$ and $\widehat{D}_{UU,\parallel}$:

$$\begin{aligned} \widehat{D}_{UU,\perp} &= \frac{1}{2} \widehat{D}_{UU,ij} \left(\delta_{ij} - \frac{\rho_i \rho_j}{\rho^2} \right) \\ &= \frac{1}{2} \frac{2\pi}{St_I^2} \frac{1}{W} (A + D \sin^2\theta) \end{aligned} \quad (2.40)$$

and,

$$\begin{aligned}\widehat{D}_{UU,\parallel} &= \widehat{D}_{UU,ij} \frac{\rho_i \rho_j}{\rho^2} \\ &= \frac{2\pi}{St_I^2} \frac{1}{W} (A - D \sin^2 \theta)\end{aligned}\tag{2.41}$$

where,

$$\sin^2 \theta = \frac{\rho_i \rho_j}{\rho^2} \frac{r_i r_j}{r^2}; \quad \cos^2 \theta = \frac{W_i W_j}{W^2} \frac{r_i r_j}{r^2}\tag{2.42}$$

We can now eliminate the dependence on W in (2.33) using (2.28). For isotropic turbulence, we write $D_{UU}(\mathbf{r})$ as:

$$D_{UU,ij}(r) = D_{UU,\perp}(r) \left(\delta_{ij} - \frac{r_i r_j}{r^2} \right) + D_{UU,\parallel}(r) \frac{r_i r_j}{r^2}\tag{2.43}$$

where

$$\begin{aligned}D_{UU,\perp} &= \frac{1}{2} \frac{2\pi}{St_I^2} \int \frac{1}{W} (A + D \sin^2 \theta) \Phi(\mathbf{W}) d\mathbf{W} \\ D_{UU,\parallel} &= \frac{2\pi}{St_I^2} \int \frac{1}{W} (A - D \sin^2 \theta) \Phi(\mathbf{W}) d\mathbf{W}\end{aligned}\tag{2.44}$$

Using the expressions for A and D from (2.38) and (2.39), respectively, we get:

$$D_{UU,\perp}(r) = \frac{1}{2} \frac{2\pi}{St_I^2} \int \frac{1}{W} \Phi(\mathbf{W}) d\mathbf{W} \\ \times \int_0^\infty \xi d\xi \int_0^{2\pi} \frac{E(\xi)}{4\pi\xi^2} [1 - \cos(\xi\rho\cos\phi)] (1 + \cos^2\phi\sin^2\theta) d\phi \quad (2.45)$$

$$D_{UU,\parallel}(r) = \frac{2\pi}{St_I^2} \int \frac{1}{W} \Phi(\mathbf{W}) d\mathbf{W} \\ \times \int_0^\infty \xi d\xi \int_0^{2\pi} \frac{E(\xi)}{4\pi\xi^2} [1 - \cos(\xi\rho\cos\phi)] (1 - \cos^2\phi\sin^2\theta) d\phi \quad (2.46)$$

where $d\mathbf{W} = W^2 \sin\theta d\theta d\psi dW$; $\psi \in [0, 2\pi]$ is the azimuthal angle.

After integrating over \mathbf{W} -space and over ϕ , equations (2.45) and (2.46) can be simplified substantially, giving us:

$$D_{UU,\perp}(r) = \frac{1}{2} \frac{2\pi^2}{St_I^2} \sqrt{\frac{1}{(2\pi)^3 W_{\text{rms}}^2}} \\ \times \int_0^\infty \frac{E(\xi)}{\xi} \left[\frac{8}{3} - \frac{4\sin(r\xi)}{r\xi} - \frac{4\cos(r\xi)}{r^2\xi^2} + \frac{4\sin(r\xi)}{r^3\xi^3} \right] d\xi \quad (2.47)$$

$$D_{UU,\parallel}(r) = \frac{2\pi^2}{St_I^2} \sqrt{\frac{1}{(2\pi)^3 W_{\text{rms}}^2}} \\ \times \int_0^\infty \frac{E(\xi)}{\xi} \left[\frac{4}{3} + \frac{4\cos(r\xi)}{r^2\xi^2} - \frac{4\sin(r\xi)}{r^3\xi^3} \right] d\xi \quad (2.48)$$

Equations (2.47) and (2.48) are substituted back into (2.43) to give us the averaged diffusion coefficient, $D_{UU,ij}$. To complete the closure of the diffusion current term, however, we require an expression for W_{rms} . This is discussed next.

2.3.3 Derivation of an expression for W_{rms}

In the limit of $St_I \gg 1$, $W_{\text{rms}} \approx u_{\text{rms}}$, where u_{rms} is the Eulerian r.m.s. fluctuating velocity of isotropic turbulence. But, when $St_I \lesssim 1$, W_{rms} needs to be estimated, which is the purpose of this section. Using the definition of W_{rms} , we can write:

$$W_{\text{rms}}^2 = \frac{1}{3} \langle (u_i - V_i)^2 \rangle = \frac{1}{3} [\langle u_i^2 \rangle + \langle V_i^2 \rangle - 2 \langle V_i u_i \rangle] \quad (2.49)$$

where V_i is the velocity of the pair center-of-mass, u_i is the fluid velocity with which eddies of size r are advected past the pair, and $\langle u_i^2 \rangle = \langle u_1^2 + u_2^2 + u_3^2 \rangle$ ($\langle V_i^2 \rangle$ follows a similar notation).

The velocity of the pair center-of-mass is governed by

$$\frac{dV_i}{dt} = \frac{u_{\text{cm},i} - V_i}{\tau_v} \quad (2.50)$$

where $u_{\text{cm},i}$ was defined in (2.6). Multiplying (2.50) with V_i and ensemble-averaging yields

$$\frac{d \langle \frac{1}{2} V_i^2 \rangle}{dt} = \frac{\langle u_i V_i \rangle - \langle V_i^2 \rangle}{\tau_v} \quad (2.51)$$

We have replaced $\langle u_{\text{cm},i} V_i \rangle$ on the RHS of (2.51) with $\langle u_i V_i \rangle$. While this approximation is not exact, it may be noted that both $u_i - V_i$ and $u_{\text{cm},i} - V_i$ are determined by eddies whose sizes are of the order of or smaller than r so that these two quantities may be expected to have similar statistics.

At steady state, $\langle V_i u_i \rangle = \langle V_i^2 \rangle$. This means that from (2.50)

$$\begin{aligned} W_{\text{rms}}^2 &= \frac{1}{3} [\langle u_i^2 \rangle - \langle V_i^2 \rangle] = \frac{1}{3} \langle u_i^2 \rangle \left(1 - \frac{\langle V_i^2 \rangle}{\langle u_i^2 \rangle} \right) \\ &= u'^2 \left(1 - \frac{V'^2}{u'^2} \right) \end{aligned} \quad (2.52)$$

where $\frac{1}{3} \langle u_i^2 \rangle = u'^2$, and similarly $\frac{1}{3} \langle V_i^2 \rangle = V'^2$. Here, u'^2 is the variance of the fluid velocity seen by the center-of-mass, and V'^2 is the variance of the center-of-mass velocity. Therefore, in order to close W_{rms} , one needs expressions for u' and the ratio V'/u' .

The well-known Tchen theory (see [42]) provides the following expression for V'^2/u'^2 :

$$\frac{V'^2}{u'^2} = \frac{T_L/\tau_v}{1 + T_L/\tau_v} \quad (2.53)$$

which was later refined by [42]:

$$\frac{V'^2}{u'^2} = \frac{\tau_\eta(\tau_v + T') + \tau_v T'}{(\tau_\eta + \tau_v)(\tau_v + T')} \quad (2.54)$$

where T_L is the fluid Lagrangian integral time-scale, $T' = T_{fp} - \tau_\eta$, τ_η is the Kolmogorov time scale and T_{fp} is the Lagrangian integral time-scale of fluid velocities seen by the particles.

$$T_{fp} = \frac{\int_0^\infty dt \langle u(t_0)u(t+t_0) \rangle}{\langle u^2(t_0) \rangle} \quad (2.55)$$

where u is the fluid velocity seen by the particles, and t_0 is a reference time. [42] provided the following expression for T_{fp} :

$$\frac{T_{fp}}{T_L} = 0.245e^{-[\ln(St_\eta/1.2)/1.3]^2} + \frac{1 + (T_E/T_L)(0.025St)^{1.5}}{1 + (0.025St)^{1.5}} \quad (2.56)$$

where $St_\eta = \tau_v/\tau_\eta$. The [42] refined theory of (2.54) showed excellent agreement with the DNS data. Hence, we will use (2.54) in the current study. Further, Jung et al. (2008) plot the ratio of particle to fluid dispersion coefficients as a function of St_η . From this plot, it can be inferred that for $St_\eta \gtrsim 4$, $u'^2 = u_{\text{rms}}^2$, i.e. for high St particles, the variance of the fluid velocity seen by the particles is nearly equal to the variance of the turbulent fluid velocity. Equation (2.56) together with (2.52) and (2.54) complete the closure for W_{rms} .

2.3.4 Consistency check of the pair diffusion coefficient

It is known that the pair diffusion coefficient of a particle pair at infinite separation is twice the diffusion coefficient of a single particle. The diffusion coefficient formulation derived above should also satisfy this requirement, and this is what we will establish in the following discussion.

Let $\mathbf{v}(t)$ and $\mathbf{y}(t)$ represent the velocity and position vectors of a single high Stokes number particle. The governing equation for \mathbf{v} is (in dimensionless form):

$$\frac{d\mathbf{v}}{dt} = -\frac{1}{\tau_v} [\mathbf{v}(t) - \mathbf{u}(\mathbf{y}, t)] \quad (2.57)$$

Using $\beta = \frac{1}{\tau_v}$, and multiplying both sides of (2.57) with $e^{\beta t}$ and simplifying gives us:

$$\mathbf{v}(t) = \beta \int_{-\infty}^t e^{\beta(\tau-t)} \mathbf{u}(\mathbf{y}, \tau) d\tau \quad (2.58)$$

Substituting (2.58) into (2.57), we get:

$$\dot{\mathbf{v}}(t) = \frac{1}{\tau_v} \mathbf{u}(\mathbf{y}, t) + O\left(\frac{1}{\tau_v^2}\right) \quad (2.59)$$

The diffusion coefficient for a single particle, D_v , can be defined as:

$$\begin{aligned} D_v &= \int_{-\infty}^t \langle \dot{\mathbf{v}}(t) \dot{\mathbf{v}}(t') \rangle dt' \\ &\approx \frac{1}{\tau_v^2} \int_{-\infty}^t \langle \mathbf{u}(\mathbf{y}, t) \mathbf{u}(\mathbf{y}, t') \rangle dt' \\ &= \frac{1}{\tau_v^2} \int_{-\infty}^0 \langle \mathbf{u}(\mathbf{y}, 0) \mathbf{u}(\mathbf{y}, t) \rangle dt \end{aligned} \quad (2.60)$$

As seen previously, we will convert the two-time, two-point Lagrangian correlation in (2.60) into a two-point Eulerian correlation:

$$\begin{aligned} D_v &= \frac{1}{\tau_v^2} \int_{-\infty}^0 \langle \mathbf{u}(\mathbf{y}, t) \mathbf{u}(\mathbf{y} + \mathbf{W}t, t) \rangle dt \\ &= \frac{1}{\tau_v^2} \int R(\mathbf{k}) d\mathbf{k} \int_{-\infty}^0 e^{i\mathbf{k} \cdot \mathbf{W}t} dt \\ &= \frac{\pi}{\tau_v^2} \int R(\mathbf{k}) \delta(\mathbf{k} \cdot \mathbf{W}) d\mathbf{k} \end{aligned} \quad (2.61)$$

Here, \mathbf{W} represents the velocity of large scale eddies there are advecting a frozen turbulent flow field past the particle. Using a procedure similar to that in (2.30)-

(2.33), we get:

$$D_{v,ij}(W) = \frac{\pi}{\tau_v^2} \frac{1}{W} \int_0^\infty \xi d\xi \int_0^{2\pi} \frac{E(\xi)}{4\pi\xi^2} \left(\delta_{ij} - \frac{\xi_i \xi_j}{\xi^2} \right) d\phi \quad (2.62)$$

We can write for isotropic turbulence:

$$D_{v,ij} = D_{v,\perp} \left(\delta_{ij} - \frac{r_i r_j}{r^2} \right) + D_{v,\parallel} \frac{r_i r_j}{r^2} \quad (2.63)$$

where $\mathbf{r} = \mathbf{v}t$. Using a procedure similar to the one laid out in Section 2.3.2.1,

$$D_{v,\perp} = \frac{1}{2} D_{v,ij} \left(\delta_{ij} - \frac{r_i r_j}{r^2} \right) = \frac{\pi}{4\tau_v^2} \frac{1}{v} (2A + A \sin^2\theta) \quad (2.64)$$

$$D_{v,\parallel} = D_{v,ij} \frac{r_i r_j}{r^2} = \frac{\pi}{2\tau_v^2} \frac{1}{v} (A + A \cos^2\theta) \quad (2.65)$$

$$A = \frac{1}{2} \int_0^\infty \frac{E(\xi)}{\xi} d\xi \quad (2.66)$$

In order to remove the dependence on W , we perform weighted integration of $D_{v,\perp}$ and $D_{v,\parallel}$ using the PDF of \mathbf{W} , $\Phi(\mathbf{W})$, as follows:

$$D_{v,\perp} = \frac{\pi}{4\tau_v^2} \int \frac{1}{v} (2A + A \sin^2\theta) \Phi(\mathbf{W}) d\mathbf{W} \quad (2.67)$$

$$D_{v,\parallel} = \frac{\pi}{2\tau_v^2} \int \frac{1}{v} (A + A \cos^2\theta) \Phi(\mathbf{W}) d\mathbf{W} \quad (2.68)$$

After performing the above integrations using $\Phi(\mathbf{W})$ from (2.27), it can be readily shown that

$$D_{v,\perp} = D_{v,\parallel} = \frac{1}{2} \lim_{r \rightarrow \infty} D_{UU,\perp} = \frac{1}{2} \lim_{r \rightarrow \infty} D_{UU,\parallel} \quad (2.69)$$

which is exactly the desired result, where $D_{UU,\perp}(r)$ and $D_{UU,\parallel}(r)$ are given by (2.47) and (2.48).

2.4 Simulations

Using the diffusion coefficient formulation derived in Section 2.3, Lagrangian stochastic simulations were performed to evolve the pair separations (\mathbf{r}) and relative velocities (\mathbf{U}). The governing equations for \mathbf{r} and \mathbf{U} are:

$$\frac{d\mathbf{r}}{dt} = \mathbf{U} \quad (2.70)$$

$$d\mathbf{U} = -\frac{\mathbf{U}}{\tau_v} dt + \mathbf{B} \cdot dW \quad (2.71)$$

Here, W represents a Wiener process, and the diffusion matrix \mathbf{B} can be written in terms of D_{UU} as:

$$\mathbf{B} \cdot \mathbf{B}^T = 2D_{UU}(r) \quad (2.72)$$

where \mathbf{B}^T is the transpose of \mathbf{B} , and \mathbf{B} is computed from a Cholesky decomposition of $D_{UU}(r)$. The matrix \mathbf{B} is a function of the state variable \mathbf{r} . Consequently, the current Langevin model captures the deviation from Gaussianity with r of the PDF of U . As discussed in [55], in spite of the white-noise (Gaussian) treatment of the diffusion of the slow variable \mathbf{U} , the fact that the fast variable $\Delta\mathbf{u}$ contained in the diffusion coefficient depends upon the state variable \mathbf{r} leads to the non-Gaussian behavior of the slow variable.

In order to compute $D_{UU}(r)$ and from it B , we will need to evaluate the \int_0^∞ integrals in (2.47) and (2.48). Numerical quadrature using the Gauss-Laguerre polynomials is ideally suited for these integrals. In our simulations, we used the 150th-order Gauss-Laguerre polynomials to evaluate these integrals. Although such high order integration may not be needed, it was used since the additional computational expense was negligible. The isotropic turbulence energy spectrum function in (2.47) and (2.48) was evaluated using the following expression [64]:

$$E(k) = C\epsilon^{2/3}k^{-5/3} f_L(kL) f_\eta(k\eta) \quad (2.73)$$

where $C = 1.5$, ϵ is the turbulence dissipation rate, and f_L and f_η are functions of the integral and Kolmogorov length scales, L and η , respectively. Expressions for f_L and f_η are provided in Pope [64] and are not reproduced here. The ratio $L/\eta \approx 156.5$ in our simulations.

Particle pairs were evolved in isotropic turbulence with a micro-scale Reynolds number, $Re_\lambda = 75$. Six particle Stokes numbers were considered: $St_\eta = \tau_v/\tau_\eta = 2, 4, 10, 20, 40$ and 80 . For each St_η , we evolved the separations and relative velocities of 60×10^6 pairs. The particle simulation domain is a sphere of radius $4L$. It was found that this domain size was sufficiently large, since the separation at which particle pairs became uncorrelated was $O(L)$ for all Stokes numbers considered in the current study. As a result, a domain size of $4L$ is sufficient even for those uncorrelated pairs that have initially large separations and relative velocities, but become correlated as their separation decreases. For all St_η , the particle pairs were

evolved for 8000 particle response times (τ_v) by which time they had attained a statistically stationary state. From this point, statistics were collected for another $1000\tau_v$ and averaged.

At the outer boundary, a specular reflection boundary condition (BC) was imposed for the particles. This meant that when a particle collides with the outer boundary, its velocity component tangential to the boundary remains unchanged, while the velocity component normal to the boundary is simply reversed. Specular reflection BC also maintains a constant number of pairs in the domain. In this sense, a domain with a specular reflection BC is analogous to a domain with a specified radially-inward particle flux BC that has attained a steady state. This is because at steady state, a system with a specified inward particle flux BC will also have constant number of pairs in the domain. The other advantages of the specular reflection BC are that it conserves particle kinetic energy, and maintains a Gaussian particle velocity PDF at the farfield boundary.

It was found that encountering pairs with separations $r \sim \eta$ (η is the Kolmogorov length scale) were low probability events. We, therefore, adopted the approach of Huber and Kim [36] that facilitates the capturing of these low probability events. In this approach, a single pair is split into multiple, equally-weighted fractional pairs whenever the separation of a pair goes below a certain value. When a parent pair is split, initially the fractional pairs have the same position and velocity vectors as the parent. Each of the fractional pairs is then evolved independently, except that it only makes a fractional contribution when computing the statistics. In our simulations, splitting is executed at three different radial locations, $r = 2\eta, 5\eta, 10\eta$. A

parent pair is split whenever the separation falls below any of these radial distances, but a fractional pair is not split again irrespective of whether the above criterion is satisfied or not. We found that splitting a pair into 10 equally-weighted fractional pairs gave us sufficient data at the smaller separations without excessively increasing the number of pairs to be tracked. Recombination of fractional pairs when their separations exceeded the specified radial distances was not undertaken.

2.5 Results and discussion

In this section, the results obtained using the closure formulation derived in Section 2.3 are discussed. First, we will present the transverse and longitudinal components of the diffusion coefficient tensor as a function of pair separation r . Subsequently, we will discuss in detail the particle statistics obtained from the Langevin simulations.

2.5.1 Transverse and longitudinal components of the diffusion coefficient tensor

The transverse and longitudinal components of the diffusion coefficient tensor plotted as a function of the dimensionless separation r/L are shown in Figure 2.1 for the $St_\eta = 20$ particles. For separations $r < \eta$, both $D_{UU,\perp}(r)$ and $D_{UU,\parallel}(r)$ vary as r^2 . This behavior arises from (2.25) in conjunction with the fact that fluid relative velocity for $r < \eta$ can be approximated as a linear function of r , i.e., $\Delta \mathbf{u} \approx \mathbf{r} \cdot \nabla \mathbf{u}$ [18]. It may be noted that the r -space diffusion coefficient for the small Stokes number particles ($St_\eta < 1$), which involves an autocorrelation of the fluid relative velocity, is

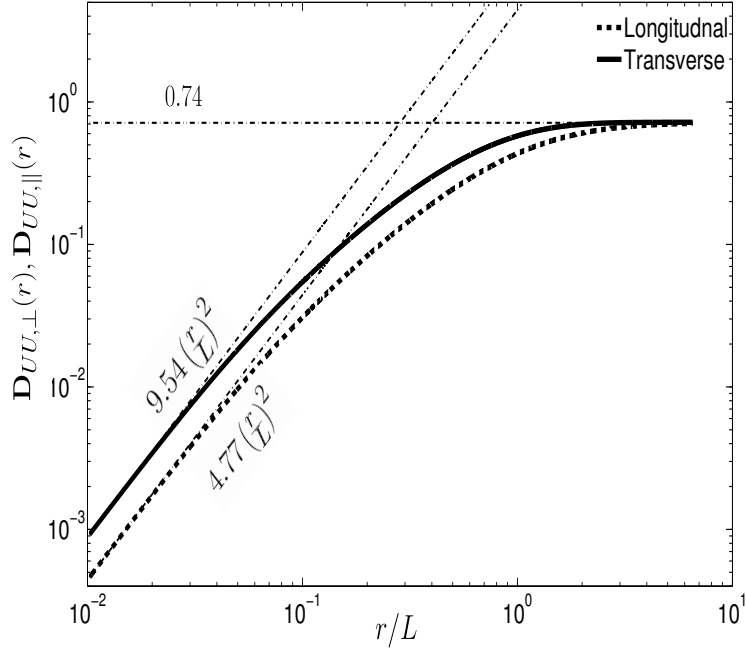


Figure 2.1: Transverse component, $D_{UU,\perp}(r)$, and longitudinal component, $D_{UU,\parallel}(r)$, of the particle-pair diffusion coefficient tensor as a function of dimensionless pair separation r/L for $St_\eta = 20$. Solid and dashed curves represent transverse and longitudinal components, respectively. At small r , transverse and longitudinal components asymptote to the lower and upper dashed lines represented by $4.77(r/L)^2$ and $9.54(r/L)^2$, respectively. At large r , transverse and longitudinal components asymptote to the value of 0.74.

also proportional to r^2 for $r < \eta$ [18]. For $r \gtrsim L$, $D_{UU,\perp}(r)$ and $D_{UU,\parallel}(r)$ approach each other, and asymptote to the same limit. This means that when the separation r exceeds L , a particle pair essentially behaves like two uncorrelated particles, with the pair diffusion coefficient being twice that of a single particle (see the discussion in Section 2.3.4). This trend is also supportive of our earlier assertion that a domain size of $4L$ was sufficiently large to capture those particle pairs that were initially uncorrelated at a large separation, but have subsequently become correlated as they moved closer. The other side of this picture is that we have also been able to show

that pairs exhibit a transition from highly correlated motion at small separations to uncorrelated motion at larger separations.

2.5.2 RDF and relative velocity PDF statistics

In this section, we present the pair relative motion statistics obtained from the Langevin stochastic simulations. Figure 2.2 shows the radial distribution functions (RDFs) as a function of the dimensionless separation r/η for the various Stokes numbers. At separations of the order of the Kolmogorov scale, the $St_\eta = 2$ particles show the maximum preferential concentration—i.e., the highest RDF values—among the Stokes numbers considered. Preferential concentration at separations $r \sim O(\eta)$ decreases with increasing Stokes number. One also notes that for the higher Stokes numbers ($St_\eta \geq 10$), the RDFs plateau, i.e. they are essentially independent of r , below certain separations. A similar qualitative trend was seen in Zaichik and Alipchenkov [100], but the plateauing was observed to begin at radial separations larger than those in the current study. The “delayed” plateauing of RDFs observed in the current study is also qualitatively supported by the study of Pan et al. [63]. In that study, Pan et al. investigated the preferential concentration of high Stokes number particles in isotropic turbulence at $Re_\lambda = 250$. The higher Stokes numbers considered by Pan et al. include $St_\eta = 10, 21, 43$. The plateauing of RDFs can be explained using the transport equations for the moments of the PDF $\Omega(\mathbf{r}, \mathbf{U})$ (see (2.23)). The moments of interest are:

$$\Omega(\mathbf{r}) = \int \Omega(\mathbf{r}, \mathbf{U}) d\mathbf{U} = \Omega(\mathbf{r}) \int \Omega(\mathbf{U}|\mathbf{r}) d\mathbf{U} \quad (2.74)$$

$$\langle \mathbf{U} \rangle = \int \mathbf{U} \Omega(\mathbf{U}|\mathbf{r}) d\mathbf{U} = \frac{1}{\Omega(\mathbf{r})} \int \mathbf{U} \Omega(\mathbf{r}, \mathbf{U}) d\mathbf{U} \quad (2.75)$$

where $\Omega(\mathbf{U}|\mathbf{r})$ is the PDF of \mathbf{U} conditioned on a given \mathbf{r} .

The governing equation for $\Omega(\mathbf{r})$ is obtained by integrating (2.23) over the \mathbf{U} space, and that for $\langle \mathbf{U} \rangle$ is obtained by premultiplying (2.23) with $\mathbf{U}/\Omega(\mathbf{r})$ and then integrating over the \mathbf{U} space. The resulting equations, written using the Einstein index notation, are:

$$\frac{\partial \Omega(\mathbf{r})}{\partial t} + \frac{\partial [\Omega(\mathbf{r}) \langle U_j \rangle]}{\partial r_j} = 0 \quad (2.76)$$

$$\frac{\partial \langle U_i \rangle}{\partial t} + \frac{\partial \langle U_i \rangle \langle U_j \rangle}{\partial r_j} + \frac{\partial \langle U'_i U'_j \rangle}{\partial r_j} = -\frac{\langle U_i \rangle}{\tau_v} - D_{ij} \frac{\partial \ln \Omega(\mathbf{r})}{\partial r_j} \quad (2.77)$$

For isotropic turbulence, $\langle U_i \rangle = 0$, thereby (2.77) becomes

$$\frac{\partial \langle U'_\alpha U'_\alpha \rangle}{\partial r_j} = -D_{\alpha\alpha} \frac{\partial \ln \Omega(\mathbf{r})}{\partial r_j} \quad (2.78)$$

where $\alpha = 1, 2, 3$ (repeated α does not denote a summation). The relationship between $\Omega(r)$ and the RDF $g(r)$ is given by

$$g(r) = \frac{\Omega(r)}{\left[\frac{N(N-1)}{2V} \right]} \quad (2.79)$$

where N is the number of individual particles in the domain and V is the volume of the domain. One can therefore see from (2.78) that the plateauing of the RDF $g(r)$ is related to the plateauing of $\langle U'_\alpha U'_\alpha \rangle$. To confirm this, Figure 2.3 plots $\langle U^2 \rangle / u_{\text{rms}}^2$ as a function of r/L for the various St_η , where u_{rms} is the turbulence r.m.s. fluctuating

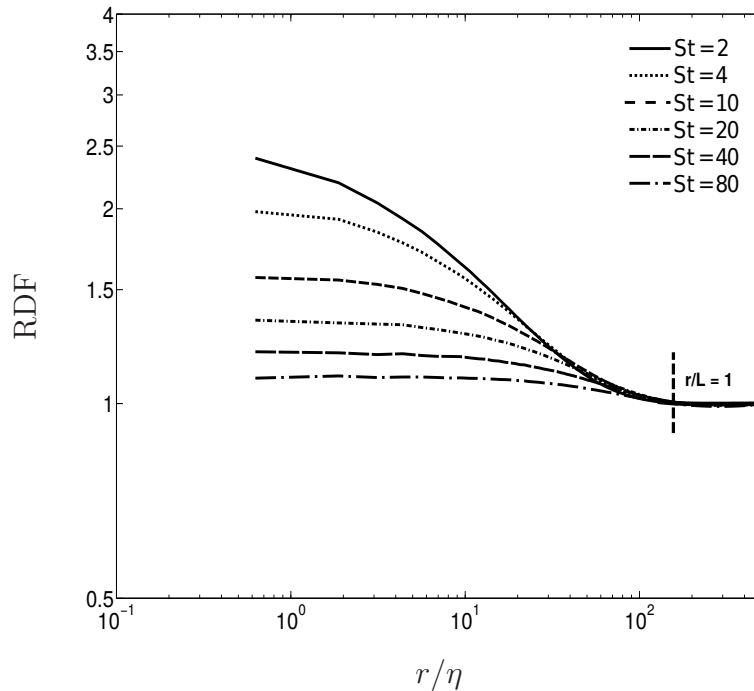


Figure 2.2: RDFs from our stochastic simulations for the various Stokes numbers as a function of dimensionless pair separation r/η . The radial location at which $r/L = 1$ is also indicated, where L is the integral length scale.

velocity. It is evident from Figure 2.3 that for $St_\eta \geq 10$, $\langle U^2 \rangle$ indeed begins to plateau at smaller separations, with the trend being more evident for $St_\eta = 40, 80$. Consequently, following (2.78), a similar behavior was also observed for the RDFs in Figure 2.2.

RDF as a function of St_η at various separations r/η is presented in Figure 2.4. Results from the current theory are compared with the DNS data of Février et al. [29], and also with the results from the theory of Zaichik and Alipchenkov [100]. Février et al. [29] data was for $Re_\lambda = 53$ and $Re_\lambda = 69$, while the Zaichik and Alipchenkov [100] results were for $Re_\lambda = 75$. There is reasonable agreement between the current theory and the DNS (note that $Re_\lambda = 75$ in the current study). For $St_\eta \geq 2$,

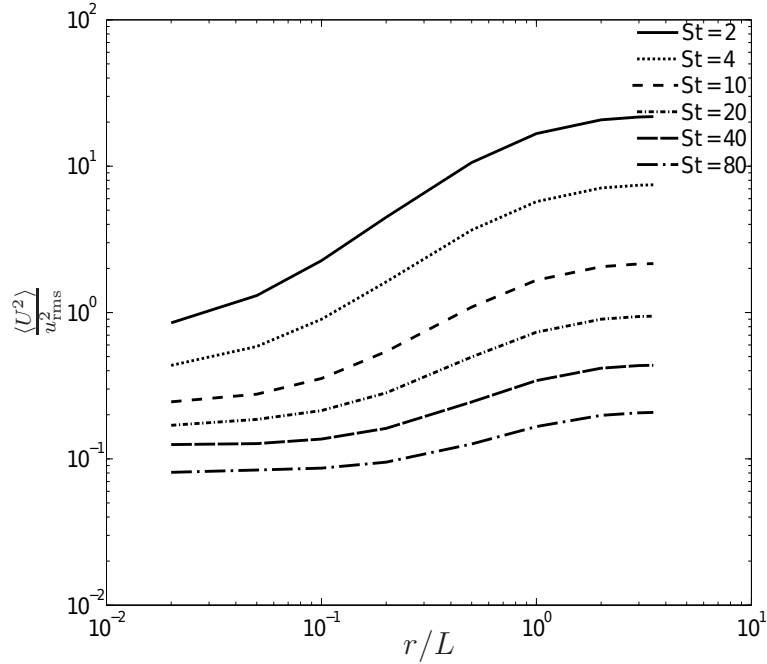


Figure 2.3: $\langle U^2 \rangle / u_{\text{rms}}^2$ as a function of dimensionless pair separation r/L and particle Stokes number St_η .

this theory agrees better with the DNS data than does the theory of Zaichik and Alipchenkov [100]. This may be attributed to the approximation in their study that the Lagrangian correlations of fluid relative velocities along inertial pair trajectories are equal to those along inertialess fluid particle-pair trajectories. Such an approximation is only appropriate for particle Stokes numbers $St_\eta < 1$. It can be inferred from Figure 2.4(c) and (d) that as the separation r increases, the Stokes number for which the maximum RDF occurs also increases. This is because the higher Stokes number particles are more responsive to eddies bigger than the Kolmogorov-sized

ones, and hence these pairs exhibit preferential concentration at length scales larger than the Kolmogorov scale.

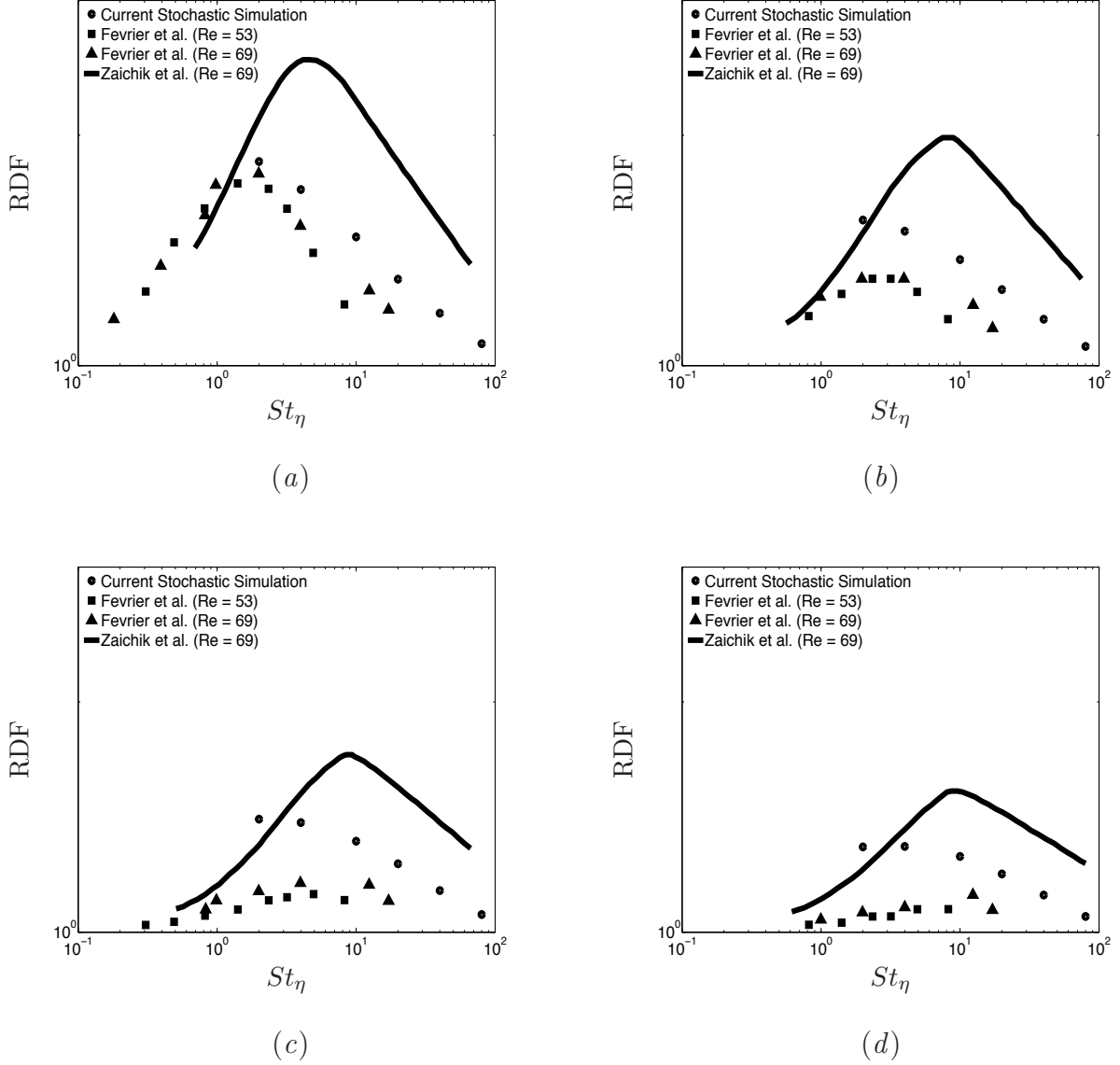


Figure 2.4: RDF versus St_η at specific radial separations: (a) $r/\eta = 6$, (b) $r/\eta = 12$, (c) $r/\eta = 18$, and (d) $r/\eta = 24$. In each plot, circles represent data from current stochastic simulations at $Re_\lambda = 75$; squares and triangles represent DNS data at $Re_\lambda = 53$ and $Re_\lambda = 69$, respectively, taken from F evrier et al. [29]. Solid line represents Zaichik and Alipchenkov [100] data for $Re_\lambda = 69$.

Next, we discuss the pair relative velocity PDF and its moments obtained from our Langevin simulations. The DNS study of Sundaram and Collins [91] demonstrated that the relative velocity PDF is Gaussian at separations of the order of the integral length scale, and that it becomes increasingly non-Gaussian tending towards exponential, as the separation decreases. It is important that the present theory captures this trend. The transition in the nature of the PDF can be demonstrated quantitatively using the relative velocity kurtosis $\langle U^4 \rangle / \langle U^2 \rangle^2$. It is well known that the kurtosis = 3 for a Gaussian PDF, and a deviation from this value is indicative of a non-Gaussian PDF. In Figure 2.5, kurtosis is plotted as a function of r/L for the various St_η . When $r \gtrsim L$, the relative velocity PDFs for all Stokes numbers are essentially Gaussian. As the separation decreases, kurtosis increases above 3. This trend is more prominent at the smaller St_η because these particles relax to the local flow conditions, whereas the higher St_η particles still retain memory of their ballistic motion at prior larger separations. It is interesting to note that at $r/L \approx 1/20$, the kurtosis ≈ 9 for the $St_\eta = 4$ particles, suggesting that at this radial separation, the relative velocities of these particles have a nearly exponential distribution. But, as the separation falls below $L/20$, kurtosis increases further implying that the relative velocities of the $St_\eta = 4$ pairs no longer have an exponential distribution. The separation at which the exponential distribution is attained decreases as the Stokes number increases.

Another interesting aspect of physics that can be gleaned from the relative velocity statistics is regarding the Stokes number dependence of pair relative velocity variance $\langle U^2 \rangle$. For high St_η particles, it is known that the single-particle velocity

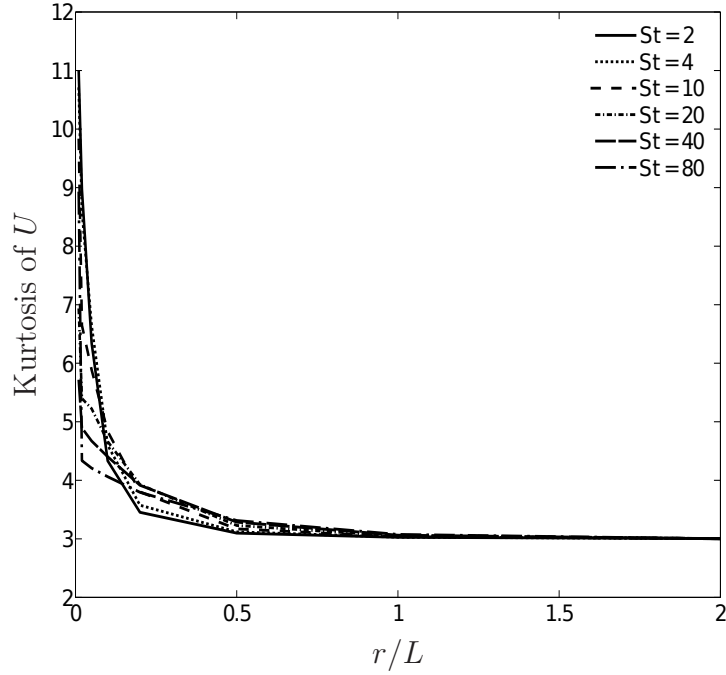


Figure 2.5: Kurtosis for various Stokes number pairs as a function of dimensionless pair separation r/L .

variance $\langle v^2 \rangle \propto \frac{1}{St}$. Also, we have shown in Section 2.3.4 that a pair at infinite separation behaves like two independent particles. These two aspects would mean that for large r , $\langle U^2 \rangle \cdot St_\eta$ should become independent of both St_η and r . This is precisely what we observe in Figure 2.6. In this figure, we plot $\frac{\langle U^2 \rangle \cdot St_\eta}{u_{\text{rms}}^2}$ as a function of r/L for various St_η , where u_{rms} is the turbulence r.m.s. fluctuating velocity. For $St_\eta \geq 20$, $\frac{\langle U^2 \rangle \cdot St_\eta}{u_{\text{rms}}^2}$ asymptotes to nearly the same value at large r . The lower St_η pairs show a greater variation of variance with radial position. This is because the faster relaxation of the low St_η particles makes it easier for them to get trapped and linger near each other.

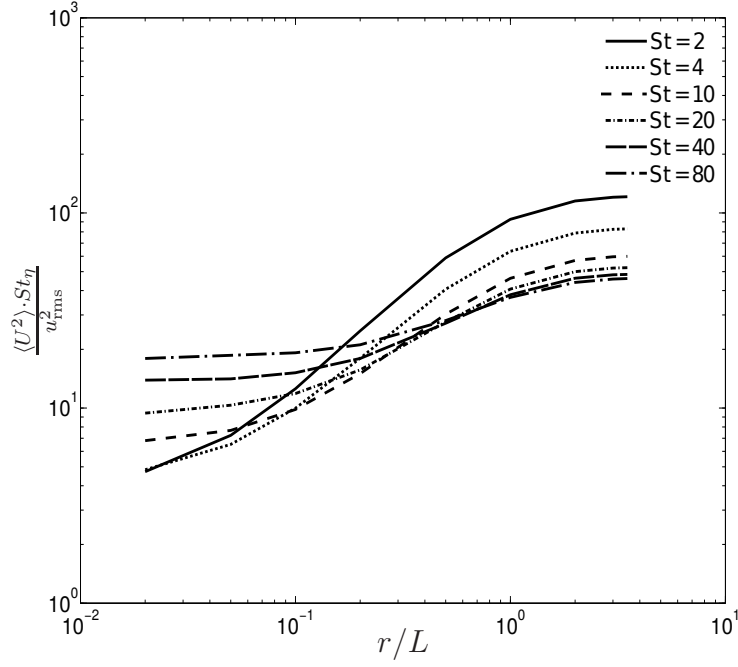


Figure 2.6: $\langle U^2 \rangle / u_{\text{rms}}^2$ as a function of dimensionless pair separation r/L and particle Stokes number St_η .

Relative velocity PDFs conditioned on the separation r , $\Omega(U|r)$, are presented for all St_η at $r/L = 3, 1, 1/10, 1/20$ (here $\eta/L = 0.0064$). These values of pair separation were chosen in order to track the transition of $\Omega(U|r)$ from a Gaussian PDF at large r to a non-Gaussian PDF at small r . Shown in Figure 2.7(a)-(d) are the PDFs at these four values of r plotted as a function of the relative velocity magnitude U normalized with $\langle U^2 \rangle^{1/2}$ at that value of r . At each r , we compare the PDFs for all the St_η under consideration in this study. It can be seen in Figure 2.7(a),(b) that the PDFs at $r/L = 3, 1$ are Gaussian for all St_η , and that there is a near-perfect collapse of the PDFs for the various Stokes numbers. This collapse of PDFs when normalized

by the standard deviation is to be expected for Gaussian PDFs. Figure 2.7(c) shows that at $r/L = 1/10$, the PDFs for all St_η deviate from being Gaussian. As we reduce the pair separation to $r/L = 1/20$, the non-Gaussianity of the PDFs increases, particularly for the smaller St_η . This is because the smaller St_η particles relax to the local flow, whereas the higher St_η particles still retain some memory of their earlier ballistic motion at larger separations. Also shown in Figure 2.7(d) is the exponential distribution. It is clear that the relative velocity PDFs are very nearly exponential, especially for $St_\eta \leq 10$, and seem to deviate from it only at the higher values of U . The transition of the PDFs, as well as the exponential nature of the PDFs at smaller separations match the trends observed in the DNS study of Sundaram and Collins [91].

Thus, it is clear from Figure 2.7 that when $r \gtrsim L$, particles become uncorrelated leading to Gaussian relative velocity PDFs. As r goes below L , particles become correlated giving rise to exponential PDFs for certain separations. Eventually, as r approaches η , the pairs can be classified into lingerers with low relative velocities, and flyers with high relative velocities (corresponding to the tails of the PDF). We also show in Figure 2.8 the PDF $\Omega(U|r)$ as a function of U at various separations r for $St_\eta = 20$. The transition in $\Omega(U|r)$ from being Gaussian at large r ($O(L)$) to being nearly exponential at small r is evident in this figure.

We will now focus on the radial component of the relative velocity $U_r = \mathbf{U} \cdot \mathbf{r}/r$ and its PDF. The significance of U_r lies in the role it plays in determining the interparticle collision rate. This is quantitatively illustrated by the collision kernel

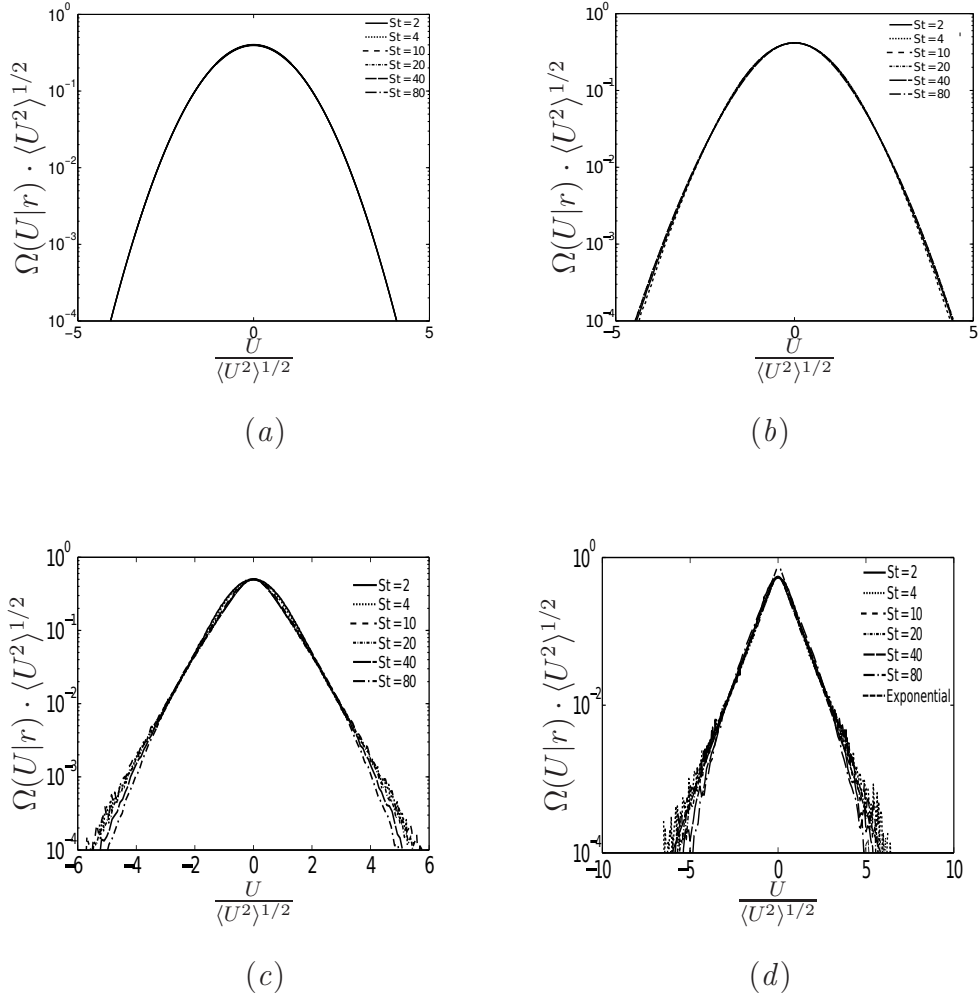


Figure 2.7: Relative velocity PDFs ($\Omega(U)$) for the various Stokes numbers at specific separations: (a) $r/L = 3$, (b) $r/L = 1$, (c) $r/L = 1/10$, (d) $r/L = 1/20$.

which for a monodisperse population of particles can be written as [91, 95]

$$4\pi\sigma^2 g(\sigma) \int_{-\infty}^0 U_r P(U_r|\sigma) dU_r, \quad (2.80)$$

where σ is the particle diameter, $g(\sigma)$ is the RDF at contact, and $P(U_r|\sigma)$ is the PDF of U_r conditioned upon a particle separation $r = \sigma$. Figure 2.9 shows the PDF of

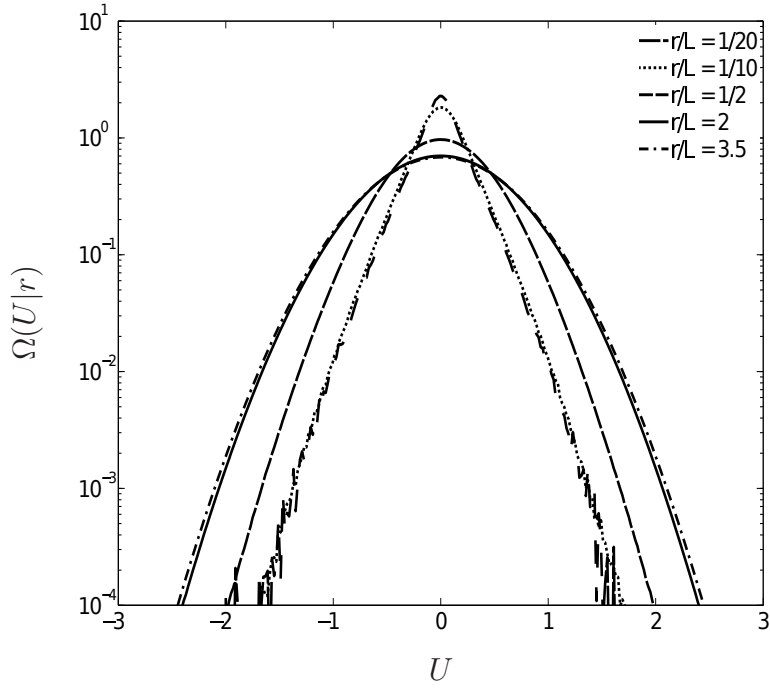


Figure 2.8: Comparison of relative velocity PDFs at various pair separations for $St_\eta = 20$.

U_r for the various Stokes numbers at $r/L = 1/20$. It is clear that U_r is negatively skewed, which is qualitatively consistent with the DNS study of Wang and Wexler [95]. Further, the skewness of U_r increases as the Stokes number decreases.

2.6 Summary and conclusions

The principal contributions of this study are twofold: (1) Derivation of a novel closure for the relative velocity-space pair diffusion coefficient for particle pairs whose Stokes numbers $St_r \gg 1$, and (2) Relaxation of the limitation on Stokes numbers so that the theory is valid for $St_I \lesssim 1$ particles as well. This relaxation significantly

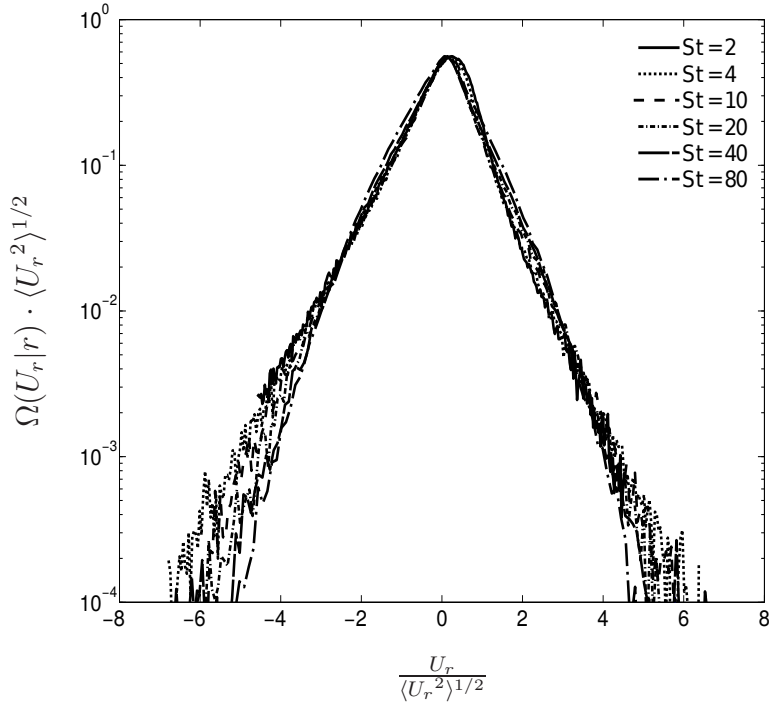


Figure 2.9: PDF of the radial component of the relative velocity U_r for the various Stokes numbers at $r/L = 1/20$.

expands the Stokes number range in which the closure is applicable. In fact, the results demonstrate that the theory shows good predictions for $St_\eta \geq 4$.

The closure formulation was motivated by a DNS study result that the PDF of particle-pair relative velocity of inertial particles was Gaussian at pair separations of the order of turbulent integral length scale, and that this PDF became non-Gaussian (exponential) at smaller separations [91]. The salient feature in this closure is that Lagrangian two-time, two-point fluid velocity correlations are systematically and consistently transformed into Eulerian two-point correlations in the limit of high Stokes number.

In the present study, the theory-predicted diffusion tensor is used to evolve, in a Langevin sense, the pair separation and velocity vectors in isotropic turbulence. When compared to solving a finite number of PDF moments equations, this approach is higher order accurate in the sense that the Langevin simulations implicitly include all moments of the pair PDF. The range of Stokes numbers considered, $St_\eta = 2, 4, 10, 20, 40$ and 80 , clearly demonstrates the relative velocity dynamics and the preferential concentration behavior of high Stokes number particles. The closure theory successfully captures the transition of relative velocity PDF from a Gaussian PDF at separations of the order of the integral length scale to an exponential PDF at smaller separations. This study is only an initial step in the effort to develop a predictive stochastic model for inertial particle dynamics. A more thorough quantitative evaluation of our theory using DNS data will be undertaken in a future study.

2.7 Appendix: PDF notation used in the current study

The following notations are used in the manuscript:

- P is the particle-pair phase-space density.
- $\langle P \rangle$ is the PDF.

The particle-pair microscopic phase-space density may be written as

$$f(\mathbf{r}, \mathbf{x}, \mathbf{U}, \mathbf{V}; t) = \sum_{i=1}^N \delta(\mathbf{r} - \mathbf{r}_i) \delta(\mathbf{x} - \mathbf{x}_i) \delta(\mathbf{V} - \mathbf{V}_i) \delta(\mathbf{U} - \mathbf{U}_i)$$

where \mathbf{r}_i , \mathbf{x}_i , \mathbf{V}_i , and \mathbf{U}_i are the separation, center-of-mass position, center-of-mass velocity, and the relative velocity vectors of the i th pair, and N is the total number of pairs.

We now consider a smoothed phase-space density defined as

$$P(\mathbf{r}, \mathbf{x}, \mathbf{U}, \mathbf{V}; t) = \frac{1}{v} \int_v f(\mathbf{r}' - \mathbf{r}, \mathbf{x}' - \mathbf{x}, \mathbf{U}' - \mathbf{U}, \mathbf{V}' - \mathbf{V}; t) d\mathbf{r}' d\mathbf{x}' d\mathbf{U}' d\mathbf{V}' \quad (2.81)$$

Here, the volume of integration v is a subvolume around $(\mathbf{r}, \mathbf{x}, \mathbf{U}, \mathbf{V})$ that is small compared to the corresponding Kolmogorov scales, but is sufficiently large to ensure that one is able to define a meaningful averaged quantity over v . Consequently, the averaging does not affect the fluid quantities so that there are no “subgrid” scale fluctuations.

The smoothed phase-space density P takes on added significance when there exists an irreversible process that causes particles to lose memory of their initial conditions. If particle motion exhibits deterministic chaos, then there is an exponential separation of trajectories with nearly identical initial conditions. Even a single realization of the turbulent flow leads to Lagrangian chaos for particle motion due to the nonlinear dependence of the velocity on position. In this case, a very small stochastic displacement of the particles can lead to the mixing of phase-space density over volumes of order v so that f approaches P . In the present situation, the small stochastic element could be the Brownian displacements of the particles. Although the Peclet number Pe of high St particles is large ($O(10^5-10^6)$), the time required for mixing in the phase space is only proportional to $\tau \ln(Pe)$, where τ is the flow time-scale

corresponding to the length scale within v . Thus, in practice even a very small-scale stochastic process can lead to a smooth phase-space density. The smoothing of phase-space density also plays an important role in kinetic theory and in statistical mechanical approaches to classical molecular systems. In such systems, the Newton's equations of motion that govern the system are deterministic (even including collisions) and it is only the small quantum effects that lead to a stochastic element. Nonetheless, the deterministic chaotic motion of the molecules leads to rapid amplification of these stochastic effects so that stochastically averaged approaches are useful.

CHAPTER 3

STOCHASTIC THEORY AND DIRECT NUMERICAL SIMULATIONS OF THE RELATIVE MOTION OF HIGH-INERTIA PARTICLE PAIRS IN ISOTROPIC TURBULENCE

3.1 Abstract

The relative velocities and positions of monodisperse high-inertia particle pairs in isotropic turbulence are studied using direct numerical simulations (DNS), as well as Langevin simulations (LS) based on a probability density function (PDF) kinetic model for pair relative motion. In a prior study [67], the authors developed a stochastic theory that involved deriving closures in the limit of high Stokes number for the diffusivity tensor in the PDF equation for monodisperse particle pairs. The diffusivity contained the time integral of the Eulerian two-time correlation of fluid relative velocities seen by pairs that are nearly stationary. The two-time correlation was analytically resolved through the approximation that the temporal change in the fluid relative velocities seen by a pair occurs principally due to the advection of smaller eddies past the pair by large scale eddies. Accordingly, two diffusivity expressions were obtained based on whether the pair center of mass remained fixed during flow time scales, or moved in response to integral-scale eddies.

In the current study, a quantitative analysis of the Rani et al. [67] stochastic theory is performed through a comparison of the pair statistics obtained using Langevin simulations (LS) with those from DNS. LS consist of evolving the Langevin equations for pair separation and relative velocity, which is statistically equivalent to solving the classical Fokker-Planck form of the pair PDF equation. Langevin simulations of particle pair dispersion were performed using three closure forms of the diffusivity—i.e., the one containing the time integral of the Eulerian two-time correlation of the seen fluid relative velocities, and the two analytical diffusivity expressions. In the first closure form, the two-time correlation was computed using DNS of forced isotropic turbulence laden with stationary particles. The two analytical closure forms have the advantage that they can be evaluated using a model for the turbulence energy spectrum that closely matched the DNS spectrum. The three diffusivities are analyzed to quantify the effects of the approximations made in deriving them. Pair relative-motion statistics obtained from the three sets of Langevin simulations are compared with the results from the DNS of (moving) particle-laden forced isotropic turbulence for $St_\eta = 10, 20, 40, 80$ and $Re_\lambda = 76, 131$. Here, St_η is the particle Stokes number based on the Kolmogorov time scale, and Re_λ is the Taylor micro-scale Reynolds number. Statistics such as the radial distribution function (RDF), the variance and kurtosis of particle-pair relative velocities, and the particle collision kernel were computed using both Langevin and DNS runs, and compared. The RDFs from the stochastic runs were in good agreement with those from the DNS. Also computed were the PDFs $\Omega(U|r)$ and $\Omega(U_r|r)$ of relative velocity U and of the radial component of relative velocity U_r respectively, both PDFs conditioned on separation r . The first

closure form, involving the Eulerian two-time correlation of fluid relative velocities, showed the best agreement with the DNS results for the PDFs.

3.2 Introduction

Turbulence-driven relative motion of high-inertia particles is relevant in astrophysical scenarios, such as the interstellar medium, protoplanetary disks, and the atmospheres of planets and dwarf stars [16, 63]. Specifically, the “sticking” of dust particles in protoplanetary disks is believed to be the mechanism for planetesimal formation. An intriguing question that the astrophysicists are investigating concerns the effects of turbulence on the dispersion, sedimentation, collisional coalescence and fragmentation of dust grains. The viscous relaxation times, τ_v , of these particles are significantly large, with estimated $St_\eta \sim 10\text{-}100$ [63], where $St_\eta = \tau_v/\tau_\eta$ is the Stokes number based on the Kolmogorov time scale τ_η .

The two principal quantities describing the relative motion of inertial particles in a turbulent flow are: (1) the radial distribution function (RDF), which is a measure of the particle spatial clustering, and (2) the probability density function (PDF) of pair relative velocities, which quantifies the particle encounter rate. The RDF and the relative velocity PDF are both key inputs to the particle collision kernel, and depend sensitively on the Stokes number. Both statistics can be determined through direct numerical simulations (DNS) of particle-laden turbulent flows. However, DNS suffers from the well-known computational limitation on the Reynolds numbers that can be achieved. This drawback of DNS is one of the motivating factors for developing PDF equation-based stochastic models for particle-laden turbulent flows.

Recently, we developed a stochastic theory for the relative velocities and positions of high-inertia monodisperse pairs in forced isotropic turbulence [67]. The theory involved deriving a closure for the diffusivity tensor characterizing the relative-velocity-space diffusion current in the PDF kinetic equation of particle-pair separation and relative velocity. Since we had considered the $St_r \gg 1$ limit, the pair PDF equation is of the classical Fokker-Planck form (St_r is the Stokes number based on the time-scale τ_r of eddies whose size is of the order of pair separation r). Using the diffusivity formulation, one can perform Langevin simulations of pair relative velocities and positions, which is equivalent to simulating the Fokker-Planck equation.

In this context, the current study has two main objectives. First, we perform a quantitative analysis of the three forms of the diffusivity derived in [67]. The insights gained will help us understand the implications of the approximations made in deriving the diffusivities, as well as guide future improvements to the theory. In the $St_r \gg 1$ limit, we perform a comparative analysis of the current and [100] diffusivity closures, as well as the predictions of relative motion statistics by the two theories. The second objective is to compute the relative motion statistics of particle pairs using both direct numerical simulations (DNS) and Langevin simulations (LS), and compare the corresponding results. The parametric inputs to the LS runs such as the Taylor micro-scale Reynolds number, dissipation rate, Kolmogorov scales, integral length scale, and the RMS fluctuating velocity were all obtained from DNS. Further, the energy spectrum needed to compute the analytical diffusivities is modeled such that it closely matches the DNS spectrum. Thus, the DNS and LS results are compared under conditions where a broad set of flow parameters, and not just Re_λ , is matched.

Such a comparison will enable us to quantify the theory’s predictive abilities for pair dynamics in isotropic turbulence.

Zaichik and Alipchenkov [100] developed a stochastic model for particle pairs that was conceived to be applicable for all Stokes numbers, provided that the Stokes drag force is applicable and is the dominant force acting on the particles. Although [67] and Zaichik and Alipchenkov [100] are both based on a kinetic equation description of pair interactions, there are important fundamental distinctions between the two studies. The principal difference lies in the approach adopted to close the diffusion current in the PDF equation. Zaichik & Alipchenkov closed the diffusion current by using the Furutsu-Novikov-Donsker (FND) formula. The FND formula relates the diffusion current to a series expansion in the cumulants of the fluid relative velocities seen by the pairs ($\Delta\mathbf{u}$) and the functional derivatives of the PDF with respect to $\Delta\mathbf{u}$ [9]. They further assumed that $\Delta\mathbf{u}$ had a Gaussian distribution, for which the series expansion exactly reduces to only the second-order cumulant of $\Delta\mathbf{u}$ [9]. In contrast, Rani et al. [67] developed a closure for the diffusion current based on a perturbation analysis of the pair PDF equation in the limit of high Stokes number. Another important difference concerns the simulation approach used in the two studies. Zaichik and Alipchenkov [100] computed the statistics of pair separation and relative velocity by solving the equations for the zeroeth, first and second relative-velocity moments of the master PDF equation. Rani *et al.* simulated the Langevin equations to evolve the relative velocities and positions of a large number of particle pairs. When compared to solving a finite number of moments equations, the Langevin approach is higher order accurate in the sense that the Langevin simulations (LS) inherently include all

moments of the pair PDF. Another advantage of the LS approach is that it allows us to explicitly compute the PDFs of pair relative velocity at various separations, enabling us to track the transition in the nature of the PDF as the separations are reduced from the order of integral scale to that of Kolmogorov scale.

Bragg and Collins [9] performed a first-principles-based comparison of the Chun et al. [18] and Zaichik and Alipchenkov [103, 104] stochastic models for inertial pair dynamics in isotropic turbulence. The focus of that paper was to compare and analyze the predictions of particle clustering at sub-Kolmogorov scale separations by the two theories. In the limit of $St_\eta \ll 1$, Chun et al. [18] developed closures for the drift and diffusion fluxes in the PDF equation for pair separation, where St_η is the Stokes number based on the Kolmogorov time scale τ_η . Using these closures, they derived a power-law expression for the radial distribution function (RDF) at sub-Kolmogorov separations, which showed good agreement with the DNS results. The Zaichik and Alipchenkov [103] study improved upon their earlier study [100] by accounting for the unequal Lagrangian correlation timescales of the strain-rate and rotation-rate tensors. Bragg & Collins showed that the power-law exponents in the RDFs predicted by the two theories were in good agreement for $St_\eta \ll 1$. They elaborated that this agreement was because the drift velocity predicted by Chun *et al.* was the same as the leading order term in the drift velocity of Zaichik and Alipchenkov [103]. As is to be expected, for $St_\eta \sim 1$, the theories diverge. Bragg & Collins also showed that the clustering of $St_\eta \ll 1$ particles was mainly due to the centrifuging process, whereas that of $St_\eta \sim 1$ particles was due to their path-history interactions with the turbulence.

In an accompanying study, Bragg and Collins [10] analyzed the theories of Zaichik and Alipchenkov [104], Pan and Padoan [57], and Gustavsson and Mehlig [35] by focusing on the second-order structure function of pair relative velocities, $\mathcal{S}_2^p(\mathbf{r}, t)$, predicted by these theories, where \mathbf{r} is the separation vector. Formulation of $\mathcal{S}_2^p(\mathbf{r}, t)$ is required to solve the governing equations for the moments of the pair PDF [104]. One may also compute the variances of the pair relative velocity and its components longitudinal and transverse to \mathbf{r} — $\langle U^2 \rangle$, $\langle U_r^2 \rangle$ and $\langle U_t^2 \rangle$ respectively—using $\mathcal{S}_2^p(\mathbf{r}, t)$ [57]. By comparing the predictions (primarily of the first two theories) with the DNS-computed $\mathcal{S}_2^p(\mathbf{r}, t)$, Bragg and Collins [10] identified possible discrepancies in the theories. In the case of Gustavsson and Mehlig [35] theory, only qualitative insights could be drawn regarding its predictions of the structure function and the RDF, since some coefficients were left unspecified in their theory.

Ireland et al. [39] performed an extensive parametric study of the effects of Reynolds number on inertial particle statistics through DNS of forced isotropic turbulence. They considered a wide range of Taylor micro-scale Reynolds numbers ($88 \leq Re_\lambda \leq 597$), and computed the statistics of single particles, as well as pairs for Stokes numbers $0.05 \leq St_\eta \leq 30$. It was observed that for $St_\eta \lesssim 1$, the RDF is essentially independent of Re_λ , whereas for $St_\eta \geq 10$, the RDF increased with Re_λ at nearly all separations. The latter trend is captured by our theory as well. As identified in Bragg and Collins [9], the effects of preferential concentration on pair relative-velocity statistics were important for $St_\eta \lesssim 0.1$, while the non-local effects due to particle sampling of turbulence become important for $St_\eta \gtrsim 0.2$. The relative velocity statistics of the $St_\eta \geq 10$ particles were found to increase strongly with Re_λ because these particles

retain for long times the effects of their interactions with the inertial and integral scale eddies.

Some of the most detailed theoretical and computational studies of high St_η particles were undertaken by Pan, Padoan, and coworkers [57, 63, 58, 59, 60, 61, 62]. Pan and Padoan [57] derived an analytical model for the relative velocity variance of inertial particles that is conceptually generalized across the entire range of particle Stokes numbers (this study will be hereafter referred to as PP10). The PP10 model is based on expressing the pair relative-velocity structure function $S_2^p(\mathbf{r}, t)$ in terms of the fluid relative-velocity structure function $S_2^f(\mathbf{r}, t)$, where $S_2^f(\mathbf{r}, t)$ is the Lagrangian correlation of fluid relative velocities along inertial particle-pair trajectories. Subsequently, they approximated $S_2^f(\mathbf{r}, t)$ as the product of the Eulerian structure tensor of turbulence and the Lagrangian autocorrelation of fluid relative velocities. Using this theory, they calculated the statistics of pair relative velocity (up to the second moment) for $1 \leq St_\eta \leq 100$, and compared these predictions with DNS data over a smaller Stokes-number range $1 \leq St_\eta \leq 10$. Good agreement between the model and DNS results was obtained. However, PP10 is limited to modeling the lower order moments of pair relative velocity, and does not provide any means to obtain the RDF, or the PDF of relative velocities.

Pan et al. [63] performed a DNS study of particle clustering in isotropic turbulence for $1 \lesssim St_\eta \lesssim 100$. In agreement with prior DNS and theoretical studies (e.g., Chun et al. [18]), they observed that the RDF shows a power-law scaling for pair separations in the dissipative range, with the exponent being a function of Stokes number. Further, particles whose response times scale with inertial-range time scales

show clustering at inertial separations, which is manifested as the peaking of RDF for these separations and subsequent plateauing for smaller separations. As seen in Chun et al. [18], the RDF of bidisperse pairs becomes flat at small scales, confirming that such pairs show weaker clustering than monodisperse ones.

Perhaps the broadest range of Stokes numbers considered thus far in particle-laden isotropic turbulence is by Pan and Padoan [58]. In that study, relative velocity statistics of $0.1 \leq St_\eta \leq 800$ particles were computed using both DNS and the model of PP10 [57]. Their goal was to investigate the relative motion statistics for separations smaller than the Kolmogorov scale, so as to draw insights on the collision rates of dust particles in protoplanetary disks. In protoplanetary turbulence, dust particles are much smaller than the Kolmogorov length scale ($\eta \sim 1$ km). Therefore, they focused on understanding and quantifying pair relative motion for separations $r \rightarrow 0$. Since such a fine resolution of separations is computationally prohibitive, Pan and Padoan [58] computed relative velocity statistics for separations as small as 0.25η , and then extrapolated these insights to smaller r . The extrapolation involved grouping the pairs into two categories: continuous and caustic types. Continuous-type pairs are those that may have started their journey as uncorrelated particles with high relative velocities at large separations, but decelerate as their separations decrease and remain correlated far longer than the flow time scales that influence their relative motion. Caustic-type pairs are those that remain uncorrelated with large relative velocities throughout their flight. It is believed that caustic pairs may significantly enhance collision rates, and that they dominate collision rates as $r \rightarrow 0$.

Predictions using PP10 of relative velocity and its components parallel and transverse to the separation vector showed good agreement with their DNS data.

Under the limits $St_r \gg 1$ and $St_I \gg 1$, Rani et al. [67] derived the transport equation for the PDF $\Omega(\mathbf{r}, \mathbf{U})$ of pair separation (\mathbf{r}) and relative velocity (\mathbf{U}). Here, the Stokes number St_r is based on the time scale τ_r of eddies whose size scales with separation r , and St_I is based on the integral time scale τ_I . The transport equation for $\Omega(\mathbf{r}, \mathbf{U})$, which is of the Fokker-Planck type, contains a diffusivity tensor in the \mathbf{U} space. We showed that the diffusivity is equal to $1/\tau_v^2$ times the time-integral of the Eulerian two-time correlation of fluid relative velocities seen by nearly stationary pairs (τ_v is the particle viscous relaxation time). In the current study, the two-time correlation is directly computed using DNS of forced isotropic turbulence containing stationary particles. The DNS-computed correlation when integrated in time yields what we will refer to as the *first closure form of diffusivity (CF1)*. An advantage of the CF1 diffusivity is that it will provide us a means to assess the the diffusivity formulation of [105, 103] in the $St_r \gg 1$ limit.

Alternatively to CF1, the Eulerian two-time correlation may be resolved analytically through the approximation that the temporal change in the fluid relative velocities seen by a pair is primarily due to the advection of size r eddies past the pair by larger eddies. Based on this physical picture and through an analogy with the Taylor hypothesis, one may transform the two-time correlation into two-point correlations of fluid velocities, allowing us to analytically formulate the diffusivity in terms of the energy spectrum. Rani et al. [67] derived two expressions based on whether the pair center of mass was held fixed or allowed to move during integral

time scales, the latter being an improvement over the former at finite St_I . We will refer to these expressions as the *second and third closure forms of diffusivity (CF2 and CF3)*, respectively.

In the current study, we first undertake a detailed analysis of the three closure forms of the diffusivity. Such an analysis will provide quantitative insights into the effects of the approximations entailed in deriving the closures, i.e. that the pairs are essentially fixed, and that the Eulerian two-time correlation may be expressed in terms of two-point correlations. Second, we perform both Langevin and direct numerical simulations to compute a number of statistics quantifying pair relative motion. Three sets of Langevin simulations are performed, corresponding to the three diffusivity forms. The LS results are compared with each other and with the DNS data. To our knowledge, this study presents the first comparison of the stochastic and DNS predictions of the relative velocity PDFs at separations spanning the entire range of turbulent scales. The pair statistics from LS are compared with those from DNS of particle-laden isotropic turbulence for $St_\eta = 10, 20, 40, 80$ and $Re_\lambda = 76, 131$. Statistics such as the RDF, relative velocity moments and PDFs, and the collision kernel are compared. Furthermore, we compare the present results with those from [105, 104] where available.

The organization of the chapter is as follows: Section 3.3 presents the important details of the closure theory, as well as identifies the three closure forms that are analyzed in this study. Section 3.4 discusses the computational details of the direct numerical and Langevin simulations. Section 3.5 presents an analysis of the diffusiv-

ity forms, as well as a comparison of the pair relative-motion statistics obtained from LS and DNS. We conclude by summarizing our findings in Section 3.6.

3.3 Theory

We begin with an overview of the Rani et al. [67] stochastic model for particle pairs in the limit of high Stokes number. A review of the theory will provide the necessary background for the subsequent discussion of the three closure forms that are investigated in this study.

[67] considered the pair phase-space density (PSD) $P(\mathbf{r}, \mathbf{U}, \mathbf{x}, \mathbf{V}; t)$, which is the PSD of a particle pair with separation \mathbf{r} , relative velocity \mathbf{U} , and center-of-mass position and velocity \mathbf{x} and \mathbf{V} , respectively. The inclusion of \mathbf{x} and \mathbf{V} in the state vector was motivated by the physical scenario that the dynamics of pair center-of-mass can influence the way a pair samples turbulence. Conservation of PSD P yields

$$\frac{\partial P}{\partial t} + \nabla_{\mathbf{r}} \cdot (\mathbf{U}P) + \nabla_{\mathbf{U}} \cdot (\dot{\mathbf{U}}P) + \nabla_{\mathbf{x}} \cdot (\mathbf{V}P) + \nabla_{\mathbf{V}} \cdot (\dot{\mathbf{V}}P) = 0 \quad (3.1)$$

where $\nabla_{\mathbf{r}}$, $\nabla_{\mathbf{x}}$, $\nabla_{\mathbf{U}}$, and $\nabla_{\mathbf{V}}$ denote gradients with respect to the corresponding state variables.

Assuming Stokes drag law to be valid, the governing equations for monodisperse pairs are:

$$\frac{d\mathbf{U}}{dt} = -\frac{1}{\tau_v} [\mathbf{U}(t) - \Delta \mathbf{u}(\mathbf{r}, \mathbf{x}, t)] \quad (3.2)$$

$$\frac{d\mathbf{V}}{dt} = -\frac{1}{\tau_v} \left[\mathbf{V}(t) - \frac{\mathbf{u}(\mathbf{R}_1(t), t) + \mathbf{u}(\mathbf{R}_2(t), t)}{2} \right] = -\frac{1}{\tau_v} [\mathbf{V}(t) - \mathbf{u}_{\text{cm}}(\mathbf{R}_1(t), \mathbf{R}_2(t), t)] \quad (3.3)$$

where τ_v is the particle response time, $\mathbf{R}_1(t)$ and $\mathbf{R}_2(t)$ are the particle positions at time t , $\Delta\mathbf{u}(\mathbf{r}, \mathbf{x}, t) = [\mathbf{u}(\mathbf{R}_2(t), t) - \mathbf{u}(\mathbf{R}_1(t), t)]$ is the seen fluid relative velocity, and $\mathbf{u}_{\text{cm}}(\mathbf{R}_1(t), \mathbf{R}_2(t), t) = [\mathbf{u}(\mathbf{R}_1(t), t) + \mathbf{u}(\mathbf{R}_2(t), t)]/2$. The velocity \mathbf{u}_{cm} can be determined from \mathbf{x} and \mathbf{r} since $\mathbf{R}_1 = \mathbf{x} - \frac{\mathbf{r}}{2}$ and $\mathbf{R}_2 = \mathbf{x} + \frac{\mathbf{r}}{2}$.

Substitution of the pair governing equations into (3.1) followed by ensemble averaging over flow realizations gives the equation for the probability density function (PDF) $\langle P \rangle$:

$$\begin{aligned} \frac{\partial \langle P \rangle}{\partial t} + \nabla_{\mathbf{r}} \cdot (\mathbf{U} \langle P \rangle) + \nabla_{\mathbf{x}} \cdot (\mathbf{V} \langle P \rangle) - \frac{1}{\tau_v} \nabla_{\mathbf{U}} \cdot (\mathbf{U} \langle P \rangle) - \frac{1}{\tau_v} \nabla_{\mathbf{V}} \cdot (\mathbf{V} \langle P \rangle) \\ + \frac{1}{\tau_v} \nabla_{\mathbf{U}} \cdot \langle \Delta \mathbf{u} P \rangle + \frac{1}{\tau_v} \nabla_{\mathbf{V}} \cdot \langle \mathbf{u}_{\text{cm}} P \rangle = 0 \end{aligned} \quad (3.4)$$

where $\langle \cdot \rangle$ denotes ensemble averaging, and the terms $\langle \Delta \mathbf{u} P \rangle$ and $\langle \mathbf{u}_{\text{cm}} P \rangle$ require closure. These terms represent turbulence-pair interactions and turbulence-center of mass interactions, respectively. In the limit of high Stokes number, they can be expressed as Fokker-Planck-type diffusion terms in the phase space.

Using the decomposition $P = \langle P \rangle + P'$, we can write $\langle \Delta \mathbf{u} P \rangle = \langle \Delta \mathbf{u} P' \rangle$ and $\langle \mathbf{u}_{\text{cm}} P \rangle = \langle \mathbf{u}_{\text{cm}} P' \rangle$, since $\langle \Delta \mathbf{u} \rangle = 0$ and $\langle \mathbf{u}_{\text{cm}} \rangle = 0$ in isotropic turbulence. This suggests that one may derive closures for these terms by solving for P' in terms of $\langle P \rangle$. Substituting $P = \langle P \rangle + P'$ into (3.1) and subtracting (3.4), the governing

equation for P' can be obtained as:

$$\begin{aligned}
& \frac{\partial P'}{\partial t} + \nabla_{\mathbf{r}} \cdot (\mathbf{U}P') + \nabla_{\mathbf{x}} \cdot (\mathbf{V}P') - \frac{1}{St_I} \nabla_{\mathbf{U}} \cdot (\mathbf{U}P') - \frac{1}{St_I} \nabla_{\mathbf{V}} \cdot (\mathbf{V}P') \\
& + \frac{1}{St_I} \nabla_{\mathbf{U}} \cdot (\Delta \mathbf{u}P') + \frac{1}{St_I} \nabla_{\mathbf{V}} \cdot (\mathbf{u}_{\text{cm}}P') = -\frac{1}{St_I} \nabla_{\mathbf{U}} \cdot (\Delta \mathbf{u}\langle P \rangle) \\
& - \frac{1}{St_I} \nabla_{\mathbf{V}} \cdot (\mathbf{u}_{\text{cm}}\langle P \rangle) + \frac{1}{St_I} \nabla_{\mathbf{U}} \cdot \langle \Delta \mathbf{u}P' \rangle + \frac{1}{St_I} \nabla_{\mathbf{V}} \cdot \langle \mathbf{u}_{\text{cm}}P' \rangle
\end{aligned} \tag{3.5}$$

where $St_I = \tau_v/\tau_I$, and terms are made dimensionless using integral length scale (L), integral time scale (τ_I), and RMS fluctuating velocity (u_{rms}).

Recognizing that P' may be expressed as a perturbation expansion in $1/St_I$ ($St_I \gg 1$), we can write to leading order $P' = \frac{1}{St}P_1$. Retaining $O(1/St_I)$ terms in (3.5), we get

$$\frac{\partial P_1}{\partial t} + \nabla_{\mathbf{r}} \cdot (\mathbf{U}P_1) + \nabla_{\mathbf{x}} \cdot (\mathbf{V}P_1) = -\nabla_{\mathbf{U}} \cdot (\Delta \mathbf{u}\langle P \rangle) - \nabla_{\mathbf{V}} \cdot (\mathbf{u}_{\text{cm}}\langle P \rangle) \tag{3.6}$$

Equation (3.6) is a Lagrangian evolution equation of P_1 in the $(\mathbf{r}, \mathbf{x}, t)$ space, with \mathbf{U} and \mathbf{V} held fixed.

In the limit of $St_I \gg 1$ and $St_r \gg 1$, Rani et al. [67] showed that the two convective terms on the LHS of (3.6) can be neglected compared to $\frac{\partial P_1}{\partial t}$. We can now solve for P_1 such that \mathbf{r} and \mathbf{x} remain fixed, giving us

$$\begin{aligned}
\langle \Delta \mathbf{u}P' \rangle = & -\frac{1}{St_I^2} \int_{-\infty}^0 dt \{ \langle \Delta \mathbf{u}(\mathbf{x}, \mathbf{r}, 0) \Delta \mathbf{u}(\mathbf{x}, \mathbf{r}, t) \rangle \cdot \nabla_{\mathbf{U}} \langle P \rangle(t) + \\
& \langle \Delta \mathbf{u}(\mathbf{x}, \mathbf{r}, 0) \mathbf{u}_{\text{cm}}(\mathbf{R}_1(0), \mathbf{R}_2(0), t) \rangle \cdot \nabla_{\mathbf{V}} \langle P \rangle(t) \}
\end{aligned} \tag{3.7}$$

$$\begin{aligned} \langle \mathbf{u}_{\text{cm}} P' \rangle = & -\frac{1}{St_I^2} \int_{-\infty}^0 dt \{ \langle \mathbf{u}_{\text{cm}}(\mathbf{R}_1(0), \mathbf{R}_2(0), 0) \Delta \mathbf{u}(\mathbf{x}, \mathbf{r}, t) \rangle \cdot \nabla_{\mathbf{U}} \langle P \rangle(t) + \\ & \langle \mathbf{u}_{\text{cm}}(\mathbf{R}_1(0), \mathbf{R}_2(0), 0) \mathbf{u}_{\text{cm}}(\mathbf{R}_1(0), \mathbf{R}_2(0), t) \rangle \cdot \nabla_{\mathbf{V}} \langle P \rangle(t) \} \quad (3.8) \end{aligned}$$

where \mathbf{r} , \mathbf{x} , particle positions \mathbf{R}_1 and \mathbf{R}_2 , and the PDF $\langle P \rangle$ undergo little change during flow time scales.

At this point, it is pertinent to discuss the similarities and differences between the above perturbation analysis, and the renormalized perturbation approach used in Reeks [70]. Reeks [70] pioneered the application of the LHDI method of Kraichnan [45] to derive the PDF equation for particle position and velocity, as well as a closure for the phase-space diffusion current. The derivation of the closure using the LHDI method entailed a renormalized perturbation expansion, which is effectively an expansion with $1/St_I$ as the perturbation parameter. Section 3.7 presents a detailed comparison of the two perturbation methods.

The time integrals of the four correlations on the RHS of equations (3.7)-(3.8) are, respectively, the diffusivities D_{UU} , D_{UV} , D_{VU} , and D_{VV} . Here D_{UU} and D_{VV} are diffusivities in the \mathbf{U} -space and \mathbf{V} -space, respectively; D_{UV} and D_{VU} are cross diffusivities. Equation (3.4) for the probability density function (PDF) $\langle P \rangle$ may now be written as:

$$\begin{aligned} \frac{\partial \langle P \rangle}{\partial t} + \nabla_{\mathbf{r}} \cdot (\mathbf{U} \langle P \rangle) + \nabla_{\mathbf{x}} \cdot (\mathbf{V} \langle P \rangle) - \frac{1}{\tau_v} \nabla_{\mathbf{U}} \cdot (\mathbf{U} \langle P \rangle) - \frac{1}{\tau_v} \nabla_{\mathbf{V}} \cdot (\mathbf{V} \langle P \rangle) \\ - \nabla_{\mathbf{U}} \cdot (D_{UU} \cdot \nabla_{\mathbf{U}} \langle P \rangle + D_{UV} \cdot \nabla_{\mathbf{V}} \langle P \rangle) \\ - \nabla_{\mathbf{V}} \cdot (D_{VU} \cdot \nabla_{\mathbf{U}} \langle P \rangle + D_{VV} \cdot \nabla_{\mathbf{V}} \langle P \rangle) = 0 \quad (3.9) \end{aligned}$$

3.3.1 Three closure forms for diffusivity D_{UU}

Since our primary interest is in the statistics of pair relative motion, we will consider a more tractable, lower dimensional PDF $\Omega(\mathbf{r}, \mathbf{U}) = \int \langle P \rangle(\mathbf{r}, \mathbf{U}, \mathbf{x}, \mathbf{V}; t) d\mathbf{V}$, where the dependence on \mathbf{x} was dropped due to homogeneity. In Rani et al. [67], we showed that (3.9) yields the following equation (in dimensional form) for $\Omega(\mathbf{r}, \mathbf{U})$:

$$\frac{\partial \Omega}{\partial t} + \nabla_{\mathbf{r}} \cdot (\mathbf{U} \Omega) - \frac{1}{\tau_v} \nabla_{\mathbf{U}} \cdot (\mathbf{U} \Omega) - \nabla_{\mathbf{U}} \cdot (D_{UU} \cdot \nabla_{\mathbf{U}} \Omega) = 0 \quad (3.10)$$

where τ_v is the particle viscous relaxation time, and \mathbf{r} and \mathbf{U} are the pair separation and relative velocity, respectively. The diffusivity D_{UU} is given by

$$D_{UU} = \frac{1}{\tau_v^2} \int_{-\infty}^0 \langle \Delta \mathbf{u}(\mathbf{r}, \mathbf{x}, 0) \Delta \mathbf{u}(\mathbf{r}, \mathbf{x}, t) \rangle dt \quad (3.11)$$

where the integrand is the Eulerian two-time correlation of fluid relative velocities, with both pair separation \mathbf{r} and center-of-mass position \mathbf{x} held fixed. This formulation of diffusivity is valid under the conditions $St_r \gg 1$ and $St_I \gg 1$.

In this study, D_{UU} in (3.11) is resolved using three approaches, giving rise to three closure forms. In the first closure form (CF1), the two-time correlation in (3.11) is directly computed from DNS of forced isotropic turbulence with stationary particles, and integrated in time to yield D_{UU} . In the second closure form (CF2), the Eulerian two-time correlation of relative velocities is converted into two-point correlations of fluid velocities, allowing us to derive an expression in terms of an integral over the wavenumber. In the third closure form (CF3), \mathbf{r} remains fixed

during flow time scales, but \boldsymbol{x} responds to integral-scale eddies, i.e. \boldsymbol{x} changes during integral time scales. Thus, CF3 attempts to improve upon and extend CF2’s validity to $St_I \sim 1$. The effects of CF3, however, are anticipated to be seen only at the lower end of the Stokes-number range considered. At higher Stokes numbers, CF2 and CF3 should show very similar behavior.

One may regard CF1 as the most accurate among the three closure forms since a DNS-based evaluation of the Eulerian two-time correlation would entail no further approximations. But, CF2 and CF3, the latter in spite of its improvements, contain approximations made to obtain analytical expressions for diffusivity. The differences between CF1 and CF2/CF3, and their implications for pair statistics are extensively analyzed in this study.

In the following discussion, we present the salient features of the derivation of CF2 and CF3 (details are in Rani et al. [67]). The computational details of the evaluation of D_{UU} for CF1 are discussed in Section 3.4.1.

3.3.2 CF2 and CF3

In arriving at (3.11), Rani et al. [67] considered the limits $St_r \gg 1$ and $St_I \gg 1$. In these Stokes number regimes, particles are nearly stationary so that the temporal change in $\Delta \boldsymbol{u}$ experienced by pairs is primarily due to the evolution of turbulent scales and not due to pair (relative) motion itself. Rani et al. [67] approximated the temporal evolution of $\Delta \boldsymbol{u}$ at two positions separated by \boldsymbol{r} as arising due to the passive advection of eddies of size r by larger, integral-scale eddies. Hence, one may replace the Eulerian two-time correlation in (3.11) by a correlation of relative velocities seen

by two pairs with the same \mathbf{r} , but with the centers of mass separated by $\mathbf{u}_I t$, where \mathbf{u}_I is the large-scale fluid velocity. This would give us closure form 2 (CF2) for D_{UU} :

$$D_{UU}^{[2]} = \frac{1}{\tau_v^2} \int_{-\infty}^0 \langle \Delta \mathbf{u}(\mathbf{x}, \mathbf{r}, 0) \Delta \mathbf{u}(\mathbf{x} + \mathbf{u}_I t, \mathbf{r}, 0) \rangle dt \quad (3.12)$$

Relaxing the $St_I \gg 1$ criterion to $St_I \sim 1$ enables us to account for the change in center-of-mass position due to interactions with eddies of timescales $\sim \tau_v$, the center-of-mass response time. This is done by replacing \mathbf{u}_I with the relative velocity \mathbf{W} between the large-scale eddies and the center of mass, yielding closure form 3 (CF3):

$$D_{UU}^{[3]}(\mathbf{r}, W) = \frac{1}{\tau_v^2} \int_{-\infty}^0 \langle \Delta \mathbf{u}(\mathbf{x}, \mathbf{r}, t) \Delta \mathbf{u}(\mathbf{x} + \mathbf{W}t, \mathbf{r}, t) \rangle dt \quad (3.13)$$

In the discussion that follows, we will focus on CF3, since the final expressions for CF2 and CF3 differ only by a constant factor.

The CF3 diffusivity can then be expressed as an average over all values of \mathbf{W} as:

$$D_{UU}^{[3]}(\mathbf{r}) = \int D_{UU}^{[3]}(\mathbf{r}, W) \Phi(\mathbf{W}) d\mathbf{W} \quad (3.14)$$

where $\Phi(\mathbf{W})$ is the PDF of \mathbf{W} , and

$$\begin{aligned}
D_{UU}^{[3]}(\mathbf{r}, W) &= \frac{1}{\tau_v^2} \int_{-\infty}^0 \langle \Delta \mathbf{u}(\mathbf{x}, \mathbf{r}, t) \Delta \mathbf{u}(\mathbf{x} + \mathbf{W}t, \mathbf{r}, t) \rangle dt \\
&= \frac{1}{\tau_v^2} \int_{-\infty}^0 \left\langle \left[\mathbf{u}\left(\mathbf{x} + \frac{1}{2}\mathbf{r}, t\right) - \mathbf{u}\left(\mathbf{x} - \frac{1}{2}\mathbf{r}, t\right) \right] \right. \\
&\quad \times \left. \left[\mathbf{u}\left(\mathbf{x} + \mathbf{W}t + \frac{1}{2}\mathbf{r}, t\right) - \mathbf{u}\left(\mathbf{x} + \mathbf{W}t - \frac{1}{2}\mathbf{r}, t\right) \right] \right\rangle dt \\
&= \frac{1}{\tau_v^2} \int_{-\infty}^0 \left\langle \mathbf{u}\left(\mathbf{x} + \frac{1}{2}\mathbf{r}, t\right) \mathbf{u}\left(\mathbf{x} + \mathbf{W}t + \frac{1}{2}\mathbf{r}, t\right) - \mathbf{u}\left(\mathbf{x} + \frac{1}{2}\mathbf{r}, t\right) \mathbf{u}\left(\mathbf{x} + \mathbf{W}t - \frac{1}{2}\mathbf{r}, t\right) \right. \\
&\quad \left. - \mathbf{u}\left(\mathbf{x} - \frac{1}{2}\mathbf{r}, t\right) \mathbf{u}\left(\mathbf{x} + \mathbf{W}t + \frac{1}{2}\mathbf{r}, t\right) + \mathbf{u}\left(\mathbf{x} - \frac{1}{2}\mathbf{r}, t\right) \mathbf{u}\left(\mathbf{x} + \mathbf{W}t - \frac{1}{2}\mathbf{r}, t\right) \right\rangle dt \tag{3.15}
\end{aligned}$$

Since \mathbf{W} is principally influenced by the large-scale fluid eddies, its PDF can be considered as Gaussian [5]:

$$\Phi(\mathbf{W}) = \frac{1}{\sqrt{(2\pi W_{\text{rms}}^2)^3}} e^{-\frac{W^2}{2W_{\text{rms}}^2}} \tag{3.16}$$

where W_{rms} is the RMS fluctuating velocity of \mathbf{W} . The two-point velocity correlations in (3.15) may be expressed in terms of the velocity spectrum tensor $R(\mathbf{k})$, allowing us to further analytically resolve this equation.

For isotropic turbulence, we can write D_{UU} as:

$$D_{UU,ij} = D_{UU,\perp} \left(\delta_{ij} - \frac{r_i r_j}{r^2} \right) + D_{UU,\parallel} \frac{r_i r_j}{r^2} \tag{3.17}$$

For CF3, Rani et al. [67] derived the following forms for $D_{UU,\perp}$ and $D_{UU,\parallel}$:

$$D_{UU,\perp}^{[3]}(r) = \frac{1}{2} \frac{2\pi^2}{\tau_v^2} \sqrt{\frac{1}{(2\pi)^3 W_{\text{rms}}^2}} \times \int_0^\infty \frac{E(\xi)}{\xi} \left[\frac{8}{3} - \frac{4\sin(r\xi)}{r\xi} - \frac{4\cos(r\xi)}{r^2\xi^2} + \frac{4\sin(r\xi)}{r^3\xi^3} \right] d\xi \quad (3.18)$$

$$D_{UU,\parallel}^{[3]}(r) = \frac{2\pi^2}{\tau_v^2} \sqrt{\frac{1}{(2\pi)^3 W_{\text{rms}}^2}} \times \int_0^\infty \frac{E(\xi)}{\xi} \left[\frac{4}{3} + \frac{4\cos(r\xi)}{r^2\xi^2} - \frac{4\sin(r\xi)}{r^3\xi^3} \right] d\xi \quad (3.19)$$

where $E(\xi)$ is the energy spectrum, ξ is the wavenumber, and the analytical expression for W_{rms} is presented in Section 3.3.3. The corresponding forms for CF2 can be obtained by simply replacing W_{rms} with u_{rms} in (3.18) and (3.19), where u_{rms} is the fluid fluctuating RMS velocity. It is anticipated that at high Stokes numbers, $W_{\text{rms}} \rightarrow u_{\text{rms}}$ so that CF2 and CF3 approach each other.

3.3.3 Expression for W_{rms}

W_{rms} is the RMS of the relative velocity between large-scale eddies and the center-of-mass velocity. It is given by

$$W_{\text{rms}}^2 = \frac{1}{3} \langle (u_i - V_i)^2 \rangle = \frac{1}{3} [\langle u_i^2 \rangle + \langle V_i^2 \rangle - 2 \langle V_i u_i \rangle] \quad (3.20)$$

where V_i is the velocity of the pair center-of-mass, u_i is the fluid velocity with which eddies of size r are advected past the pair by larger eddies, and $\langle u_i^2 \rangle = \langle u_1^2 + u_2^2 + u_3^2 \rangle$ ($\langle V_i^2 \rangle$ follows a similar notation).

The velocity V_i is governed by

$$\frac{dV_i}{dt} = \frac{u_{\text{cm},i} - V_i}{\tau_v} \quad (3.21)$$

where $u_{\text{cm},i}$ was defined in (3.3). Multiplying (3.21) with V_i and ensemble-averaging yields

$$\frac{d\langle \frac{1}{2}V_i^2 \rangle}{dt} = \frac{\langle u_i V_i \rangle - \langle V_i^2 \rangle}{\tau_v} \quad (3.22)$$

where $\langle u_{\text{cm},i} V_i \rangle$ is approximated with $\langle u_i V_i \rangle$ on the RHS of (3.22). This is reasonable since both $u_i - V_i$ and $u_{\text{cm},i} - V_i$ are determined by eddies with sizes of the order of or smaller than r , so that these two quantities are expected to have similar statistics.

At steady state, $\langle V_i u_i \rangle = \langle V_i^2 \rangle$. This means that from (3.21)

$$\begin{aligned} W_{\text{rms}}^2 &= \frac{1}{3} [\langle u_i^2 \rangle - \langle V_i^2 \rangle] = \frac{1}{3} \langle u_i^2 \rangle \left(1 - \frac{\langle V_i^2 \rangle}{\langle u_i^2 \rangle} \right) \\ &= u'^2 \left(1 - \frac{V'^2}{u'^2} \right) \end{aligned} \quad (3.23)$$

where $\frac{1}{3} \langle u_i^2 \rangle = u'^2$, and similarly $\frac{1}{3} \langle V_i^2 \rangle = V'^2$. To close W_{rms} , one needs expressions for u' and the ratio V'/u' . The latter was obtained from [42]:

$$\frac{V'^2}{u'^2} = \frac{\tau_\eta(\tau_v + T') + \tau_v T'}{(\tau_\eta + \tau_v)(\tau_v + T')} \quad (3.24)$$

where T_L is the fluid Lagrangian integral time-scale, $T' = T_{fp} - \tau_\eta$, τ_η is the Kolmogorov time scale and T_{fp} is the Lagrangian integral time-scale of fluid velocities seen by the particles. Jung et al. (2008) provided an expression for T_{fp} in terms of

fluid Eulerian and Lagrangian integral time scales. Further, it can be inferred from their study that $u'^2 = u_{\text{rms}}^2$ for high St particles, i.e. variance of fluid velocity seen by high-inertia particles is nearly equal to the variance of turbulent velocity fluctuations.

3.4 Computational Details

In this section, we present a discussion of the two types of simulations performed in this study: direct numerical simulations and Langevin simulations. DNS with stationary particles were used to compute the Eulerian two-time correlation in (3.11) that is needed for CF1. DNS with moving particles were used to validate the LS predictions for four Stokes numbers $St_\eta = 10, 20, 40, 80$, at two Reynolds numbers $Re_\lambda = 76, 131$.

3.4.1 DNS

Fluid Phase

In homogeneous isotropic turbulence (HIT), there is no inherent production of turbulent kinetic energy. As a result, when performing DNS of HIT, the turbulence decays monotonically in time. To achieve statistical stationarity, one applies forcing to the low wavenumber velocity components, i.e., one adds energy to the large scales of turbulence. The assumption implicit to the forcing of low wavenumbers is that the time-averaged small-scale quantities are not significantly influenced by the mechanism of energy production at the large scales, but will only depend on the gross effects such as the turbulent kinetic energy and its production rate [25]. For this assumption to

be appropriate, it is necessary that the high-wavenumber regions of the computed spectral quantities do not depend on the details of the forcing scheme. Eswaran and Pope [25] investigated the effects of a stochastic forcing scheme on the isotropy of small-scale statistics. They concluded that the forcing scheme did not have an undue effect on the values of the spectral statistics at high wavenumbers. However, it is not entirely clear from their study if the forcing affects the spatial and temporal coherence of large scale eddies. Since the coherence of eddies has a direct effect on the diffusivity tensor D_{UU} through the fluid relative velocity correlations, the nature of the forcing may impact the dynamics of particle pairs for the Stokes numbers under consideration. This aspect needs to be studied in greater detail, and is outside the scope of the current work.

Direct numerical simulations of forced isotropic turbulence were performed using a discrete Fourier-expansion-based pseudospectral method. Simulations were performed over a cubic domain of length 2π discretized using N^3 grid points, with periodic boundary conditions. The fluid velocity is advanced in time by solving the Navier-Stokes equations in rotational form, as well as the continuity equation for an incompressible fluid [12, 38]:

$$\begin{aligned} \nabla \cdot \mathbf{u} &= 0 \\ \frac{\partial \mathbf{u}}{\partial t} + \boldsymbol{\omega} \times \mathbf{u} &= -\nabla (p/\rho_f + \mathbf{u}^2/2) + \nu \nabla^2 \mathbf{u} + \mathbf{f}_f \end{aligned} \tag{3.25}$$

where \mathbf{u} is the fluid velocity, $\boldsymbol{\omega} = \nabla \times \mathbf{u}$ is the vorticity, ρ_f is the fluid density, p is the pressure, ν is the kinematic viscosity, and \mathbf{f}_f is the external forcing applied

Table 3.1: Flow parameters in DNS of isotropic turbulence (arbitrary units). N is the number of grid points in each direction, $Re_\lambda \equiv u_{\text{rms}}\lambda/\nu$ is the Taylor micro-scale Reynolds number, $u_{\text{rms}} \equiv \sqrt{(2k/3)}$ is the fluid RMS fluctuating velocity, k is the turbulent kinetic energy, ν is the fluid kinematic viscosity, $\epsilon \equiv 2\nu \int_0^{\kappa_{\text{max}}} \kappa^2 E(\kappa) d\kappa$ is the turbulent energy dissipation rate, $L \equiv 3\pi/(2k) \int_0^{\kappa_{\text{max}}} E(\kappa)/\kappa d\kappa$ is the integral length scale, $\lambda \equiv u_{\text{rms}}\sqrt{(15\nu/\epsilon)}$ is the Taylor microscale, $\eta \equiv \nu^{3/4}/\epsilon^{1/4}$ is the Kolmogorov length scale, $T_{\text{eddy}} \equiv L/u'$ is the large-eddy turnover time, $\tau_\eta \equiv \sqrt{(\nu/\epsilon)}$ is the Kolmogorov time scale, κ_{max} is the maximum resolved wavenumber, Δt is the time step, and N_p is the number of particles per Stokes number.

Parameter	DNS I	DNS II
N	128	256
Re_λ	76	131
u_{rms}	0.9683	1.0894
ν	0.0071	0.0028
ϵ	0.3189	0.4315
L	1.4942	1.4225
λ	0.5622	0.3438
η	0.0327	0.0152
T_{eddy}	1.5431	1.3057
τ_η	0.1499	0.0814
$\kappa_{\text{max}}\eta$	1.9610	1.8287
Δt	0.0025	0.0010
N_p	100000	262144

to maintain a statistically stationary turbulence. The particle loading is assumed to be dilute so that the influence of particles on the fluid is negligible. The various turbulence parameters for the two Re_λ are summarized in Table 3.1. Further details of the pseudospectral algorithm may be found in Ireland et al. [38] and Brucker et al. [12].

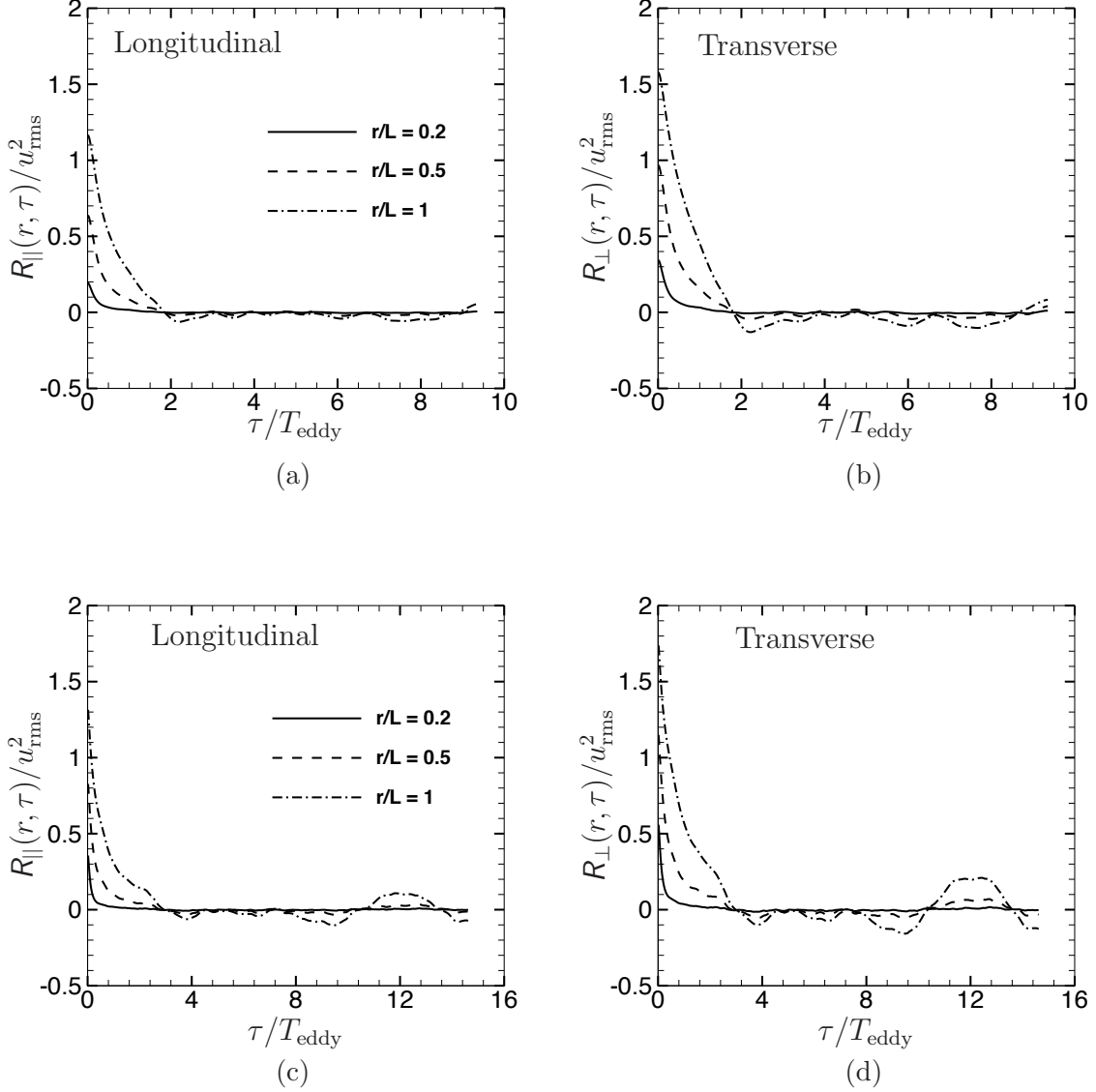


Figure 3.1: The Eulerian two-time correlation of fluid relative velocities $R(r, \tau) = \langle \Delta \mathbf{u}(\mathbf{r}, t) \Delta \mathbf{u}(\mathbf{r}, t + \tau) \rangle$. The longitudinal and transverse components of $R(r, \tau)$, i.e. $R_{\parallel}(r, \tau)$ and $R_{\perp}(r, \tau)$, are shown as a function of time at separations $r/L = 0.2, 0.5, 1$. Figures (a,b) $Re_\lambda = 76$, and (c,d) $Re_\lambda = 131$. The integral length scale $L = \pi / (2u^2) \int_0^{\kappa_{\text{max}}} E(\kappa) / \kappa d\kappa$, and time scale $T_{\text{eddy}} = L / u_{\text{rms}}$.

Relative Velocity Correlation in CF1

For closure form 1 (CF1), computing the diffusivity D_{UU} requires the correlation $\langle \Delta \mathbf{u}(\mathbf{r}, \mathbf{x}, 0) \Delta \mathbf{u}(\mathbf{r}, \mathbf{x}, t) \rangle$ as input. This correlation was evaluated using DNS of forced isotropic turbulence with stationary disperse particles. Two simulation parameters that impact the computed correlation are the number of particles (thereby, pairs), and the bin size (Δr) for pair separations. Bin size refers to the thickness of the radial shell spanning $r - \Delta r/2$ to $r + \Delta r/2$, within which we search for pairs. An important consideration in determining the number of particles is the need to obtain converged correlations at separations $r \sim \eta$, where η is Kolmogorov length scale. In this regard, we varied the number of particles from 10^5 to 10^6 . Although smooth statistics were obtained for 5×10^5 particles, we used 10^6 particles or $\sim 5 \times 10^{11}$ pairs for computing the two-time correlation. It may be recalled that these particles are stationary, and are to be distinguished from those indicated in Table 3.1 that are in motion. The “optimal” bin size for pair separations is determined by balancing two competing requirements: convergence of statistics at $r \sim \eta$, and the reduction of statistical noise associated with too small a bin size. We considered bin sizes varying between $\eta/20$ and 2η , and found that a bin size of $\eta/8$ satisfied the two constraints.

Evaluation of the two-time correlation of seen fluid relative velocities for nearly half a trillion pairs is a highly computationally intensive process. We adopted the following procedure to compute these correlations from DNS of isotropic turbulence with fixed particles. Considering two snapshots of flow separated by a time interval τ in a DNS run, the longitudinal and transverse components of the product

$\Delta\mathbf{u}(\mathbf{r}, \mathbf{x}, t)\Delta\mathbf{u}(\mathbf{r}, \mathbf{x}, t + \tau)$ for a particle pair are stored in the appropriate r bin, and then averaged over all pairs within a bin. Next, we average the two components over pairs of flow snapshots with the same time separation τ . For each value of τ , we averaged over 200 such pairs of flow snapshots. In Figure 3.1(a) and (b), we show the longitudinal and transverse components, respectively, of the relative velocity correlation as a function of τ at separations $r = L/5, L/2, L$ for $Re_\lambda = 76$. Here L is the integral length scale. The corresponding plots for $Re_\lambda = 131$ are shown in Figure 3.1(c) and (d). The correlations at various separations are then integrated in time to yield D_{UU} for CF1.

Particle phase

The governing equations for the motion of a dense spherical particle smaller than the Kolmogorov length scale may be written as [51]

$$\frac{d\mathbf{x}_p}{dt} = \mathbf{v}_p, \quad (3.26)$$

$$\frac{d\mathbf{v}_p}{dt} = \frac{\mathbf{u}(\mathbf{x}_p, t) - \mathbf{v}_p}{\tau_v}, \quad (3.27)$$

where \mathbf{x}_p and \mathbf{v}_p are the particle position and velocity, respectively, and $\tau_v = \rho_p d_p^2 / 18\mu$ is the particle response time (ρ_p is the particle density, d_p its diameter, and μ is fluid dynamic viscosity). In Eq. (3.27), $\mathbf{u}(\mathbf{x}_p, t)$ is the fluid velocity at the particle's location. In the DNS runs, the seen fluid velocity is evaluated through an 8th order Lagrange interpolation method involving a stencil of $8 \times 8 \times 8$ fluid velocities surrounding the particle location.

Temporal update of particle motion is achieved through a modified second-order Runge-Kutta (RK2) method in which the standard RK2 weights are replaced by exponential integrators as follows [38]:

$$\mathbf{v}_p(t_0 + h) = e^{-h/\tau_v} \mathbf{v}_p(t_0) + w_1 \mathbf{u}_p[\mathbf{x}_p(t_0)] + w_2 \mathbf{u}[\mathbf{x}_p(t_0) + \mathbf{v}_p(t_0)h] \quad (3.28)$$

where h is the time step, and the exponential integrators w_1 and w_2 are given by

$$w_1 \equiv \left(\frac{h}{\tau_v}\right) \left[\phi_1\left(\frac{-h}{\tau_v}\right) - \phi_2\left(\frac{-h}{\tau_v}\right) \right], \quad w_2 \equiv \left(\frac{h}{\tau_v}\right) \phi_1\left(\frac{-h}{\tau_v}\right) \quad (3.29)$$

$$\phi_1(z) \equiv \frac{e^z - 1}{z}, \quad \phi_2(z) \equiv \frac{e^z - z - 1}{z^2} \quad (3.30)$$

In the DNS runs, the particles are evolved for at least $6\tau_v$'s for the $St_\eta = 80$ particles, and $45\tau_v$'s for the $St_\eta = 10$ particles, before we begin collecting their statistics. Subsequently, the particle statistics are averaged for nearly $10\tau_v$'s for the $St_\eta = 80$ particles, and $75\tau_v$'s for the $St_\eta = 10$ particles.

3.4.2 Langevin simulations

Using the CF1, CF2 and CF3 closures for D_{UU} discussed in Section 3.3, three sets of Langevin stochastic simulations were performed to evolve pair separations \mathbf{r}

and relative velocities \mathbf{U} . The governing equations for \mathbf{r} and \mathbf{U} are:

$$\frac{d\mathbf{r}}{dt} = \mathbf{U} \quad (3.31)$$

$$d\mathbf{U} = -\frac{\mathbf{U}}{\tau_v} dt + \mathbf{B} \cdot dW \quad (3.32)$$

Here, W represents a Wiener process, and the diffusion matrix \mathbf{B} can be written in terms of D_{UU} as:

$$\mathbf{B} \cdot \mathbf{B}^T = 2D_{UU}(r) \quad (3.33)$$

where \mathbf{B}^T is the transpose of \mathbf{B} , and \mathbf{B} is computed from a Cholesky decomposition of $D_{UU}(r)$. Simulation of Langevin equations (3.31) and (3.32) is statistically equivalent to solving the Fokker-Plank equation (3.10) for the PDF $\Omega(\mathbf{r}, \mathbf{U})$.

To be able to consistently compare pair statistics from the Langevin and DNS runs, it is important that the Langevin simulations use the same turbulence parameters as those in statistically stationary DNS. Hence, inputs to Langevin runs such as the Kolmogorov and integral length scales, dissipation rate, kinematic viscosity, u_{rms} , and Re_λ are all identical to those in Table 3.1. In particular, one also has to ensure that the model energy spectrum used in CF2 and CF3 closely matches the DNS energy spectrum. This was achieved by suitably selecting the parametric inputs to the model spectrum provided in Pope [64], as follows:

Table 3.2: Parameters for the model energy spectrum. After determining c_L and c_η , the parameter C was adjusted to match the DNS energy spectrum. [64] suggested $C = 1.5$.

Parameter	$Re_\lambda = 76$	$Re_\lambda = 131$
C	1.908	1.866
c_L	0.3855	0.3643
c_η	0.4165	0.4078
κ_{\max}	60	120

$$E(\kappa) = C\epsilon^{2/3}\kappa^{-5/3}f_L(\kappa L)f_\eta(\kappa\eta) \quad (3.34)$$

$$f_L(\kappa L) = \left(\frac{\kappa L}{[(\kappa L)^2 + c_L]^{1/2}} \right)^{5/3+p_0} \quad (3.35)$$

$$f_\eta(\kappa\eta) = \exp \left\{ -\beta \left[(\kappa\eta)^4 + c_\eta^4 \right]^{1/4} - c_\eta \right\} \quad (3.36)$$

where $\beta = 5.2$ and $p_0 = 2$ [64]. The parameters c_L and c_η are determined from the following constraints:

$$\frac{3}{2}u_{\text{rms}}^2 = \int_1^{\kappa_{\max}} E(\kappa) d\kappa \quad (3.37)$$

$$\epsilon = 2\nu \int_1^{\kappa_{\max}} \kappa^2 E(\kappa) d\kappa \quad (3.38)$$

where ϵ is the dissipation rate, and the wavenumber limits $[1, \kappa_{\max}]$ are the same as in DNS. These wavenumber limits are also used in (3.18) and (3.19) for CF2 and CF3. The parameters c_L and c_η are numerically evaluated using the DNS values of u_{rms} , ϵ and ν from Table 3.1. The resulting values are shown in Table 3.2. In Figure 3.2, the model spectra calculated from Eqs. (3.34)-(3.36) are compared with the DNS energy

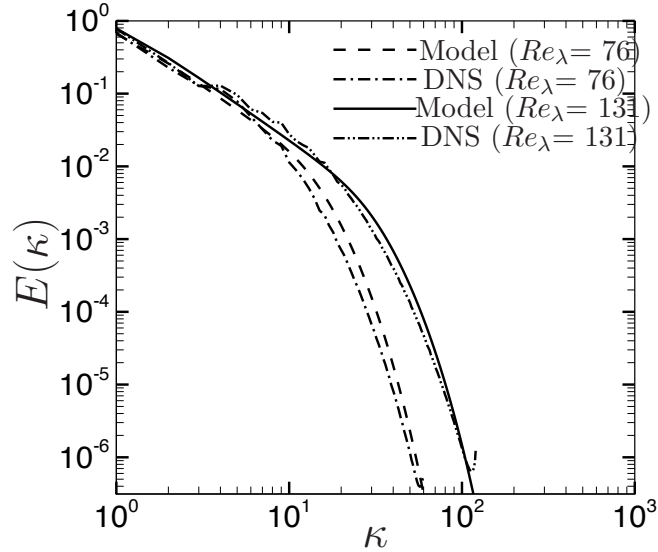


Figure 3.2: Comparison of the DNS and model energy spectra at $Re_\lambda = 76$ and $Re_\lambda = 131$. The model spectrum is used to compute the CF1 and CF2 diffusivities.

spectra for $Re_\lambda = 76$ and $Re_\lambda = 131$. Good agreement is seen between the model and DNS spectra.

The computational domain in the Langevin simulations is a sphere of diameter $8L$, where L is the integral length scale. This domain size is sufficiently large, since particle pairs become decorrelated at separations of $O(L)$ for all the Stokes numbers considered in this study. A specular reflective boundary condition was imposed at the outer boundary of the domain. This meant that a particle colliding with the outer boundary is reflected back into the domain, with its velocity component tangential to the boundary unaffected, and the velocity component normal to the boundary reversed.

For each St_η , pair statistics are averaged for at least $1000\tau_v$'s. Such a large averaging time was necessary due to the strong dependence of the statistical errors on the sample size in Langevin simulations. Further, in order to increase the sample size at separations of the order of Kolmogorov length scale, a single pair is split into multiple, equally-weighted fractional pairs whenever the separation of a pair goes below a certain value [67]. When a parent pair is split, initially the fractional pairs have the same position and velocity vectors as the parent. Each of the fractional pairs is then evolved independently, except that it only makes a fractional contribution when computing the statistics. In our simulations, splitting is executed at three different radial locations, $r = 2\eta, 5\eta, 10\eta$. However, fractional pairs are not split again. We found that splitting a pair into 10 equally-weighted fractional pairs gave us sufficient data at the smaller separations without excessively increasing the number of pairs to be tracked. Recombination of fractional pairs when their separations exceeded the specified radial distances was not undertaken.

3.5 Results and discussion

Langevin and DNS runs were performed for Stokes numbers $St_\eta = 10, 20, 40, 80$ at $Re_\lambda = 76$ and 131. Three sets of Langevin simulations—a total of 24 simulations—were conducted corresponding to the closure forms CF1, CF2 and CF3. In each LS, 60×10^6 pairs per Stokes number were considered. The number of particles in the DNS runs are provided in Table 3.1.

The discussion of the results is presented in three subsections. In Section 3.5.1, we first compare the three forms of the diffusivity D_{UU} . Subsequently, CF1 and the

Zaichik et al. [105], Zaichik and Alipchenkov [103] theory are compared in the limit of $St_r \gg 1$. In Section 3.5.2, the radial distribution functions (RDFs) obtained using CF1, CF2 and CF3 are compared with the respective DNS RDFs. The trends in the RDFs obtained from the closures are explained through the moments equations of the master PDF equation (3.10). After the RDF discussion, the relative velocity statistics and relative velocity PDFs obtained from the LS and DNS runs are presented and compared in Section 3.5.3. Throughout the discussion of the results, we will regard CF1 as being the most accurate among the three closures. We will elaborate on the differences in the statistical predictions of CF1 and CF2/CF3, as well as provide quantitative and qualitative explanations for the differences.

3.5.1 Diffusivity tensor

We first compare the diffusivity tensors from the three closure forms considered in this study. In addition, the CF1 and CF2 diffusivities are analyzed in greater detail for pair separations in the integral range, where one can derive analytical estimates for these. Subsequently, we compare CF1 with the diffusivity closure of [100, 103]. As CF1 is computed through DNS, it is essentially exact for $St_r \gg 1$, presenting us an opportunity to assess the Zaichik & Alipchenkov closure in this limit. Such an analysis of their diffusivity had not been undertaken previously.

In Figure 3.3, the longitudinal and transverse components of the diffusivity for CF1, CF2 and CF3 are plotted as a function of the dimensionless separation r/L (L is the integral length scale). Shown in Figure 3.3(a) and (b) are the diffusivity components at $Re_\lambda = 76$ and 131, respectively, for the $St_\eta = 10$ pairs. It may be

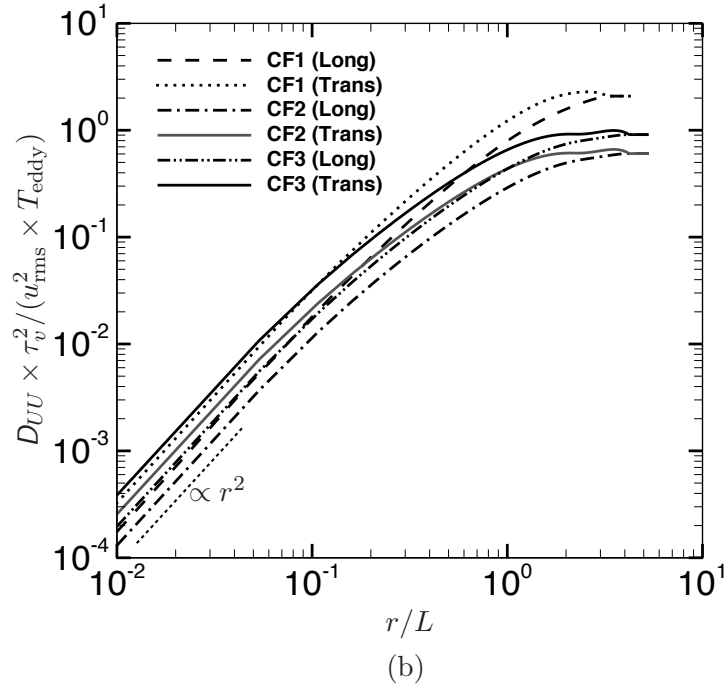
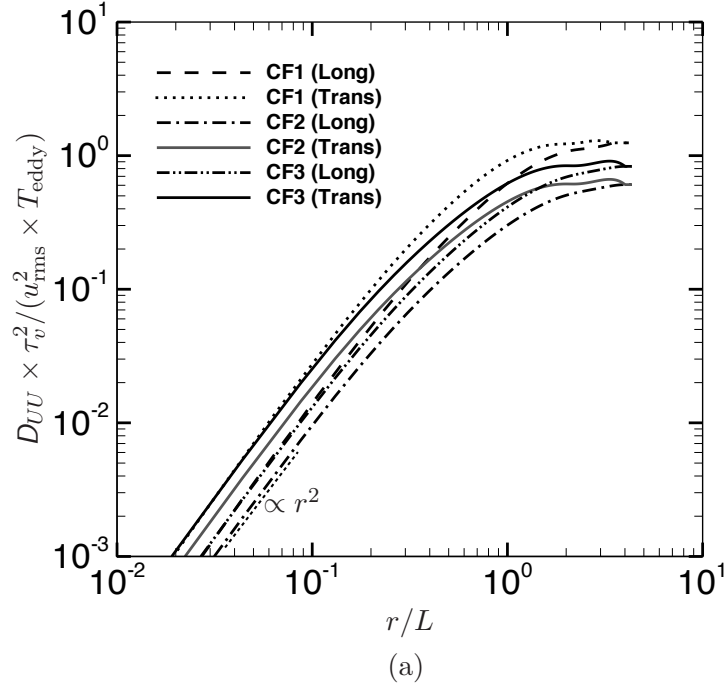


Figure 3.3: The transverse component, $D_{UU,\perp}(r)$, and the longitudinal component, $D_{UU,\parallel}(r)$, of the diffusivity tensor for $St_\eta = 10$ as a function of dimensionless pair separation r/L . Diffusivity tensor components for CF1, CF2 and CF3 are shown. *Upper black solid line denotes CF3 transverse component, and lower grey solid line denotes CF2 transverse component.* (a) $Re_\lambda = 76$, and (b) $Re_\lambda = 131$. Transverse and longitudinal components of D_{UU} for CF1, CF2 and CF3 in the viscous range at $Re_\lambda = 76$ and 131 are shown in Table 3.3.

Table 3.3: Transverse and longitudinal components of D_{UU} for CF1, CF2 and CF3 in the viscous range at $Re_\lambda = 76$ and 131. The values shown are for $St_\eta = 10$. The following notation is used:

$$D_{UU,\parallel}^{[1,2,3],*} = \left[D_{UU,\parallel}^{[1,2,3]} \times \tau_v^2 / (u_{\text{rms}}^2 \times T_{\text{eddy}}) \right] / (r/L)^2.$$

Re_λ	$D_{UU,\parallel}^{[1],*}$	$D_{UU,\perp}^{[1],*}$	$D_{UU,\parallel}^{[2],*}$	$D_{UU,\perp}^{[2],*}$	$D_{UU,\parallel}^{[3],*}$	$D_{UU,\perp}^{[3],*}$
76	0.98	1.96	0.81	1.62	1.37	2.74
131	1.52	3.04	1.35	2.70	2.06	4.12

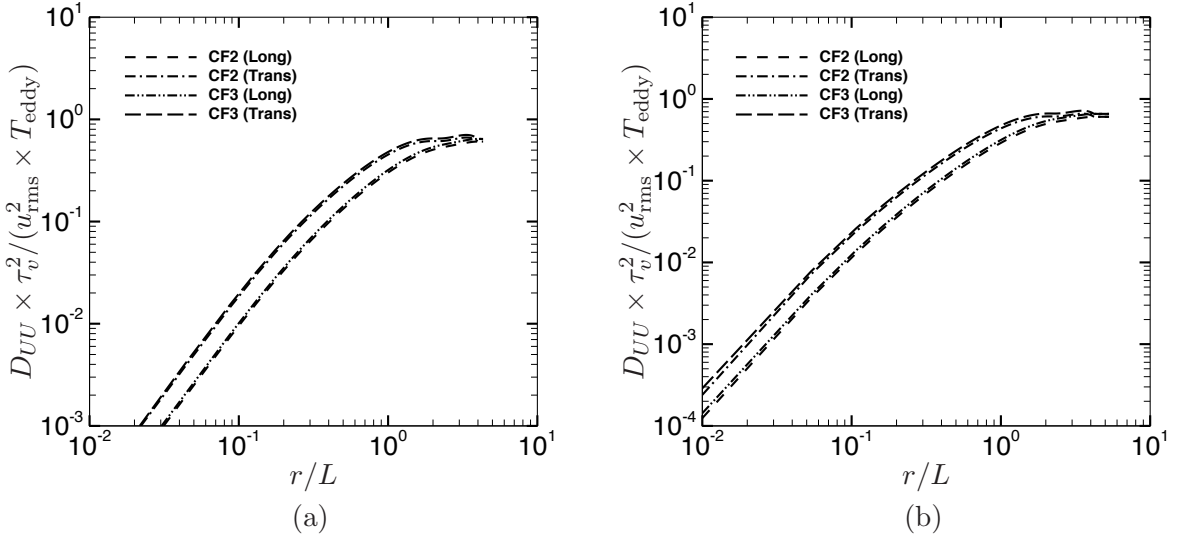
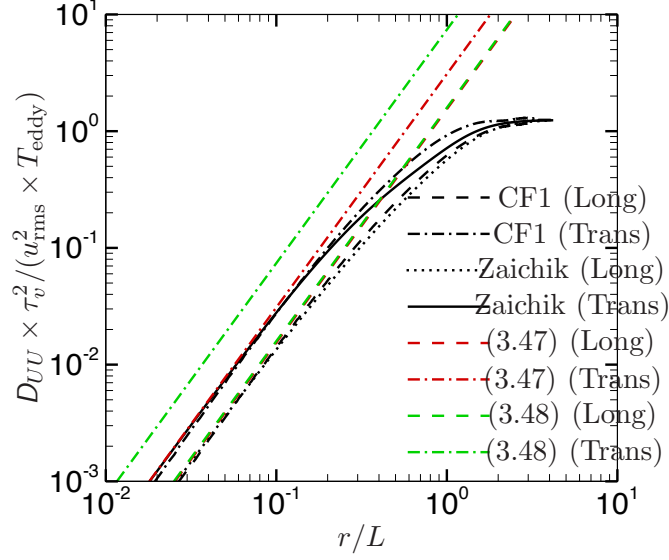
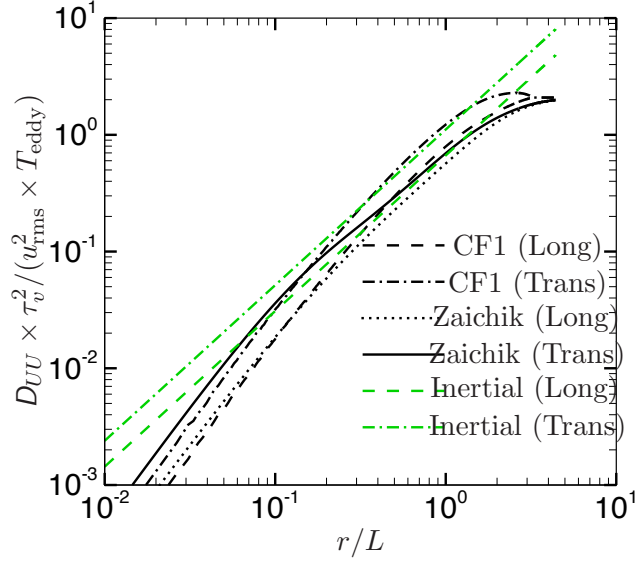


Figure 3.4: Transverse component, $D_{UU,\perp}(r)$, and longitudinal component, $D_{UU,\parallel}(r)$, of the diffusion coefficient tensor for $St_\eta = 80$ as a function of dimensionless pair separation r/L at: (a) $Re_\lambda = 76$, and (b) $Re_\lambda = 131$. CF2 and CF3 diffusivities are compared.



(a)



(b)

Figure 3.5: Comparison of Closure Form 1 (CF1) of \mathbf{D}_{UU} with the diffusivity of Zaichik and Alipchenkov [100, 103] in the limit $St_r \gg 1$. $\mathbf{D}_{UU,\parallel}(r)$ and $\mathbf{D}_{UU,\perp}(r)$ are the longitudinal and transverse components of \mathbf{D}_{UU} , respectively. “Zaichik” refers to the diffusivity calculated from Equation 3.51–Equation 3.53. Diffusion coefficient is plotted as a function of dimensionless pair separation r/L at: (a) $Re_\lambda = 76$, and (b) $Re_\lambda = 131$. Also shown in figure (a) are the diffusivities obtained using the two scaling expressions for the viscous time scale: Equation 3.44 and Equation 3.47, and Equation 3.44 and Equation 3.48. In (b) we show diffusivities obtained from the scaling expressions in the inertial subrange: Equation 3.45 and Equation 3.49. For the viscous range, two forms of scaling expressions are plotted: one in which strain-rate and rotation-rate have identical time scales ($\tau_\sigma = \tau_\omega$), and the second in which they are different ($\tau_\sigma \neq \tau_\omega$).

noted that $D_{UU} \times \tau_v^2$ is independent of the Stokes number for CF1 and CF2, but not for CF3 due to the presence of W_{rms} on the RHS of Eqs. (3.18) and (3.19). The diffusivities are shown for the lowest Stokes number $St_\eta = 10$, since the differences between CF2 and CF3 are more pronounced at low Stokes numbers. For Kolmogorov scale separations, i.e. $r \sim \eta$, $D_{UU,\perp}(r)$ and $D_{UU,\parallel}(r)$ show an r^2 scaling for all three closures (numerical values of the scaling coefficients are shown in Table 3.3). This scaling arises because for $r < \eta$, the fluid velocity field may be regarded as locally linear, i.e. $\Delta \mathbf{u} \approx \mathbf{r} \cdot \nabla \mathbf{u}$, which in conjunction with (3.11) gives rise to the r^2 scaling. At both $Re_\lambda = 76$ and 131, it is seen that CF3 is in reasonable agreement with CF1 for inertial range separations. However, in the transition region between the inertial and integral ranges, as well as in the integral range, CF1 is higher than CF3. The diffusivity components of CF1 exceed those of CF2 at all separations. These trends are to be expected, especially at $St_\eta = 10$, since CF3 does a better job at lower Stokes numbers than does CF2.

For integral scale separations, i.e. $r \gtrsim L$, one can perform a more detailed comparison of CF1 and CF2, since one can derive estimates for these closures in this region. It may be recalled that in deriving the CF2 diffusivity expression, we assumed that the temporal change of the fluid relative velocities seen by a pair is primarily due to the passive advection of size r eddies past the pair by large-scale eddies with velocity u_I . This physical picture is valid only when $r/u_I \ll r/u_r = \tau_r$, i.e. when r is small enough such that the time taken to advect the size r eddies past the pair is smaller than their turnover time. Therefore, one expects CF2 to perform poorly at large separations.

For $r \gtrsim L$, the particle pairs are effectively uncorrelated and behave like two independent particles. Consequently, the pair diffusivity is equal to twice the single-particle diffusivity. Using this principle, we can write for CF1:

$$\begin{aligned} D_{UU}^{[1]}(r \gtrsim L) &= \frac{1}{\tau_v^2} \int_{-\infty}^0 \langle \Delta \mathbf{u}(\mathbf{r}, \mathbf{x}, 0) \Delta \mathbf{u}(\mathbf{r}, \mathbf{x}, t) \rangle dt \\ &\approx \frac{2}{\tau_v^2} \int_{-\infty}^0 \langle \mathbf{u}(\mathbf{x}, 0) \mathbf{u}(\mathbf{x}, t) \rangle dt = \frac{2}{\tau_v^2} u_{\text{rms}}^2 T_E \delta_{ij} \end{aligned} \quad (3.39)$$

where T_E is the Eulerian integral time scale.

In the case of CF2, noting that $D_{UU,\parallel}^{[2]} = D_{UU,\perp}^{[2]}$ when $r \gtrsim L$, we have

$$D_{UU}^{[2]}(r \gtrsim L) \approx \delta_{ij} \frac{2\pi^2}{\tau_v^2} \sqrt{\frac{1}{(2\pi)^3 u_{\text{rms}}^2}} \times \frac{4}{3} \int_0^\infty \frac{E(\xi)}{\xi} d\xi \quad (3.40)$$

$$= \delta_{ij} \frac{2\pi^2}{\tau_v^2} \sqrt{\frac{1}{(2\pi)^3 u_{\text{rms}}^2}} \times \frac{4}{3} \times \frac{u_{\text{rms}}^2}{\pi} L \quad (3.41)$$

$$= \frac{0.53}{\tau_v^2} u_{\text{rms}}^2 T_{\text{eddy}} \delta_{ij} \quad (3.42)$$

where we replaced W_{rms} with u_{rms} in Eqs. (3.18) and (3.19), and the RHS of (3.40) is the limiting value of the RHS of ((3.18)) as $r \rightarrow \infty$. We have also used the identity $\int_0^\infty \frac{E(\xi)}{\xi} d\xi = \frac{u_{\text{rms}}^2}{\pi} L$, and $T_{\text{eddy}} = L/u_{\text{rms}}$, where L is the integral length scale. The ratio $T_{\text{eddy}}/T_E \sim 1.2$ - 1.5 so that from (3.39) and (3.42), the ratio $D_{UU}^{[1]}/D_{UU}^{[2]}$ is now estimated to be ~ 2.5 - 3.2 for $r \gtrsim L$.

In Figure 3.3, for $r \gtrsim L$, we see that $D_{UU}^{[1]}/D_{UU}^{[2]} \approx 2.05$ when $Re_\lambda = 76$, and ≈ 3.45 when $Re_\lambda = 131$, in accordance with the preceding scaling estimate. Further, $D_{UU}^{[1]}/D_{UU}^{[3]} \approx 1.5$ when $Re_\lambda = 76$, and ≈ 2.29 when $Re_\lambda = 131$. The lower

values of $D_{UU}^{[1]}/D_{UU}^{[3]}$ are because CF3 exceeds CF2 for smaller St_η . We will also see in Section 3.5.3 that for $r \gtrsim L$, the pair relative-velocity variance computed using CF1 is in good agreement with an analytical expression for the relative velocity variance of uncorrelated pairs [58]. However, both CF2 and CF3 underpredict this analytical variance by nearly the same factors as $D_{UU}^{[1]}/D_{UU}^{[2]}$ and $D_{UU}^{[1]}/D_{UU}^{[3]}$ for $r \gtrsim L$ in Figure 3.3.

In Figure 3.4, we compare only CF2 and CF3 for the highest Stokes number considered. Figure 3.4(a) and (b) show the diffusion tensor components for the $St_\eta = 80$ particles at $Re_\lambda = 76$ and 131, respectively. At high Stokes numbers, $W_{\text{rms}} \approx u_{\text{rms}}$, so that one expects CF2 and CF3 to have similar diffusivities, which is confirmed in Figure 3.4.

We now present a comparative analysis of CF1 and the Zaichik and Alipchenkov [100, 103] closures. As already mentioned, CF1 may be regarded as “exact” for $St_r \gg 1$. In this limit, the Zaichik & Alipchenkov diffusivity in \mathbf{U} -space may be written as:

$$D_{UU}^{\text{Zaichik}} = \frac{1}{\tau_v} \frac{T_{Lr}}{\tau_v \tau_v + T_{Lr}} \mathcal{S}(\mathbf{r}) \rightarrow \frac{1}{\tau_v^2} \mathcal{S}(\mathbf{r}) T_{Lr} \quad (3.43)$$

where $\mathcal{S}(\mathbf{r})$ is the Eulerian structure function tensor, and T_{Lr} is the Lagrangian two-point time scale at separation r . We can now calculate D_{UU}^{Zaichik} using the well-known scaling expressions of $\mathcal{S}(r)$ and T_{Lr} for separations r in the dissipative, inertial and integral ranges. The expressions for the longitudinal and transverse components of

$S(r)$ are [100]:

$$\text{Viscous range: } S_{\parallel}(r) = \frac{\epsilon r^2}{15\nu}; \quad S_{\perp}(r) = \frac{2\epsilon r^2}{15\nu} \quad (3.44)$$

$$\text{Inertial range: } S_{\parallel}(r) = C_1(\epsilon r)^{2/3}; \quad S_{\perp}(r) = \frac{4}{3}C_1(\epsilon r)^{2/3} \quad (3.45)$$

$$\text{Integral range: } S_{\parallel}(r) = S_{\perp}(r) = 2u_{\text{rms}}^2 \quad (3.46)$$

where $C_1 = 2.0$.

The corresponding expressions for $T_{Lr}(r)$ are also provided in Zaichik and Alipchenkov [100]. It is, however, relevant to elaborate on T_{Lr} in the dissipative range. To determine T_{Lr} in this range, [100] approximated the fluid relative velocity as being linear in the separation vector: $\Delta \mathbf{u} \approx \mathbf{r} \cdot \nabla \mathbf{u}$. Accordingly, the viscous T_{Lr} would need to be found in terms of the correlation time scales, τ_{σ} and τ_{ω} , of the strain-rate and rotation-rate tensors constituting the velocity gradient. [105] considered $\tau_{\sigma} = \tau_{\omega} = A_1\tau_{\eta}$, where τ_{η} is the Kolmogorov time scale. Subsequently, [103] reconsidered this analysis with separate forms for τ_{σ} and τ_{ω} . We can now write the expressions for $T_{Lr}(r)$ as:

$$\text{Viscous range [Z \& A (2003)]: } T_{Lr} = A_1\tau_{\eta} \quad (3.47)$$

$$\text{Viscous range [Z \& A (2007)]: } \tau_{\sigma} = A_{\sigma}\tau_{\eta}; \quad \tau_{\omega} = A_{\omega}\tau_{\eta}$$

$$T_{Lr,\parallel} = \tau_{\sigma}; \quad T_{Lr,\perp} = \left(\frac{\tau_{\sigma}}{5} + \frac{\tau_{\omega}}{3} \right) \quad (3.48)$$

$$\text{Inertial range: } T_{Lr} = A_2\epsilon^{-1/3}r^{2/3} \quad (3.49)$$

$$\text{Integral range: } T_{Lr} = T_L \quad (3.50)$$

where $A_1 = \sqrt{5}$ [47], $A_\sigma = 2.3$, $A_\omega = 7.2$, $A_2 = 1/\sqrt{6}$, and T_L is the Lagrangian integral time scale. The relationship between the viscous-range $T_{Lr,\perp}$ and τ_σ and τ_ω in (3.48) was obtained from the [13] study of tracer pair diffusion and coagulation in isotropic random velocity fields.

Conveniently, the scaling expressions given in [105] can be combined into unified forms for the entire range of turbulent scales. These are [101, 58]:

$$S_{\parallel}(r) = 2u_{\text{rms}}^2 \left[1 - \exp \left(-\frac{(r/\eta)}{(15C_K)^{3/4}} \right) \right]^{4/3} \left[\frac{(r/\eta)^4}{(r/\eta)^4 + (2u_{\text{rms}}^2/(C_K u_\eta^2))^6} \right]^{1/6} \quad (3.51)$$

$$S_{\perp}(r) = 2u_{\text{rms}}^2 \left[1 - \exp \left(-\frac{(r/\eta)^{4/3}}{(15C_{Kn}/2)} \right) \right] \left[\frac{(r/\eta)^4}{(r/\eta)^4 + (2u_{\text{rms}}^2/(C_{Kn} u_\eta^2))^6} \right]^{1/6} \quad (3.52)$$

$$T_{Lr}(r) = T_L \left[1 - \exp \left(-\left(\frac{C_T}{\sqrt{5}} \right)^{3/2} \left(\frac{r}{\eta} \right) \right) \right]^{-2/3} \left[\frac{(r/\eta)^4}{(r/\eta)^4 + (T_L/(C_T \tau_\eta))^6} \right]^{1/6} \quad (3.53)$$

where u_η is the Kolmogorov velocity scale, $C_K = 2$, $C_{Kn} \approx 2.5$, and $C_T = 0.4$.

We now compare CF1 with $D_{UU}^{\text{Zaichik}}(r)$ in Figure 3.5. The latter is computed from Eq. (3.43) in conjunction with Eqs. (3.51)-(3.53). The agreement between CF1 and D_{UU}^{Zaichik} is good at $Re_\lambda = 76$ and reasonable at $Re_\lambda = 131$. In the dissipative range, $D_{UU,\parallel}^{\text{Zaichik}}$ and $D_{UU,\perp}^{\text{Zaichik}}$ are higher than their CF1 counterparts at $Re_\lambda = 131$. It is to be noted that in the integral range $T_L \approx T_E/1.1$ is used [58], where T_E is the Eulerian integral time scale evaluated from DNS using $T_E = u_{\text{rms}}^2 \times \int_0^\infty \rho(t) dt$. Here $\rho(t)$ is the Eulerian autocorrelation of fluid velocities. The unified expressions (3.51)-(3.53) result in a rather broad inertial region at $Re_\lambda = 76$. Moreover, at $Re_\lambda = 131$, it is surprising that the Zaichik transverse component falls below even the CF1 longitudinal component in the inertial region. These trends suggest that

the combined expressions need improvement in the inertial range, as well as in the transition region between the inertial and integral ranges. To elaborate on this aspect, in Figure 3.5(b), we also plot the scaling expressions $\mathcal{S}_{\parallel}(r) \times T_{Lr}$ and $\mathcal{S}_{\perp}(r) \times T_{Lr}$ for inertial range r , computed from Eqs. (3.45) and (3.49). These are in good agreement with $D_{UU,\parallel}^{[1]}$ and $D_{UU,\perp}^{[1]}$ in the inertial region, suggesting that the scaling laws for the inertial subrange are accurate, but the unified expressions fail to accurately capture the transition from the inertial to integral scale separations. The effects of the unified expressions on the RDF predictions of [105] are elaborated in Section 3.5.2.

We also explored the differences between the viscous time scale of [100] (Eq. (3.47)), and of [103] (Eq. (3.48)). The transverse and longitudinal diffusivities obtained from these two forms of the viscous time scale are plotted in Figure 3.5(a). It can be seen that the longitudinal diffusivities from the two Zaichik & Alipchenkov studies are identical, and are in good agreement with $D_{UU,\parallel}^{[1]}(r)$. The transverse diffusivity corresponding to (3.47) is also in good agreement with $D_{UU,\perp}^{[1]}(r)$, but that computed using (3.48) significantly overpredicts the current $D_{UU,\perp}^{[1]}(r)$. The transverse diffusivity based on a Lagrangian time scale [103] exceeding that based on an Eulerian time scale (CF1) is evidently problematic. The viscous time scale $T_{Lr,\perp} = (\tau_{\sigma}/5 + \tau_{\omega}/3)$ arises in the context of tracer pair diffusion in isotropic random velocity fields [13]. It is not clear if this time scale can be applied for isotropic turbulence. We believe that the rather simple scaling $T_{Lr} = A_1 \tau_{\eta}$ with $A_1 = \sqrt{2}$ [47] is sufficiently accurate, obviating the need for the more complex form presented in [103] at least for Stokes numbers greater than one.

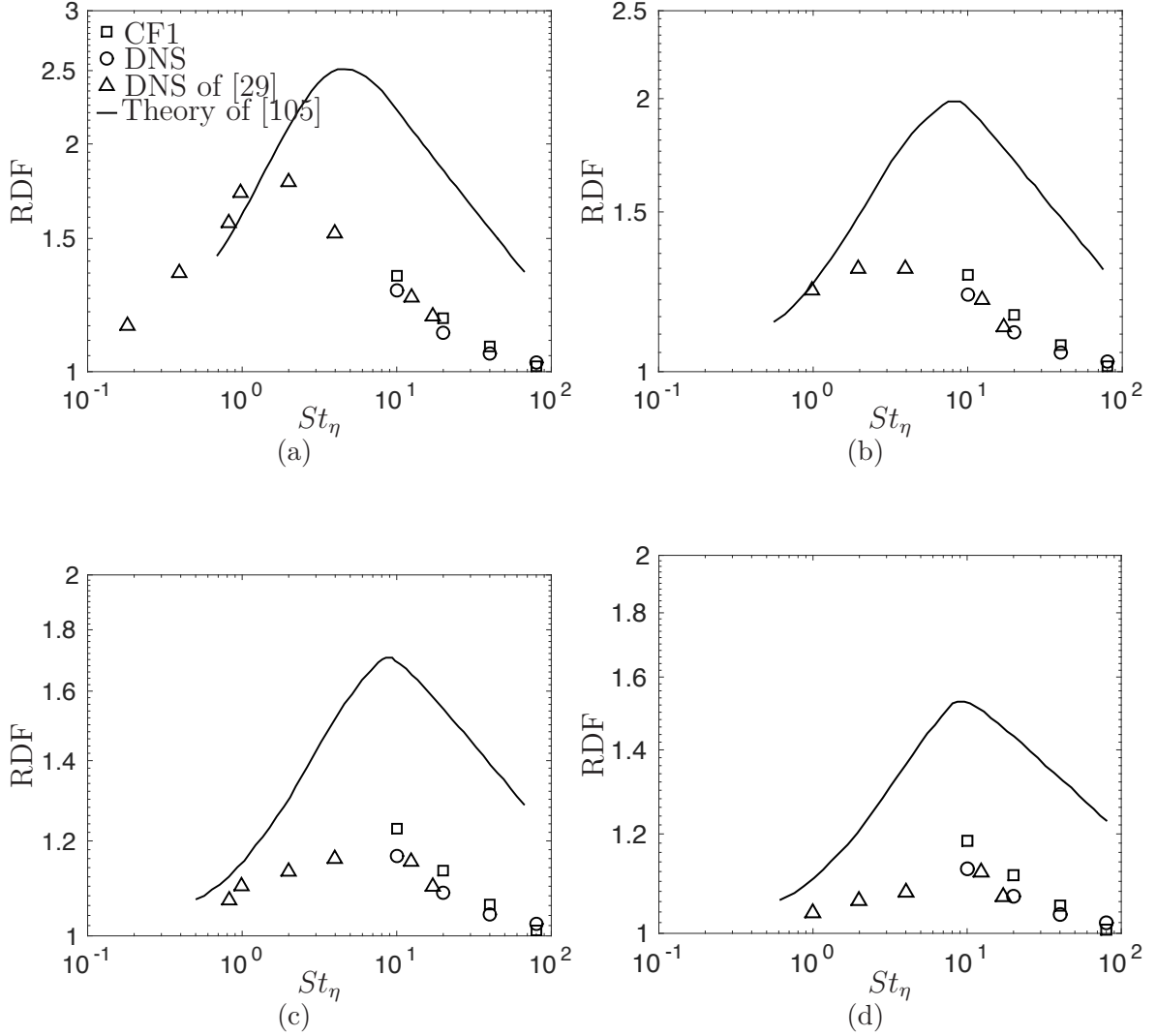


Figure 3.6: Radial distribution function (RDF) as a function of St_η at specific separations: (a) $r/\eta = 6$, (b) $r/\eta = 12$, (c) $r/\eta = 18$, and (d) $r/\eta = 24$. In each plot, squares and circles represent data from CF1 and current DNS at $Re_\lambda = 76$; triangles represent DNS data of [29] at $Re_\lambda = 69$. Solid line represents data from Zaichik et al. [105] theory for $Re_\lambda = 69$.

3.5.2 Radial distribution function

The radial distribution function (RDF) is a well-established measure of particle clustering. In Figure 3.6, the RDF is presented as a function of St_η at four separations

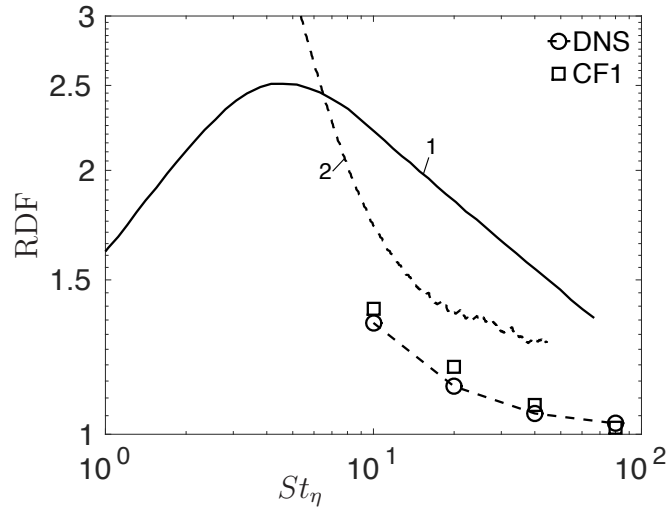


Figure 3.7: Radial distribution function (RDF) versus St_η at separation $r/\eta = 1$. Squares and circles represent data from CF1 and current DNS at $Re_\lambda = 76$. Curve 1 represents Zaichik et al. [105] theory for $Re_\lambda = 69$; and Curve 2 represents Zaichik and Alipchenkov [104] theory for $Re_\lambda = 75$.

$r/\eta = 6, 12, 18,$ and 24 . The results from the CF1-based Langevin simulations are compared with the data from the current DNS, the F evrier et al. [29] DNS, and also with the results from the Zaichik et al. [105] theory. The F evrier et al. [29] data were for $Re_\lambda = 69$, while the current DNS data are for $Re_\lambda = 76$. There is excellent agreement between the CF1 RDF and the two sets of DNS RDFs at all four separations, particularly for $St_\eta > 10$. The RDFs obtained from the Zaichik and Alipchenkov [100] theory are significantly higher than the DNS values at all separations.

In subsequent studies [103, 104], they endeavored to improve the theory, principally by dropping their earlier assumption that the Lagrangian correlation time scales of the strain-rate and rotation-rate tensors are equal. For $St_\eta < 1$, the power-law exponent C_3 of the RDF ($\sim (\eta/r)^{C_3}$ for $r \ll \eta$) obtained using the modified

theory showed good agreement with the RDF exponents computed using DNS and the theory of [18]. In Figure 3.7, we compare the RDFs from CF1 and the current DNS with those from the Zaichik and Alipchenkov [104] theory at separation $r/\eta = 1$. Also shown are the RDF values from Zaichik and Alipchenkov [100]. We observe that the RDFs computed using their modified theory move closer to, but still overpredict, the current DNS data for $St_\eta \gtrsim 10$.

We attribute this overprediction to two features of the Zaichik & Alipchenkov theory. First, we believe that the discrepancy may principally be due to the way in which the RDFs were computed in their study, i.e. through the solution of the transport equations for the moments of the PDF $\Omega(\mathbf{r}, \mathbf{U})$ (see ((3.10))). This aspect is elaborated in the following discussion.

Considering the pair PDF $\Omega(\mathbf{r}, \mathbf{U})$, the moments of interest are

$$\begin{aligned}\omega(\mathbf{r}) &= \int \Omega(\mathbf{r}, \mathbf{U}) d\mathbf{U} \\ \langle U_i \rangle &= \frac{1}{\omega(\mathbf{r})} \int U_i \Omega(\mathbf{r}, \mathbf{U}) d\mathbf{U} \\ \langle U_i U_j \rangle &= \frac{1}{\omega(\mathbf{r})} \int U_i U_j \Omega(\mathbf{r}, \mathbf{U}) d\mathbf{U}\end{aligned}$$

The governing equation for the marginal PDF $\omega(\mathbf{r})$ is obtained by integrating (3.10) over the \mathbf{U} space, and that for $\langle U_i \rangle$ is obtained by premultiplying (3.10) with $U_i/\omega(\mathbf{r})$ and then integrating over \mathbf{U} . Similarly, one also obtains the transport equation for $\langle U_i U_j \rangle$ by taking the second relative-velocity moments of (3.10). It may be noted that $\omega(r)$ and the RDF $g(r)$ are related through $g(r) = \omega(r)/\omega(r \rightarrow \infty)$.

The transport equation for $\omega(\mathbf{r})$ is given by [100]

$$\frac{\partial \omega}{\partial t} + \frac{\partial(\omega U_k)}{\partial r_k} = 0 \quad (3.54)$$

which only tells us that at steady state, in isotropic turbulence $\langle U_i \rangle = 0$. In fact, $\omega(\mathbf{r})$ has to be obtained from the $\langle U_i \rangle$ equation. However, when one attempts to solve the equations for the first or higher moments (of U_i), one encounters additional closure problems. For instance, the equation for $\langle U_i \rangle$ contains the unclosed moment $\langle U_i U_j \rangle$ [100]. To obtain $\langle U_i U_j \rangle$, one writes the transport equation for $\langle U_i U_j \rangle$, which in turn involves $\langle U_i U_j U_k \rangle$, and so on. This leads to an infinite hierarchy of moments equations, which is typically broken by introducing further closure approximations. For example, in Zaichik and Alipchenkov [100], a “quasi-Gaussian” approximation (QGA) was introduced for U_i , allowing them to approximate the fourth-order moments of relative velocities in terms of the second-order moments. Even for $St_\eta \gg 1$ particles, QGA may be problematic for separations $r < L$, where the relative velocity PDF is far from Gaussian and the second moments may be transported over distances much larger than r . Further, as pointed out by Bragg and Collins [10], for larger Stokes numbers, the PDF of \mathbf{U} in the dissipation range may be extremely intermittent. These closure approximations may be an important contributing factor to the errors in the RDFs of Zaichik & Alipchenkov. A more detailed analysis of the predictions of the Zaichik & Alipchenkov theory may be found in Bragg and Collins [9, 10].

The second reason for the differences between the DNS and Zaichik RDFs in Figure 3.6 may be the use of the unified expressions for the diffusivity in their theory.

As shown in Figure 3.5(b) and in the discussion following Eq. (3.43), the unified expressions used for S and T_{Lr} need improvement in the inertial region, as well as the transition region between the inertial and integral ranges. The discrepancies in the diffusivity in these regions may have contributed to the overprediction of RDFs by their theory, since the high St_η particles preferentially respond to these scales.

Figure 3.8(a) and (b) compare the RDFs obtained using CF1, CF2 and CF3 with the DNS RDF for $St_\eta = 10$ and 80, respectively, at $Re_\lambda = 76$. Figure 3.8(c) and (d) show the corresponding plots at $Re_\lambda = 131$. For $St_\eta = 10$, the CF1 and CF3 RDFs show good qualitative and quantitative agreement with the DNS RDF at both Reynolds numbers. For $St_\eta = 10$ and both Re_λ , CF2 overpredicts clustering as compared to DNS for both viscous and inertial separations. For $St_\eta = 80$, all the RDFs are close to unity, suggesting only a small amount of particle clustering. One also notices that the RDFs plateau, i.e. become essentially independent of r , for separations in the inertial subrange. The plateauing is delayed, i.e. starts at smaller separations, for the $St_\eta = 10$ pairs than for the $St_\eta = 80$ pairs. The above RDF trends can be deduced by considering the governing equation for $\langle U_i \rangle$, given by:

$$\frac{\partial \langle U_i \rangle}{\partial t} + \frac{\partial \langle U_i \rangle \langle U_j \rangle}{\partial r_j} + \frac{\partial \langle U'_i U'_j \rangle}{\partial r_j} = -\frac{\langle U_i \rangle}{\tau_v} - \langle U'_i U'_j \rangle \frac{\partial \ln \omega(\mathbf{r})}{\partial r_j} \quad (3.55)$$

For isotropic turbulence, $\langle U_i \rangle = 0$, so that (3.55) becomes

$$\frac{\partial \langle U'_\alpha U'_\alpha \rangle}{\partial r_\alpha} = -\langle U'_\alpha U'_\alpha \rangle \frac{\partial \ln \omega(\mathbf{r})}{\partial r_\alpha} \quad (3.56)$$

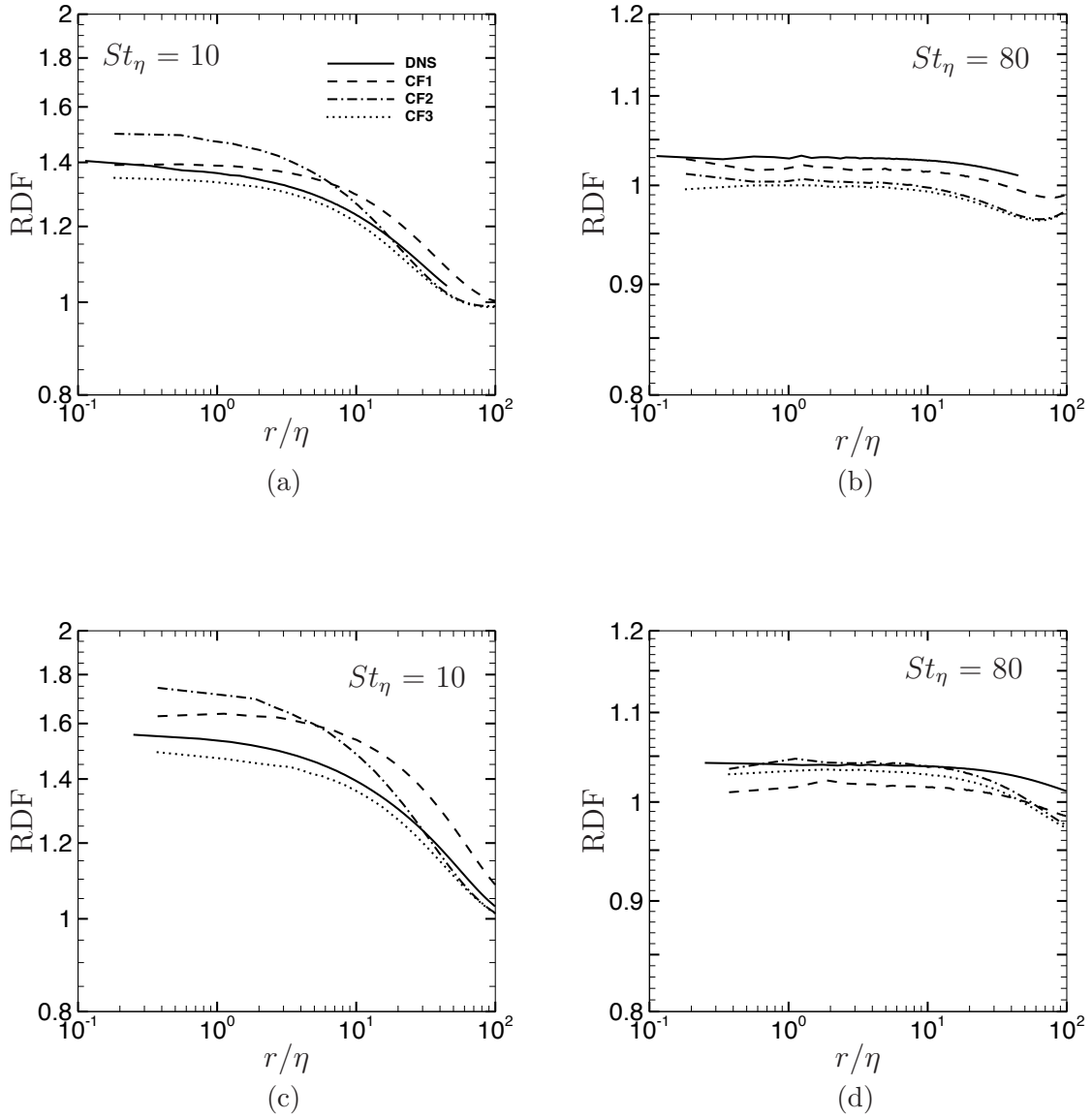


Figure 3.8: RDFs from Langevin simulations (CF1, CF2, and CF3) and from DNS as a function of dimensionless pair separation r/η for the indicated values of $St_\eta = 10, 80$. (a,b) $Re_\lambda = 76$, and (c,d) $Re_\lambda = 131$.

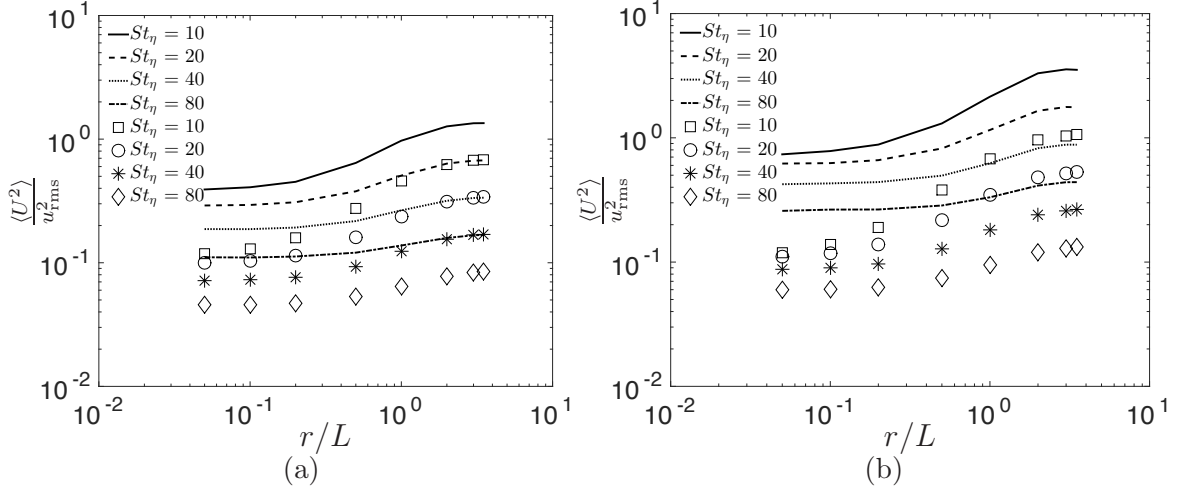


Figure 3.9: $\langle U^2 \rangle / u_{\text{rms}}^2$ as a function of r/L for all Stokes numbers. (a) $Re_\lambda = 76$, and (b) $Re_\lambda = 131$. Lines denote CF1 and symbols denote CF2.

where $\alpha = 1, 2, 3$ (repeated α does not denote a summation). We can now write

$$\frac{\partial \ln \langle U'_\alpha U'_\alpha \rangle}{\partial r_\alpha} + \frac{\partial \ln \omega(\mathbf{r})}{\partial r_\alpha} = 0 \quad (3.57)$$

which yields the rather elegant result for $St_r \gg 1$ pairs:

$$\omega(r) = C(St) \langle U'_\alpha U'_\alpha \rangle^{-1}(r) = C(St) \langle U^2 \rangle^{-1} \quad (3.58)$$

where $C(St)$ is an unknown coefficient that depends on the Stokes number. This dependence of the RDF may be contrasted with the power-law scaling of the RDF for the $St_\eta \ll 1$ particles at separations $r \lesssim \eta$ [18]:

$$g(r) = C_2 \left(\frac{r}{\eta} \right)^{-C_3} \quad (3.59)$$

where $C_3 \sim St_\eta$.

From (3.56), we can readily see that the flattening of the RDFs is related to the flattening of $\langle U^2 \rangle$. By reading Figure 3.8(a) and (c) in conjunction with Figure 3.9(a) and (b), one can see that the delayed plateauing of RDF for the $St_\eta = 10$ particles is related to the correspondingly delayed plateauing of $\langle U^2 \rangle$ at both Reynolds numbers. The overprediction of RDFs by CF2 for the viscous and inertial separations may also be inferred from (3.58) which shows that the RDF is inversely proportional to the relative-velocity variance. Since CF2 yields the lowest variances among the three closures, we see the associated overprediction of RDFs.

Figure 3.9(a) and (b) also suggest that $\langle U^2 \rangle$ remains finite as the separation $r \rightarrow 0$ for all the St_η considered in this study. Bec et al. [7] performed a DNS study of the low order velocity structure functions of inertial particles in isotropic turbulence, and found that the structure functions were independent of separation in the dissipation range for $St_\eta > 7$. In Rani et al. [67], we had classified high-inertia particle pairs into “lingerers” and “flyers”. Lingerers are low-relative-velocity particles that are highly correlated and remain correlated far longer than the timescales of fluid that influence their relative motion. Flyers are uncorrelated particles with large relative velocities, i.e., they undergo essentially ballistic motion so that their relative motion is unaffected by fluid eddies with sizes comparable to the pair separation. Flyers are responsible for maintaining a finite $\langle U^2 \rangle$ as the separation $r \rightarrow 0$.

In Figure 3.10, the RDFs from CF1, CF2, CF3, and DNS are plotted as a function of St_η at four separations for $Re_\lambda = 76$. The corresponding plots for $Re_\lambda = 131$ are shown in Figure 3.11. In general, the CF1 RDFs show the best

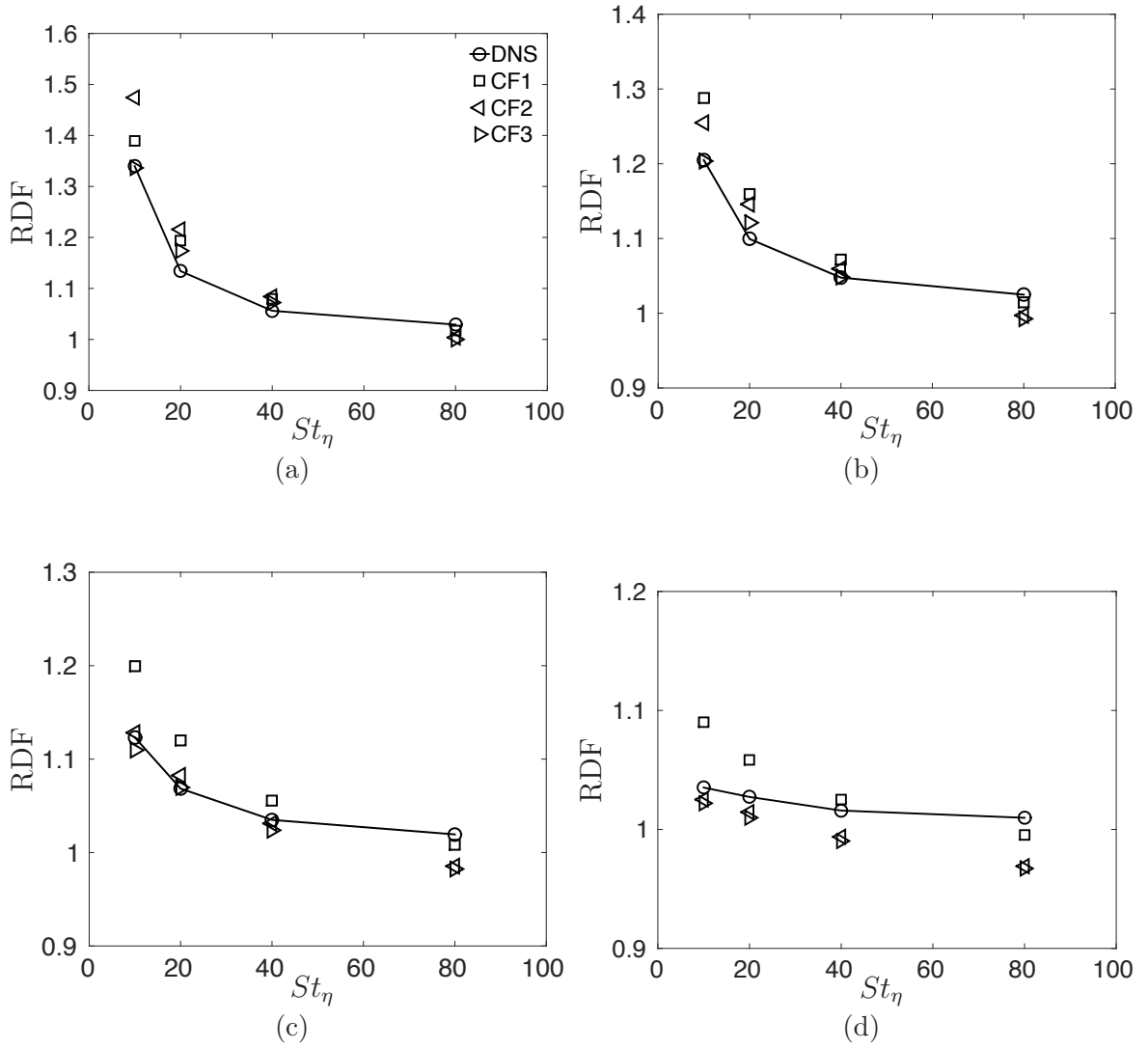


Figure 3.10: RDF versus St_η at $Re_\lambda = 76$ and at specific pair separations: (a) $r/\eta = 1$, (b) $r/\eta = 11$, (c) $r/\eta = 22$, and (d) $r/\eta = 44$ ($\approx L$). CF1, CF2, CF3, and DNS are compared.

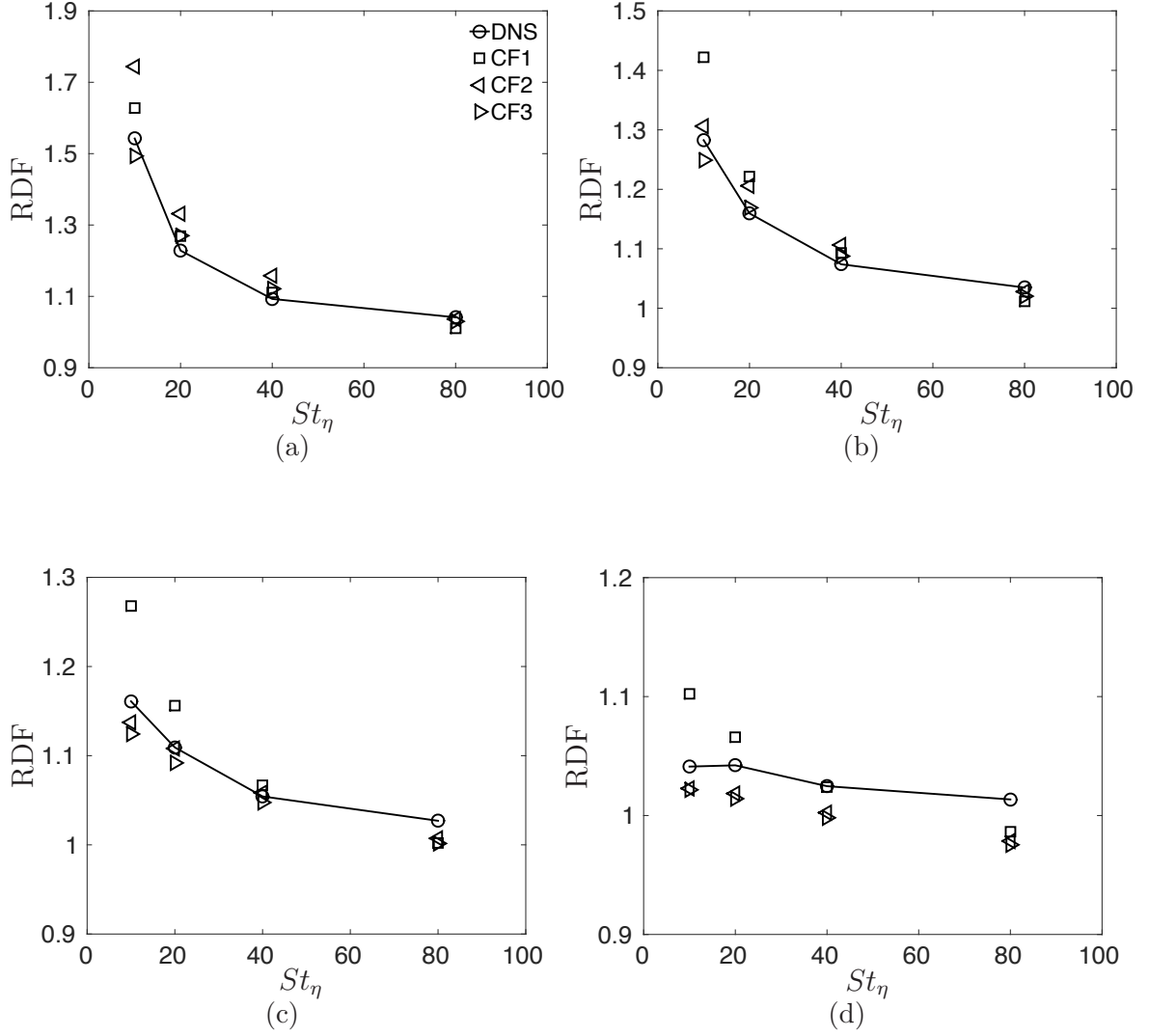


Figure 3.11: RDF versus St_η at $Re_\lambda = 131$ and at specific pair separations: (a) $r/\eta = 1$, (b) $r/\eta = 23$, (c) $r/\eta = 46$, and (d) $r/\eta = 92 (\approx L)$. CF1, CF2, CF3, and DNS are compared.

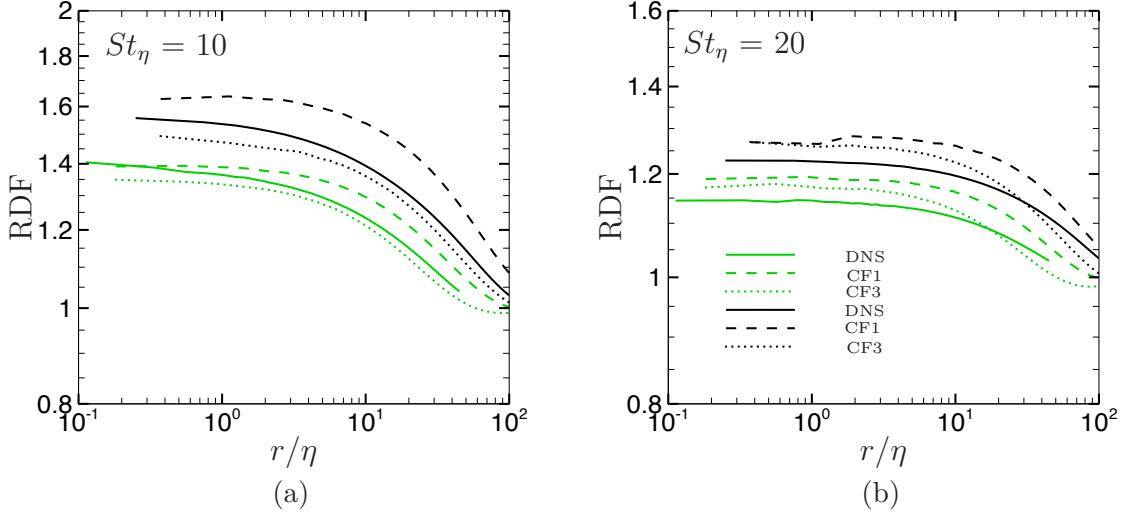


Figure 3.12: RDF versus pair separation r/η for (a) $St_\eta = 10$, and (b) $St_\eta = 20$. Black curves are for $Re_\lambda = 131$, and green curves are for $Re_\lambda = 76$. CF1, CF3 and DNS are compared.

agreement with the DNS RDFs. At larger separations ($r = L/2, L$), one notices that the agreement of CF1 with DNS improves with Stokes number, while the agreement of CF2 and CF3 with DNS deteriorates at higher Stokes numbers. This may be attributed to the underprediction of D_{UU} at large separations by CF2 and CF3. For lower Stokes numbers at both Re_λ , CF3 shows better agreement with DNS than CF2. At higher Stokes numbers, CF2 and CF3 approach each other, as is to be expected.

In Figure 3.12, the effects of Re_λ on particle accumulation are shown by comparing the RDFs for $St_\eta = 10, 20$ at $Re_\lambda = 76$ and 131. The RDFs are shown for the two lower Stokes numbers (and for CF1 and CF3 only) so as to clearly illustrate the effects of Re_λ variation on clustering. It can be seen from Figure 3.12(a) and (b) that for both Stokes numbers, the RDFs increase with Re_λ . This is because the response

times of the particles considered are of the order of inertial time scales. An increase in Re_λ , with its concomitant broadening of the inertial subrange, would mean that the particles respond to a greater number of scales, thereby resulting in increased clustering at these separations. This observation is consistent with the findings in the study of Ireland et al. [39].

3.5.3 Pair relative velocity statistics

Figure 3.13 shows the pair relative-velocity variance as a function of Stokes number at four separations for $Re_\lambda = 76$. The variances obtained from the Langevin simulations using the three diffusivities are compared with the DNS variances. It is seen that CF1 shows the best agreement with the DNS for all Stokes numbers and separations. CF3 agrees better with DNS than does CF2, especially at the smaller Stokes numbers considered. One also notices a slow change in the variances from $r \approx 4.5\eta$ in Figure 3.13(b) to $r \approx 2.5\eta$ in Figure 3.13(a). This may be attributed to the high inertia of particles because of which they retain memory of their relative velocities even after their separations have transitioned from the inertial range to the dissipative range. In Figure 3.13(c) and (d), i.e. at $r/L = 1/2$ and 1 respectively, one can see that CF1 overpredicts the DNS variances for $St_\eta = 10$, but the comparison improves significantly for $St_\eta > 10$. This is to be expected since CF1 involves modeling D_{UU} as the time integral of the two-time correlation of fluid relative velocities seen by nearly stationary pairs. Thus, CF1 becomes more accurate at high Stokes numbers where the modeled pair dynamics approaches the pair behavior in DNS. In Figure 3.13(d), corresponding to $r \approx L$, we also show the analytical expression for the relative velocity

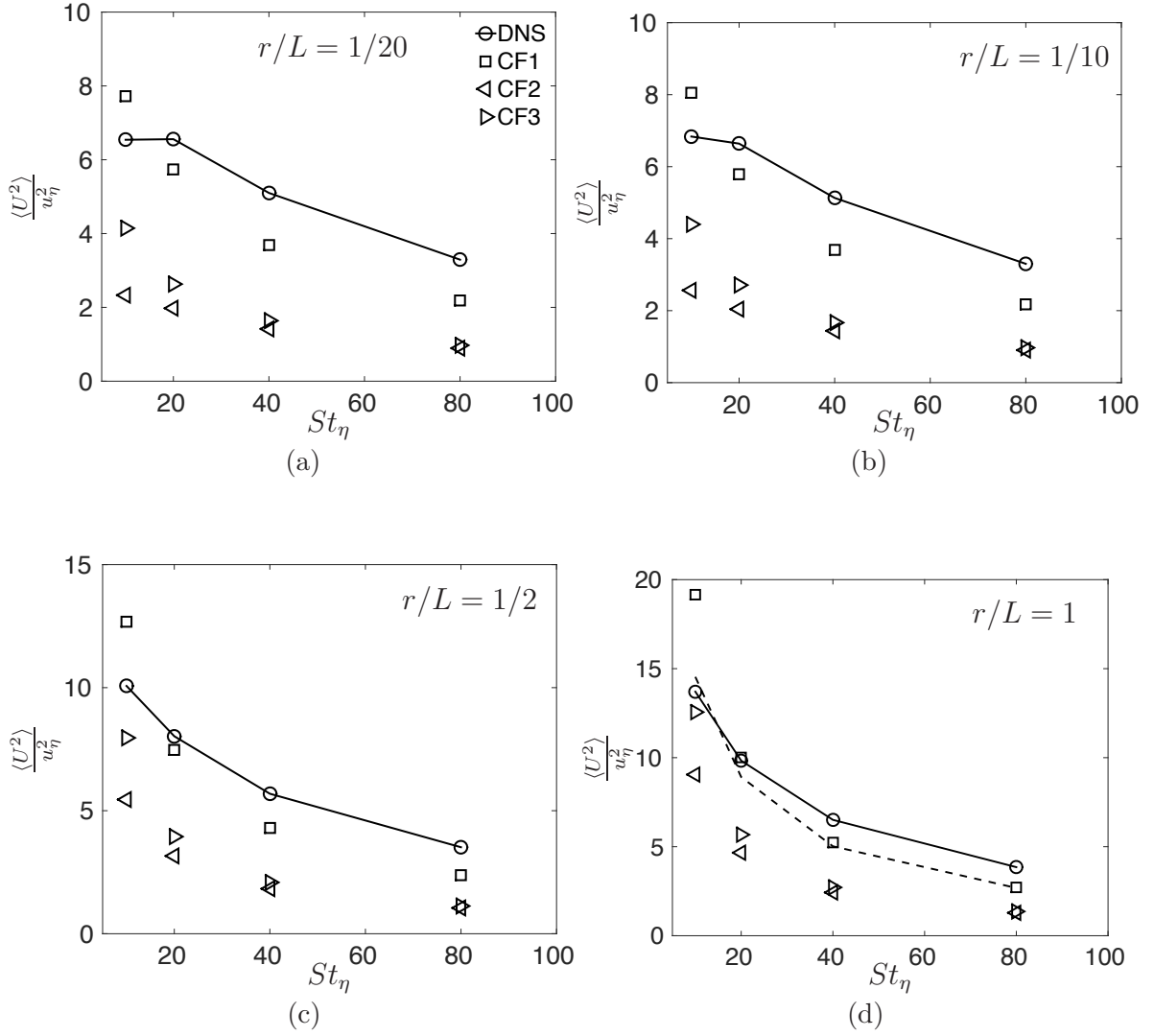


Figure 3.13: $\langle U^2 \rangle / u_\eta^2$ versus St_η at $Re_\lambda = 76$ for various separations. (a) $r/L = 1/20$, (b) $r/L = 1/10$, (c) $r/L = 1/2$, and (d) $r/L = 1$. Dashed line in (d) corresponds to the analytical expression for the variance of uncorrelated pairs, $\langle U^2 \rangle = 2u_{\text{rms}}^2 \frac{T_L}{T_L + \tau_v}$, where T_L is the Lagrangian integral time scale. T_L is obtained using $T_L = T_E / 1.1$ [58].

variance of uncorrelated pairs, $\langle U^2 \rangle = 2u_{\text{rms}}^2 T_L / (T_L + \tau_v)$, where T_L is the Lagrangian integral time scale of turbulence [58]. Except at $St_\eta = 10$, CF1 shows excellent agreement with this expression.

In Figure 3.13(d), the CF1 to CF2 and CF1 to CF3 variance ratios are 2.12 and 1.52 for $St_\eta = 10$, and 2.13 and 2.00 for $St_\eta = 80$. As already seen in Figure 3.3, for $St_\eta = 10$ and $r \gtrsim L$, we see that $D_{UU}^{[1]}/D_{UU}^{[2]} \approx 2.05$ and $D_{UU}^{[1]}/D_{UU}^{[3]} \approx 1.50$. For $St_\eta = 80$ and $r \gtrsim L$, Figure 3.4 shows that $D_{UU}^{[1]}/D_{UU}^{[2]}$ and $D_{UU}^{[1]}/D_{UU}^{[3]}$ are 2.05 and 1.93, respectively. The correspondence between the variances and diffusivities at integral-scale separations becomes evident from these ratios. From (3.39) and (3.42), when $r \gtrsim L$, the relative velocity variance limits to $\frac{2}{\tau_v} u_{\text{rms}}^2 T_E$ for CF1, and to $\frac{0.53}{\tau_v} u_{\text{rms}}^2 T_{\text{eddy}}$ for CF2.

In Figure 3.14, the relative velocity variances computed using CF1, CF2 and CF3 are compared with the DNS variances for $Re_\lambda = 131$. Both CF2 and CF3 underpredict the DNS variances, although CF3 performs better for smaller Stokes numbers. In contrast to its behavior at $Re_\lambda = 76$, CF1 now overpredicts the DNS variances, although the comparison gets better as the Stokes number increases. The improved agreement at higher St_η is expected, since the validity of the principal approximation in CF1—pairs are essentially fixed during flow time scales—improves as the Stokes number increases. It will also be seen in subsequent discussion that the CF1 behavior at $Re_\lambda = 131$ can be explained by considering the effects of Re_λ on the diffusivity D_{UU} . In Figure 3.14(d), at $r/L = 1$, CF1 approaches the analytical limit, except for $St_\eta = 10$.

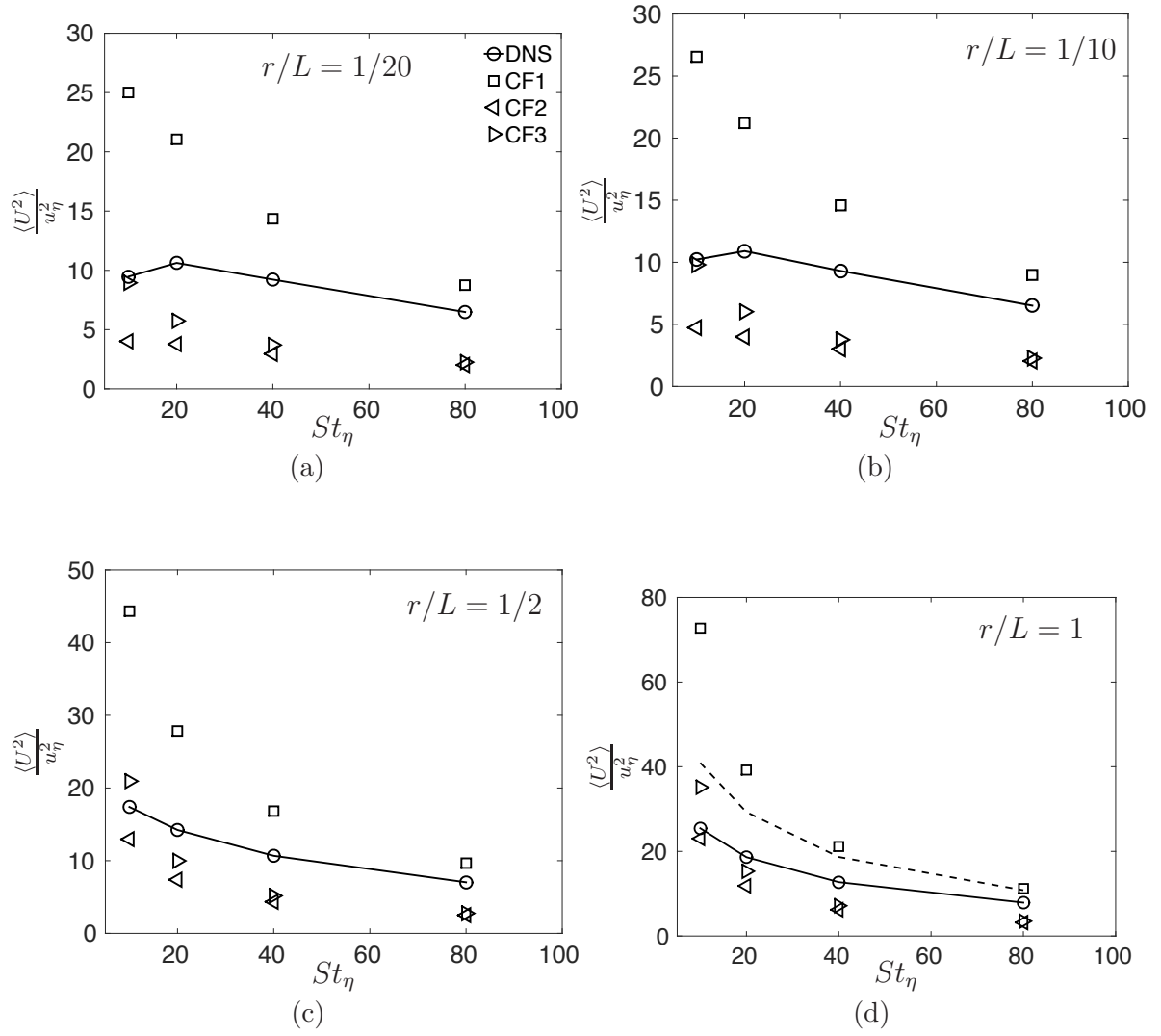


Figure 3.14: $\langle U^2 \rangle / u_\eta^2$ versus St_η at $Re_\lambda = 131$ for various separations. (a) $r/L = 1/20$, (b) $r/L = 1/10$, (c) $r/L = 1/2$, and (d) $r/L = 1$. Dashed line in (d) corresponds to $\langle U^2 \rangle = 2u_{\text{rms}}^2 \frac{T_L}{T_L + \tau_v}$, where T_L is the Lagrangian integral time scale. T_L is obtained using $T_L = T_E/1.1$ [58].

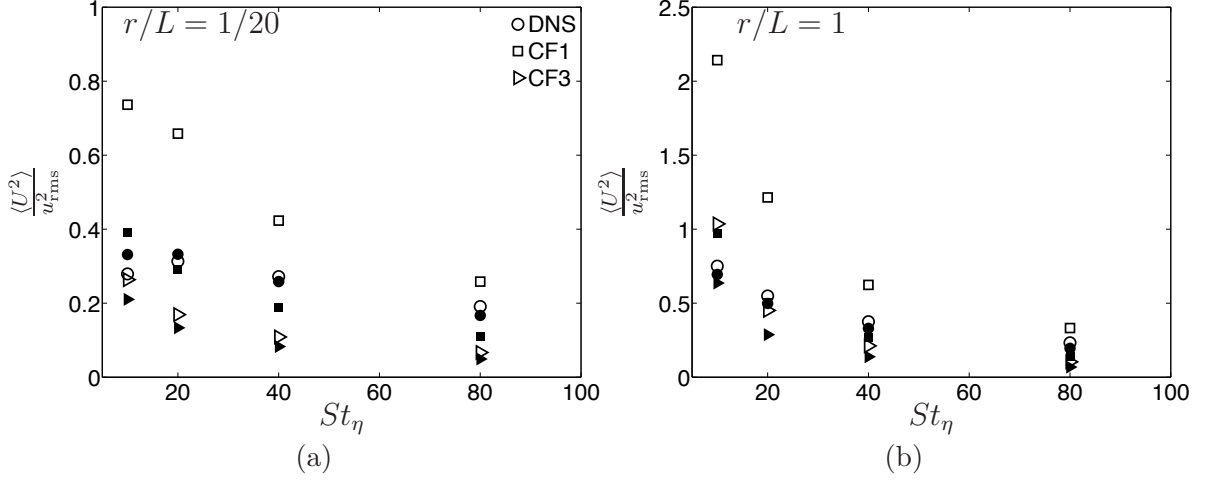


Figure 3.15: $\langle U^2 \rangle / u_{\text{rms}}^2$ versus St_η . (a) $r/L = 1/20$, and (b) $r/L = 1$. Open symbols denote $Re_\lambda = 131$, and filled symbols $Re_\lambda = 76$.

The effects of Re_λ on the relative velocity variances are illustrated in Figure 3.15. In Figure 3.15(a), the variances obtained from CF1, CF3 and DNS are compared for $Re_\lambda = 76$, and 131 at $r = L/20$. The corresponding comparison of variances for $r = L$ is shown in Figure 3.15(b). At both separations, increase in Re_λ has only a marginal impact on the DNS variances. The variation of Re_λ , however, has a substantial effect on the CF1 variances at both separations. This can be attributed to the strong dependence of the CF1 diffusivity on Re_λ , as will be demonstrated in the following discussion. The CF3 variances also show a rather weak dependence on Re_λ . This behavior of CF3, as compared to CF1, seems surprising, but will also be explained below.

We will now elucidate the trends in Figure 3.14 and Figure 3.15, specifically those concerning the effects of increase in Re_λ on the CF1 and CF3 variances. First, we present the ratios of dimensionless diffusivities at $Re_\lambda = 131$ and $Re_\lambda = 76$, where

the diffusivities are normalized using integral scale quantities. These ratios are (at $St_\eta = 10$ and $r > L$):

$$\frac{\tilde{D}_{UU}^{[1]}(Re_\lambda = 131)}{\tilde{D}_{UU}^{[1]}(Re_\lambda = 76)} \approx 1.32$$

$$\frac{\tilde{D}_{UU}^{[3]}(Re_\lambda = 131)}{\tilde{D}_{UU}^{[3]}(Re_\lambda = 76)} \approx 0.86$$

where $\tilde{D}_{UU} = D_{UU}/(u_{\text{rms}}^2 \times T_{\text{eddy}})$, and the values of u_{rms} and $T_{\text{eddy}} = L/u_{\text{rms}}$ for the respective Re_λ are obtained from Table 3.1. It is interesting to note that at large separations, the CF1 diffusivity shows a significant increase, while the CF3 diffusivity shows a marginal decrease with the Reynolds number.

The principal reason for the strong and weak dependence of CF1 and CF3, respectively, on Re_λ may be attributed to the relevant time scales for these closures. For CF1, the relevant time scale at large separations is the Eulerian integral time scale, T_E , while for CF2 and CF3, the time scales are L/u_{rms} and L/W_{rms} respectively. It is clear from Table 3.1 that L and u_{rms} , and thereby T_{eddy} , do not change significantly between the two DNS runs. This is because the turbulent kinetic energy also changes slowly in the two DNS runs. Consequently, the integral length scale L , which is determined by the mean dissipation rate and u_{rms} , is also nearly the same in the two DNS runs. However, for CF1, we find that $T_E(Re_\lambda = 131)/T_E(Re_\lambda = 76) \approx 1.4$, which is close to the ratio of diffusivities $D_{UU}^{[1]}(Re_\lambda = 131)/D_{UU}^{[1]}(Re_\lambda = 76)$ for $r > L$. Since $D_{UU}^{[1]}(r \gtrsim L) = \langle U^2 \rangle(r \gtrsim L)/\tau_v$, an increase in the diffusivity directly results in higher relative velocity variances at large separations. The ‘‘flyer’’ pairs with high variances at large separations then result in increased variances at smaller separations

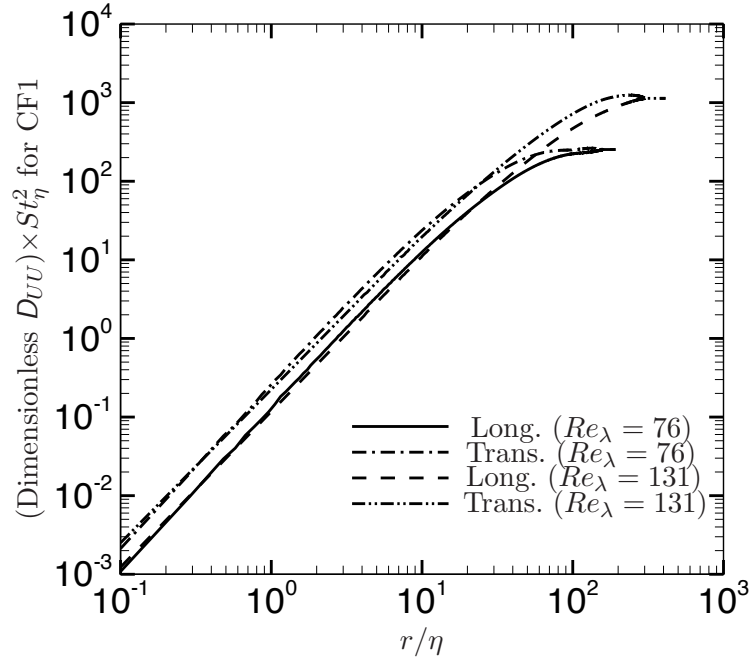


Figure 3.16: Dimensionless $D_{UU} \times St_\eta^2$ is plotted as a function of r/η for $Re_\lambda = 76, 131$. Effects of Re_λ on the CF1 closure are shown. The longitudinal and transverse components of $D_{UU}^{[1]}$ are compared at the two Re_λ . D_{UU} is made dimensionless with the Kolmogorov-scale quantities, and then multiplied with St_η^2 .

through their ballistic motion. We believe that the increase in T_E may be due to the forcing methodology used to achieve stationary isotropic turbulence. As in [38], we use a deterministic forcing method that involves resupplying the energy dissipated during each simulation time step. The dissipated energy is added at low wavenumbers so that the medium and high wavenumbers are, hopefully, not significantly influenced by the forcing. From the current DNS runs, it seems that the deterministic forcing of small wavenumbers has the effect of increasing the temporal coherence of large scale eddies as Re_λ is increased.

We now present further illustration of the effects of increasing Re_λ on the CF1 closure of D_{UU} . In Figure 3.16, the dimensionless $D_{UU}^{[1]} \times St_\eta^2$ is plotted as a function of r/η at $Re_\lambda = 76$ and 131, where D_{UU} has been made dimensionless using the Kolmogorov scale quantities.

In CF1, we have

$$D_{UU}^{[1]} = \frac{1}{\tau_v^2} \int_{-\infty}^0 \langle \Delta \mathbf{u}(\mathbf{r}, \mathbf{x}, 0) \Delta \mathbf{u}(\mathbf{r}, \mathbf{x}, t) \rangle dt \quad (3.60)$$

The effects of Re_λ on CF1 can be understood by approximating the Eulerian two-time relative velocity correlation on the right-hand side of (3.60) as the product of the Eulerian two-point structure function and an Eulerian autocorrelation of fluid relative velocities. This allows us to write:

$$D_{UU}^{[1]} \times \tau_v^2 \approx \mathcal{S}(\mathbf{r}) T_r \quad (3.61)$$

where $\mathcal{S}(\mathbf{r})$ is the structure function, and T_r is the Eulerian two-point time scale at separation r . In both viscous and inertial ranges, it can be shown from Eqs. (3.44)-(3.45) and (3.47)-(3.49) that $\mathcal{S}(\mathbf{r})T_r/(u_\eta^2\tau_\eta)$ is independent of Re_λ .

In the integral range, however, $\mathcal{S}_\parallel/u_\eta^2$ and $\mathcal{S}_\perp/u_\eta^2 \sim (u'/u_\eta)^2$. Using u'/u_η values from Yeung and Pope [99], one arrives at the following scaling: $u'/u_\eta = 0.50505\sqrt{Re_\lambda} - 0.0061$ for $38 \leq Re_\lambda \leq 93$. Using the DNS data of Ireland et al. [39], we get the scaling: $u'/u_\eta = 0.50626\sqrt{Re_\lambda} + 0.018761$ for $88 \leq Re_\lambda \leq 597$, which to leading order is nearly identical to the Young & Pope scaling. For the

Eulerian integral time scale T_E , we obtain the following scaling from Ireland et al. [39]: $T_E/\tau_\eta = 0.1039Re_\lambda + 2.8525$. Therefore, at integral-scale separations, the Re_λ dependence of $D_{UU}^{[1],\text{non-dim}}$ arises from both S and T_r . It can be seen in Figure 3.16 that in the dissipative and inertial ranges, the Re_λ effects on $D_{UU}^{[1],\text{non-dim}}$ are weak, but in the integral range, increase in Re_λ dependence leads to the higher values of diffusivity for $Re_\lambda = 131$.

In Figure 3.17, the PDF of relative velocity conditioned on separation r , i.e. $\Omega(U|r)$, normalized by $\langle U^2 \rangle^{1/2}$ is presented at $r = L/20$ for $St_\eta = 10, 80$ and $Re_\lambda = 76$. The normalization of a PDF by the standard deviation sheds light on the shape of the PDF, e.g., its deviation from Gaussianity. In Figure 3.17, the PDFs obtained from LS using CF1 and CF3 are compared with the DNS PDFs. It is known that for separations of the order of the integral length scale L , particle pairs are effectively uncorrelated so that they behave like individual particles. In such a scenario, the relative velocity PDF should be Gaussian. Indeed, this is what we see in the DNS, as well as LS (figure not shown here). As seen in Figure 3.17, at smaller separations, the PDFs become non-Gaussian (increasingly so as the separation decreases). The non-Gaussianity is manifested in the form of PDFs with wider tails and sharper peaks than a Gaussian PDF. The wider tails are representative of uncorrelated pairs with high relative velocities, referred to as flyers. The higher peaks at low relative velocities are representative of pairs whose relative motion is strongly correlated, referred to as lingerers. Thus, the transition from a Gaussian PDF at large separations to non-Gaussian PDF at small separations is characterized by two distinct trends: flyers that become lingerers, and flyers that remain as flyers. At

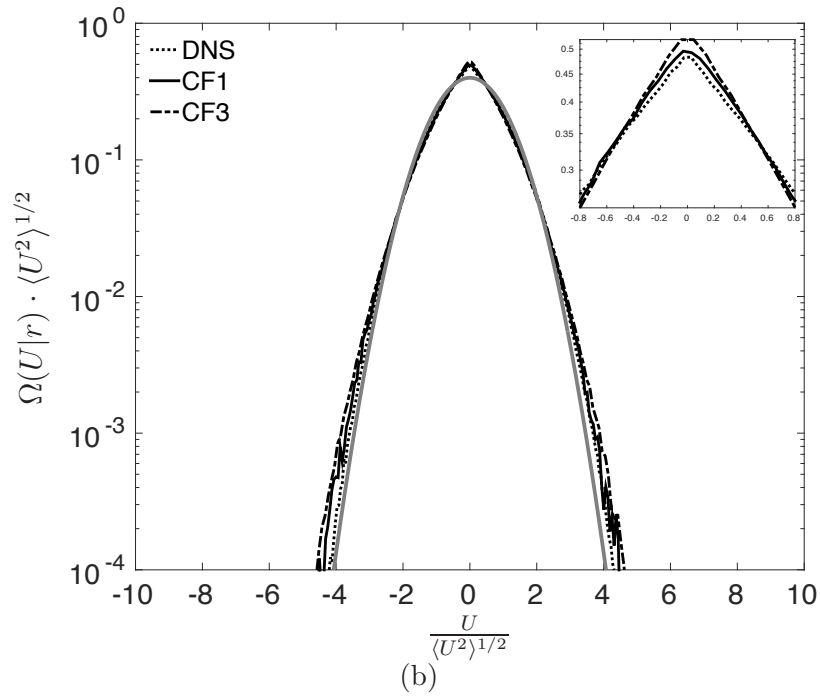
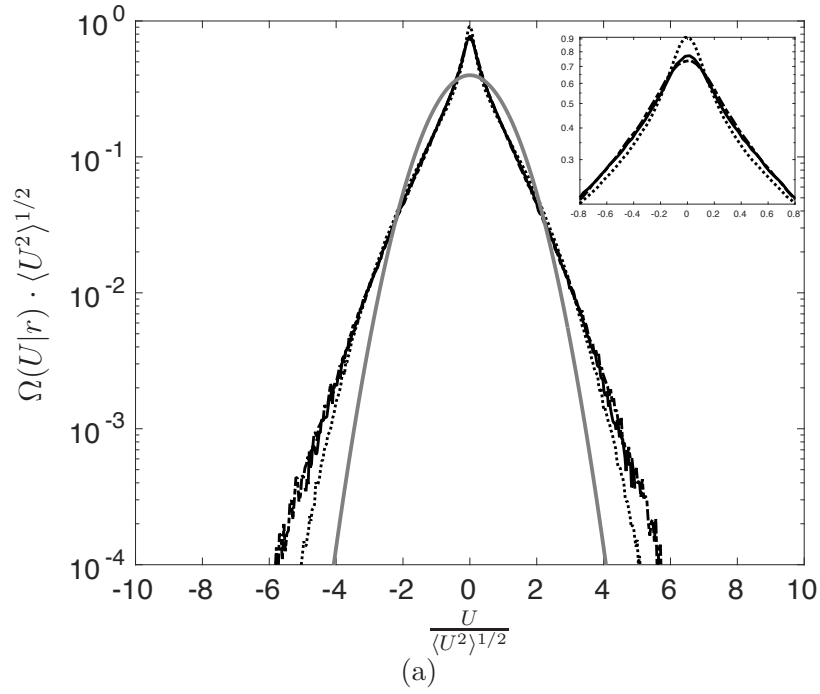


Figure 3.17: Relative velocity PDF $\Omega(U|r)$ normalized by $\langle U^2 \rangle^{1/2}$ for $Re_\lambda = 76$ and at $r/L = 1/20$. (a) $St_\eta = 10$, and (b) $St_\eta = 80$. Grey line represents the normal distribution.

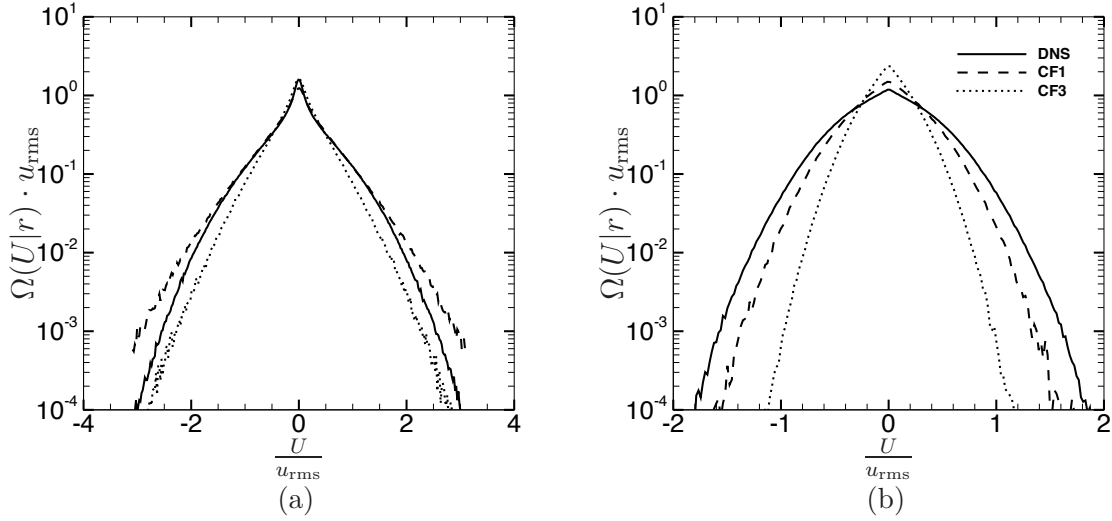


Figure 3.18: Relative velocity PDF $\Omega(U|r)$ scaled by u_{rms} for $Re_\lambda = 76$ and at $r/L = 1/20$. (a) $St_\eta = 10$, and (b) $St_\eta = 80$.

$r = L/20$, the transition of pairs into lingerers is more prominent for the $St_\eta = 10$ pairs than for the $St_\eta = 80$ pairs, as manifested by the higher peak in Figure 3.17(a). This is because the smaller St_η particles relax to the local flow more effectively than do the higher St_η particles that still retain some memory of their ballistic motion at larger separations. For both Stokes numbers, the PDFs of CF1 and CF3 have wider tails than the DNS PDF, suggesting that they overpredict the number of flyers. For $St_\eta = 10$, the inset of Figure 3.17(a) shows that both CF1 and CF3 underpredict the occurrence of lingerers.

The PDF $\Omega(U|r)$ scaled by the turbulence intensity u_{rms} is shown in Figure 3.18. The PDFs obtained using CF1 and CF3 are compared with those computed from DNS. These PDFs enable us to understand the trends in relative velocity statistics such as the variance $\langle U^2 \rangle$. Among the closures, the CF1 PDF's show the best

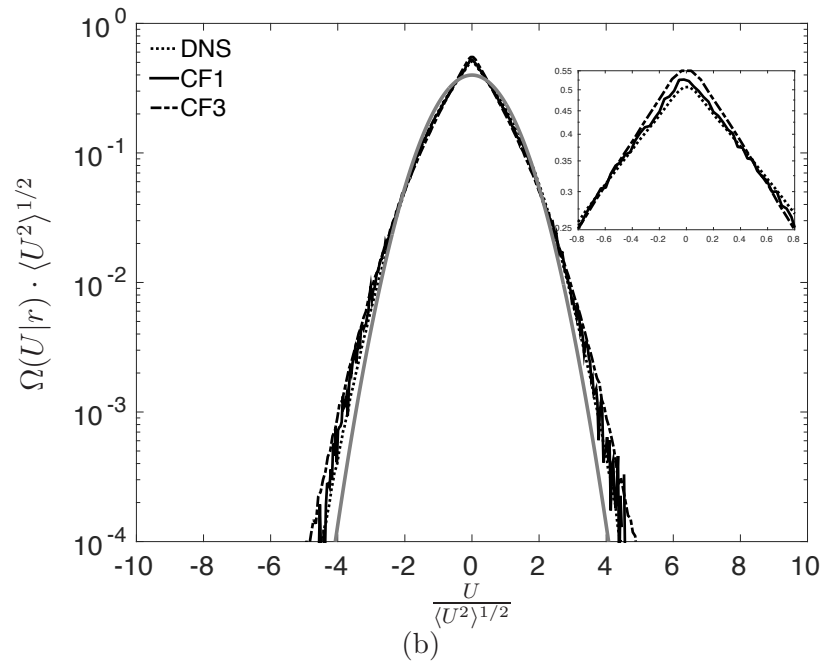
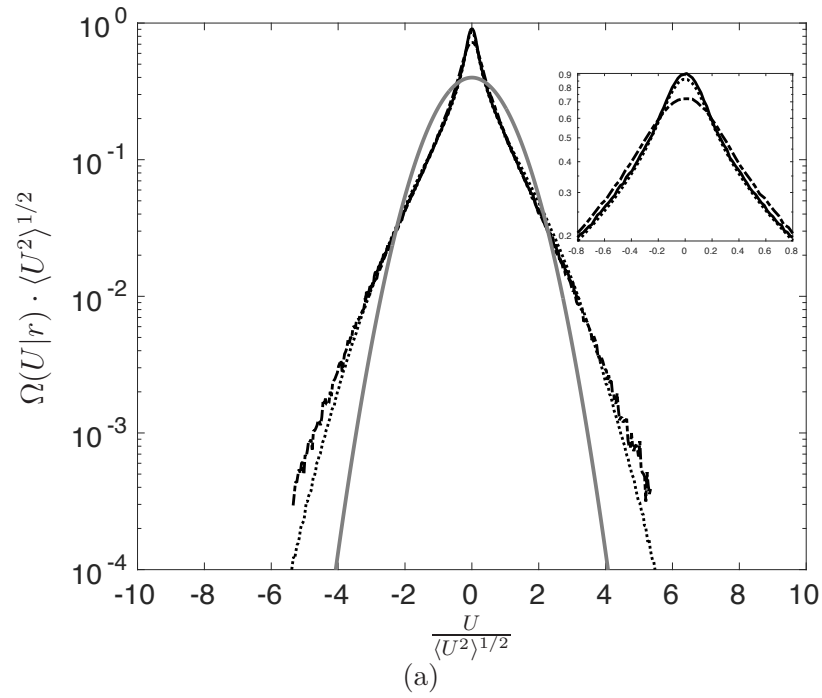


Figure 3.19: Relative velocity PDF $\Omega(U|r)$ normalized by $\langle U^2 \rangle^{1/2}$ for $Re_\lambda = 131$ and at $r/L = 1/20$. (a) $St_\eta = 10$, and (b) $St_\eta = 80$. Grey line represents the normal distribution.

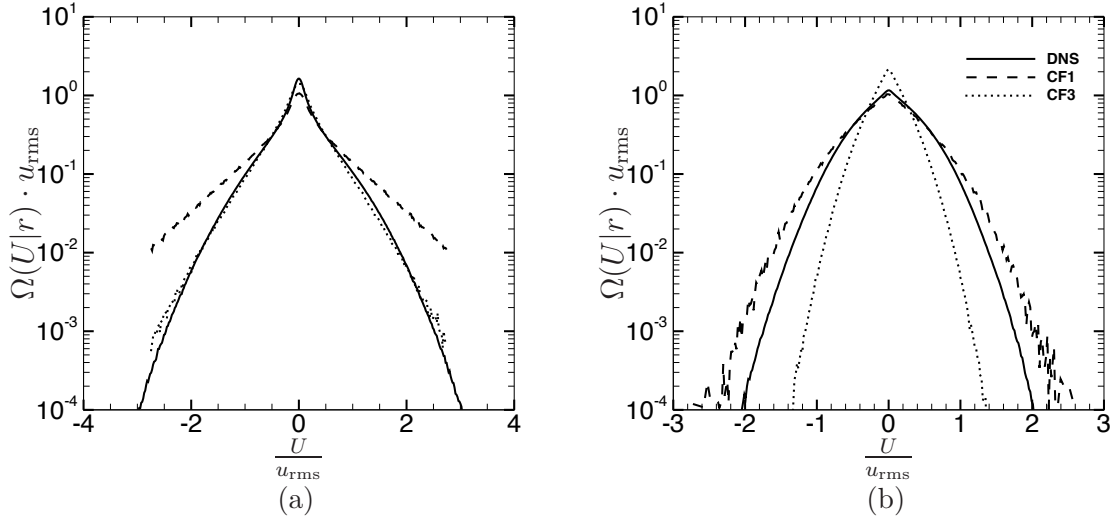


Figure 3.20: Relative velocity PDF $\Omega(U|r)$ scaled by u_{rms} for $Re_\lambda = 131$ and at $r/L = 1/20$. (a) $St_\eta = 10$, and (b) $St_\eta = 80$.

agreement with the DNS PDF's. At $r = L/20$, the CF1 PDF's for $St_\eta = 10$ have wider tails than the corresponding DNS PDF's, which leads to an overprediction of variance by CF1, as seen in Figure 3.13(a). For $St_\eta = 80$, however, we see that the CF1 PDF has narrower tails than the DNS PDF, which explains the lower CF1 variance compared to the DNS variance in Figure 3.13(d). These trends suggest that CF1 overpredicts (underpredicts) the number of high-relative-velocity flyers at low (high) Stokes numbers. At both Stokes numbers, the CF3 PDFs are narrower than the DNS PDFs.

In Figure 3.19, we present the normalized relative velocity PDFs at $Re_\lambda = 131$. For both $St_\eta = 10$ and $St_\eta = 80$, CF1 shows good agreement with DNS for low to moderate relative velocities ($-4 \lesssim U/\langle U^2 \rangle^{1/2} \lesssim 4$), but has wider tails than DNS for higher relative velocities. For $St_\eta = 10$, when the relative velocity $U/\langle U^2 \rangle^{1/2} \sim \pm 2$,

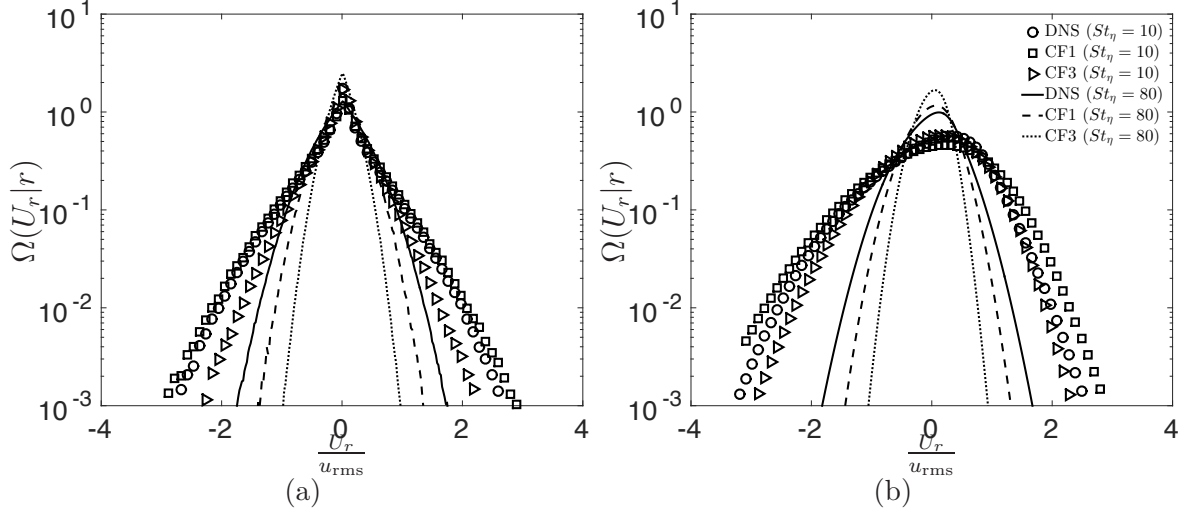


Figure 3.21: PDF of radial relative velocity $\Omega(U_r|r)$ scaled by u_{rms} for $St_\eta = 10, 80$ at $Re_\lambda = 76$ and at specific separations: (a) $r/L = 1/20$, and (b) $r/L = 1$.

one notices an inflection point in the DNS PDF. It is interesting to note that CF1 captures the inflection point, but not CF3. Further, CF3 predicts lower peaks than DNS for $St_\eta = 10$, and higher peaks than DNS for $St_\eta = 80$.

The PDF $\Omega(U|r)$ scaled by u_{rms} for $Re_\lambda = 131$ is shown in Figure 3.20. We see that CF1 gives rise to PDFs with wider tails than does DNS, particularly for $St_\eta = 10$. This is consistent with the significant overprediction of variances by CF1 for low Stokes numbers at $Re_\lambda = 131$ (Figure 3.14). However, for $St_\eta = 80$, the CF1 PDF shows reasonable agreement with the DNS PDF. For $St_\eta = 80$, the CF3 PDF is narrower than the DNS PDF. As a result, CF3 underpredicts the DNS variances.

Next, we present in Figure 3.21 the PDF of the radial component of relative velocity $U_r = \mathbf{U} \cdot \mathbf{r}/r$ at $Re_\lambda = 76$. The PDF $\Omega(U_r|r)$ is of interest since it is a key input to the collision kernel. We compare CF1 and CF3 with the DNS for $St_\eta =$

10 and 80 at two separations $r = L/20$ and L . The most important property of these PDFs is the transition from a negatively skewed PDF at $r = L$ to a nearly symmetric PDF at $r = L/20$. The transition in skewness suggests that the clustering of high-inertia particles at small separations is driven by the inward-migration bias occurring at much larger separations. At both $r = L/20$ and L , the PDFs for the $St_\eta = 10$ particles are more negatively skewed than those for the $St_\eta = 80$ particles. This means that lower Stokes-number particles tend to have higher radially inward relative velocities, which may cause the increased clustering of these particles. For $r = L/20$ and $St_\eta = 10$, the CF1 PDF is more negatively skewed than the DNS PDF, which explains the higher RDF for CF1 in Figure 3.10. The CF3 PDF is less negatively skewed than the DNS PDF, and hence the lower RDF of CF3.

The transition from Gaussian to non-Gaussian relative velocities can also be demonstrated using the kurtosis of relative velocity, $\langle U^4 \rangle / \langle U^2 \rangle^2$. A kurtosis of 3 denotes a Gaussian distribution, and a deviation from this value is indicative of a non-Gaussian PDF. In Figure 3.22(a) and (b), the kurtosis is plotted as a function of separation r/L for the various St_η at $Re_\lambda = 76$ and 131. In Figure 3.22(a), at $Re_\lambda = 76$, we see that CF1 and CF3 compare well with DNS at larger separations. For smaller pair separations ($r/L \lesssim 0.5$), CF1 shows the best agreement with DNS. It is also evident that for $r \sim L$, kurtosis approaches 3, indicating the gaussianity of relative velocities. At smaller r , the kurtosis for the $St_\eta = 80$ pairs deviates more slowly from 3 when compared to the $St_\eta = 10$ pairs. This suggests that the relative motion of the former pairs retains the ballistic nature for a wider range of separations as compared to the latter pairs. In Figure 3.22(b), for $Re_\lambda = 131$ and $St_\eta = 10$,

the CF1 kurtosis exceeds the CF3 kurtosis at all separations. As already seen, the increased Re_λ leads to a noticeably higher CF1 diffusivity at large separations, which in turn impacts the CF1 kurtosis. When we compare Figure 3.22(a) and (b), it can be seen that the non-Gaussianity increases with Reynolds number.

3.5.4 Collision kernel

The collision kernel $K(\sigma)$ for monodisperse particles is [68]:

$$K(\sigma) = 4\pi\sigma^2 g(\sigma) \int_{-\infty}^0 (-U_r) P(U_r|\sigma) dU_r \quad (3.62)$$

where σ is the particle diameter, $g(\sigma)$ the RDF of particle pairs at contact, $U_r = \mathbf{U} \cdot \mathbf{r}/r$ is the radial component of relative velocity, and $P(U_r|\sigma)$ is the probability density function (PDF) of U_r at contact. Equation (3.62) shows that the collision kernel depends on the RDF and the PDF of U_r , the former a measure of particle spatial concentration, and the latter a measure of the rate of particle encounters. Figure 3.23 and Figure 3.24 show the collision kernels for all St_η and at $Re_\lambda = 76$ and 131, respectively. It is relevant to mention that the “collision kernels” for CF1, CF3, and the current DNS are presented at separation $r = 2.3\eta$ for $Re_\lambda = 76$, and $r = 4.7\eta$ for $Re_\lambda = 131$, since these are the smallest separations for which a statistically stationary $P(U_r|r)$ could be computed in the respective Langevin simulations. At both Re_λ , CF1 shows the best agreement with DNS. At $Re_\lambda = 131$, the comparison of CF1 with DNS improves with Stokes number.

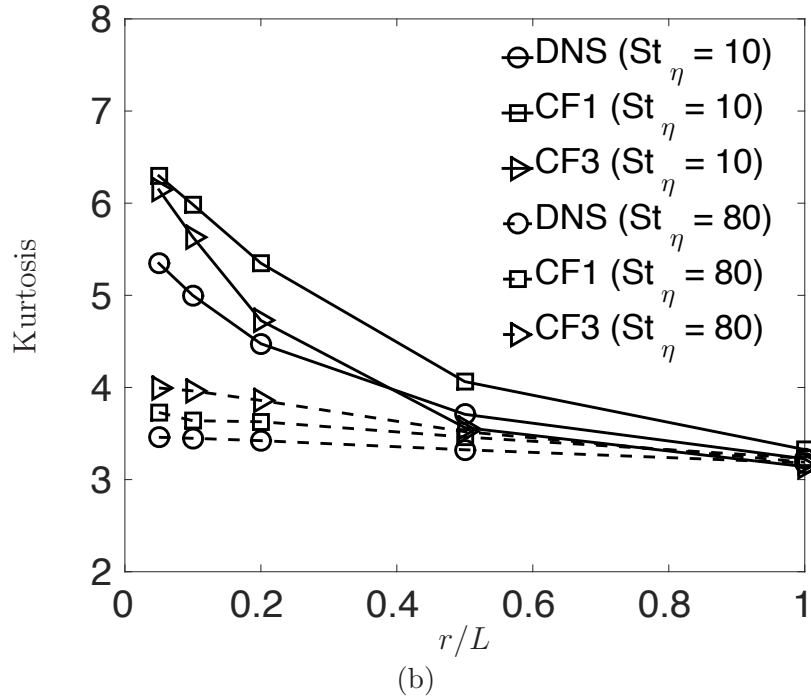
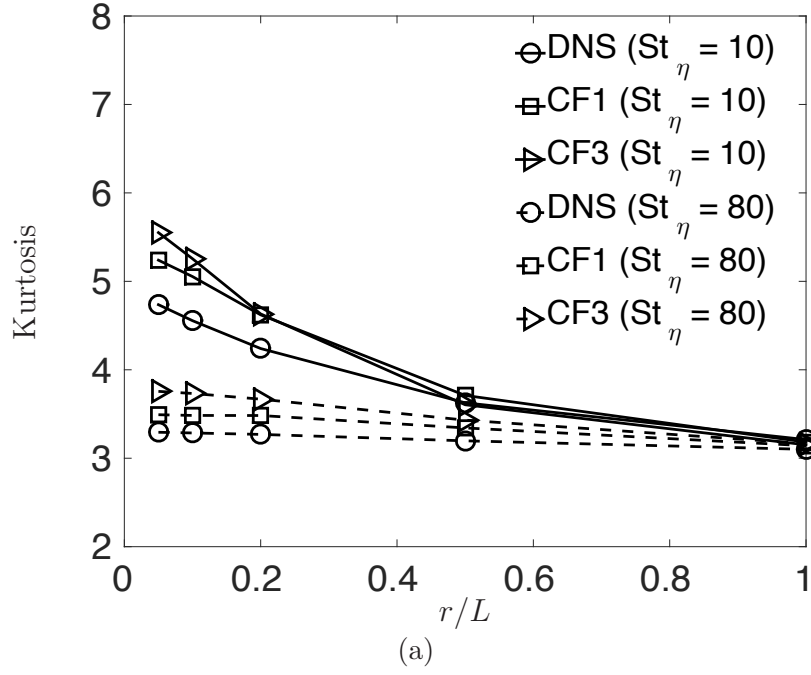


Figure 3.22: Kurtosis as a function of dimensionless pair separation r/L at: (a) $Re_\lambda = 76$, and (b) $Re_\lambda = 131$. CF1, CF3 and DNS are compared for $St_\eta = 10$ and 80.

In Figure 3.23, curve 2 represents the collision kernel at $r = \eta$ computed by Zaichik and Alipchenkov [104] from [95]

$$K(d) = 2\pi d^2 \langle |U_r(d)| \rangle g(d) \quad (3.63)$$

where the particle diameter $d = \eta$, and $\langle |U_r(d)| \rangle = \sqrt{\frac{2}{\pi} \langle U_r^2(d) \rangle}$. Curve 3 represents the collision kernel of Abrahamson [1] (cf. Zaichik and Alipchenkov [104]). Curve 4 represents the collision kernel computed from the theory of Mehlig et al. [53]. Finally, curve 5 is the kernel computed from eq. (3.63), with $\langle |U_r(d)| \rangle$ and $g(d)$ values from the current DNS. It can be seen that the collision kernel of Zaichik and Alipchenkov [104] overpredicts the DNS values for $St_\eta < 20$, and approaches the DNS for $St_\eta > 40$. One also notices that curve 5 obtained from eq. (3.63) is in good agreement with the curve computed from eq. (3.62).

The use of $\langle |U_r| \rangle = \sqrt{\frac{2}{\pi} \langle U_r^2 \rangle}$ by Zaichik and Alipchenkov [104] assumes that the pair relative velocities are normally distributed. They recognized that such an assumption was, at the best, reasonable only at large Stokes numbers. However, it was shown by Wang et al. [97] that even for zero Stokes number particles, the ratio $\langle |U_r| \rangle / \sqrt{\langle U_r^2 \rangle} = 0.77$, which is quite close to $\sqrt{\frac{2}{\pi}} = 0.798$ for normally distributed relative velocities.

Also indicated in Figure 3.23 and Figure 3.24 are the collision kernels when particle pairs are uncorrelated, corresponding to $g(r) = 1$ and $P(U_r|r)$ being Gaussian. Interestingly, the collision kernels of high-Stokes-number pairs in isotropic turbulence are smaller than the collision rates of uncorrelated pairs. Since $g(r) > 1$ when particles

cluster, we can attribute the higher collision kernels for the uncorrelated pairs as arising from the integral over U_r in the kernel equation (3.62). This scenario is confirmed in Figure 3.25, where we compare the PDF $P(U_r|r)$ for the $St_\eta = 10, 80$ pairs at both Re_λ with the Gaussian PDF for uncorrelated velocities. It is clear that the wider tails of the Gaussian PDF result in the corresponding higher collision kernels. In addition, comparison of Figure 3.23 and Figure 3.24 shows that the collision kernel increases with Re_λ , due to an increase in both the RDF and the relative velocities (i.e., relative velocity PDFs with wider tails) with Re_λ . This is confirmed in Figure 3.25 where we see that for a given St_η , the PDF tails become wider as Re_λ is increased. The higher collision kernels for CF1 than CF3 at all St_η and both Re_λ can also be explained by the PDFs in Figure 3.25.

3.6 Conclusions

We performed a detailed assessment of the [67] stochastic model for the relative motion of high-Stokes-number particle pairs in statistically stationary isotropic turbulence. The principal contributions of the [67] study were to: (1) derive a formulation for the relative-velocity-space diffusivity in the PDF kinetic equation for pairs with $St_r \gg 1$, and (2) develop closure(s) for this diffusivity. The fundamental diffusivity formulation (CF1) in [67] involved the time-integral of the Eulerian two-time correlation of fluid relative velocities “seen” by nearly stationary particles. The two-time correlation was resolved by converting it into a combination of Eulerian two-point correlations of fluid velocities. As a result, two closed-form expressions were obtained for the diffusivity, referred to as CF2 and CF3, depending upon whether

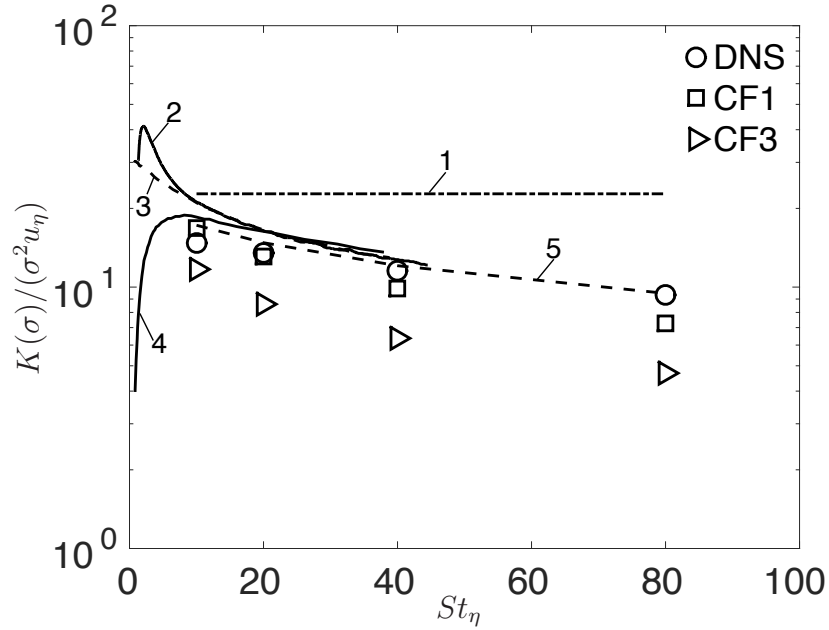


Figure 3.23: Collision kernel as a function of Stokes number at $Re_\lambda = 76$. CF1, CF3 and DNS are compared. Curve 1 shows the collision kernel when the RDF $g(r) = 1$ and the PDF $P(U_r|r)$ is Gaussian. Curve 2 represents the collision kernel computed using the Zaichik and Alipchenkov [104] theory. Curve 3 represents the collision kernel computed using the Abrahamson theory [1, 104]. Curve 4 represents the collision kernel from the Mehlig et al. [53] theory. Curve 5 represents the collision kernel computed using eq. (56) of Zaichik and Alipchenkov [104]. Curves 2 through 4 are at $r/\eta = 1$ and $Re_\lambda = 75$. Curve 5 is at $r/\eta = 2.3$ and $Re_\lambda = 76$.

the center-of-mass position was held fixed or allowed to move during flow time scales. That study, however, involved only a preliminary analysis of the developed closures. A detailed comparison of the relative motion statistics predicted by the model with DNS data was also not undertaken.

In the current study, a detailed analysis of the CF1, CF2 and CF3 diffusivities was performed by: (1) comparing their limiting values for separations in the integral range, and (2) comparing CF1 with the Zaichik and Alipchenkov [100] closure that involved expressing the diffusivity as the product of an Eulerian structure function

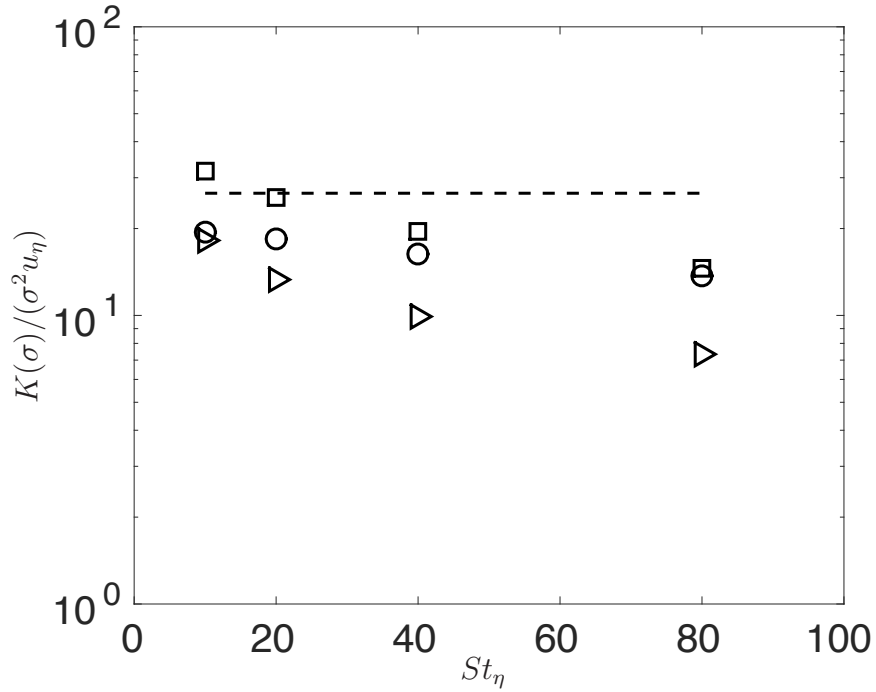


Figure 3.24: Collision kernel as a function of Stokes number at $Re_\lambda = 131$. CF1, CF3 and DNS are compared.

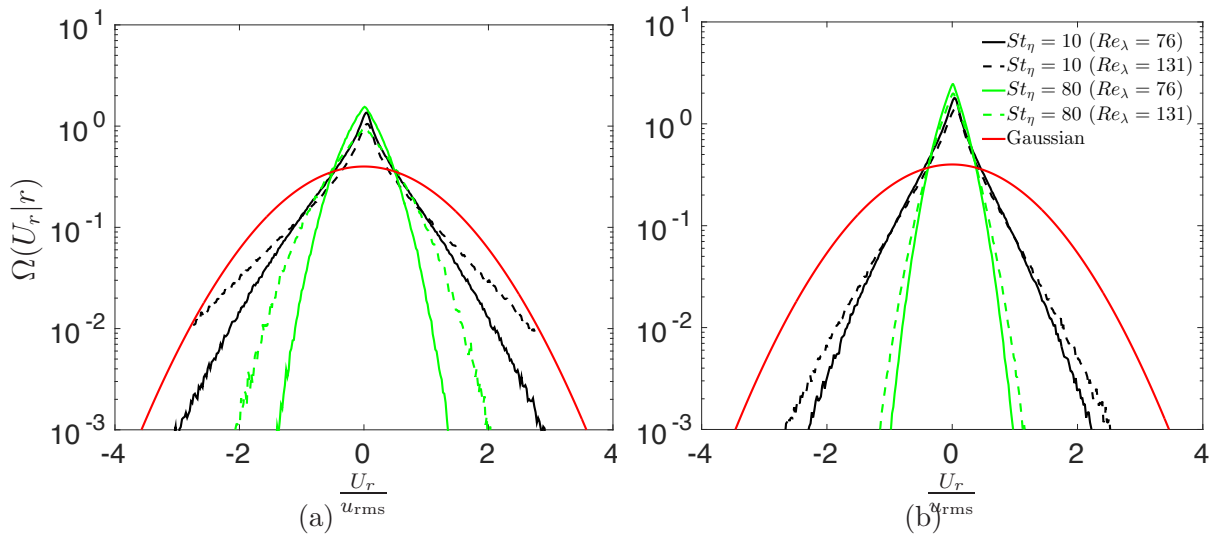


Figure 3.25: Effects of Reynolds number on the PDF of radial relative velocity $\Omega(U_r|r)$ for $St_\eta = 10, 80$. (a) CF1 closure, and (b) CF3 closure. The PDFs for $Re_\lambda = 76$ are shown for $r = 2.3\eta$, and those for $Re_\lambda = 131$ are for $r = 4.7\eta$.

and a Lagrangian time scale of eddies whose size scales with the pair separation. These comparisons establish that CF1 is the most accurate among the three closure forms considered.

Subsequently, a rigorous quantitative analysis of the stochastic model was performed through a direct comparison of Langevin simulation results with the DNS data for four Stokes numbers at two values of the Taylor micro-scale Reynolds number. Langevin simulations were performed using the three closure forms of the diffusivity. We compared LS predictions of the RDF, relative velocity variance and kurtosis, and the relative velocity PDF with the corresponding DNS data. For each of the statistics, it is evident that the predictions of CF1 follow the trends one would expect from the original premise of the [67] theory for high-inertia particles.

The RDFs obtained from the Langevin simulations based on CF1 showed excellent agreement with the DNS RDFs. The differences between the RDFs from the [100] theory and the DNS RDFs were attributed to: (1) the moments-based approach used to compute the RDFs, and (2) the inaccuracies in the inertial-range diffusivity as calculated from the unified expressions for the Eulerian structure function and the Lagrangian time scale. We derived an elegant power-law expression relating the RDF to the inverse of the relative-velocity variance. Relative velocity variances computed using CF1 showed good agreement with the variances from DNS, particularly at higher Stokes numbers. For separations in the integral range, the CF1 variances showed good agreement with the analytical limit for the relative velocity variance of two uncorrelated particles.

The effects of Reynolds number on the relative velocity statistics were also considered, where it was established that CF1 has a stronger dependence on Re_λ than CF2 and CF3. Consequently, we see that as the Reynolds number is increased, the CF1 variances were significantly higher than the DNS variances, especially for low Stokes numbers at small separations. However, at large separations, the CF1 variances showed good agreement with the expression for the relative velocity variance of uncorrelated pairs. The PDFs $\Omega(U|r)$ when normalized with the standard deviation $\langle U^2 \rangle^{1/2}$ and when scaled with u_{rms} were presented separately. The former allow us to understand the deviation of the PDFs from Gaussianity at various pair separations, as well as provide insights into how uncorrelated pairs at large separations transition into lingerers. The PDF of the radial component of the relative velocity, $\Omega(U_r|r)$, presents the startling picture of the transition from a negatively skewed PDF at large separations to a nearly symmetric PDF at small separations. The smaller the Stokes number, the greater the skewness of the PDF $\Omega(U_r|r)$. The transition in the PDF $\Omega(U_r|r)$ suggests that the clustering of high-Stokes-number particles at small separations originates in the inward-migration bias at much larger separations. This physical picture is analogous to the [9] analysis that the clustering of $St_\eta \sim 1$ particles was primarily due to their path-history interactions with turbulence.

The transition from Gaussian to non-Gaussian relative velocities as pair separations decreased was also quantified through the kurtosis of relative velocity. Kurtosis was presented both as a function of Stokes number and Reynolds number, and the predictions of CF1 and CF3 were compared with the DNS data. It was observed that the lower the Stokes number, the higher the Kurtosis. Finally, collision ker-

nels were also computed, and good agreement was found between CF1 and DNS. More importantly, in the context of planetesimal formation, it was found that the collision kernels increased with the Reynolds number due to an increase in both the RDF and the relative velocities with Re_λ . Equally relevant is the observation that at high Stokes numbers, the collision kernels were smaller than those of particles with randomly distributed relative velocities and positions.

The analysis and validation of the CF1 closure have established that the stochastic model of [67] captures both the qualitative and quantitative features of the relative motion of high-inertia particle pairs. The limitations of CF2 and CF3 were also clearly identified. In this context, two advancements to the closure that will be considered in a future study are: (1) improve the behavior of CF1 at higher Reynolds numbers, and (2) improve CF3 so that it approaches the consistent limit at large separations.

3.7 Appendix: Comparison with Renormalized Perturbation Expansion of LHDI

In Rani et al. [67], the diffusion current was closed through a perturbation analysis of the pair PDF equation in the limit of high Stokes number. In the discussion that follows, this perturbation method is compared with the renormalized perturbation approach used in the LHDI approximation [45, 70]. We begin by presenting an overview of Reeks' application of the LHDI method for closing the diffusion current in the particle phase space [70]. Our focus is on the salient features of this approach, rather than on its rigorous mathematical formalism. Subsequent to the

discussion of the LHDI method, we will present the relevant aspects of the current method, and draw comparisons and contrasts between the two methods.

In deriving a closure for the diffusion current, Reeks begins by considering the instantaneous phase-space density $\widehat{G}(\mathbf{r}, \mathbf{U}, t; \mathbf{r}_1, \mathbf{U}_1, t_1)$ arising from the introduction into the flow of a particle pair with relative position \mathbf{r}_1 and relative velocity \mathbf{U}_1 at time t_1 . (Here, we are applying Reeks' original formulation for single particle dynamics to the relative motion of particle pairs.) The Green's function \widehat{G} is governed by the Liouville's equation, namely

$$\frac{\partial \widehat{G}}{\partial t} + \nabla_{\mathbf{r}} \cdot (\mathbf{U} \widehat{G}) + \nabla_{\mathbf{U}} \cdot (\dot{\mathbf{U}} \widehat{G}) = 0 \quad \forall t > t_1 \quad (3.64)$$

and $\widehat{G}(\mathbf{r}, \mathbf{U}, t; \mathbf{r}_1, \mathbf{U}_1, t_1) = \delta(\mathbf{r} - \mathbf{r}_1) \delta(\mathbf{U} - \mathbf{U}_1) \delta(t - t_1)$ when $t = t_1$. In equation (3.64), $\nabla_{\mathbf{r}}$ and $\nabla_{\mathbf{U}}$ represent gradients with respect to \mathbf{r} and \mathbf{U} , respectively.

Substituting the particle-pair governing equation

$$\frac{d\mathbf{U}}{dt} = -\frac{1}{\tau_v} [\mathbf{U}(t) - \Delta \mathbf{u}(\mathbf{r}(t), t)] \quad (3.65)$$

into (3.64) gives

$$\frac{\partial \widehat{G}}{\partial t} + \nabla_{\mathbf{r}} \cdot (\mathbf{U} \widehat{G}) - \frac{1}{\tau_v} \nabla_{\mathbf{U}} \cdot (\mathbf{U} \widehat{G}) = -\frac{1}{\tau_v} \nabla_{\mathbf{U}} \cdot [\Delta \mathbf{u}(\mathbf{r}(t), t) \widehat{G}] \quad (3.66)$$

Ensemble averaging (3.66) over flow realizations yields

$$\frac{\partial G}{\partial t} + \nabla_{\mathbf{r}} \cdot (\mathbf{U} G) - \frac{1}{\tau_v} \nabla_{\mathbf{U}} \cdot (\mathbf{U} G) = -\frac{1}{\tau_v} \nabla_{\mathbf{U}} \cdot \langle \Delta \mathbf{u} \widehat{G} \rangle \quad (3.67)$$

where $G = \langle \widehat{G} \rangle$. The correlation $\langle \Delta \mathbf{u} \widehat{G} \rangle$ presents a closure problem, which is resolved through the LHDI method.

An important step in the LHDI approach of Reeks is to transform (3.66) to a new phase space such that the convective terms on the LHS of (3.66) drop out. This is achieved through the transformation

$$\mathbf{w} = \mathbf{U} e^{t/\tau_v} \quad (3.68)$$

$$\mathbf{y} = \mathbf{r} + \tau_v \mathbf{U} (1 - e^{t/\tau_v}) \quad (3.69)$$

Applying this transformation, and introducing the generalized Lagrangian Green's function in place of the above \widehat{G} as in Kraichnan [45], the transformed Liouville's equation becomes

$$\frac{\partial \widehat{G}}{\partial t} = -\frac{1}{\tau_v} \Delta \mathbf{u} \cdot \mathbf{l} \widehat{G} \quad (3.70)$$

where the $\widehat{G} = \widehat{G}(\mathbf{y}, \mathbf{w}, t | s; \mathbf{y}_1, \mathbf{w}_1, t_1 | s_1)$ is the generalized Green's function in the transformed space, and the operator \mathbf{l} is given by

$$\mathbf{l} = -e^{t/\tau_v} \nabla_{\mathbf{w}} - \tau_v (1 - e^{t/\tau_v}) \nabla_{\mathbf{y}} \quad (3.71)$$

Broadly speaking, the next step in LHDI is to solve (3.70) for \widehat{G} . This could be readily accomplished by expressing \widehat{G} as a series expansion in terms of $\widehat{G}^{(0)}$ that is the solution of (3.70) with its RHS set to zero. This series expansion involving functional

powers of $\widehat{G}^{(0)}$ is often referred to as a primitive perturbation series. Truncated forms of primitive expansions are quite inaccurate, except for very small values of the perturbation parameter. To avoid the problems with the primitive perturbation method, Kraichnan applied the renormalized perturbation expansions.

Renormalization involves inverting the original series so as to express $\widehat{G}^{(0)}$ in terms of G , where $G = \langle \widehat{G} \rangle$; this method was outlined in Kraichnan [45] for the case of a random oscillator. Eventually, by replacing $\widehat{G}^{(0)}$ with the renormalized expression, one is able to write $\widehat{G}(\mathbf{y}, \mathbf{w}, t | s; \mathbf{y}_1, \mathbf{w}_1, t_1 | s_1)$ as an expansion in terms of functional powers of $G(\mathbf{y}, \mathbf{w}, t | s; \mathbf{y}_1, \mathbf{w}_1, t_1 | s_1)$. It may be pointed out that this renormalized expansion is effectively a series in terms of $1/\tau_v$, or in dimensionless sense $1/St_I$, where St_I is the Stokes number based on the integral time scale. However, unlike a primitive expansion, the renormalized expansion does not require $1/St_I$ to be a small quantity, making such expansions reliably accurate even after truncation of the series. Substituting the renormalized \widehat{G} series into $\langle \Delta \mathbf{u} \widehat{G} \rangle$, retaining only the first term containing G , and transforming back to the original phase space gives us a closure for the diffusion current in terms of $G(\mathbf{r}, \mathbf{U}, t; \mathbf{r}_1, \mathbf{U}_1, t_1)$ and the dispersion tensors. Further averaging over the initial conditions of particle pairs yields the final desired closure for $\langle \Delta \mathbf{u} W \rangle$ in terms of $\langle W(\mathbf{r}, \mathbf{U}, t; \mathbf{r}_1, \mathbf{U}_1, t_1) \rangle$, where W is the fine-grained phase space density, and $\langle W \rangle$ is the PDF of particle pair relative position and velocity. Having set the background for the LHDI method, we will now compare and contrast LHDI with the perturbation expansion based closure derived in the current study.

It is to be noted that the current method was developed independently of the LHDI-based method of Reeks. In this study, we begin by considering the following conservation equation for the phase space density $P(\mathbf{r}, \mathbf{U}, \mathbf{x}, \mathbf{V}; t)$

$$\frac{\partial P}{\partial t} + \nabla_{\mathbf{r}} \cdot (\mathbf{U}P) + \nabla_{\mathbf{U}} \cdot (\dot{\mathbf{U}}P) + \nabla_{\mathbf{x}} \cdot (\mathbf{V}P) + \nabla_{\mathbf{V}} \cdot (\dot{\mathbf{V}}P) = 0 \quad (3.72)$$

which upon ensemble averaging (and dropping the \mathbf{x} and \mathbf{V} terms in the interest of brevity) yields the PDF transport equation

$$\frac{\partial \langle P \rangle}{\partial t} + \nabla_{\mathbf{r}} \cdot (\mathbf{U} \langle P \rangle) - \frac{1}{\tau_v} \nabla_{\mathbf{U}} \cdot (\mathbf{U} \langle P \rangle) = -\frac{1}{\tau_v} \nabla_{\mathbf{U}} \cdot \langle \Delta \mathbf{u} P \rangle \quad (3.73)$$

The closure problem is now represented by the term $\langle \Delta \mathbf{u} P \rangle$ on the RHS of (3.73). Quite analogous to the renormalized expansions in LHDI but without its detailed mathematical formalism, we write P as an expansion in which $\langle P \rangle$ is the first term, and $1/St_I$ is the small quantity. The motivation for writing such an expansion was that while the ensemble averaging $\langle \dots \rangle$ is equivalent to averaging over flow time scales, P evolved over longer time scales of the order of the particle response time τ_v . Hence, one may anticipate a perturbation in P with respect to $\langle P \rangle$. It is important to note that the expansion of P in terms of $\langle P \rangle$ and higher order terms is analogous to the renormalized expansion of \widehat{G} in terms of $G (= \langle \widehat{G} \rangle)$, and NOT to that of \widehat{G} in terms of $G^{(0)}$. The expansion of \widehat{G} in terms of $G^{(0)}$ is a primitive perturbation series, and we do not consider an analogous expansion of P in terms of $P^{(0)}$.

In spite of this similarity between the present and renormalized expansions, the current method is only applicable when $St_r \gg 1$, whereas LHDI, in principle, is valid for all Stokes numbers. The reason for this limitation may be attributed to an important assumption in the current method—i.e., the pair relative position \mathbf{r} remains essentially constant during flow time scales. This assumption effectively means that $\mathbf{U} = 0$ so that the two convective terms on the LHS of (3.72) dropout (without any transformation of the phase space). Thus, the PSD P is governed by the equation

$$\frac{\partial P}{\partial t} = -\frac{1}{\tau_v} \nabla_{\mathbf{U}} \cdot (\Delta \mathbf{u} P) \approx -\frac{1}{\tau_v} \nabla_{\mathbf{U}} \cdot (\Delta \mathbf{u} \langle P \rangle) \quad (3.74)$$

which may be solved for P in terms of $\langle P \rangle$. Substitution of the resulting P into $\langle \Delta \mathbf{u} P \rangle$ yields the diffusion current closure. Comparison of (3.70) and (3.74) shows that (3.70) reduces to (3.74) for asymptotically large particle Stokes numbers. Consideration of this limit allows us to go one step beyond LHDI in deriving a closed form expression for the diffusivity characterizing the phase-space diffusion current. Here, we are referring to our conversion of the Eulerian two-time correlation of fluid relative velocities to an Eulerian two-point correlation, which then allowed us to derive an expression for diffusivity that is closed to an integration in the wavenumber.

As the above discussion elaborates, the present expansion is, in fact, qualitatively similar to the renormalized perturbation series. The reason for the $1/St_I \ll 1$ requirement is due to effectively neglecting the convective terms on the LHS of the phase space density equation; whereas, in Reeks' approach, the singularly important

step is to perform a phase space transformation so that the convective terms are naturally zeroed out.

Finally, a brief comment on the source of perturbations in the current and LHDI methods. In the LHDI method of Reeks [70], the perturbation in the particle phase-space density arises due to the introduction into the flow of a particle pair with relative position \mathbf{r}_1 and relative velocity \mathbf{U}_1 at time t_1 . In the current study, the source of perturbation lies in the fact that the particles relax over times longer than flow time scales. Therefore, when one averages over flow realizations, there is a perturbation in the particle phase space density.

CHAPTER 4

EFFECTS OF DETERMINISTIC AND STOCHASTIC FORCING SCHEMES ON THE RELATIVE MOTION OF INERTIAL PARTICLES IN DNS OF ISOTROPIC TURBULENCE

4.1 Abstract

In direct numerical simulations (DNS) of isotropic turbulence, statistical stationarity is achieved by artificially forcing, i.e. adding energy to, the low-wavenumber scales of turbulence. In this work, the effects of two such forcing schemes on the relative positions and velocities of heavy, monodisperse, “point” particle pairs are studied. The first forcing scheme considered is a deterministic method in which the turbulent kinetic energy is maintained constant [98] by resupplying the energy dissipated during a time step to the velocity components in a low-wavenumber band. The second is the stochastic forcing method of Eswaran and Pope [25], where one adds a random acceleration to the fluid momentum equation at the low wavenumbers. The stochastic approach involves three main input parameters that allow us to estimate, *a priori*, the approximate value of the Taylor micro-scale Reynolds number Re_λ that can be obtained in a DNS run. One of these parameters is the correlation time scale

T_f of the random acceleration. Among our objectives is to assess the effects of varying T_f on the relative-motion statistics of particle pairs.

Direct numerical simulations of isotropic turbulence containing disperse particles were undertaken using both the deterministic and the stochastic forcing schemes for three grid sizes (128^3 , 256^3 , and 512^3). At each grid size, DNS runs based on the stochastic forcing were performed for five values of the forcing time scale $T_f = T_E/4$, $T_E/2$, T_E , $2T_E$, and $4T_E$, where T_E is the large-eddy time scale obtained from the corresponding DNS run with deterministic forcing. Thus, six DNS runs (one deterministic and five stochastic) were performed for each grid resolution, with Re_λ held nearly constant (varying by less than 5%) among these runs. The nominal values of Re_λ were ≈ 80 , 131, and 210 for the three grids. In each DNS run, heavy, monodisperse particles were tracked corresponding to twelve Stokes numbers ranging from $St_\eta = 0.05$ to 40, where St_η is the Stokes number based on the Kolmogorov time-scale τ_η . The motivation was to determine how the applied forcing impacted particle-pair relative motion in the three main Stokes number regimes, namely $St_\eta < 1$, $St_\eta \sim 1$, and $St_\eta > 1$. We focus our attention on three statistics quantifying the relative positions and velocities of particles: the radial distribution function (RDF), and the variance and the probability density function (PDF) of the component of pair relative velocity along the separation vector (U_r). Using the RDF and the PDF $P(U_r)$, we computed the particle collision kernel for the various DNS cases. The pair statistics are also compared with those from the deterministic DNS study of Ireland et al. [39], whose objective was to study the effects of variation in Re_λ and St_η on the relative-motion statistics.

At all three Reynolds numbers, we find that the forcing method and the time scale T_f have a noticeable effect on the RDFs for both $St_\eta < 1$ and $St_\eta > 1$. For $St_\eta < 1$ (at a given Re_λ), the differences between the RDFs for the various forcing cases increased with Stokes number, reaching a maximum around $St_\eta = 0.4$. However, for $St_\eta \sim 1$ ($St_\eta = 0.7$ and 1), the RDFs seem to be relatively unaffected by the forcing schemes. When $St_\eta > 1$, we find that the RDFs for the various forcings differed the most at $St_\eta = 2$, with the differences decreasing thereafter for higher Stokes numbers. When considering the effects of Re_λ , it is seen that the RDFs computed from the DNS with deterministic forcing were more sensitive to Re_λ variation than those obtained from DNS with stochastic forcing of various time scales. For $St_\eta \leq 0.4$, we notice that the deterministic RDFs decreased significantly as Re_λ varied from 80 to 131, but then increased as Re_λ increased to 210. In the study of Ireland et al. [39], the RDFs were found to be essentially independent of Re_λ for $St_\eta \leq 1$. But, a distinguishing feature of their study was that they hold the fluctuating RMS velocity u_{rms} , mean dissipation rate $\langle \epsilon \rangle$, and the resolution parameter $k_{\text{max}}\eta$ constant even as Re_λ is increased (k_{max} and η are the maximum resolved wavenumber and the Kolmogorov length scale, respectively). In the current study, however, our focus was only on keeping Re_λ fixed across the various forcing cases.

For $St_\eta < 1$, the variance $\langle U_r^2 \rangle$ showed only a weak sensitivity to forcing at the two lower Reynolds numbers, but a much clearer dependence is seen for $Re_\lambda = 210$. When $St_\eta \geq 1$, forcing has a relatively significant impact on the variances at all Reynolds numbers, and these effects are amplified as Re_λ is increased. The effects of forcing, Stokes number, and pair separation on the relative velocity PDFs are shown.

It is seen that the shapes of the PDFs were little affected by forcing. Using the RDF and $P(U_r)$, we also computed the collision kernels. At the two lower Re_λ , collision kernels were found to be weakly dependent on Re_λ for $St_\eta < 1$, but showed significant increase with Re_λ for $St_\eta \gtrsim 1$. However, when Re_λ is increased to 210, the collision kernel is seen to increase at all Stokes numbers.

4.2 Introduction

The collision kernel K for a monodisperse population of particles suspended in isotropic turbulence is given by [91, 95, 68]

$$K(\sigma) = 4\pi\sigma^2 g(\sigma) \int_{-\infty}^0 (-U_r) P(U_r|\sigma) dU_r \quad (4.1)$$

where σ is the particle diameter, $g(\sigma)$ is the radial distribution function (RDF) at contact (i.e., when particle-pair separation is equal to the sum of particle radii), U_r is the component of pair relative velocity along the pair separation vector (referred to as the radial relative velocity), and $P(U_r|\sigma)$ is the probability density function (PDF) of U_r at contact. It is evident from Eq. (4.1) that the two key statistics needed to compute the collision kernel are the RDF, and the PDF of pair radial relative velocity. When particles are smaller than the Kolmogorov length scale (η), the most accurate way to compute these statistics is via direct numerical simulations (DNS) of isotropic turbulence laden with disperse “point” particles. However, homogeneous, isotropic turbulence is inherently not stationary, due to the absence of the production of turbulent kinetic energy. To achieve stationarity in DNS of isotropic turbulence,

low-wavenumber turbulent scales are numerically forced, with the expectation that the forcing does not unduly alter the dynamics of high-wavenumber, i.e. small scale, turbulence. In this study, we consider two such forcing schemes, one “deterministic” [98] and the other “stochastic” [25], to perform DNS of isotropic turbulence containing monodisperse, non-settling particles. The effects of forcing on pair relative positions and velocities are quantified and compared. In the case of the stochastic method, we are also interested in understanding the sensitivity of pair relative motion to the correlation time scale of the forcing. Three grid resolutions and twelve particle Stokes numbers ranging from $St_\eta < 1$ to $St_\eta \geq 1$ are considered, where St_η is the particle Stokes number defined with the respect to the Kolmogorov time scale. These parameters were chosen so as to explore how the effects of forcing on relative motion varied with the Reynolds and Stokes numbers.

The forcing schemes for pseudo-spectral DNS of isotropic turbulence are commonly categorized into deterministic and stochastic schemes. The former are principally based on keeping fixed through the entire simulation either the energy $E(\kappa)$ in certain wavenumber shells, or the total kinetic energy $\int E(\kappa)d\kappa$ [86, 14, 90, 98]. For instance, in the forcing method of Sullivan et al. [90], they fix $E(\kappa)$ in the wavenumber shells $0 < \kappa \leq 2\sqrt{2}$ by multiplying the velocities in these shells with a real number evaluated from the energy change during a time step. Similarly, Wang et al. [96] maintained the energy levels of the first two wavenumber shells ($0.5 < \kappa < 1.5$ and $1.5 < \kappa < 2.5$) constant. In the current study, we employ the deterministic scheme of Witkowska et al. [98], which is based on keeping the total kinetic energy constant during the simulation.

In stochastic schemes, typically, a random acceleration that is active in a low-wavenumber band is added to the fluid momentum equations. Alvelius[2] developed a scheme in which the applied force $\widehat{\mathbf{f}}(\boldsymbol{\kappa}, t) = A(\boldsymbol{\kappa}, t)\mathbf{e}^{(1)}(\boldsymbol{\kappa}) + B(\boldsymbol{\kappa}, t)\mathbf{e}^{(2)}(\boldsymbol{\kappa})$, where $\mathbf{e}^{(1)}$ and $\mathbf{e}^{(2)}$ are unit vectors orthogonal to each other and to the wavenumber vector $\boldsymbol{\kappa}$, and A and B are random complex functions that are computed from a prescribed spectrum of the applied force. In this study, we implemented the Eswaran and Pope[25] stochastic scheme that computes the complex acceleration using six independent Uhlenbeck-Ornstein processes.

A forcing scheme for isotropic turbulence should satisfy two essential criteria. First, it should not significantly affect the high-wavenumber turbulent structure [25, 15, 90, 56]. Further, it should not destroy the homogeneity and isotropy of the flow field. For instance, it was seen in the study of Eswaran and Pope [25] that small-scale statistics, such as the fourth-order velocity derivative moment and the dissipation skewness, showed a rather weak dependence on the correlation time scale of the stochastic forcing. Eswaran and Pope [25] also showed that the variation of forcing parameters had little effect on the high-wavenumber regions of the energy and dissipation spectra. While the effects of forcing on the statistics of turbulence have been extensively studied and established, the influence of forcing on the relative-motion statistics of inertial particle pairs remains relatively unexplored. Accordingly, the focus of this work is investigate and quantify the dependence, if any, of pair statistics such as the RDF and the relative velocity PDF on forcing.

Indeed, there are multiple reasons to suggest that pair statistics may show a non-negligible dependence on both the nature and the parameters of forcing. Firstly,

it is known that pair relative positions and velocities are most influenced by eddies whose size scales with separation r . This is evident from the governing equations for the relative-motion statistics such as the RDF, and the second-order particle velocity structure function $\langle \mathbf{U}^p(t) \mathbf{U}^p(t) \rangle_{\mathbf{r}}$, where $\mathbf{U}^p(t)$ is the instantaneous relative velocity of a particle pair, and $\langle \cdot \cdot \rangle_{\mathbf{r}}$ denotes ensemble averaging conditioned upon the separation being equal to the configuration space value \mathbf{r} . These governing equations contain dispersion tensors that are, broadly speaking, functions of the fluid velocity structure function (a detailed discussion of the equations may be found in the references [100, 103, 104, 9, 10]). The fluid velocity structure function is a covariance tensor of the fluid relative velocities “seen” by the particle pairs, with the implication that pair relative motion is principally driven by eddies of size r . Consequently, when the large-scale eddies are forced, it may be anticipated that for separations in the energy-containing range, forcing may affect pair relative motion. Indeed, at smaller Reynolds numbers, where there may not be a clear separation among turbulent scales, the effects of forcing may even be felt for separations in the inertial subrange. Another reason for the expectation that forcing may influence pair statistics is related to the effects of Stokes number on pair relative motion. It has recently been established that for $St_\eta \gtrsim 1$, particle clustering at sub-Kolmogorov-scale separations is governed by a non-local phenomenon referred to as the “path history, symmetry breaking mechanism” [9, 10, 11]. Due to this St_η -dependent non-local mechanism, pair interactions with eddies at larger separations continue to influence their relative motion even after their separations have decreased substantially. In view of the preceding discussion,

this work aims to not only quantify the effects of forcing on the relative motion, but also determine how these effects depended on the Reynolds and Stokes numbers.

Two recent studies [75, 74] considered the dependence of particle relative positions and velocities on the forcing scheme in DNS of isotropic turbulence. Rosa et al. [75] studied the collision statistics of monodisperse, settling and non-settling particles, using both the deterministic scheme of Wang et al. [96] and the stochastic scheme of Eswaran and Pope [25]. They considered six grid resolutions from 32^3 to 1024^3 , and fourteen Stokes numbers in the range $0.063 \leq St_\eta \leq 2.28$. It was observed that for a given grid, deterministic forcing yielded significantly higher Re_λ than stochastic forcing. Thus, only the grid size, and not a flow parameter or a turbulence statistic, was the common factor when comparing deterministic and stochastic DNS runs. In the current study, however, the DNS runs with the two forcings have essentially the same Re_λ for a given grid size. Rosa et al. [75] studied the effects of St_η , Re_λ , and forcing scheme on the RDF and the radial relative velocities, both statistics computed when the particles are in contact. They found that for the non-settling particles, at all Re_λ , the RDFs obtained using the two forcing schemes were close to each other for $St_\eta < 0.5$, but the deterministic scheme predicted higher RDFs for $St_\eta \geq 0.5$. Rosa et al. [75] noticed that the gravity and Re_λ had no effect on the radial relative velocities for $St_\eta < 0.5$ particles. However, for $St_\eta > 0.5$, the relative velocities for settling particles were significantly lower than those for non-settling particles. Also, for $St_\eta > 0.5$, the relative velocities decreased with Re_λ for the non-settling particles, whereas the opposite trend was observed for the settling particles. The radial relative velocities for both settling and non-settling particles were found to be independent

of the forcing scheme. Rosa et al. [75] then computed the collision kernels using the RDFs and radial relative velocities. They observed that the collision kernels for $St_\eta < 0.5$ were independent of the forcing scheme, Re_λ , and of whether the particles were settling or not. For $St_\eta > 0.5$, the collision kernels for non-settling particles were higher than those for settling particles. They also saw that for $St_\eta > 0.5$, deterministic forcing yielded higher collision kernels than did stochastic forcing.

In a subsequent study, Rosa et al. [74] considered the stochastic scheme of Eswaran and Pope [25], and studied the effects of varying the forcing time scale (T_f) on the relative motion of settling particles in DNS of isotropic turbulence. They considered six forcing time scales in the range $0.1 \leq T_f/\tau_\eta \leq 594$, where τ_η is the Kolmogorov time scale. In their simulations, they kept constant the reference dissipation rate ϵ_0 , which is an input parameter to the stochastic scheme. Here $\epsilon_0 = 4N_f\sigma_f^2T_f$, where σ_f^2 is the acceleration variance, and N_f is the number of wavenumbers that are forced. In contrast, we focus on varying the forcing time scale T_f while keeping Re_λ nearly constant. Rosa et al. [74] observed that Re_λ and the dissipation rate $\langle\epsilon\rangle$ are independent of forcing time scale when $T_f \leq \tau_\eta$, but decrease with T_f for $T_f > \tau_\eta$. As in their earlier study [75], they computed statistics such as the RDF and the mean radial relative velocity $\langle|U_r|\rangle$, both at contact, for nine Stokes numbers in the range $0.063 \leq St_\eta \leq 2.28$, and at two grid resolutions of 128^3 and 256^3 . For $St_\eta < 0.5$ and both grid sizes, the RDFs and radial relative velocities were found to be weakly sensitive to the forcing time scale for $T_f/\tau_\eta < 594$. When $T_f/\tau_\eta = 594$, they found that for the 128^3 case, the RDFs showed a marginal decrease for $St_\eta > 0.5$, but for the 256^3 case, the RDFs showed a strong decrease for $St_\eta > 0.5$. Finally, they concluded

that the flow and particle statistics became independent of the forcing time scales for $T_f \leq \tau_\eta$.

In the current study, we perform direct numerical simulations of forced isotropic turbulence laden with monodisperse, non-settling particles. The deterministic scheme of Witkowska et al. [98], and the stochastic scheme of Eswaran and Pope [25] are considered, and their effects on the statistics of particle pairs are studied. DNS are performed for three grid sizes 128^3 , 256^3 , and 512^3 , where the nominal values of Re_λ were ≈ 80 , 131, and 210, respectively. For DNS with stochastic forcing, we consider five forcing time scales $T_f = T_E/4$, $T_E/2$, T_E , $2T_E$, and $4T_E$, where T_E is the large-eddy time scale obtained from the corresponding DNS run with deterministic forcing. Particles with twelve Stokes numbers ranging from $St_\eta = 0.05$ to 40 were considered.

The organization of the chapter is as follows. Section 4.3 presents the computational details of the direct numerical simulations. In Section 4.4, we present a comparison of pair relative-motion statistics such as the RDF, and the variances and PDFs of radial relative velocity obtained from the various DNS runs. Section 4.5 summarizes the key findings.

4.3 Computational Method

4.3.1 Fluid Phase

Direct numerical simulations of forced isotropic turbulence were performed using a pseudo-spectral method that utilizes discrete Fourier expansions of flow variables. Simulations were performed over a cubic domain of length 2π discretized into

N^3 grid points, with periodic boundary conditions along the three directions. The details of the pseudospectral algorithm are identical to those in Ireland et al. [38] and Brucker et al. [12]

We consider the Navier-Stokes equations in rotational form and the continuity equation [12, 38]

$$\frac{\partial \mathbf{u}}{\partial t} + \boldsymbol{\omega} \times \mathbf{u} = -\nabla (p/\rho_f + \mathbf{u}^2/2) + \nu \nabla^2 \mathbf{u} + \mathbf{f} \quad (4.2)$$

$$\nabla \cdot \mathbf{u} = 0 \quad (4.3)$$

where $\boldsymbol{\omega} = \nabla \times \mathbf{u}$ is the vorticity, ρ_f is the fluid density, p is the pressure, and \mathbf{f} is the external forcing applied to maintain a statistically stationary turbulence.

Transforming Eqs. (4.2) and (4.3) into Fourier space and eliminating pressure using the spectral form of continuity yields

$$\left(\frac{\partial}{\partial t} + \nu k^2 \right) \widehat{\mathbf{u}} = - \left(\mathbf{I} - \frac{\mathbf{k}\mathbf{k}}{k^2} \right) \cdot \widehat{\boldsymbol{\omega} \times \mathbf{u}} + \widehat{\mathbf{f}} \quad (4.4)$$

where $k^2 = \mathbf{k} \cdot \mathbf{k}$. Direct evaluation of the convolution $\widehat{\boldsymbol{\omega} \times \mathbf{u}}$ is extremely computationally intensive. Hence, a pseudo-spectral approach is adopted wherein $\boldsymbol{\omega} \times \mathbf{u}$ is first computed in physical space, and then transformed into the spectral space.

Since the time-derivative and viscous stress terms on the LHS of Eq. (4.4) are linear in $\widehat{\mathbf{u}}$, one may evolve these terms in time exactly by multiplying Eq. (4.4) with the integrating factor, $\exp(\nu k^2 t)$. This yields the following equation (in index

notation):

$$\frac{\partial}{\partial t} [\exp(\nu k^2 t) \widehat{u}_i] = \text{RHS}_i \exp(\nu k^2 t), \quad (4.5)$$

where $\text{RHS}_i = (-\delta_{im} + \frac{k_i k_m}{k^2}) \epsilon_{mjk} \mathcal{F} \{ \omega_j u_k \}$ represents the right-hand side of Eq. (4.4), and $\epsilon_{mjk} \mathcal{F} \{ \omega_j u_k \}$ represents the convolution $\widehat{\boldsymbol{\omega} \times \mathbf{u}}$, and ϵ_{mjk} is the Levi-Civita tensor.

Equation (4.5) is then discretized in time using the second-order Runge-Kutta (RK2) method giving

$$\widehat{u}_i^{n+1} = \widehat{u}_i^n \exp[-\nu k^2 t] + \{ \text{RHS}_i^n \exp[-\nu k^2 t] + \text{RHS}_i^{n+1} \} \quad (4.6)$$

where n is the the previous time-step level and h is the time-step size. To prevent convective instabilities, time-step size h is chosen such that the CFL number ≤ 0.5 . The pseudospectral algorithm introduces aliasing errors which are removed by zeroing the fluid velocities in spectral space for wavenumbers satisfying $k \geq k_{\max}$, where k is the wavenumber magnitude, $k_{\max} = \sqrt{2}N/3$ and N is the number of grid points along each dimension. A brief description of the deterministic and stochastic forcing schemes used in the current study is provided next.

4.3.1.1 Deterministic Forcing Scheme

We employ the deterministic forcing method developed by Witkowska et al. [98], wherein the turbulent kinetic energy dissipated during a time step is added back to the flow at the low wavenumbers. It may be noted that in this method, as opposed to the stochastic scheme, there is no explicit forcing term \mathbf{f} added to the

Navier-Stokes equations. Instead, one scales the velocity components in the forcing wavenumber band $[\kappa_{\min}, \kappa_{\max}]$ by a factor such that the energy dissipated during a given time step is resupplied, as follows.

$$\widehat{\mathbf{u}}(\boldsymbol{\kappa}, t + \Delta t) = \widehat{\mathbf{u}}(\boldsymbol{\kappa}, t) \sqrt{1 + \frac{\Delta E_{\text{diss}}(\Delta t)}{\int_{\kappa_{\min}}^{\kappa_{\max}} E(\boldsymbol{\kappa}, t + \Delta t) d\boldsymbol{\kappa}}} \quad \forall \boldsymbol{\kappa} \in [\kappa_{\min}, \kappa_{\max}] \quad (4.7)$$

where $\widehat{\mathbf{u}}(\boldsymbol{\kappa})$ is the Fourier coefficient of the velocity at wavenumber $\boldsymbol{\kappa}$, ΔE_{diss} is the total energy dissipated during Δt , and $E(\boldsymbol{\kappa}, t + \Delta t)$ is the spectral turbulent kinetic energy in a wavenumber shell with magnitude $\boldsymbol{\kappa}$ at time $t + \Delta t$. In the current study, the velocity components in the range $\boldsymbol{\kappa} \in (0, 2]$ are forced using eq. (4.7).

4.3.1.2 Stochastic Forcing Scheme

The stochastic forcing scheme implemented in this study is that proposed by Eswaran and Pope [25]. Unlike the deterministic forcing discussed above, in this method an explicit acceleration term is added to the Navier-Stokes equations. The forcing term $\widehat{\mathbf{f}}$ in equation (4.4) is non-zero only in the wavenumber band $\boldsymbol{\kappa} \in (0, 2]$, and is computed using six independent Uhlenbeck-Ornstein (UO) processes at each of the forced wavenumbers.

The UO processes denoted by $\widehat{\mathbf{b}}(\boldsymbol{\kappa}, t)$ can be written as [17]

$$\widehat{\mathbf{b}}(\boldsymbol{\kappa}, t + \Delta t) = \widehat{\mathbf{b}}(\boldsymbol{\kappa}, t) \left(1 - \frac{\Delta t}{T_f}\right) + \boldsymbol{\theta} \left(\frac{2\sigma^2 \Delta t}{T_f}\right)^{1/2} \quad (4.8)$$

where Δt is the time step, $\boldsymbol{\theta}$ is a vector of complex random numbers whose components are drawn from a standard normal distribution, and σ^2 and T_f are the variance and time-scale respectively, of the UO process. The stochastic process $\widehat{\mathbf{b}}(\boldsymbol{\kappa}, t)$ has the following properties[25]:

$$\langle \widehat{\mathbf{b}}(\boldsymbol{\kappa}, t) \rangle = 0 \quad (4.9)$$

$$\langle \widehat{\mathbf{b}}(\boldsymbol{\kappa}, t) \widehat{\mathbf{b}}^*(\boldsymbol{\kappa}, t + s) \rangle = 2\sigma^2 \delta_{ij} \exp(-s/T_f) \quad (4.10)$$

where an asterisk denotes the complex conjugate. The forcing term, $\widehat{\mathbf{f}}$ in eq. (4.4) is the projection of $\widehat{\mathbf{b}}(\boldsymbol{\kappa}, t)$ onto the plane normal to $\boldsymbol{\kappa}$

$$\widehat{\mathbf{f}} = \widehat{\mathbf{b}}(\boldsymbol{\kappa}, t) - \boldsymbol{\kappa} \boldsymbol{\kappa} \cdot \widehat{\mathbf{b}}(\boldsymbol{\kappa}, t) / (\boldsymbol{\kappa} \cdot \boldsymbol{\kappa}) \quad (4.11)$$

When investigating the effects of stochastic forcing, we considered five values of the forcing time scale $T_f = 4T_E, 2T_E, T_E, T_E/2$, and $T_E/4$, where $T_E = L/u_{\text{rms}}$ is the large-eddy turnover time obtained from the corresponding DNS run based on deterministic forcing, and L and u_{rms} are the integral length scale and the RMS fluctuating velocity, respectively.

4.3.2 Particle Phase

The governing equations of motion for a heavy spherical particle, whose diameter is much smaller than the Kolmogorov length scale, may be written as

$$\frac{d\mathbf{x}_p}{dt} = \mathbf{v}_p, \quad (4.12)$$

$$\frac{d\mathbf{v}_p}{dt} = \frac{\mathbf{u}(\mathbf{x}_p, t) - \mathbf{v}_p}{\tau_v}, \quad (4.13)$$

where we assumed Stokes drag to be the principal force on the particle, \mathbf{x}_p and \mathbf{v}_p are the particle position and velocity, respectively, and τ_v is the particle viscous relaxation time. In Eq. (4.13), $\mathbf{u}(\mathbf{x}_p, t)$ is the fluid velocity at the particle's location. In order to solve Eqs. (4.12) and (4.13) numerically, $\mathbf{u}(\mathbf{x}_p, t)$ needs to be evaluated. This is achieved by interpolating to the particle position fluid velocities at a stencil of grid points surrounding the particle. We use the 8th order Lagrange interpolation method that is based on a stencil of $8 \times 8 \times 8$ fluid velocities. Also, the particle loading is assumed to be dilute in this study so that the influence of particles on the fluid is negligible.

Temporal update of particle motion is achieved through a modified second-order Runge-Kutta (RK2) method in which the standard RK2 weights are replaced by exponential integrators as follows [38]:

$$\mathbf{v}_p(t_0 + h) = e^{-h/\tau_v} \mathbf{v}_p(t_0) + w_1 \mathbf{u}_p[\mathbf{x}_p(t_0)] + w_2 \mathbf{u}[\mathbf{x}_p(t_0) + \mathbf{v}_p(t_0)h] \quad (4.14)$$

where h is the time step, and the exponential integrators w_1 and w_2 are given by

$$w_1 \equiv \left(\frac{h}{\tau_v}\right) \left[\phi_1\left(\frac{-h}{\tau_v}\right) - \phi_2\left(\frac{-h}{\tau_v}\right) \right], \quad w_2 \equiv \left(\frac{h}{\tau_v}\right) \phi_1\left(\frac{-h}{\tau_v}\right) \quad (4.15)$$

$$\phi_1(z) \equiv \frac{e^z - 1}{z}, \quad \phi_2(z) \equiv \frac{e^z - z - 1}{z^2} \quad (4.16)$$

4.4 Results

Direct numerical simulations of homogeneous, isotropic turbulence were conducted using both deterministic forcing (DF) and stochastic forcing (SF) at three values of $Re_\lambda \approx 80, 131,$ and 210 , corresponding to grid sizes of $128^3, 256^3,$ and 512^3 , respectively. At each Re_λ , one DNS run using DF, and five DNS runs using SF with different forcing time scales T_f were performed. The DNS + SF simulations corresponded to $T_f = 4T_E, 2T_E, T_E, T_E/2,$ and $T_E/4$, which are denoted as SF1, SF2, SF3, SF4, and SF5, respectively. Here T_E is the eddy turnover time obtained from the DNS + DF case. In each DNS run, monodisperse, non-settling, inertial particles of twelve Stokes numbers ranging from $St_\eta = 0.05$ to 40 were tracked, where St_η is the Stokes number based on the Kolmogorov time scale. The statistics of particle-pair relative motion obtained from these simulations are compared and analyzed to understand the effects of variations in the forcing scheme (and time scale for SF), Re_λ , and St_η . Results from a second set of deterministic forcing (DF2) simulations, obtained from the study of Ireland et al. [39], are also included for comparison. The current DF runs and the DF2 simulations of Ireland et al. [39] differ in the values of

turbulence parameters such as u_{rms} , $\langle \epsilon \rangle$, and $k_{\text{max}}\eta$. Further, they maintained these parameters constant while varying Re_λ , but our focus was on keeping Re_λ nearly the same for the DF and SF1-SF5 simulations at a given grid size.

The turbulence parameters for the three grids and the various forcings are summarized in Table 4.1-Table 4.3. In all the simulations, the flow field is first allowed to achieve statistical stationarity by evolving it for more than $12T_L$, where $T_L = L/u_{\text{rms}}$ is the respective large-eddy turnover time. The particles are then introduced into the flow and evolved for about $6T_L$, before collecting their statistics. The particle statistics are then collected for the next $10-12T_L$ and averaged over this duration. Note that the particles do not modify the flow turbulence, and are also collision-free. The DF2 turbulence parameters of Ireland et al. [39] are given in Table 4.4.

In Figure 4.1, the energy spectra obtained from the 256^3 and 512^3 DNS runs are compared. Figure 4.1(a) and (b) compare the energy spectrum of DF with the spectra from SF1-SF5 for the two grids. For both grids, the forcing type and the forcing time scale (for SF) do not significantly affect the spectra. Figure 4.1(c) and (d) show the normalized energy spectra on a log-linear scale. Also included are the corresponding energy spectra from the DF2 simulations of Ireland et al. [39]. These figures clearly show that the current DNS simulations have a higher $k_{\text{max}}\eta$, i.e. resolve smaller scales, than the DF2 runs. Next, we present the particle statistics obtained from the DF and SF1-SF5 cases, as well as from DF2 where available.

Table 4.1: Flow parameters in 128^3 DNS of isotropic turbulence (arbitrary units). $Re_\lambda \equiv u_{\text{rms}}\lambda/\nu$ is the Taylor micro-scale Reynolds number, $u_{\text{rms}} \equiv \sqrt{(2k/3)}$ is the fluid RMS fluctuating velocity, ν is the fluid kinematic viscosity, $\epsilon \equiv 2\nu \int_0^{\kappa_{\text{max}}} \kappa^2 E(\kappa) d\kappa$ is the turbulent energy dissipation rate, $L \equiv 3\pi/(2k) \int_0^{\kappa_{\text{max}}} E(\kappa)/\kappa d\kappa$ is the integral length scale, $\lambda \equiv u_{\text{rms}}\sqrt{(15\nu/\epsilon)}$ is the Taylor microscale, $\eta \equiv \nu^{3/4}/\epsilon^{1/4}$ is the Kolmogorov length scale, $T_E \equiv L/u'$ is the large-eddy turnover time, $\tau_\eta \equiv \sqrt{(\nu/\epsilon)}$ is the Kolmogorov time scale, κ_{max} is the maximum resolved wavenumber, Δt is the time step, and N_p is the number of particles per Stokes number.

Parameter	DF	SF1	SF2	SF3	SF4	SF5
Re_λ	80.712	82.008	78.136	77.519	76.216	77.110
u_{rms}	1.067	1.106	1.029	0.992	0.953	0.970
ν	0.0071	0.0071	0.0071	0.0071	0.0071	0.0071
ϵ	0.421	0.475	0.392	0.345	0.304	0.318
L	1.482	1.479	1.461	1.487	1.505	1.507
λ	0.539	0.530	0.543	0.559	0.574	0.568
η	0.0304	0.0298	0.031	0.032	0.033	0.033
T_E	1.388	1.336	1.420	1.499	1.579	1.553
τ_η	0.130	0.125	0.138	0.147	0.158	0.153
$\kappa_{\text{max}}\eta$	1.829	1.789	1.879	1.938	2.001	1.977
Δt	2.5×10^{-3}	2.5×10^{-3}	2.5×10^{-3}	2.5×10^{-3}	2.5×10^{-3}	2.5×10^{-3}
N_p	262,144	262,144	262,144	262,144	262,144	262,144

Table 4.2: Flow parameters in 256^3 DNS of isotropic turbulence (arbitrary units). Definitions of parameters is provide in the caption of Table 4.1.

Parameter	DF	SF1	SF2	SF3	SF4	SF5
Re_λ	128.24	133.134	134.06	129.43	130.6	128.82
u_{rms}	0.999	1.135	1.126	1.072	1.073	1.042
ν	0.0028	0.0028	0.0028	0.0028	0.0028	0.0028
ϵ	0.321	0.503	0.487	0.423	0.416	0.384
L	1.466	1.401	1.258	1.416	1.426	1.427
λ	0.366	0.337	0.341	0.345	0.348	0.353
η	0.016	0.0149	0.015	0.0154	0.0155	0.0158
T_E	1.467	1.241	1.257	1.32	1.328	1.369
τ_η	0.0945	0.0779	0.079	0.084	0.084	0.088
$\kappa_{\text{max}}\eta$	1.969	1.784	1.801	1.855	1.858	1.899
Δt	1×10^{-3}	1×10^{-3}	1×10^{-3}	1×10^{-3}	1×10^{-3}	1×10^{-3}
N_p	262,144	262,144	262,144	262,144	262,144	262,144

Table 4.3: Flow parameters in 512^3 DNS of isotropic turbulence (arbitrary units). Definitions of parameters is provide in the caption of Table 4.1.

Parameter	DF	SF1	SF2	SF3	SF4	SF5
Re_λ	212.16	214.35	208.26	210.02	207.32	207.7
u_{rms}	1.114	1.136	1.124	1.119	1.089	1.092
ν	0.0012	0.0012	0.0012	0.0012	0.0012	0.0012
ϵ	0.438	0.472	0.488	0.473	0.431	0.425
L	1.426	1.342	1.338	1.348	1.359	1.384
λ	0.225	0.222	0.218	0.221	0.224	0.225
η	0.0078	0.0077	0.0077	0.0077	0.0079	0.0079
T_E	1.281	1.182	1.189	1.204	1.247	1.267
τ_η	0.052	0.050	0.050	0.0511	0.053	0.053
$\kappa_{\text{max}}\eta$	1.891	1.861	1.852	1.869	1.908	1.912
Δt	5×10^{-4}	5×10^{-4}	5×10^{-4}	5×10^{-4}	5×10^{-4}	5×10^{-4}
N_p	2,097,152	2,097,152	2,097,152	2,097,152	2,097,152	2,097,152

Table 4.4: DF2 flow parameters in DNS of isotropic turbulence (arbitrary units) study of Ireland et al. [39]. N is the number of grid points in each direction, and definitions of other parameters is provide in the caption of Table 4.1.

Parameter	DNS I	DNS II	DNS III
N	128	256	512
Re_λ	88	140	224
u_{rms}	0.914	0.914	0.915
ν	0.005	0.002	0.0008289
ϵ	0.270	0.267	0.253
L	1.46	1.41	1.40
η	0.026	0.0132	0.0068
T_E	1.60	1.54	1.53
τ_η	0.137	0.087	0.057
$\kappa_{\text{max}}\eta$	1.59	1.59	1.66
N_p	262,144	262,144	2,097,152

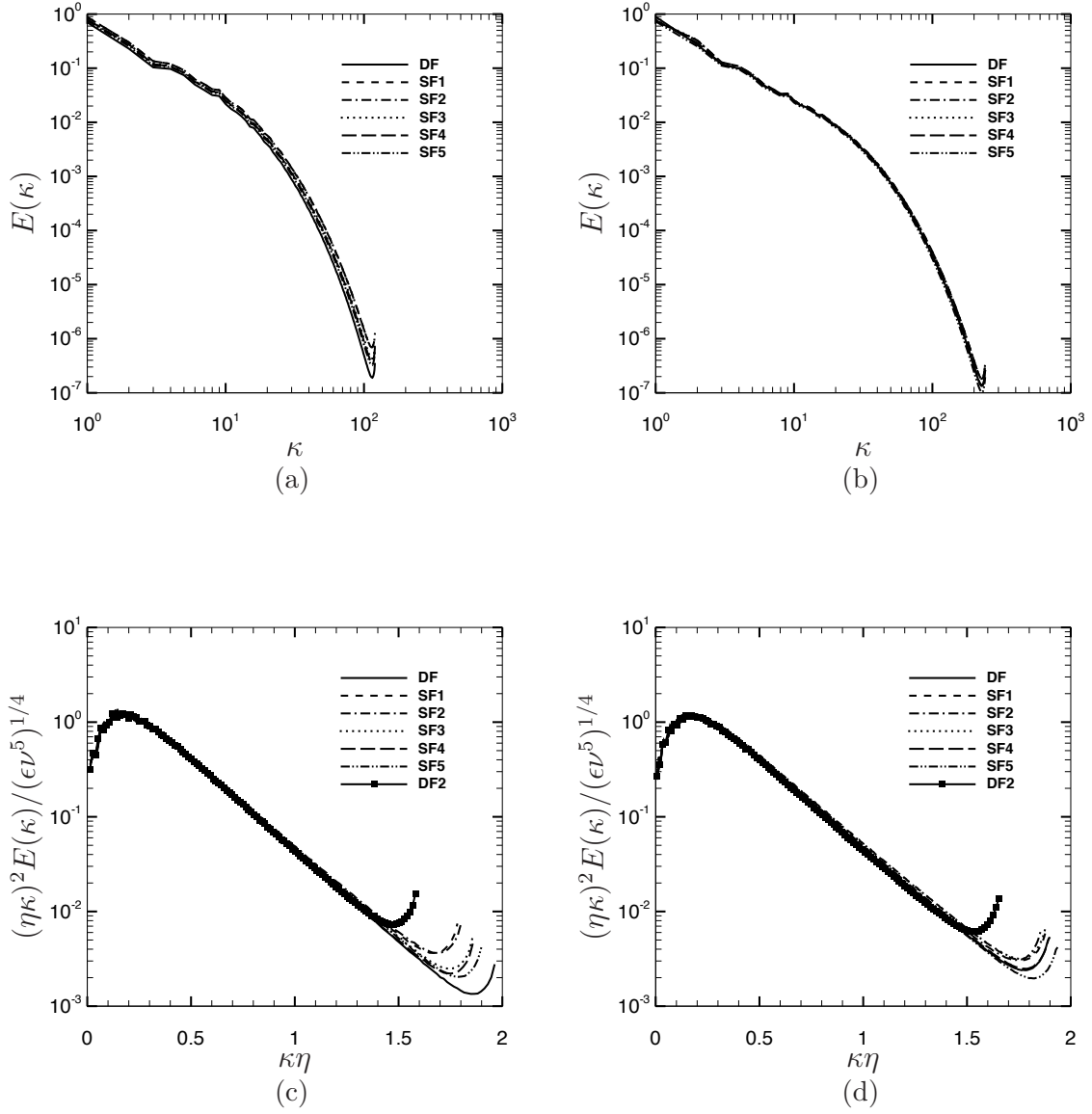


Figure 4.1: Energy Spectra at (a) 256^3 and (b) 512^3 grid resolutions, and for DF, SF1, SF2, SF3, SF4, and SF5 forcings. Normalized energy Spectra at (c) 256^3 and (d) 512^3 grid resolutions, and for DF, DF2, SF1, SF2, SF3, SF4, and SF5 forcings.

4.4.1 Particle Clustering

The radial distribution function (RDF) is a widely used statistical measure of particle clustering in isotropic turbulence. It is also a key input to the collision kernel of particle pairs. The RDF, $g(r)$, is defined as the ratio of the actual number of particle pairs at a given separation r to the expected number of particle pairs at that separation when the particles are uniformly distributed [39], giving us

$$g(r) = \frac{\left[\frac{N_{\text{pair}}(r)}{\Delta V_p} \right]}{\left[\frac{N(N-1)}{2V} \right]} \quad (4.17)$$

In Eq. (4.17), $N_{\text{pair}}(r)$ is the actual number of particle pairs that lie within a spherical shell whose average radius is r , radial thickness is Δr and volume is ΔV_p ; whereas V is the total volume of the flow domain containing N number of particles. In the absence of clustering, particles would be uniformly distributed throughout the volume, so that the RDF is unity. Accordingly, $g(r) > 1$ is indicative of particle clustering.

During the past three decades, significant insights have been gained into the effects of turbulence on the clustering of particles smaller than the Kolmogorov length scale. For instance, it is now well-known that heavy, low-Stokes-number particles cluster because they are centrifuged out of high-vorticity regions into high strain-rate regions, the so-called “centrifuge mechanism” [52, 89, 23, 18]. Recent studies have also made vital contributions in elucidating the mechanisms by which turbulence drives the spatial clustering and the relative velocities of spherical particles [9, 10, 11]. Through detailed theoretical analyses, supported by DNS data, these studies [9, 10, 11] identified that the centrifuging is the dominant clustering mechanism only

when the particle Stokes number St_η is $\ll 1$. It was further recognized that the mechanism responsible for particle clustering when $St_\eta \geq \mathcal{O}(1)$ is of an entirely different nature. Namely, when $St_\eta \geq \mathcal{O}(1)$ the centrifuge mechanism gives way to a “path-history symmetry breaking mechanism” [11]. We anticipate that these differences in the clustering mechanisms for the $St_\eta < 1$ and $St_\eta \geq 1$ particles will be important when considering the effects of forcing, Reynolds number Re_λ , and separation r on the RDFs. Therefore, we will discuss the RDF results separately for the two Stokes number regimes.

We begin by comparing the RDFs of the $St_\eta < 1$ particles obtained from the DF, DF2 and SF1-SF5 simulations at each of the three values of Re_λ in Figure 4.2-4.4. Here, DF refers to the DNS with deterministic forcing in the current study, and DF2 refers to that in Ireland et al. [39]. SF1-SF5 are the DNS runs using stochastic forcing, with the forcing time scale varying from $T_f = 4T_E$ to $T_E/4$, where T_E is the large-eddy turnover time obtained from DF. This comparison will enable us to quantify the effects of forcing on the RDFs, as well as discern how these effects vary with Re_λ . In Figure 4.2, the RDFs are plotted as a function of dimensionless pair separation r/η at $Re_\lambda \approx 80$ and for $St_\eta = 0.05, 0.2, 0.4$ and 0.7 . It is to be noted that $Re_\lambda = 88$ for the DF2 simulation, and that η represents the respective Kolmogorov length scale for each of the seven forcing cases (DF, DF2 and SF1-SF5). Firstly, we note from Figure 4.2 that forcing can significantly influence the values of RDF for separations $r \lesssim \eta$. By the effects of forcing, we are referring to the differences between the RDFs for a given r and St_η .

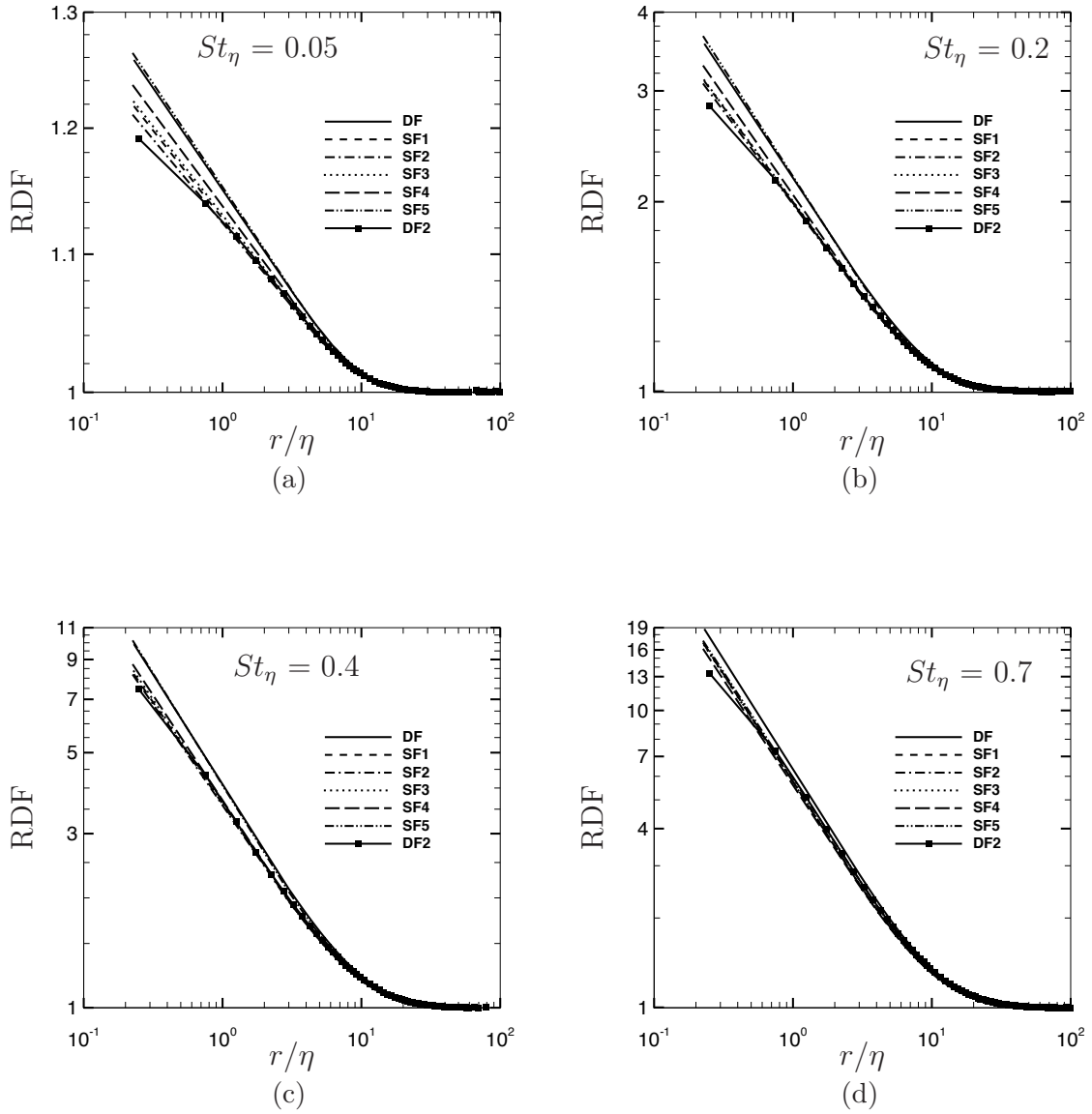


Figure 4.2: RDFs from stochastic (SF1-SF5) and deterministic (DF and DF2) forcing schemes as a function of dimensionless pair separation r/η for the indicated values of St_η at $Re_\lambda = 80$.

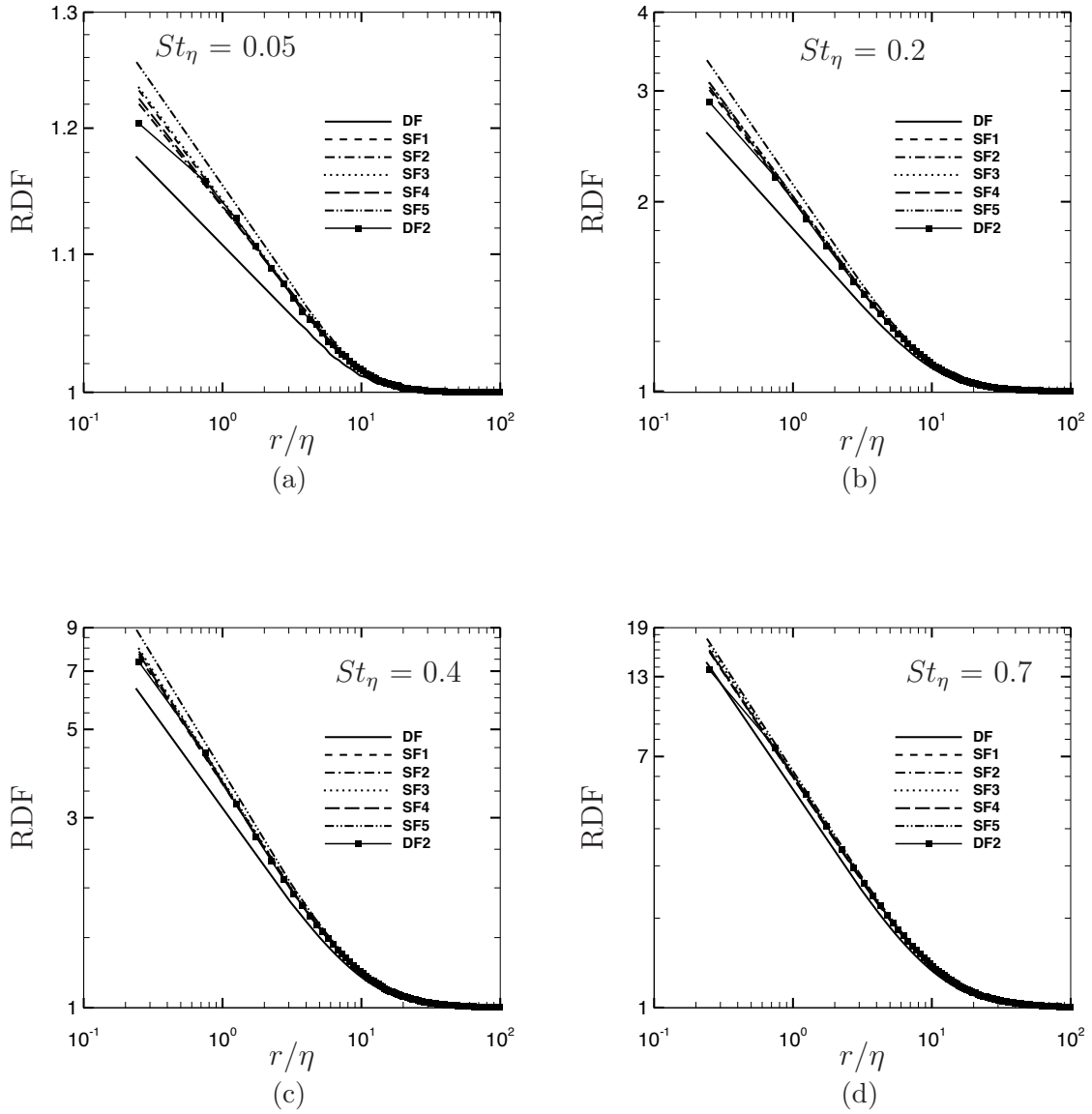


Figure 4.3: RDFs from stochastic (SF1-SF5) and deterministic (DF and DF2) forcing schemes as a function of dimensionless pair separation r/η for the indicated values of St_η at $Re_\lambda = 131$.

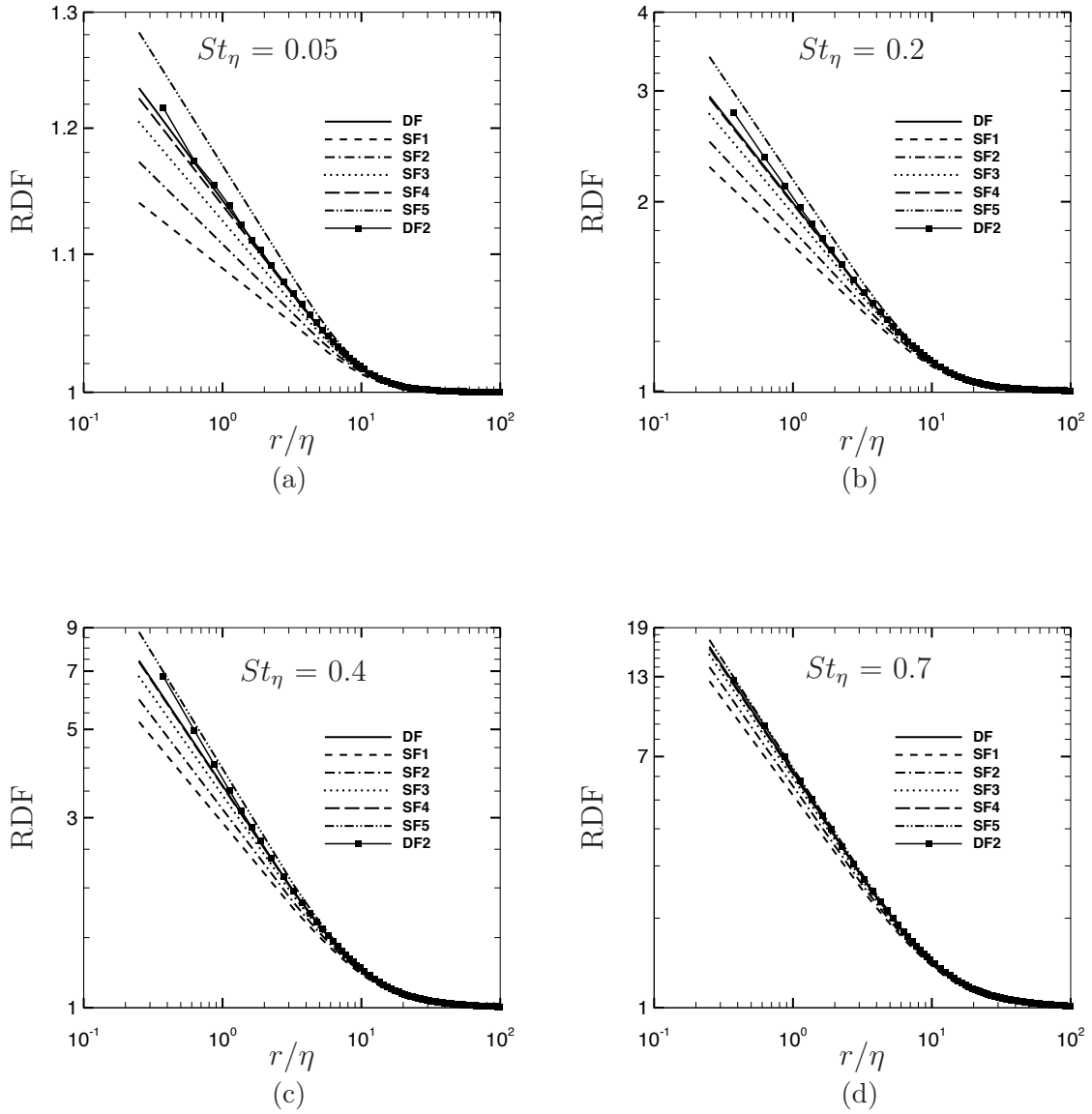


Figure 4.4: RDFs from stochastic (SF1-SF5) and deterministic (DF and DF2) forcing schemes as a function of dimensionless pair separation r/η for the indicated values of St_η at $Re_\lambda = 210$.

Figure 4.2(a)-(d) indicate that the RDFs show increasing sensitivity to forcing as the Stokes number is varied from $St_\eta = 0.05$ till at least $St_\eta = 0.4$. The RDFs are affected by both the nature of forcing (DF versus SF), and the forcing parameters (SF1-SF5). The RDFs for DF and DF2 are also significantly different, with DF and DF2 forming the upper and lower extrema, at the grid size of 128^3 (or $Re_\lambda \approx 80$). Although the DF and DF2 simulations are essentially identical in terms of the numerical algorithm and the forcing scheme, there are substantial differences in their large-scale statistics. For instance, their RMS fluctuating velocities are $u_{\text{rms}} = 1.067$ and 0.914 , and the mean dissipation rates are $\langle \epsilon \rangle = 0.421$ and 0.27 , respectively. Consequently, in the $St_\eta < 1$ regime, where pair relative motion is largely determined by the Kolmogorov-scale eddies, we see the differences between the RDFs of DF and DF2. Among the five stochastic forcing cases, the SF1/SF2 and SF5 RDFs have the highest and lowest RDFs, where SF1, SF2 and SF5 correspond to the forcing time scales $T_f = 4T_E$, $2T_E$ and $T_E/4$, respectively. In general, SF3 and SF4, corresponding to $T_f = T_E$ and $T_E/2$, respectively, are quite close to each other for the four Stokes numbers shown in Figure 4.2.

In Figure 4.3, we compare the RDFs from DF with those from SF1-SF5 at $Re_\lambda \approx 131$. Also shown are the RDFs from DF2 at $Re_\lambda = 140$. The RDFs of DF are the lowest, while those of SF5 are the highest at all four Stokes numbers, although the differences between the two extrema are smaller as compared to those for $Re_\lambda \approx 80$. The RDFs for the two deterministic cases again show substantial differences. Furthermore, the differences among the various RDFs seem to persist till $St_\eta = 0.4$, and decrease thereafter as the Stokes number is increased. The time

scale T_f of stochastic forcing seems to have only a marginal effect on the RDFs. The DF2 case shows good agreement with all of the stochastic cases (except for the small variation from SF5).

Analogous to Figure 4.2 and Figure 4.3, in Figure 4.4 we compare the RDFs obtained from the various forcings for $Re_\lambda = 210$ (DF2 corresponds to $Re_\lambda = 224$). The trends in the RDFs for this case present a rather interesting and clarificatory picture. First, the RDFs for DF, DF2, SF3 and SF4 are reasonably close to one another for all four Stokes numbers $St_\eta = 0.05, 0.2, 0.4$ and 0.7 . This trend may be attributed to the higher grid resolution, which yields a relatively clearer separation between the numerically forced low-wavenumber velocity components and the dissipative high-wavenumber components. Due to this scale separation, the small-scale dynamics driving the clustering of $St_\eta < 1$ particles are nearly uniform across the various cases. The RDFs of SF1 and SF5 with $T_f = 4T_E$ and $T_E/4$ form the lower and upper bounds, where as those of SF2-SF4 are in reasonable agreement with the DF and DF2 results. This suggests that stochastic forcing with artificially high/low forcing time scales may result in seemingly unphysical trends in the particle clustering statistics.

We now discuss the clustering behavior of $St_\eta \geq 1$ particles. In Figure 4.5, we compare the RDFs of the various forcing cases for $St_\eta = 1, 2, 4$ and 10 at $Re_\lambda = 80$. For $St_\eta = 1$, the RDFs of DF, DF2, SF3 and SF4 are in reasonable agreement. For $St_\eta = 2$ and 4 , we notice that SF5 shows significant deviations from the other RDFs. At $St_\eta = 2$, except for SF5, the other RDFs are close to one another, but at $St_\eta = 4$, we see some differences among the DF and SF cases. For $St_\eta = 10$, DF and DF2 have

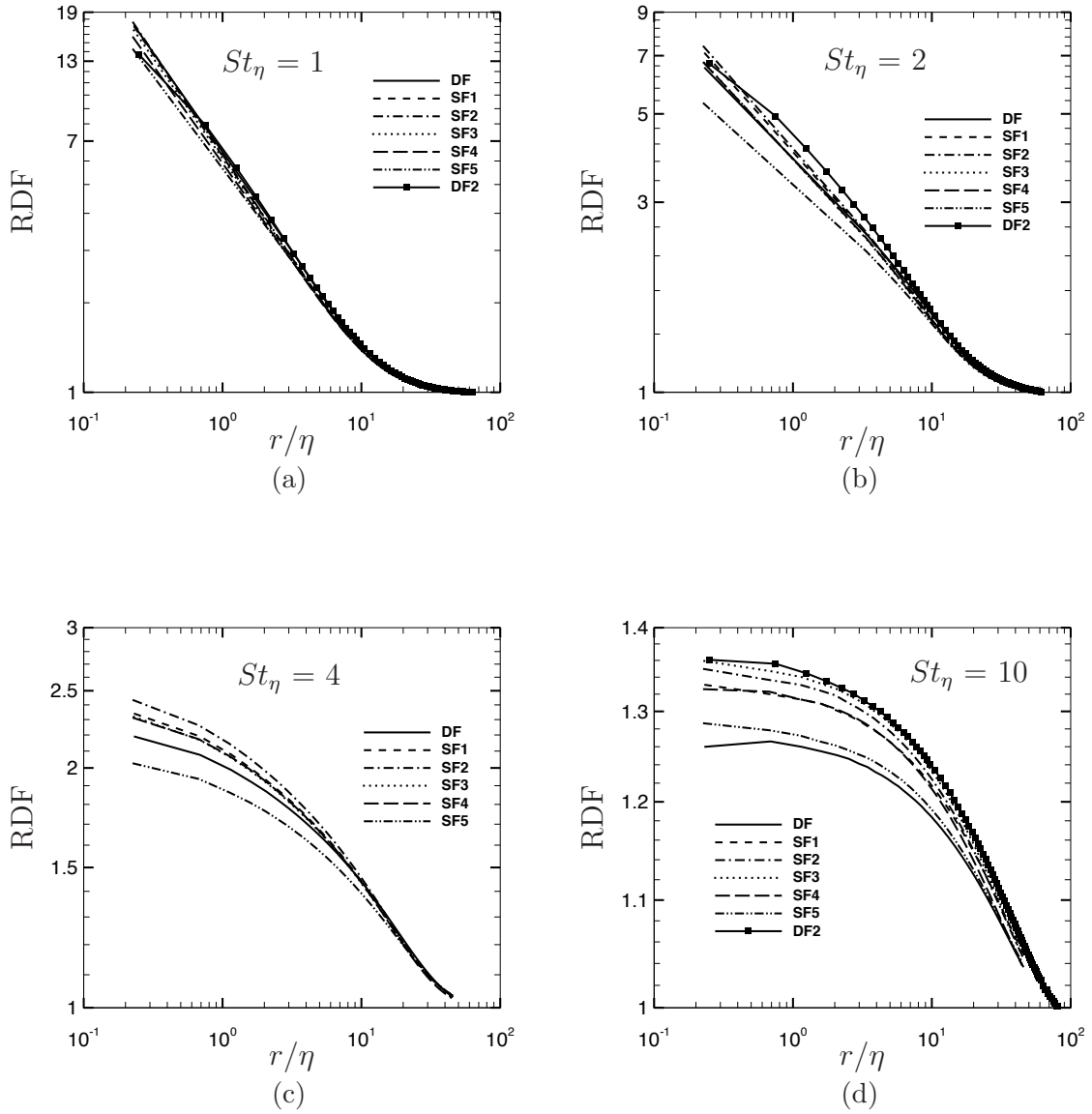


Figure 4.5: RDFs from stochastic (SF1-SF5) and deterministic (DF and DF2) forcing schemes as a function of dimensionless pair separation r/η for the indicated values of St_η at $Re_\lambda = 80$. DF2 data is not available for $St_\eta = 4$ in (c).

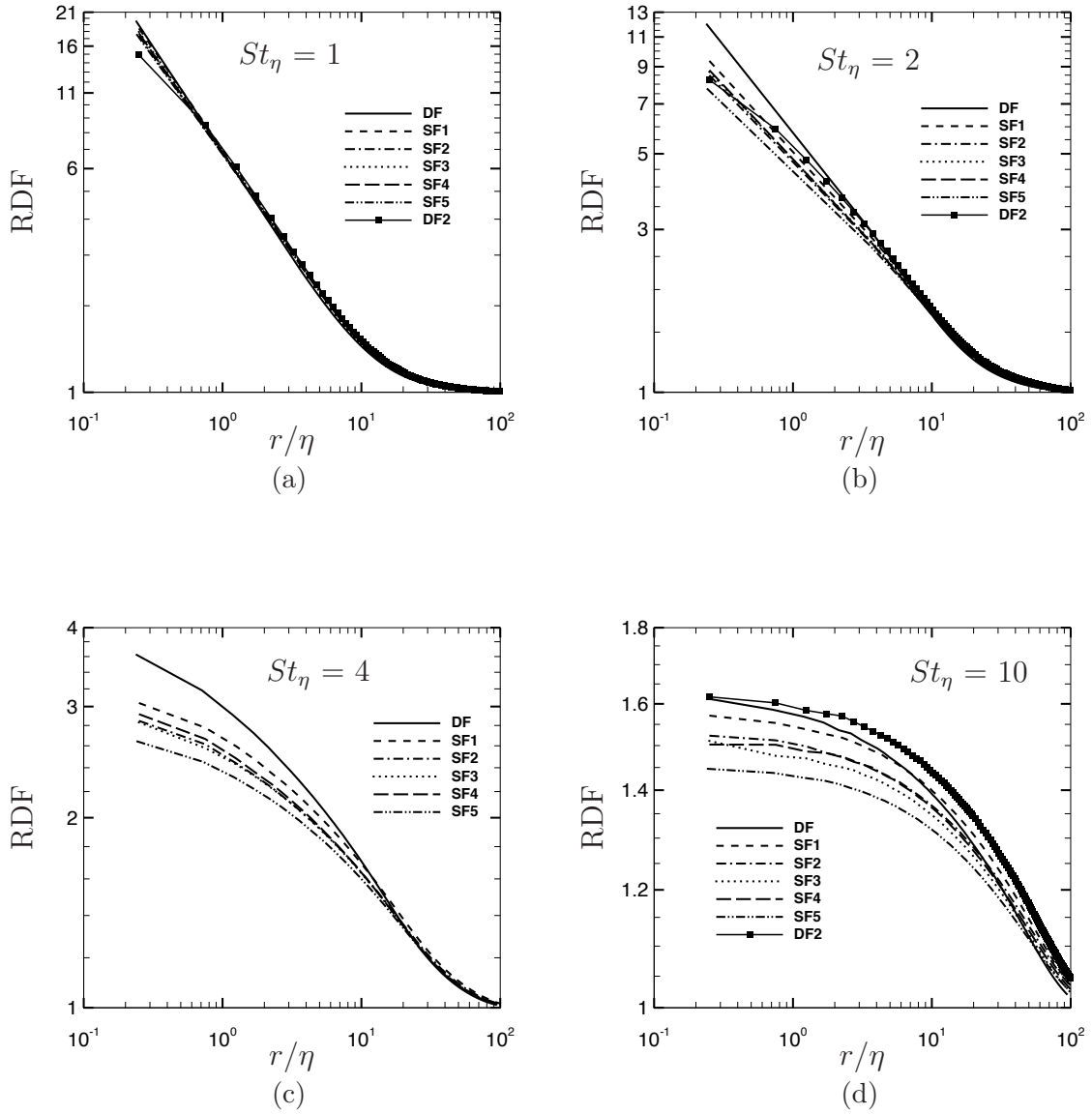


Figure 4.6: RDFs from stochastic (SF1-SF5) and deterministic (DF and DF2) forcing schemes as a function of dimensionless pair separation r/η for the indicated values of St_η at $Re_\lambda = 131$. DF2 data is not available for $St_\eta = 4$ in (c).

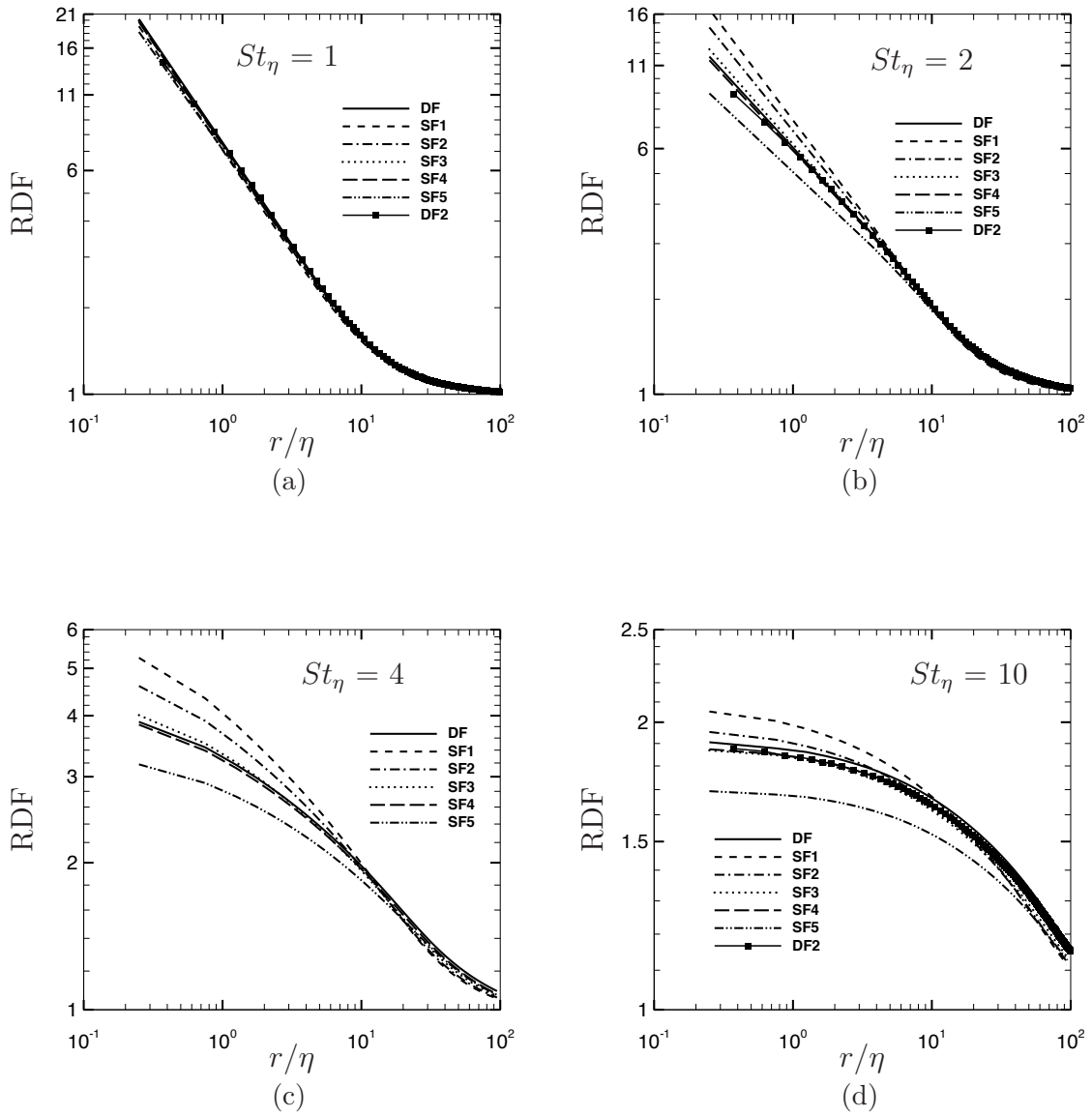


Figure 4.7: RDFs from stochastic (SF1-SF5) and deterministic (DF and DF2) forcing schemes as a function of dimensionless pair separation r/η for the indicated values of St_η at $Re_\lambda = 210$. DF2 data is not available for $St_\eta = 4$ in (c).

the lowest and highest RDFs, respectively, although the overall difference between them is less than 10%. The general conclusion here is that forcing has a smaller effect on the clustering of $St_\eta \geq 1$ particles than on the clustering of $St_\eta < 1$ particles at $Re_\lambda = 80$.

In Figure 4.6, we consider the dependence of the RDFs on forcing for $St_\eta \geq 1$ particles at $Re_\lambda = 131$. Figure 4.6(a) shows that the RDFs at $St_\eta = 1$ are essentially independent of forcing. For $St_\eta = 2$, shown in Figure 4.6(b), the RDF of DF is higher than the rest, which is also the case for $St_\eta = 4$. However, for $St_\eta = 2$, DF2 is in reasonable agreement with the stochastic forcing cases (DF2 data not available for $St_\eta = 4$). At $St_\eta = 10$, shown in Figure 4.6(d), we see that there is good agreement among the RDFs of DF, DF2, SF3, and SF4. At all Stokes numbers, SF5 forms the lower bound of the RDFs, again indicating that the forcing time scale of $T_f = T_E/4$ is artificially low.

Figure 4.7 shows the effects of forcing on the RDFs of $St_\eta \geq 1$ particles at $Re_\lambda = 210$. Again, we notice that forcing has virtually no impact on the RDFs at $St_\eta = 1$. For $St_\eta = 2, 4$ and 10 , SF1 and SF5 consistently form the upper and lower bounds of the RDFs. We also see that there is good agreement among the RDFs of DF, DF2, SF3, and SF4 at all Stokes numbers. The inference one may draw from these trends is that at higher Re_λ , where well-defined energy-containing, inertial, and viscous ranges of turbulence exist, the nature of forcing and the forcing parameters (within some constraints) do not unduly influence the clustering behavior of $St_\eta \geq 1$ particles.

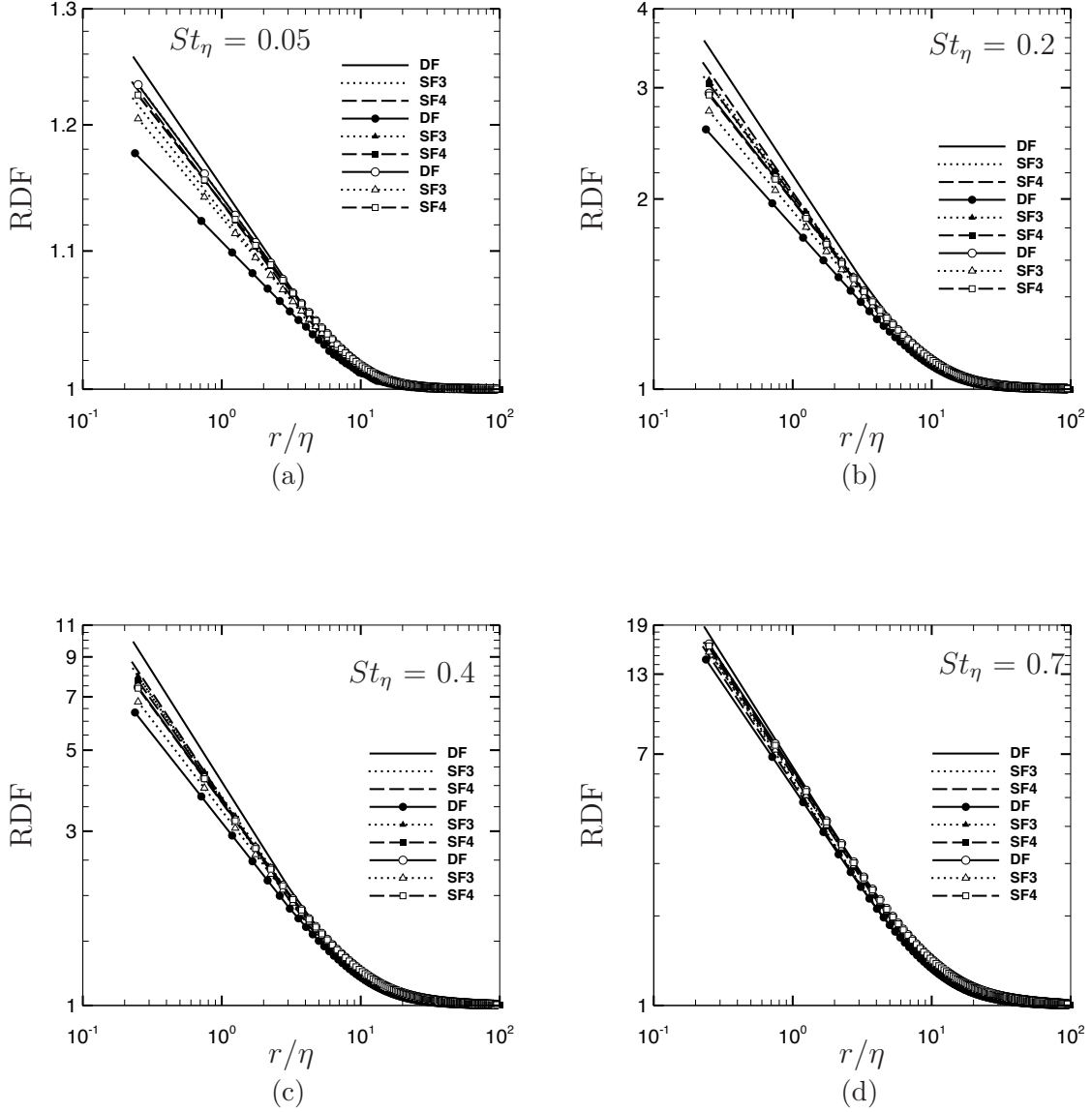


Figure 4.8: RDFs as a function of dimensionless pair separation r/η for the indicated values of St_η . DF, SF3, and SF4 are compared. Curves without symbols correspond to $Re_\lambda = 80$ data, filled and open symbols correspond to $Re_\lambda = 131$ and 210 data, respectively.

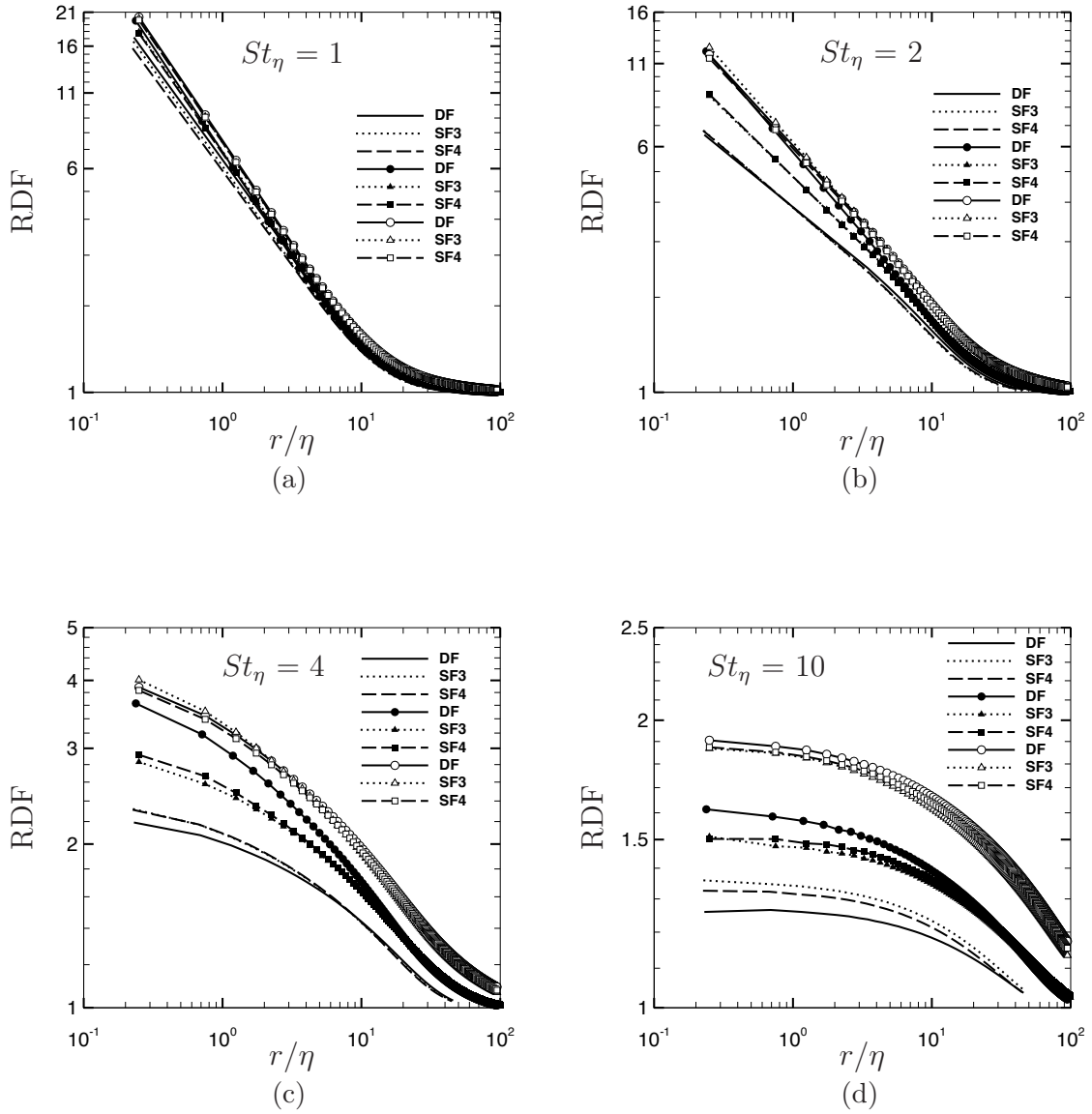


Figure 4.9: RDFs as a function of dimensionless pair separation r/η for the indicated values of St_η . DF, SF3, and SF4 are compared. Curves without symbols correspond to $Re_\lambda = 80$, filled and open symbols correspond to $Re_\lambda = 131$ and 210 data respectively.

Next, we focus on the impact of Re_λ variation on the clustering of $St_\eta < 1$ particles first, and of $St_\eta \geq 1$ particles thereafter. In Figure 4.8, we illustrate the effects of Re_λ on the RDFs for $St_\eta < 1$ particles. The RDFs of only three forcing cases—DF, SF3 and SF4—are compared at the three values of Re_λ . The corresponding DF2 results are not shown since Ireland et al. [39] concluded that the RDFs were only weakly sensitive to the Reynolds number for Re_λ up to 600. Let us focus first on the trends with regard to the current DF. At all Stokes numbers, we see that the RDFs of DF decrease with the increase in Re_λ from 80 to 131. However, when going from $Re_\lambda = 131$ to 210, the RDFs of DF increase, but are still smaller than the respective RDFs at $Re_\lambda = 80$. As compared to DF, the RDFs of SF3 and SF4 show lesser sensitivity to an increase in Re_λ . It is clear from Figure 4.8 that the Re_λ effects on the RDF are not insignificant as seen in Ireland et al. [39]. As already discussed, the differences between the two studies may be because Ireland et al. [39] explicitly maintained a number of large- and small-scale turbulence statistics constant when increasing Re_λ , whereas we make no such effort.

The corresponding plots for $St_\eta \geq 1$ are shown in Figure 4.9. Firstly, at $St_\eta = 1$, we can see from Figure 4.9(a) that the Re_λ variation has a relatively weak impact on the RDFs of all three forcings. However, at $St_\eta = 2$, we see that the RDFs increase for all three forcings as we increase Re_λ from 80 to 131. This increase is the highest for DF. With a further increase in Re_λ from 131 to 210, the DF case is not significantly affected, but the RDFs of SF3 and SF4 are again augmented. From Figure 4.9(c) and (d), we see that the RDFs increase monotonically with Re_λ for $St_\eta = 4$, and more so for $St_\eta = 10$. These trends, particularly those for $St_\eta = 4, 10$

are consistent with the results of Ireland et al. [39]. At these high Stokes numbers, particle response times are in the inertial subrange, which means that their relative motion is most responsive to the inertial eddies. As a result, the RDFs begin to plateau earlier, i.e. at higher r , than the RDFs for smaller Stokes numbers.

The Reynolds number effects on clustering may be further illustrated by plotting the RDFs as a function of St_η at four separations $r/\eta = 0.25, 4, 10$ and 20 , as shown in Figure 4.10. The dependence of RDFs on Re_λ is particularly discernible for both higher Stokes numbers and larger separations. In Figure 4.10(d), we notice that for $St_\eta < 1$, the RDFs are not sensitive to the change in Re_λ from 80 to 131, but then show a clear increase for $Re_\lambda = 210$. At all four separations, the RDFs for $St_\eta > 1$ particles show greater sensitivity to an increase in Re_λ than those for $St_\eta < 1$ particles. Further, the Re_λ dependence of RDFs for $St_\eta > 1$ is augmented as the separation increases. These trends are along expected lines, since at higher Reynolds numbers, there is clearer separation between the energy-containing and energy-dissipating turbulent scales, i.e., the inertial subrange becomes more distinct as Re_λ increases. As a result, particles with relaxation times of the order of inertial time scales respond to these eddies and show increased clustering with Re_λ at these separations.

In Figure 4.11, we plot the RDFs as a function of St_η at four separations $r/\eta = 0.25, 4, 10$ and 20 for $Re_\lambda = 210$. The RDFs are shown for DF and SF1-SF5. We see that at the smallest separation, the maximum RDF occurs at $St_\eta = 1.0$. As the separation is increased, the RDF peaks at progressively higher St_η . Thus, for $r/\eta = 4$ and 10 , the RDF peaks at $St_\eta \approx 2.0$ and 4.0 , respectively. For $r/\eta = 20$,

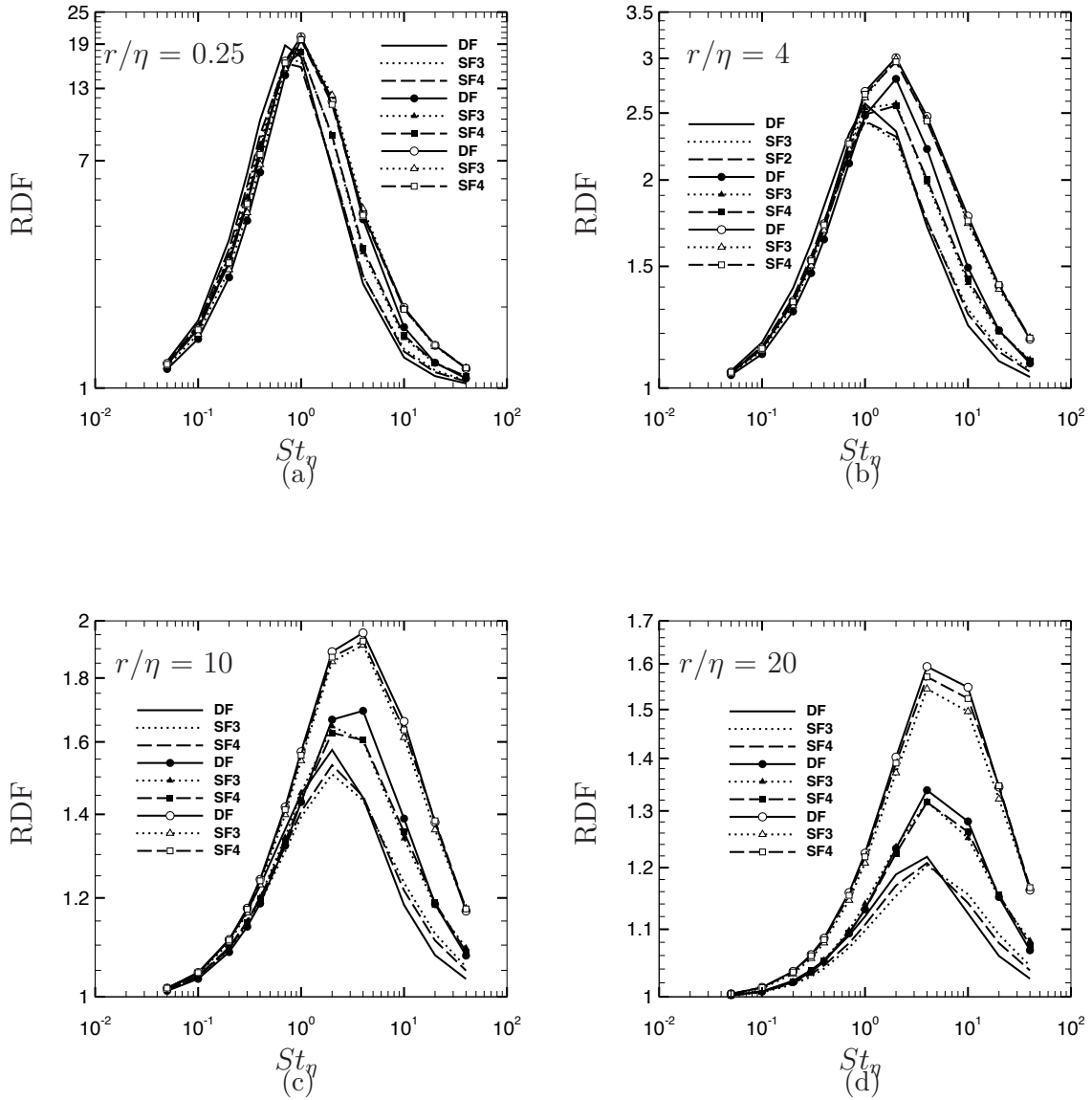


Figure 4.10: RDFs versus St_η at the indicated pair separations. DF, SF3, and SF4 are compared. Curves without symbols correspond to $Re_\lambda = 80$ data, filled and open symbols correspond to $Re_\lambda = 131$ and 210 data, respectively.

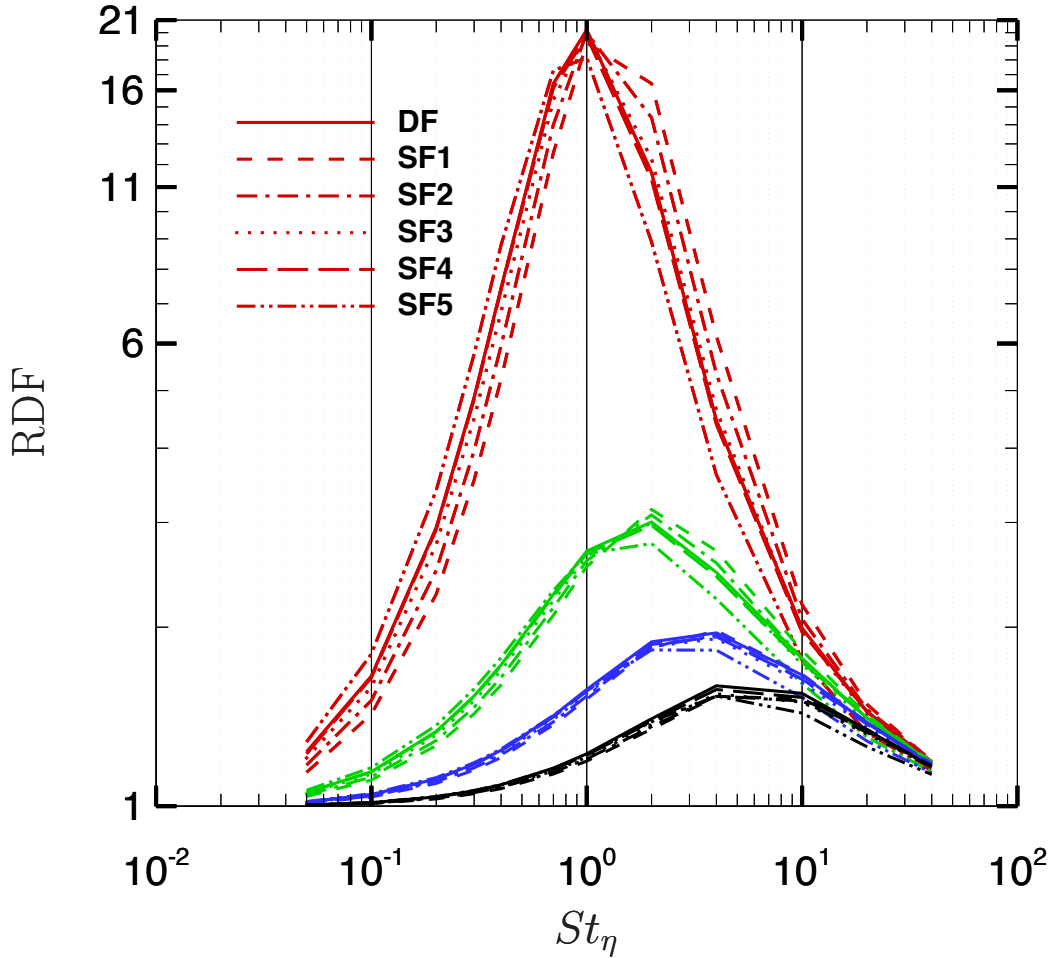


Figure 4.11: RDF versus St_η at $Re_\lambda = 210$. DF, SF1, SF2, SF3, SF4, and SF5 results are compared. Red, green, blue and black curves correspond to separation of $r = 0.25\eta$, $r = 4\eta$, $r = 10\eta$ and $r = 20\eta$, respectively.

the maximum RDF occurs in the $St_\eta \sim 4-10$ range. This is consistent with our earlier observation that at higher Stokes numbers, the particles are more responsive to inertial-scale eddies, so that they show maximum clustering at separations lying in the inertial subrange.

4.4.2 Variance of Radial Relative Velocities

In this section, we discuss the effects of forcing, Reynolds number and Stokes number on the variance $\langle U_r^2 \rangle$, where $U_r = \mathbf{U} \cdot \mathbf{r}/r$ is the radial relative velocity, and \mathbf{U} and \mathbf{r} are the relative velocity and separation vectors, respectively. Following the approach adopted for the RDF discussion, we will first present the variances for the $St_\eta < 1$ particles, and subsequently for the $St_\eta \geq 1$ particles.

Figure 4.12 plots $\langle U_r^2 \rangle$ as a function of pair separation r/η for $St_\eta < 1$ at $Re_\lambda = 80$. For the $St_\eta = 0.05$ and 0.2 particles, $\langle U_r^2 \rangle$ follows an r^2 scaling for separations ranging from $r < \eta$ to those nearly as large as $6-8\eta$. This behavior is consistent with earlier observations based on DNS of isotropic turbulence [40] that the fluid velocity variance followed the dissipation-range scaling for separations $r \leq 10\eta$. Similar scaling behavior for the low St_η particles was also seen in Ireland et al. [39]. The r^2 scaling is to be expected for small St_η since these particles only deviate marginally from fluid particles whose relative velocities are known to have an r^2 scaling in the dissipation range [67]. However, for $St_\eta \geq 0.4$, we see a deviation away from this behavior, which is manifested as higher variances for separations $r \lesssim \eta$. The higher relative velocities at small separations may be attributed to a “bifurcation” in the mechanism responsible for the radially inward drift of particle pairs. The bifurcation involves a shift from the local centrifuge mechanism that drives the drift when $St_\eta < 1$ [18] to the non-local, path-history symmetry breaking mechanism [9, 10, 11] that is dominant when $St_\eta \geq 1$. That is, with an increase in Stokes number, particle pairs retain greater memory of their interactions with the

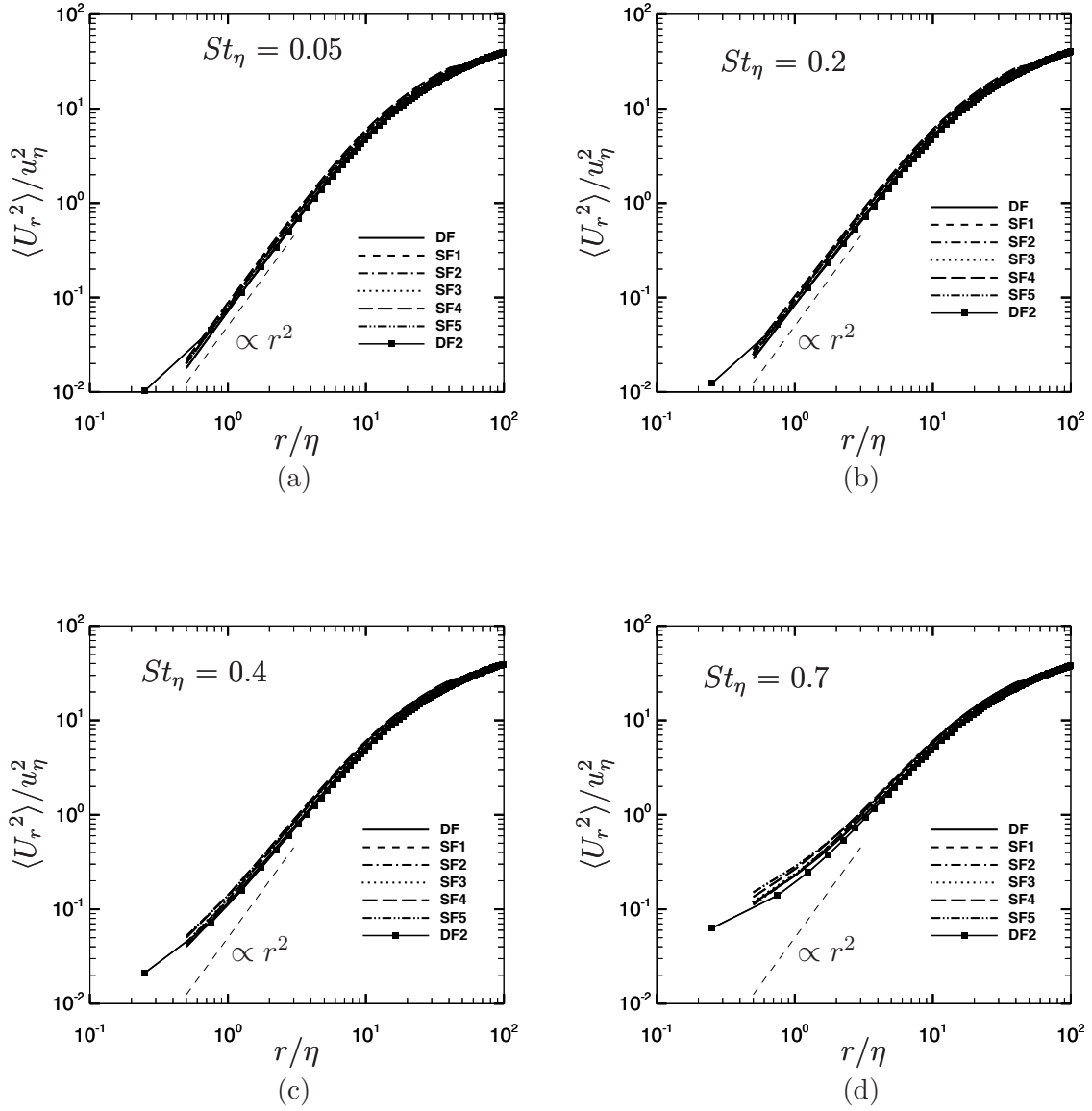


Figure 4.12: $\langle U_r^2 \rangle / u_\eta^2$ from stochastic (SF1-SF5) and deterministic (DF and DF2) forcing schemes as a function of r/η for the indicated values of St_η at $Re_\lambda = 80$.

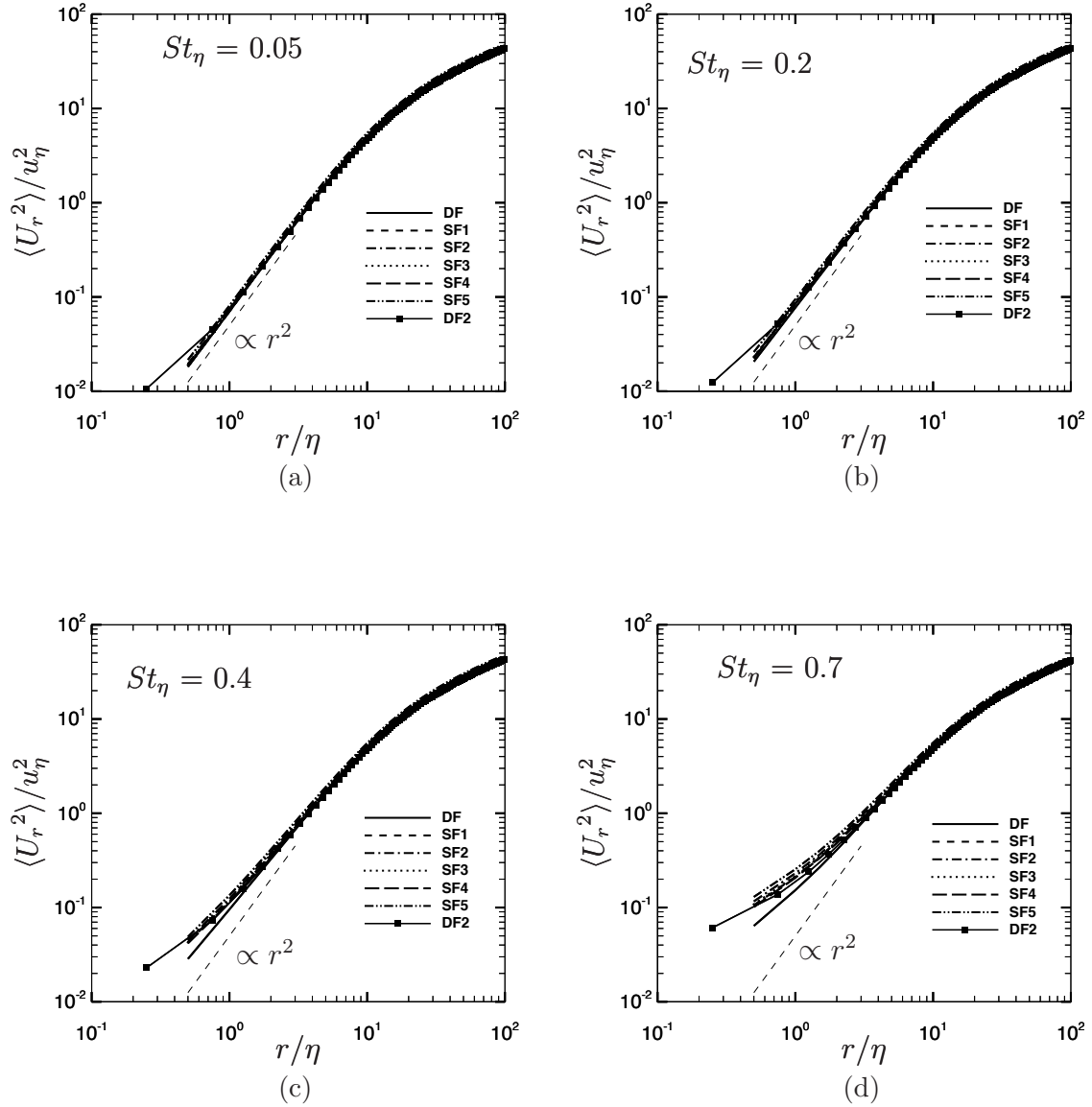


Figure 4.13: $\langle U_r^2 \rangle / u_\eta^2$ from stochastic (SF1-SF5) and deterministic (DF and DF2) forcing schemes as a function of r/η for the indicated values of St_η at $Re_\lambda = 131$.

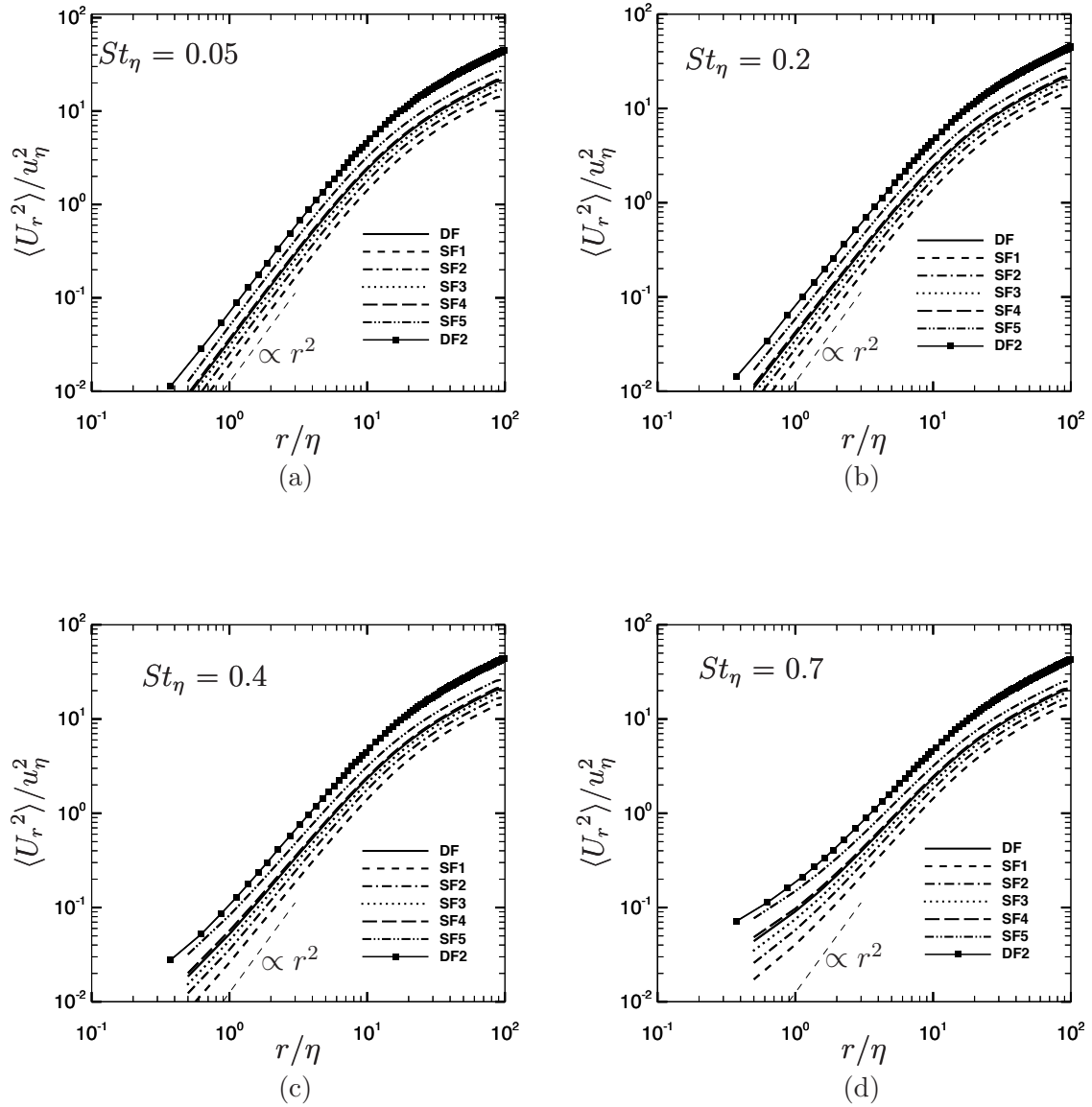


Figure 4.14: $\langle U_r^2 \rangle / u_\eta^2$ from stochastic (SF1-SF5) and deterministic (DF and DF2) forcing schemes as a function of r/η for the indicated values of St_η at $Re_\lambda = 210$.

turbulence at larger separations, where their relative motion was driven by (more energetic) eddies whose size scaled with the pair separation. One also notices that the variances show a rather weak sensitivity to forcing. For $St_\eta = 0.7$, we see that SF5 leads to marginally higher variances, which may be an artifact of the low forcing time scale for this case. The above trends at $Re_\lambda = 80$ are more or less repeated for $Re_\lambda = 131$, as shown in Figure 4.13.

Variances $\langle U_r^2 \rangle$ as a function of r/η for $St_\eta < 1.0$ at $Re_\lambda = 210$ are shown in Figure 4.14. The effects of forcing on $\langle U_r^2 \rangle$ are far more discernible here than at the two lower Re_λ . For all Stokes numbers, the variances for the deterministic forcing case DF2 of Ireland et al. [39] are higher than the variances of DF and SF1-SF5. But, SF3 and SF4 are in good agreement with DF, where as SF5 and SF1 form the upper and lower bounds for the six cases simulated in this study. We again notice that the variances for $St_\eta = 0.05$ and 0.2 show an r^2 scaling in the dissipation range. We will revisit the differences between DF2 and the current cases in a subsequent discussion of the effects of Re_λ on the variances.

Having considered the effects of forcing on the variances at low Stokes numbers, we now turn our attention to the high Stokes number particles. Figure 4.15 shows $\langle U_r^2 \rangle$ as a function of pair separation for the $St_\eta \geq 1$ particles at $Re_\lambda = 80$. In general, when $St_\eta \geq 1$, forcing has a more significant effect on $\langle U_r^2 \rangle$ as compared to that seen for $St_\eta < 1$. For separations $r \lesssim 6-8\eta$ and $St_\eta = 1$ and 2 , the DF2 variances are smaller than the variances for DF, as well as SF1-SF5. But for $St_\eta = 10$, the DF2 variances are in good agreement with the DF, SF1 and SF4 variances. Further, for $St_\eta = 1, 2$ and 4 , the variances for SF2 and SF5 form the lower and upper bounds

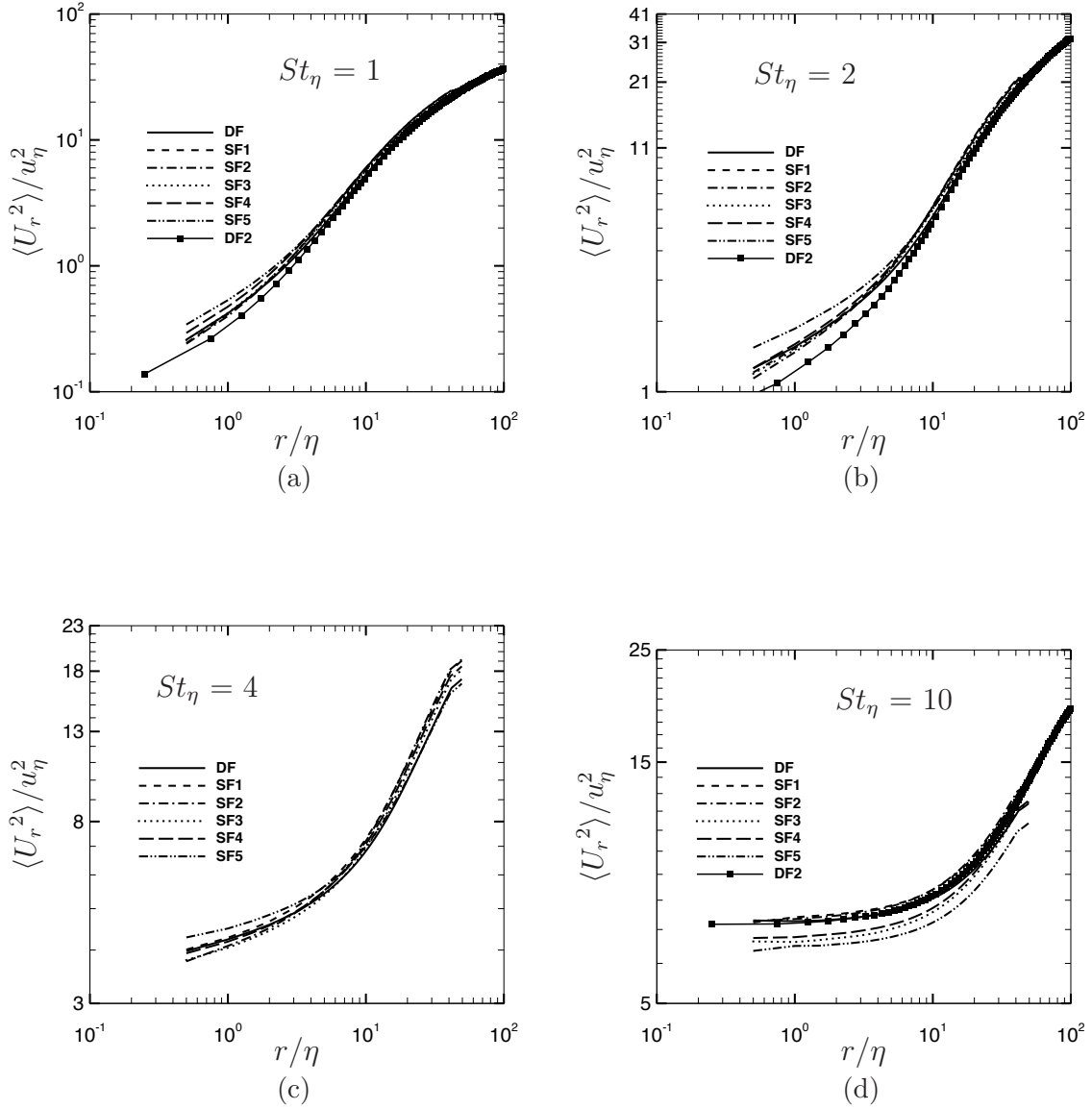


Figure 4.15: $\langle U_r^2 \rangle / u_\eta^2$ from stochastic (SF1-SF5) and deterministic (DF and DF2) forcing schemes as a function of r/η for the indicated values of St_η at $Re_\lambda = 80$. DF2 data is not available for $St_\eta = 4$ in (c).

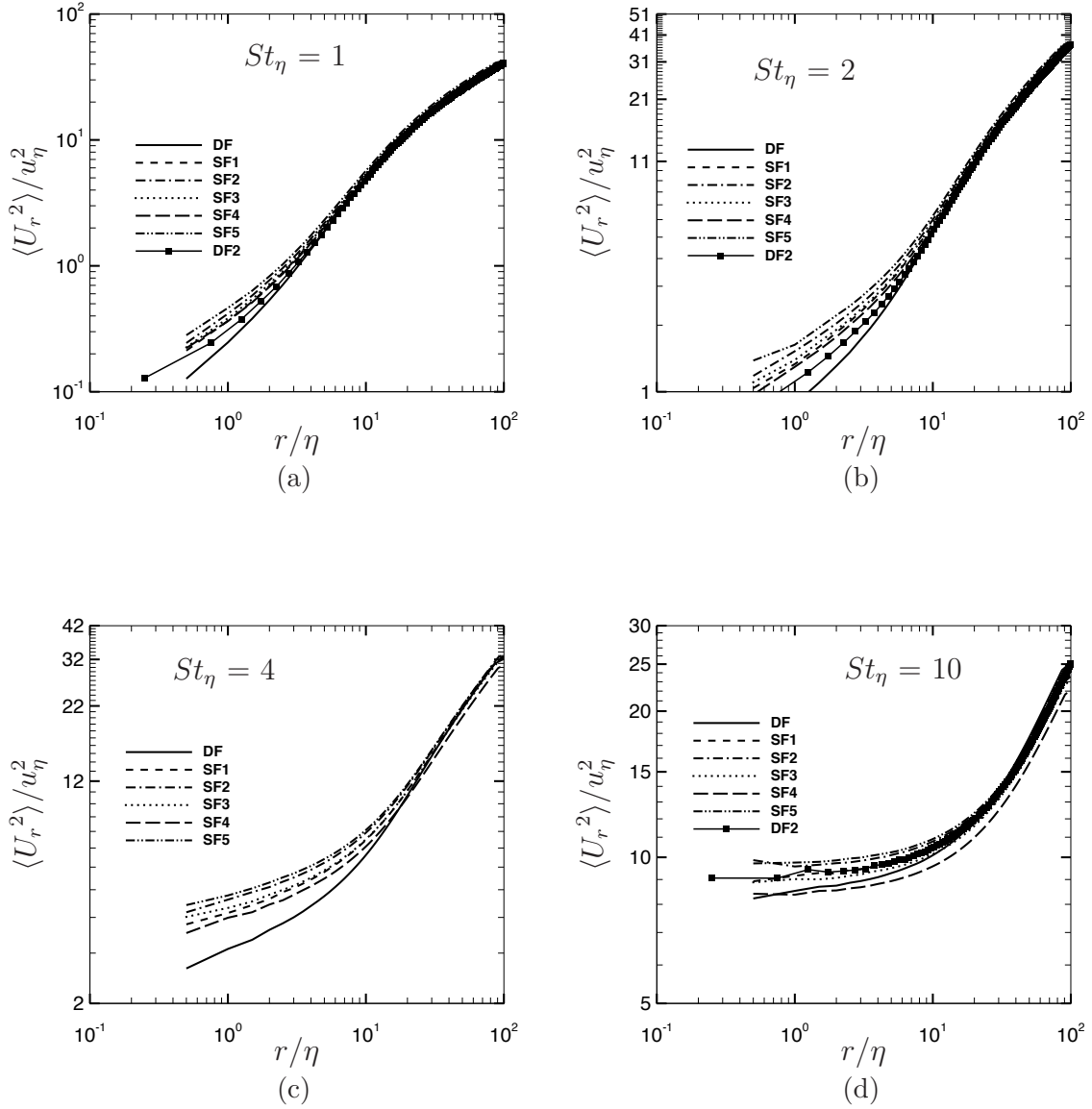


Figure 4.16: $\langle U_r^2 \rangle / u_\eta^2$ from stochastic (SF1-SF5) and deterministic (DF and DF2) forcing schemes as a function of r/η for the indicated values of St_η at $Re_\lambda = 131$. DF2 data is not available for $St_\eta = 4$ in (c).

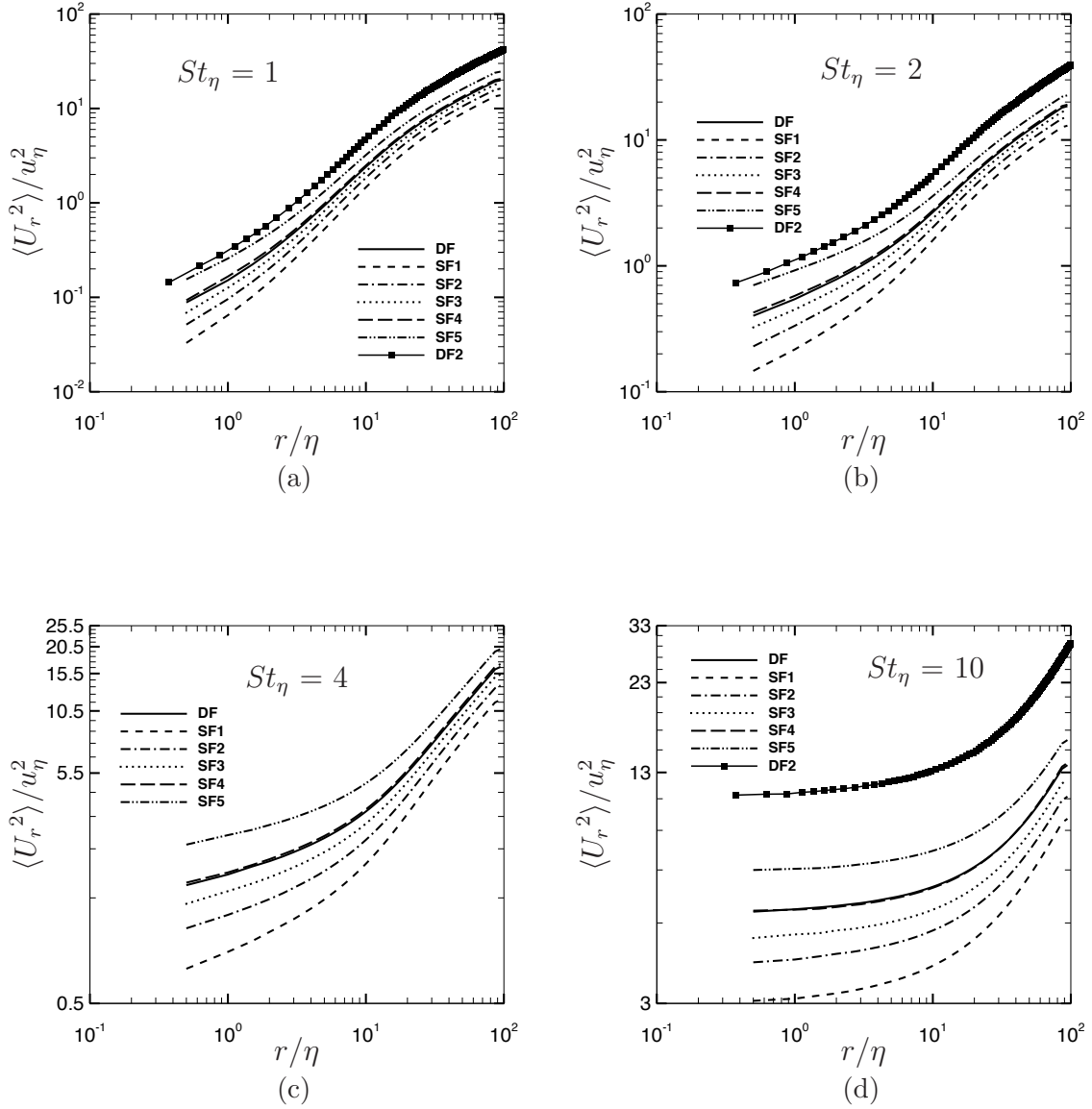


Figure 4.17: $\langle U_r^2 \rangle / u_\eta^2$ from stochastic (SF1-SF5) and deterministic (DF and DF2) forcing schemes as a function of r/η for the indicated values of St_η at $Re_\lambda = 210$. DF2 data is not available for $St_\eta = 4$ in (c).

of the six cases considered in this study. For the $St_\eta = 10$ particles, the variances are nearly independent of separation for $r \lesssim \eta$, indicating that the relative velocities of these particles are not affected by the small-scale eddies and that they undergo ballistic motion in the dissipative regime.

The variances for the $St_\eta \geq 1$ particles at $Re_\lambda = 131$ are shown in Figure 4.16. It is seen that the variances show increased sensitivity to forcing, as Re_λ is augmented from 80 to 131. For $St_\eta = 1, 2$ and 10, DF and DF2 are in reasonable agreement, although DF2 slightly overpredicts DF for smaller r (note that DF2 data is not available for $St_\eta = 4$). At all Stokes numbers except $St_\eta = 10$ and at separations $r \lesssim 10\eta$, the variances for SF1-SF5 are all higher than those for DF.

As can be seen in Figure 4.17, the effects of forcing on the variances are further amplified at $Re_\lambda = 210$. We see that at all Stokes numbers (except $St_\eta = 4$), the DF2 variances are higher than the variances for all six forcing cases considered in this study (note that DF2 data is not available for $St_\eta = 4$). This behavior of DF2 from Ireland et al. [39] is surprising, particularly because the DF2 variances at the two smaller Re_λ are in reasonable agreement with the variances from at least some of the current cases. For all Stokes numbers, DF/SF4 and DF/SF3 are in excellent and reasonable agreement, respectively, while the SF5 and SF1 variances are the highest and lowest. We now examine the Re_λ dependence of $\langle U_r^2 \rangle$, first for $St_\eta < 1$ particles, and then for $St_\eta \geq 1$ particles.

The effects of Reynolds number on $\langle U_r^2 \rangle$ for the low-Stokes-number particles ($St_\eta < 1$) are shown in Figure 4.18. We only show a comparison of the DF, SF3 and SF4 forcing cases. It can be seen that the change in Re_λ from 80 to 131 has only a weak

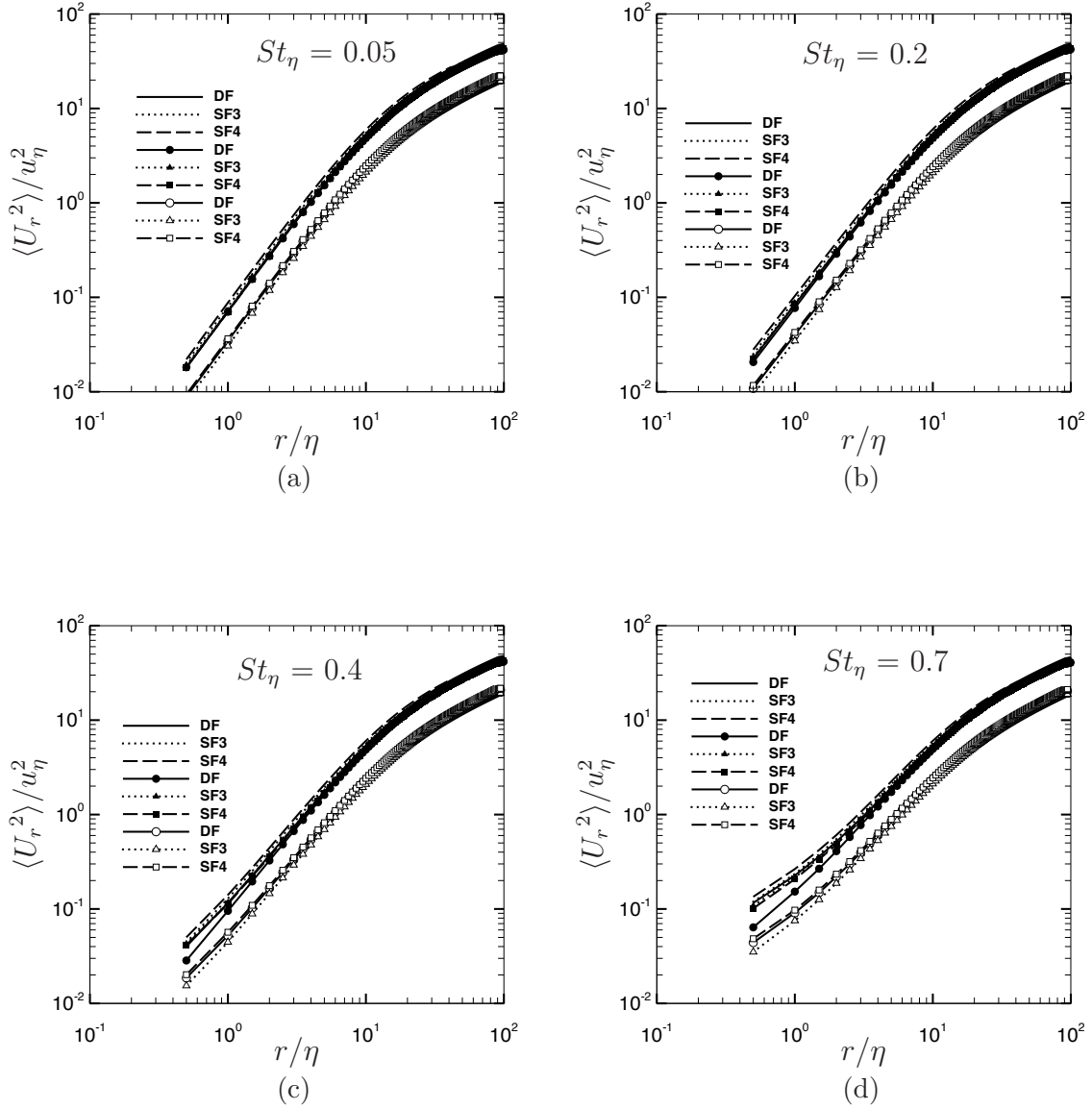


Figure 4.18: $\langle U_r^2 \rangle / u_\eta^2$ as a function of r/η for the indicated values of St_η . DF, SF3, and SF4 are compared. Curves without symbols correspond to $Re_\lambda = 80$ data, filled and open symbols correspond to $Re_\lambda = 131$ and 210 data, respectively.

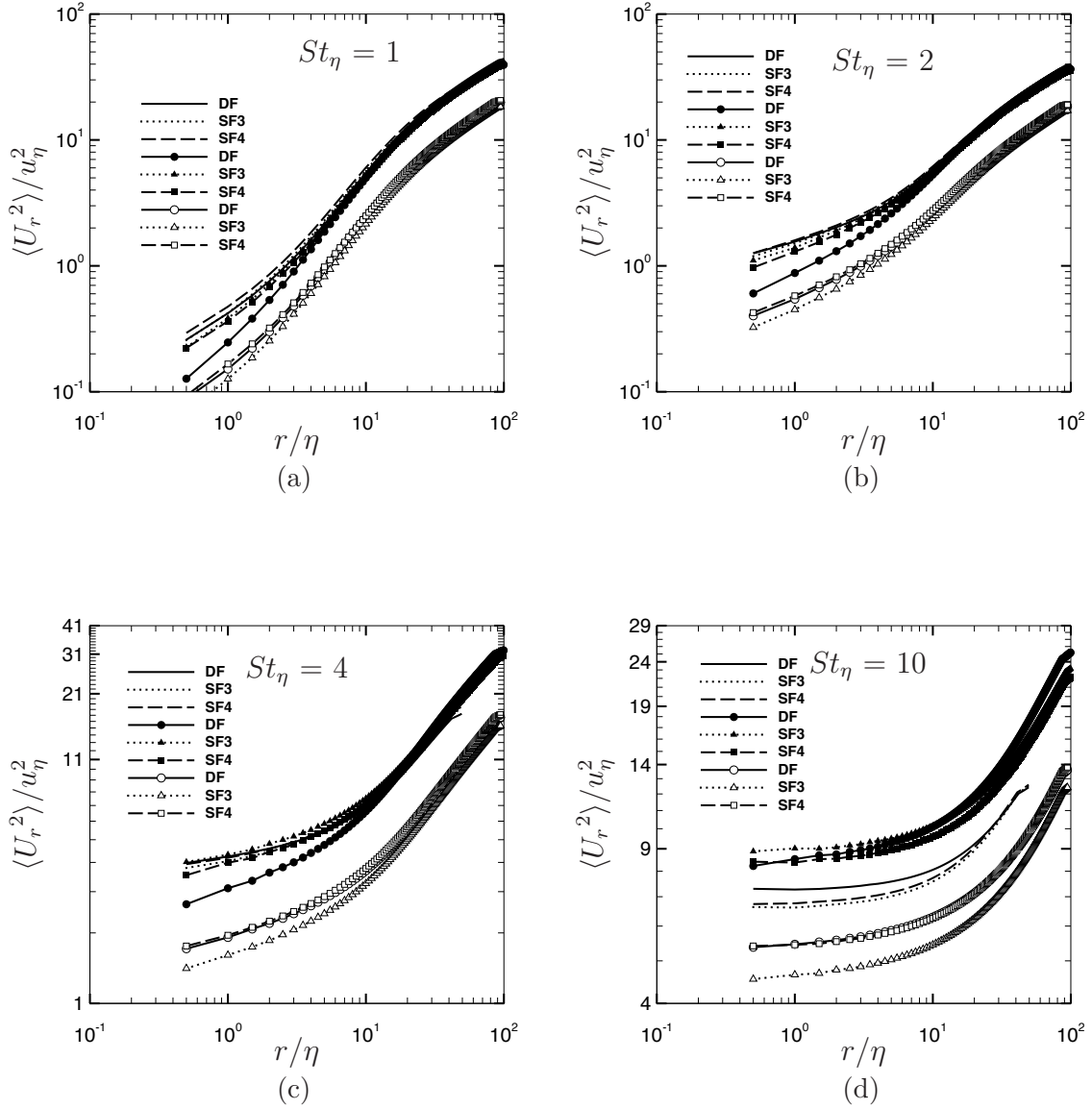


Figure 4.19: $\langle U_r^2 \rangle / u_\eta^2$ as a function of r/η for the indicated values of St_η . DF, SF3, and SF4 are compared. Curves without symbols correspond to $Re_\lambda = 80$ data, filled and open symbols correspond to $Re_\lambda = 131$ and 210 data, respectively.

effect on the variances for the three forcings shown. However, the increase in Re_λ from 131 to 210 leads to a decrease in the variances at all four St_η . The corresponding plots for the $St_\eta \geq 1$ particles are shown in Figure 4.19. At $St_\eta = 1, 2,$ and $4,$ the trends are similar to those for $St_\eta < 1,$ i.e. there is only a weak dependence on Reynolds number for the two lower values of $Re_\lambda = 80$ and $131,$ but there is a significant decrease in variances with further increase in Re_λ to $210.$ However, at smaller separations, the DF variances do show a decrease going from $Re_\lambda = 80$ to $131.$ For the $St_\eta = 10$ particles, we observe that the variances increase as Re_λ is increased from 80 to $131,$ but then decrease as Re_λ is increased from 131 to $210.$ Figure 4.19 also shows us that, in general, the DF, SF3 and SF4 variances are in reasonable agreement for all four Stokes numbers and the three Reynolds numbers. For $St_\eta = 10$ and $Re_\lambda = 210,$ however, SF3 variances are smaller than those of both DF and SF4.

We will now discuss the effects of separation r on the variance $\langle U_r^2 \rangle,$ while simultaneously focusing on the differences arising due to different forcings. Figure 4.20, Figure 4.21 and Figure 4.22 show $\langle U_r^2 \rangle$ as a function of St_η for $Re_\lambda = 80, 131,$ and $210,$ respectively, and at four separations ranging from the sub-Kolmogorov range to the inertial range. These plots allow us to better illustrate the effects of forcing on the variances at various separations. Figure 4.20(a)-(d) show the variances at four separations $r/\eta = 0.25, 4, 10,$ and $20,$ respectively. At $Re_\lambda = 80$ and $r/\eta = 0.25,$ shown in Figure 4.20(a), the forcing scheme has only a marginal effect on the variances at all Stokes numbers. These effects are, however, amplified at larger separations. For instance, in Figure 4.20(c) at $r/\eta = 10,$ DF underpredicts the variances of SF1-SF5 at the smaller Stokes numbers, but agrees well with variances of SF3 and SF4 at higher

Stokes numbers. At $r/\eta = 20$, SF1 and DF5 have the highest and lowest variances for $St_\eta \lesssim 2$. The general conclusion one can draw from Figure 4.20 is that at larger separations, the variances for all St_η show a reasonably strong dependence on the nature of forcing (DF versus SF), as well as the forcing time scale. Similar trends are seen at $Re_\lambda = 131$, shown in Figure 4.21. We do see, however, see an increased sensitivity to forcing at this Reynolds number.

$\langle U_r^2 \rangle$ as a function of St_η at four separations $r/\eta = 0.25, 4, 10$ and 20 , and $Re_\lambda = 210$ are shown in Figure 4.22. The effects of forcing are much more apparent at $Re_\lambda = 210$ than at the two lower Re_λ . At $r/\eta = 0.25$, DF, SF3 and SF4 are in good agreement. At all the separations, SF1 and SF5 form the lower and upper bounds of the variances, respectively. The increased dependence of variance on forcing at larger separations may be anticipated, since at these separations, pair relative motion is primarily driven by the large-scale eddies that are also most directly impacted by the forcing.

Next, we illustrate the effects of Re_λ on $\langle U_r^2 \rangle$ at the four separations under consideration. In Figure 4.23, $\langle U_r^2 \rangle$ is plotted as a function of St_η at $r/\eta = 0.25, 4, 10$ and 20 . At each separation, we compare the variances of DF, SF3 and SF4 for $Re_\lambda = 80, 131, \text{ and } 210$. The general trend here is that at the two lower values of Re_λ , the variances show weak sensitivity to the Reynolds number. However, at $Re_\lambda = 210$, the variances are smaller than those at the lower Reynolds numbers. The effects of increase in Re_λ from 131 to 210 on the variances become more prominent as the separation becomes larger. Further, at the two larger separations of $r/\eta = 10$

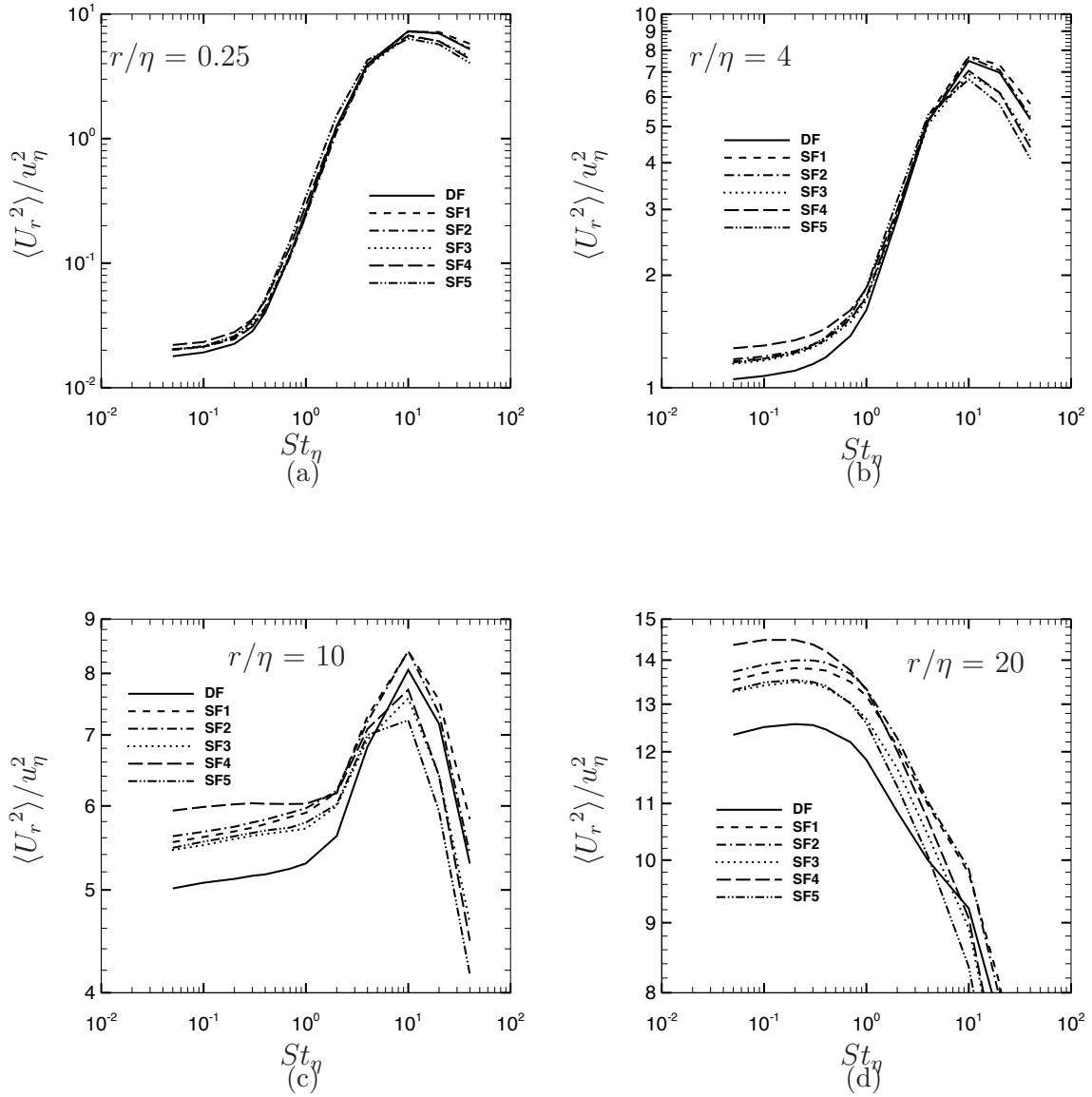


Figure 4.20: $\langle U_r^2 \rangle / u_\eta^2$ versus St_η at $Re_\lambda = 80$ and at the indicated pair separations. DF, SF1, SF2, SF3, SF4, and SF5 results are compared.

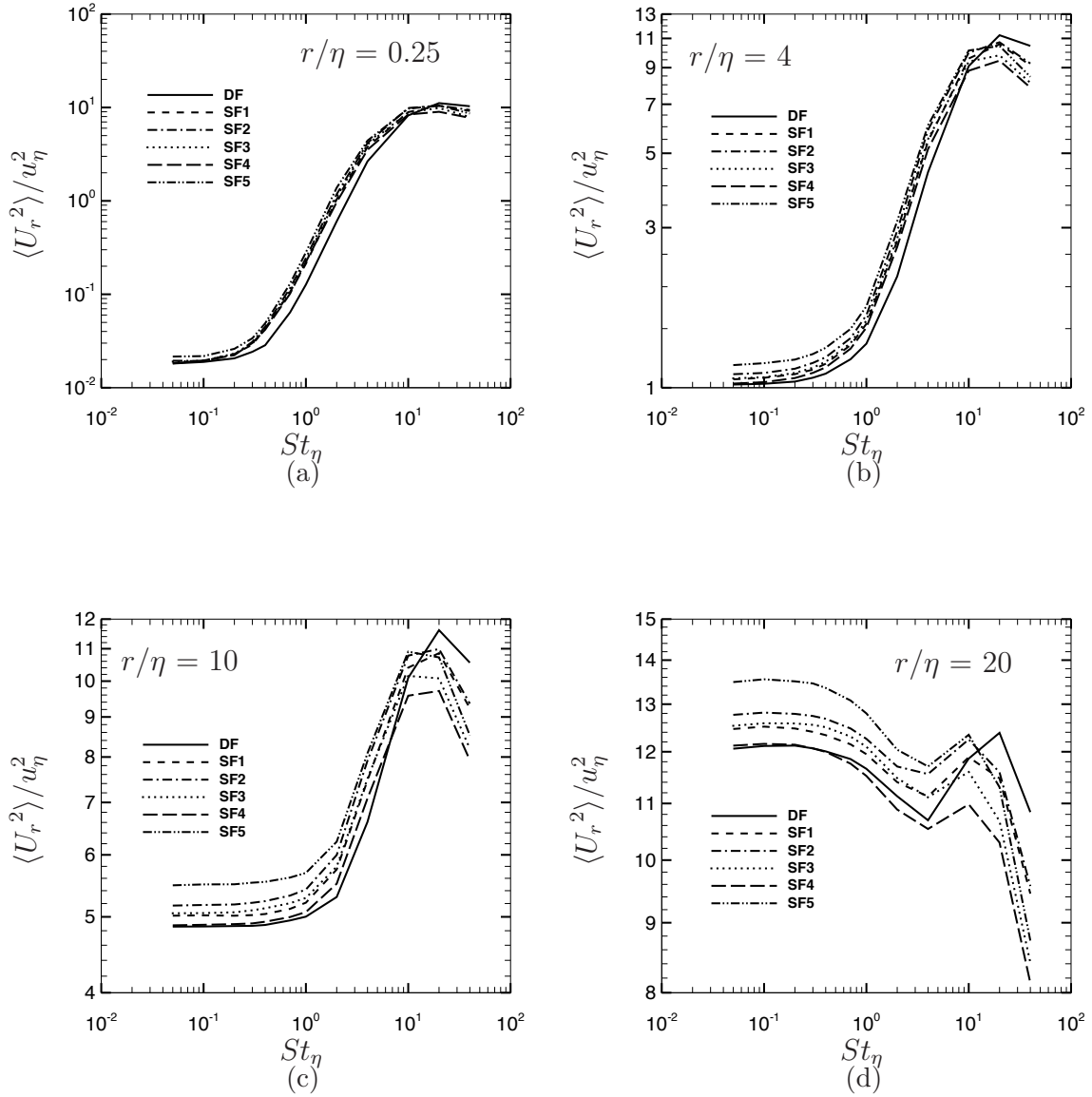


Figure 4.21: $\langle U_r^2 \rangle / u_\eta^2$ versus St_η at $Re_\lambda = 131$ simulations and at the indicated pair separations. DF, SF1, SF2, SF3, SF4, and SF5 results are compared.

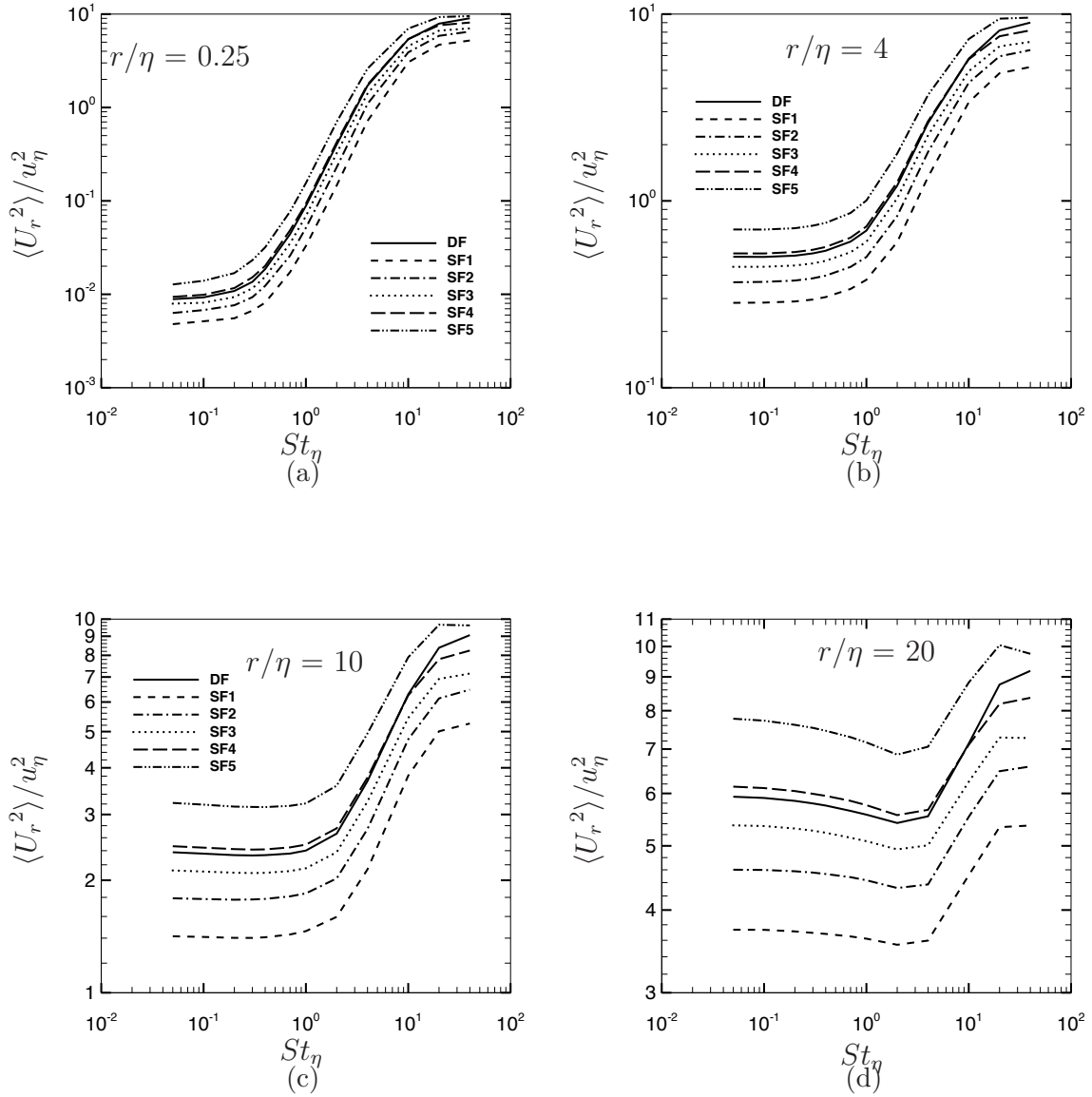


Figure 4.22: $\langle U_r^2 \rangle / u_\eta^2$ versus St_η at $Re_\lambda = 210$ simulations and at the indicated pair separations. DF, SF1, SF2, SF3, SF4, and SF5 results are compared.

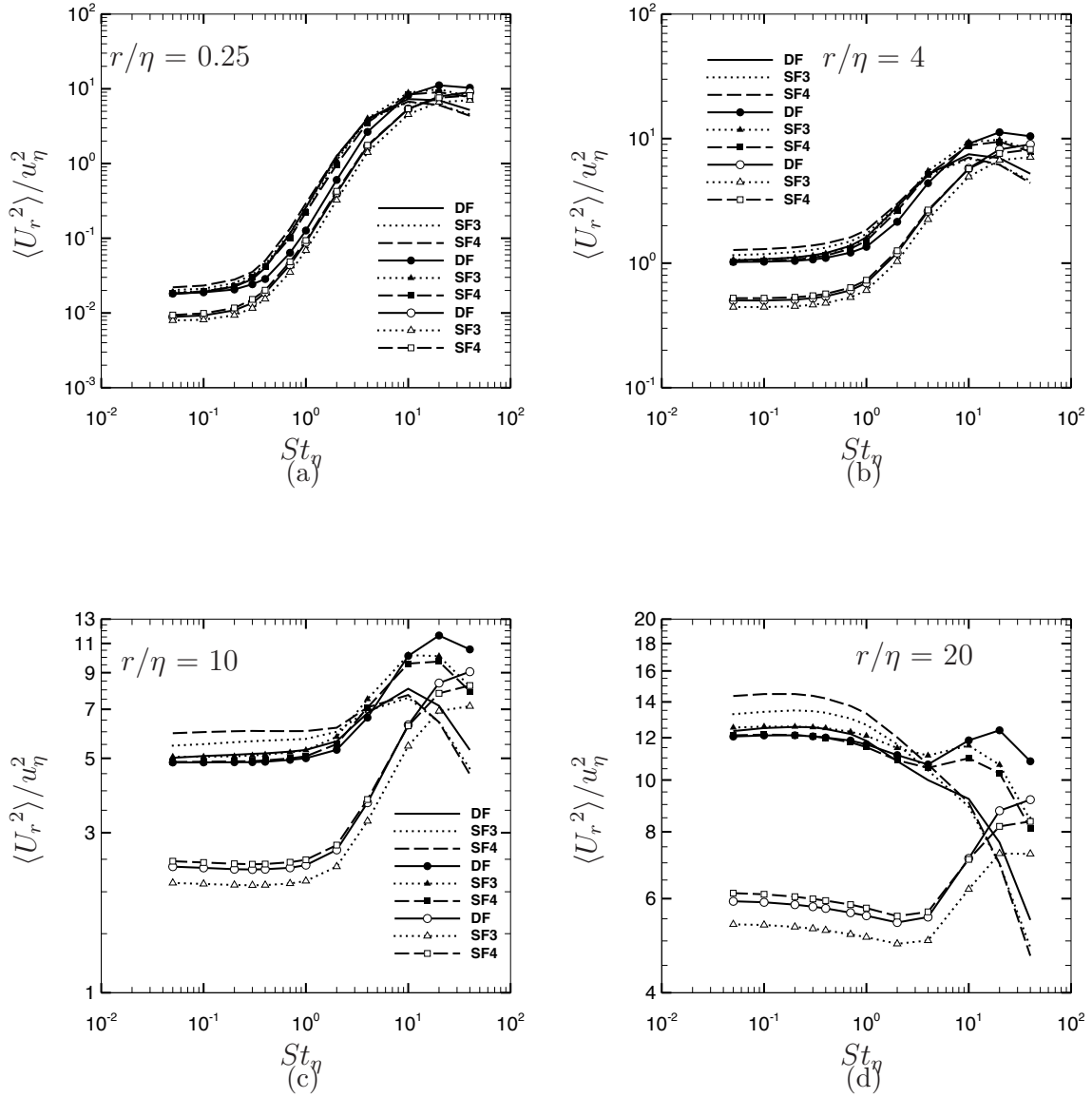


Figure 4.23: $\langle U_r^2 \rangle / u_\eta^2$ versus St_η at the indicated pair separations. DF, SF3, and SF4 are compared. Curves without symbols correspond to $Re_\lambda = 80$ data, filled and open symbols correspond to $Re_\lambda = 131$ and 210 data, respectively.

and 20, we see that for $St_\eta \gtrsim 4$, the variances do show an increase from $Re_\lambda = 80$ to 131.

The Reynolds-number-dependence of the variances in the current study presents an interesting contrast with the trends seen in Ireland et al. [39]. They presented plots analogous to those in Figure 4.23 at $r/\eta = 0.25, 1.75$ and 9.75 , with Re_λ varying from 88 to ~ 600 . They observed that for $St_\eta \gtrsim 10$, the variances increased strongly and monotonically with Re_λ , but only a weak dependence was seen at smaller Stokes numbers (both trends were observed at all three separations). In the current study, however, we see that the dependence of variances on Re_λ is a bit more complex and not necessarily monotonic. We also observe here that the sensitivity of variances to Re_λ becomes more prominent at larger r/η . Furthermore, for $St_\eta \gtrsim 10$, we see an increase in the variances as Re_λ is increased from 88 to 131, but observe a decrease in the variances as Re_λ goes from 131 to 210. For $St \leq 3$, Ireland et al. [39] observed that the relative velocity variances are only weakly dependent on Re_λ . Upon closer examination, a weak increase with Re_λ was seen for the variances when $St_\eta \lesssim 1$ (at $r = 0.25\eta$). However, we see a weak decrease in variances when Re_λ is increased from 88 to 131, but a stronger decrease when Re_λ becomes 210. For $1 \lesssim St_\eta \lesssim 3$, Ireland et al. [39] observed an overall decrease in variances with increasing Re_λ . A similar behavior is seen in our study as well. The inference we can draw from the comparison of RDFs and variances for DF and DF2 is that the observations of Ireland et al. [39] are attributable to their tightly controlled set of DNS runs. Specifically, in that study, a number of large- and small-scale turbulence statistics were maintained constant even while varying Re_λ significantly. No such effort was made explicitly in our study, but that we attempted to keep Re_λ constant across the DF and SF1-SF5 runs for a given grid size.

In the next section, we will discuss the PDF, $P(U_r)$, of radial relative velocities, and its dependence on the forcing, Reynolds number, and separation.

4.4.3 PDF of Radial Relative Velocities

Figure 4.24 shows the PDF $P(U_r)$ of the radial relative velocity U_r for $St_\eta = 0.2, 0.4, 2$ and 10 at $Re_\lambda = 210$. In each of the Figure 4.24(a)-(d), we plot the PDFs for two separations $r = 2\eta, L/2$, shown in blue and green curves, respectively. Here η and L are the Kolmogorov and integral length scales respectively. In these figures, we compare the PDFs for DF, SF3 and SF4. The PDFs are normalized with $\langle U_r^2 \rangle^{1/2}$ so that we can visualize and understand their proximity to (or deviation from) a normal distribution. We can see in Figure 4.24(a) and (b) that the PDFs for both $St_\eta = 0.2$ and 0.4 are negatively skewed at $r = 2\eta$, and nearly symmetric for $r = L/2$. In fact, at $r = L/2$, the PDFs for $St_\eta = 0.2$ and 0.4 are appreciably closer to the normal PDF than at $r = 2\eta$. The forcing scheme also seems to have no significant effect on the shapes of the PDFs. At the higher Stokes numbers, one notices from Figure 4.24(c) and (d) that the PDFs at $r = 2\eta$ are now nearly symmetric, with sharp peaks and wide tails, whereas at $r = L/2$, the PDFs are negatively skewed. The negative skewness at $r = L/2$ is higher for the $St_\eta = 10$ particles than for the $St_\eta = 2$ particles. Again, the forcing seems to have essentially no effect on the PDF shapes at the higher Stokes numbers.

In Figure 4.25, we present the effects of Stokes number on $P(U_r)$ at four separations and for $Re_\lambda = 210$. Only the PDFs obtained from the DF runs are shown, since we have already seen that forcing has a minimal effect on the shapes

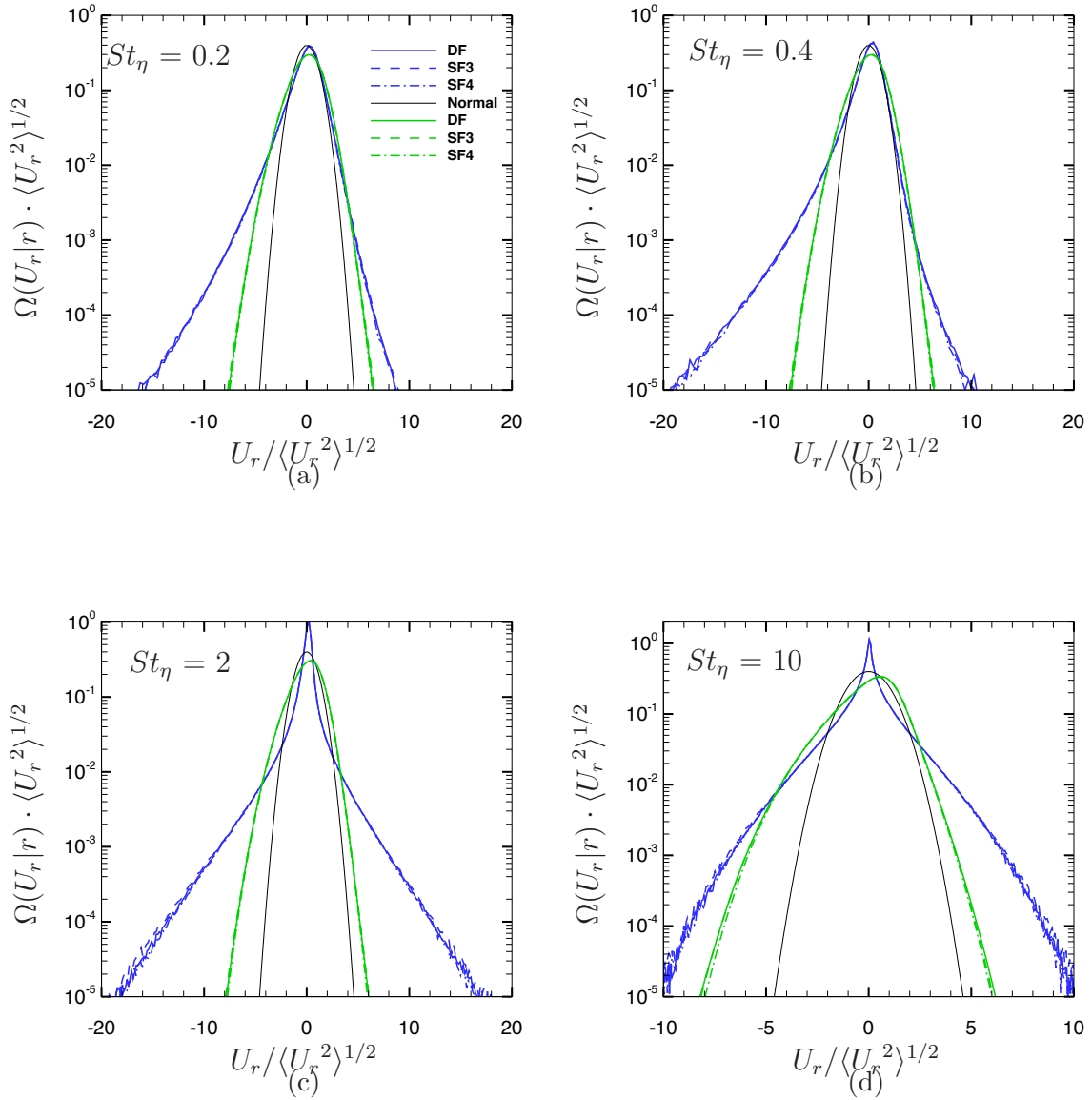


Figure 4.24: PDF of radial relative velocity $\Omega(U_r|r)$ normalized by $\langle U_r^2 \rangle^{1/2}$ at $Re_\lambda = 210$, and at the indicated values of St_η . DF, SF3, and SF4 are compared. Blue and green curves correspond to PDF at pair separation of $r = 2\eta$ and $r = L/2$ respectively. Black curve represents the normal distribution.

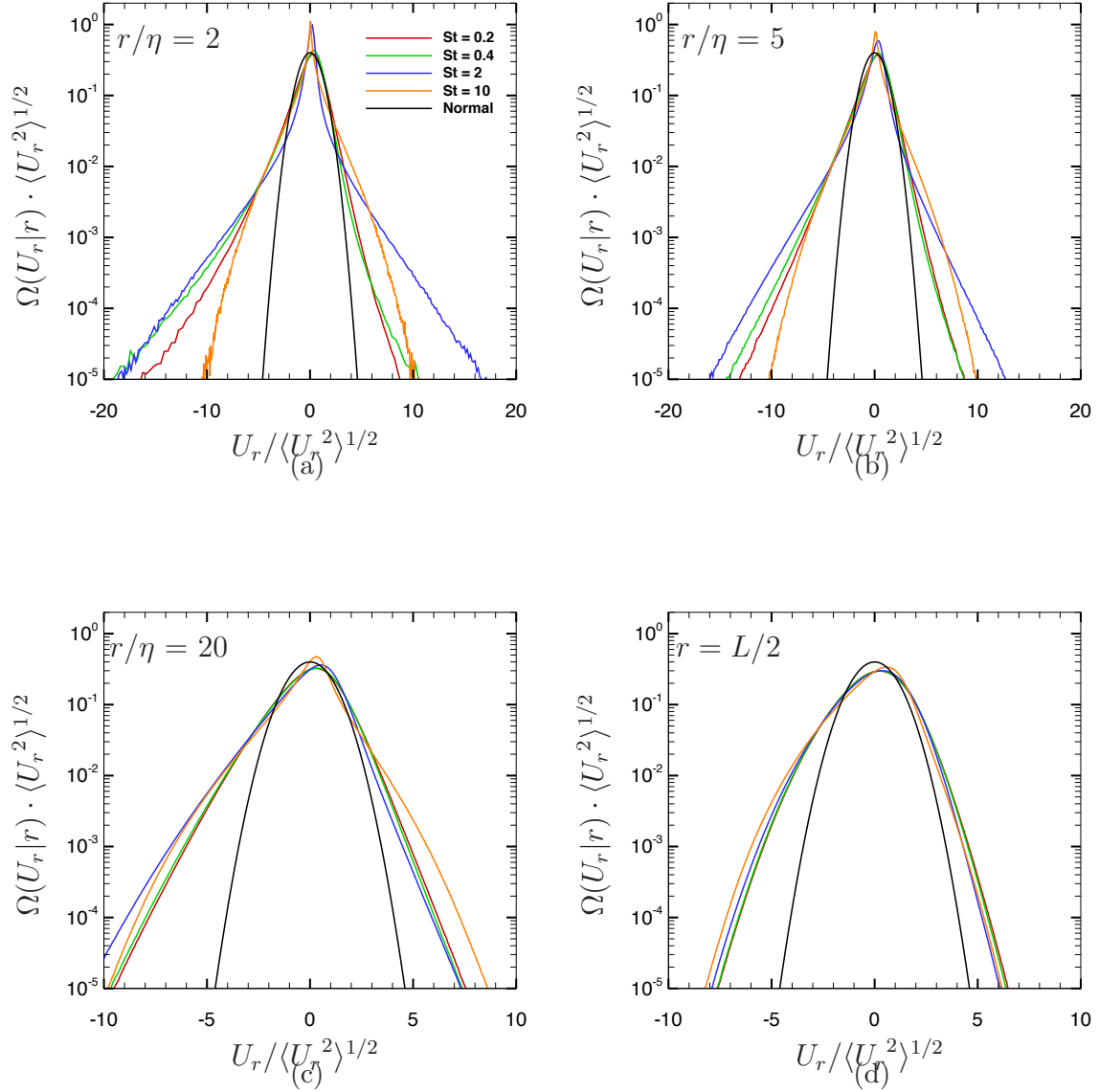


Figure 4.25: PDF of radial relative velocity $\Omega(U_r|r)$ normalized by $\langle U_r^2 \rangle^{1/2}$ at $Re_\lambda = 210$, and at the indicated values of St_η and pair separations. PDFs shown correspond to DF forcing scheme. Black curve represents the normal distribution.

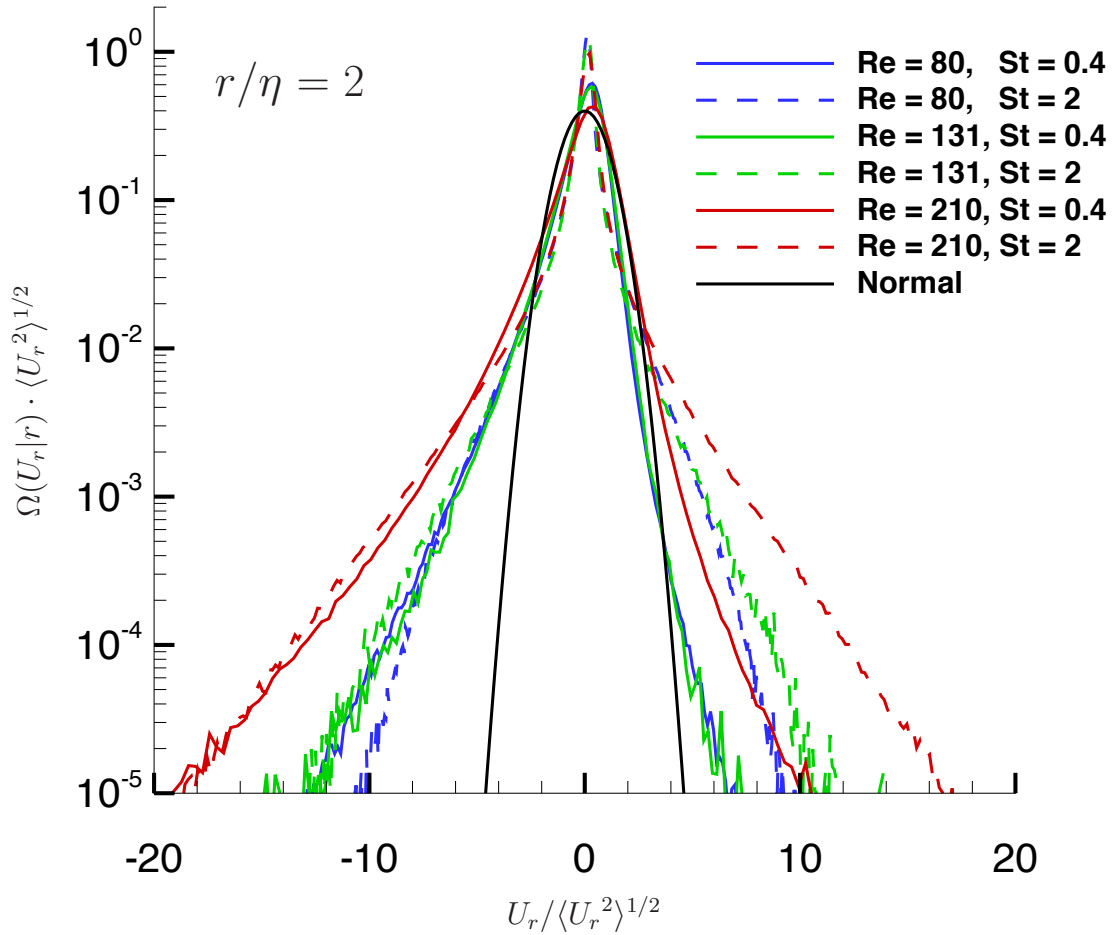


Figure 4.26: PDF of radial relative velocity $\Omega(U_r|r)$ normalized by $\langle U_r^2 \rangle^{1/2}$ at $Re_\lambda = 210$ and DF forcing scheme. PDFs shown are at $r = 2\eta$. Solid and dashed curves correspond to $St_\eta = 0.4$ and 2, respectively. Blue, green, and red curves represent $Re_\lambda = 80, 131,$ and 210 data, respectively. Normal distribution is shown by black curve.

of these PDFs. Figure 4.25(a) shows that at $r = 2\eta$, PDFs for low St_η ($= 0.2$ and 0.4) are negatively skewed, whereas the PDFs for high St_η ($= 2$ and 10) are nearly symmetrical. The PDF for $St_\eta = 0.4$ has a wider negative tail compared to the PDF for $St_\eta = 0.2$ particles. This suggests that the $St_\eta = 0.4$ particles have higher inward (negative) radial relative velocities, which leads to increased clustering and higher RDFs at $r = 2\eta$. Further, in Figure 4.25(a), it can be seen that the PDF for $St_\eta = 2$ is marginally negatively skewed, while that for $St_\eta = 10$ is nearly symmetric. The trends in the PDFs at $r = 4\eta$ are qualitatively similar to those at $r = 2\eta$. However, the PDF tails are not as wide as those at $r = 2\eta$. As the pair separations are further increased, we see in Figure 4.25(c) and (d) that the PDFs for $St_\eta = 0.2$ and 0.4 become less negatively skewed and the tails become less wide, as compared to the PDFs at smaller separations. This suggests a decrease in the net inward relative velocity, and thereby a reduction in particle accumulation at higher r . However, the PDFs for $St_\eta = 2$ and 10 become more negatively skewed compared to those at the two smaller separations. The higher negative skewness of the PDF for $St_\eta = 10$ as compared to that for $St_\eta = 2$ suggests that the $St_\eta = 10$ particles will have higher clustering at large separations than the $St_\eta = 2$ particles.

In Figure 4.26, we present the effects of Re_λ on the PDF $P(U_r)$ for $St_\eta = 0.4$ and 2 at $r = 2\eta$. We only show the PDFs for the DF runs. The PDF for $St_\eta = 0.4$ shows only a weak sensitivity to increase in Re_λ from 80 to 131 . But the increase in Re_λ from 131 to 210 leads to a PDF with much wider tails that are negatively skewed. For $St_\eta = 2$, we see a marginal widening of the PDF with the increase in Re_λ from 80 to 131 , and a much greater widening when Re_λ goes from 131 to 210 . In

general, the PDFs for $St_\eta = 2$ are less skewed (more symmetric) compared to those for $St_\eta = 0.4$. The higher negative skewness of the $St_\eta = 0.4$ particles at $r = 2\eta$ is also responsible for the greater accumulation and higher RDFs of these particles at these separations, as compared to the $St_\eta = 2$ particles.

4.4.4 Collision Kernel

We evaluate the collision kernel $K(\sigma)$ using Eq. (4.1) at the separation $r = 0.25\eta (= \sigma)$, which is the smallest separation at which we have well-averaged data. Figure 4.27 and Figure 4.28 show the collision kernel normalized in two ways. In Figure 4.27, we plot $K(\sigma)/(\sigma^2 u_\eta)$, and in Figure 4.28, $K(\sigma)/(\sigma^2 \langle U_r^2 \rangle^{1/2})$. The former normalization has been extensively used in prior studies [39, 105, 103, 104], while the latter is being used for the first time (to our knowledge). It is important to consider both forms since one gets rather different pictures of the collision kernel from them.

Figure 4.27(a)-(c) present the collision kernel $K(\sigma)/(\sigma^2 u_\eta)$ as a function of St_η at $Re_\lambda = 80, 131$ and 210 , respectively. Collision data from the DF and SF1-SF5 cases are presented. At all three Re_λ , the collision kernels initially increase rapidly and then decrease with Stokes number. The Stokes numbers where the peak collision rate occurs are $St_\eta \sim 1, 4$ and 10 at $Re_\lambda = 80, 131$ and 210 , respectively. Thus, the peak shifts toward higher St_η with increasing Re_λ . At the two lower Re_λ , forcing has only a marginal effect on the collision kernel for $St_\eta < 1$, but has a greater impact on the collision kernel for $St_\eta \geq 1$. At $Re_\lambda = 210$, the collision kernel is sensitive to forcing at all Stokes numbers. Also shown in Figure 4.27(a)-(c) are the collision ker-

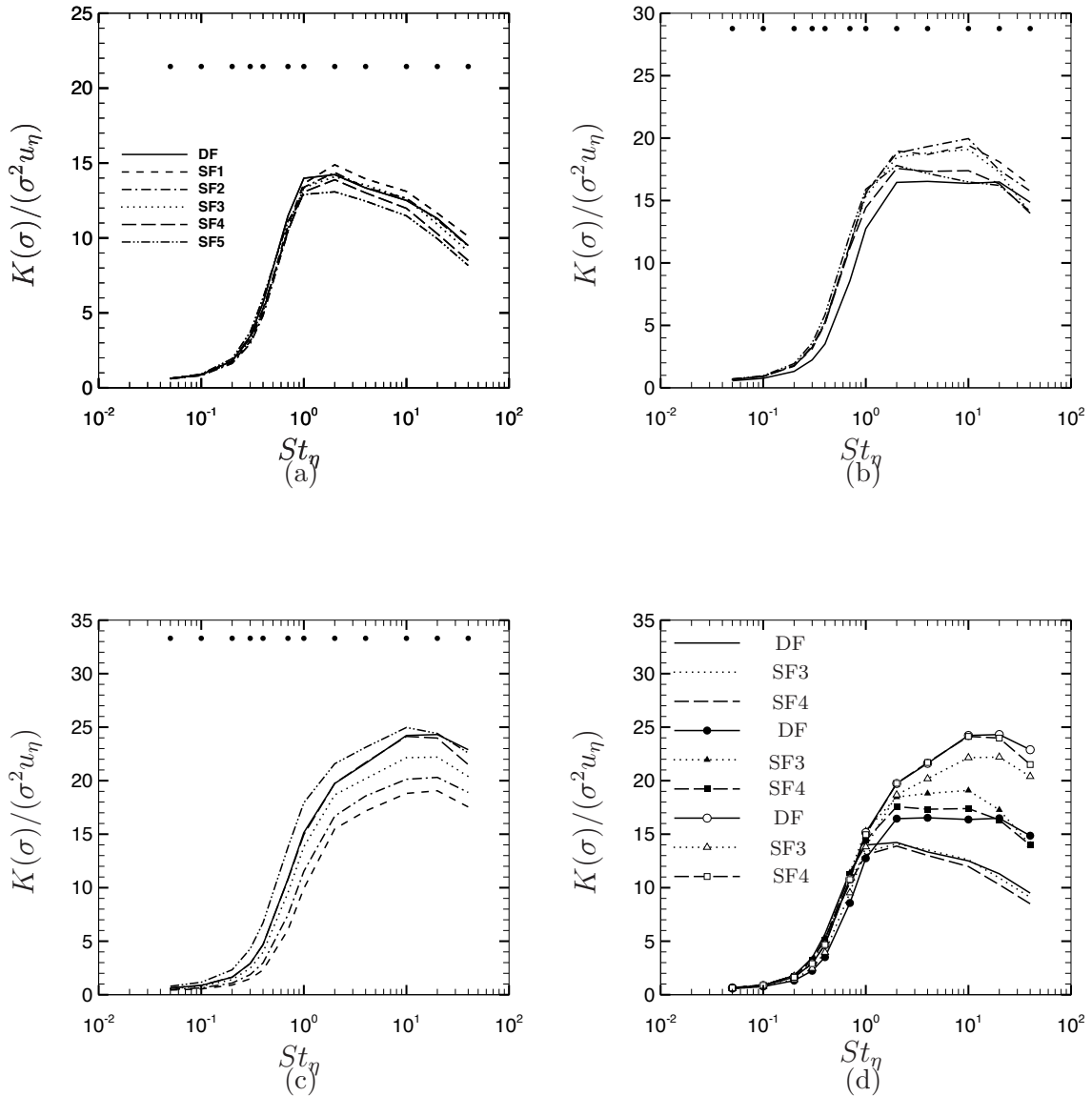


Figure 4.27: Collision Kernel a function of St_η at (a) $Re_\lambda = 80$, (b) $Re_\lambda = 131$, and (c) $Re_\lambda = 210$. DF, SF1, SF2, SF3, SF4, and SF5 are compared in (a)-(c). DF, SF3, and SF4 are compared in (d). Curves without symbols represent data for $Re_\lambda = 80$, filled and open symbols correspond to data for $Re_\lambda = 131$ and 210, respectively in (c).

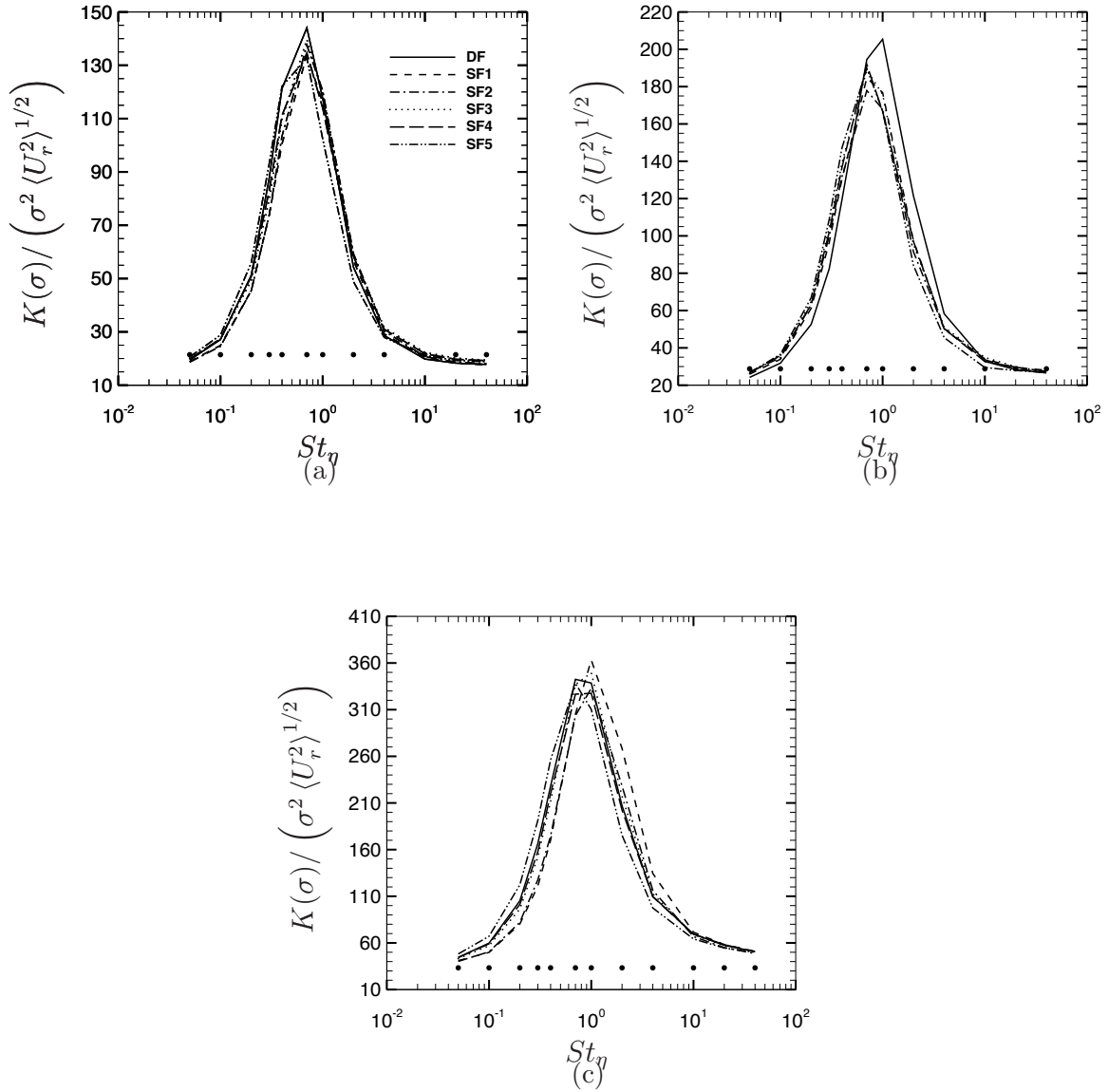


Figure 4.28: Collision Kernel a function of St_η at (a) $Re_\lambda = 80$, (b) $Re_\lambda = 131$, and (c) $Re_\lambda = 210$. DF, SF1, SF2, SF3, SF4, and SF5 are compared. Black circles represent the collision kernel when RDF $g(r) = 1$ and the PDF $P(U_r|r)$ is Gaussian.

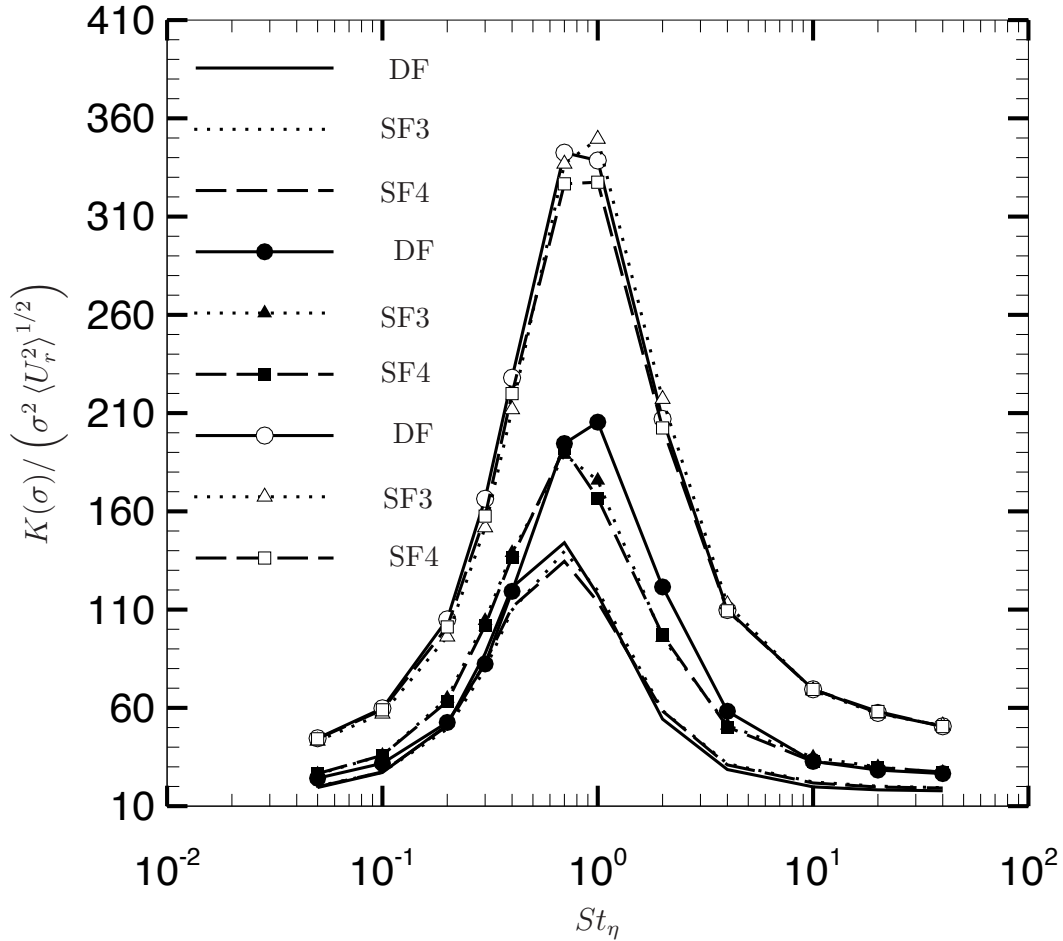


Figure 4.29: Collision Kernel a function of St_η is shown. DF, SF3, and SF4 are compared. Curves without symbols represent data at $Re_\lambda = 80$, filled and open symbols correspond to data at $Re_\lambda = 131$ and 210 , respectively.

nels for particles that are uniformly distributed in the flow, i.e. $g(\sigma) = 1$, and whose relative velocities are uncorrelated, i.e. $P(U_r)$ is normally distributed. With the normalization used in this figure, it would seem that turbulence-driven particle clustering and relative velocities suppress the collision kernel. This trend contradicts the view that turbulence enhances the collision rates of inertial particles, as compared to the collision rates of uncorrelated particles. The apparent contradiction can be resolved

by considering the second normalization discussed above. Finally, in Figure 4.27(d), we compare the collision kernels for DF, SF3 and SF4 at the three Reynolds numbers. For $St_\eta < 1$, the collision kernel shows a relatively weaker dependence on Re_λ , while for $St_\eta \geq 1$, the collision kernel shows a clear, significant, and monotonic increase with Re_λ .

In Figure 4.28, the collision kernel $K(\sigma) / \left(\sigma^2 \langle U_r^2 \rangle^{1/2} \right)$ is shown as a function of St_η for the three values of Re_λ at $r = 0.25\eta$. These collision kernels are computed by using the PDFs of Figure 4.24 in Eq. (4.1). The normalization of the PDFs performed in Figure 4.24 allows us to make a direct comparison of the collision kernels from the current cases with those for uncorrelated particle pairs. Thus, we also show in Figure 4.28 the collision kernels corresponding to uncorrelated particle pairs, i.e., pairs with $g(r) = 1$ and $P(U_r)$ normally distributed. One observes important differences between Figure 4.28 and Figure 4.27. Firstly, and rather strikingly, the peak value of the collision kernel in Figure 4.28 occurs at $St_\eta \sim 1$ at the three Re_λ , whereas in Figure 4.27, we see that the peak value shifts towards higher St_η . Secondly, for $Re_\lambda = 80$ and 131 , we see that the collision kernel of uncorrelated particles exceeds that of inertial particles for very low and high Stokes numbers, i.e., $St_\eta < 0.1$ and $St_\eta > 10$. However, for $Re_\lambda = 210$, we see that the collision kernel of uncorrelated particles is always smaller than of inertial particles. The comparison of the inertial-pair and uncorrelated-pair collision kernels has important implications in cloud physics, where turbulence-driven particle clustering and turbulence-enhanced relative velocities are considered to be the mechanisms for the hastening of rain formation.

Finally, we consider the effects of Re_λ on the collision kernel $K(\sigma)/\left(\sigma^2 \langle U_r^2 \rangle^{1/2}\right)$.

In Figure 4.29, the collision kernels obtained using DF, SF3 and SF4 are presented for the three Re_λ . At the two lower values of Re_λ , i.e. $Re_\lambda = 80$ and 131 , we see a weak dependence on Re_λ for $St_\eta \leq 0.7$. However, a further increase in Re_λ to 210 results in an increase in the kernel for $St_\eta \leq 0.7$. For $St_\eta \gtrsim 1$, we see that the collision kernels show a consistent increase with Re_λ . These trends may again be compared with the observations in Ireland et al. [39]. When $St_\eta \lesssim 0.2$, the collision rates in Ireland et al. [39] were essentially independent of Re_λ . For larger St_η , they observed a weak decrease in the collision kernel with Re_λ . For $1 < St_\eta \leq 3$, the collision kernel increases weakly as Re_λ increases. Finally, for $St_\eta \geq 10$, collision kernels increase strongly with Re_λ . The principal difference in the collision kernel statistics of the two studies is that we observe a consistent and significant increase in collision rates as Re_λ increases, for $St_\eta > 1$.

4.5 Concluding Remarks

We investigated the effects of forcing on the relative-motion statistics of inertial particles in DNS of isotropic turbulence. Both deterministic and stochastic forcing schemes, DF and SF respectively, were considered. In the case of SF, the effects of varying the forcing time scale on particle relative motion were studied by considering five values of T_f ranging from $4T_E$ to $T_E/4$, where T_E is the large-eddy turn over time obtained from DF. Statistics such as the RDF, the PDF of radial relative velocities,

and the collision kernel obtained using DF, SF1-SF5 and DF2 (from the study of Ireland et al. [39]) are compared for $St_\eta < 1$, $St_\eta \sim 1$ and $St_\eta > 1$ at three Re_λ .

For $St_\eta < 1$, the RDFs show an appreciable dependence on both the nature of forcing (DF versus SF), and the forcing time scale (SF1 through SF5). The differences between the RDFs for DF and SF1-SF5 increase with St_η , with the maximum difference being observed for $St_\eta = 0.4$. The effects of forcing on the RDFs manifested most clearly at $Re_\lambda = 210$, which may be due to the clear separation of turbulent scales at this high Re_λ . At $Re_\lambda = 210$, the RDFs for SF3 and SF4 (corresponding to forcing time scales $T_f = T_E$ and $T_E/2$, respectively) were in the best agreement with the RDFs of DF. The forcings seemed to have no effect on the RDFs for $St_\eta \sim 1$ (specifically, $St_\eta = 0.7$ and 1) particles.

For $St_\eta > 1$, the RDFs again reflected a substantial impact of both the forcing type, and the forcing time scale for SF. The differences among the RDFs for DF and SF1-SF5 were maximum for $St_\eta = 2$, and decreased thereafter with an increase in St_η . We also considered the effects of Re_λ on the RDFs. For $St_\eta \leq 0.4$, the RDFs computed using DF decreased while going from $Re_\lambda = 80$ to 131, and then increased when Re_λ was increased to 210. The RDFs obtained using DNS with SF showed less sensitivity to Re_λ . The RDFs for $St_\eta \geq 4$ showed a monotonic increase with Re_λ for DF and all the SF cases.

We also considered the effects of forcing on the relative velocity statistics. For $St_\eta < 1$, the variance of radial relative velocity $\langle U_r^2 \rangle$ showed only a weak dependence on forcing for $Re_\lambda = 80$ and 131, but the forcing effects were much clearer and significant for $Re_\lambda = 210$. At $Re_\lambda = 210$, the DF2 variances [39] were higher than

those of DF and SF1-SF5. For $St_\eta > 1$, forcing had a significant impact on the variances in the dissipation-range separations for $Re_\lambda = 80$ and 131, and at all pair separations for $Re_\lambda = 210$. Similar to the trends observed for the RDFs, the variances from SF3 and SF4 showed the best agreement with those obtained using DF. For $St_\eta < 1$ and $1 \leq St_\eta < 10$, $\langle U_r^2 \rangle$ showed weak dependence on Re_λ while going from $Re_\lambda = 80$ to 131, but $\langle U_r^2 \rangle$ decreased when Re_λ was further increased to 210. For $St_\eta = 10$, the variances initially increased from $Re_\lambda = 80$ to 131, and then decreased for $Re_\lambda = 210$.

Finally, collision kernels were computed from the RDFs and relative velocity PDFs. Two types of normalizations were used for the collision kernel, one based on $\sigma^2 u_\eta$, and the other using $\sigma^2 \langle U_r^2 \rangle^{1/2}$. The collision kernels showed weaker dependence on Re_λ for $St_\eta < 1$, but the dependence became stronger for $St_\eta \gtrsim 1$. For $St_\eta \geq 1$, the collision kernels showed a monotonic increase with Reynolds number for all three Re_λ . Ireland et al. [39], who also used the first normalization, observed similar trends for the collision rates. It is shown that when comparing the collision rates of inertial particle pairs with those of uncorrelated particle pairs, normalization using $\sigma^2 \langle U_r^2 \rangle^{1/2}$ provides a more physically accurate comparison.

Perhaps, the most important inference that one can draw from this study is that the conclusions on pair relative motion arrived at by Ireland et al. [39] will have to be interpreted in light of the fact that they undertook a set of well-controlled DNS runs, wherein many of the determining large- and small-scale statistics were kept fixed while varying the Reynolds number. Further, even when considering a fixed Re_λ , the deviations between the DF and DF2 results may be attributed to the differences in

statistics such as u_{rms} , $\langle \epsilon \rangle$, and more importantly, the resolution parameter $k_{\text{max}}\eta$. Finally, the relative motion statistics of inertial particles obtained using SF3 and SF4 (corresponding to forcing time scales $T_f = T_E, T_E/2$, respectively) showed good agreement with those of DF. But, too high ($T_f = 4T_E$) or too low ($T_f = T_E/4$) forcing time scales may lead to artificial extrema in the values of these statistics.

CHAPTER 5

CONCLUSIONS

5.1 Summary

1. In Chapter 2, a novel closure was developed for the relative velocity-space diffusion current in the PDF equation describing the relative positions and velocities of $St_r \gg 1$ particle pairs in isotropic turbulence.
 - (a) We began the development of closure form for diffusivity tensor in the the limit of $St_I \gg 1$ and $St_r \gg 1$. Subsequently, the closure was extended to $St_I \lesssim 1$ particles by accounting for the motion of the pair center of mass.
 - (b) The diffusion tensor contained the time-integral of the Lagrangian correlation of fluid relative velocities along particle pair trajectories.
 - (c) In the limit of $St_r \gg 1$ but $St_I \lesssim 1$, the Lagrangian two-point, two-time correlation was systematically converted first into an Eulerian two-time correlation, and subsequently into an Eulerian two-point correlation.
 - (d) For isotropic turbulence, Eulerian fluid-velocity correlations were expressed as Fourier transforms of the velocity spectrum tensor, enabling us to derive a closed-form expression for the diffusivity tensor.

- (e) Using this diffusivity closure, Langevin equations were solved to evolve particle-pair relative velocities and separations in stationary isotropic turbulence.
 - (f) The radial distribution functions (RDFs) computed from these simulations showed good quantitative agreement with those from the DNS study of Février et al. [29] for $St_\eta \geq 10$.
 - (g) The stochastic theory successfully captured the transition of relative velocity PDF from a Gaussian PDF at separations of the order of the integral length scale to an exponential PDF at smaller separations, consistent with the study of Sundaram and Collins [91].
2. In Chapter 3, a quantitative analysis of the stochastic theory presented in Chapter 2 was performed through a comparison of the particle pair statistics obtained using Langevin simulations with those from DNS.
- (a) Simulations were performed at $Re_\lambda = 76$ and 131 , and for $St_\eta = 10, 20, 40$ and 80 .
 - (b) Langevin simulations were performed using three closure forms (CF) of diffusion tensor:
 - CF1: Here, the diffusion tensor was closed by computing the Eulerian two-time correlation via DNS containing disperse stationary particles, and integrating the correlation in time.

- CF2: This refers to the closure form of the diffusivity tensor derived in Chapter 2 for stationary particles having both the pair separation and the pair center-of-mass position stationary.
 - CF3: This refers to the closure form of the diffusivity tensor for particle pairs whose separation does not change, but whose center-of-mass position changes during flow time scales.
- (c) CF1 was most accurate among three closure forms as the two-time Eulerian relative velocity correlations are computed using DNS.
- (d) The RDFs obtained from the Langevin simulations based on CF1 showed excellent agreement with the DNS RDFs.
- (e) The relative velocity variances computed using CF1 showed good agreement with the variances from DNS, particularly at higher Stokes numbers.
- (f) The effects of Reynolds number on the relative velocity variances were also considered, and it was seen that the CF1 variances showed a stronger dependence on the Reynolds number than did the CF2 and CF3 variances, especially at lower Stokes numbers.
- (g) The collision kernels obtained using CF1 were found to be in good agreement with those obtained using DNS. It was also found that the collision kernels increased with the Reynolds number due to an increase in both the RDF and the relative velocities.
3. In Chapter 4, we investigated the effects of the forcing of large-scale eddies on the relative motion of dense inertial particles in DNS of isotropic turbulence.

Two forcing schemes—deterministic (DF) and stochastic (SF)—were considered.

- (a) The effects of varying the forcing time scale on particle relative motion were studied by considering five values of T_f ranging from $4T_E$ to $T_E/4$, where T_E is the large-eddy turn over time obtained from DF. These five stochastic cases are referred to as SF1-SF5.
- (b) For $St_\eta < 1$, forcing had a significant effect on the RDFs, and the differences between the RDFs for DF and SF1-SF5 increased with St_η . The maximum difference was observed for $St_\eta = 0.4$.
- (c) For $St_\eta > 1$, the differences among the RDFs for DF and SF1-SF5 were maximum for $St_\eta = 2$, and decreased thereafter with an increase in St_η .
- (d) The RDFs obtained using DNS with SF showed less sensitivity to Re_λ . The Reynolds number had only a marginal impact on RDFs for $St_\eta \sim 1$ particles at all forcings.
- (e) For $St_\eta < 1$, the variance of radial relative velocity $\langle U_r^2 \rangle$ showed only a weak dependence on forcing for $Re_\lambda = 80$ and 131, but the forcing effects were much clearer and significant for $Re_\lambda = 210$.
- (f) For $St_\eta < 1$ and $1 \leq St_\eta < 10$, $\langle U_r^2 \rangle$ showed weak dependence on Re_λ while going from $Re_\lambda = 80$ to 131, but $\langle U_r^2 \rangle$ decreased when Re_λ was further increased to 210. For $St_\eta = 10$, the variances initially increased from $Re_\lambda = 80$ to 131, and then decreased for $Re_\lambda = 210$.

- (g) Collision kernels were computed using two types of normalizations, one based on $\sigma^2 u_\eta$, and the other using $\sigma^2 \langle U_r^2 \rangle^{1/2}$.
- (h) The collision kernels obtained using the first kind of normalization were independent of Re_λ for $St_\eta < 1$, but showed strong dependence on Re_λ for $St_\eta \gtrsim 1$. Ireland et al. [39], who also used the first normalization, observed the same trends in collision kernels.
- (i) The collision kernels corresponding to the second type of normalization showed weak dependence on the type of forcing used and peaked around $St_\eta \sim 1$. The collision kernels for $St_\eta < 0.7$ showed weak dependence on the Reynolds number for $Re_\lambda = 80$ and 131, but increased for $Re_\lambda = 210$. For $St_\eta \geq 1$, the collision kernels showed a monotonic increase with Reynolds number for all three Re_λ .
- (j) The relative motion statistics of inertial particles obtained using SF3 and SF4 (corresponding to forcing time scales $T_f = T_E, T_E/2$, respectively) showed good agreement with those of DF. But, too high ($T_f = 4T_E$) or too low ($T_f = T_E/4$) forcing time scales may lead to artificial extrema in the values of these statistics.

5.2 Future work

1. It was noted in Chapter 3 that the relative velocity variances obtained using CF1 showed a stronger dependence on Reynolds number than CF2 and CF3. The goal of a future study can therefore be to improve the behavior of CF1 at

higher Reynolds numbers, thereby extending the applicability of the stochastic theory to larger range of Reynolds numbers.

2. Another future direction can be to develop a stochastic theory to study the effects of gravity on the pair relative motion. A preliminary effort to derive this theory is presented in Appendix A, where the stochastic theory presented in Chapter 2 has been modified to include the effects of gravitational sedimentation on the particle-pair relative motion. The next step will be to perform a quantitative analysis of the theory by comparing particle relative motion statistics obtained using theory with those computed using DNS.

APPENDICES

APPENDIX A

STOCHASTIC THEORY FOR MONODISPERSE SETTLING

PARTICLE PAIRS

The objective of this appendix is to appropriately modify the stochastic theory of Rani et al. [67] to include the effects of gravitational settling on particle-pair relative motion. In this appendix, only monodisperse settling particles are considered so that there is no differential settling.

The governing equations for the relative position (separation vector) \mathbf{r} , relative velocity \mathbf{U} , center-of-mass position \mathbf{x} , and center-of-mass velocity \mathbf{V} of a settling, like particle pair are:

$$\frac{d\mathbf{r}}{dt} = \mathbf{U} \tag{A.1}$$

$$\frac{d\mathbf{U}}{dt} = -\frac{1}{\tau_v} [\mathbf{U}(t) - \Delta\mathbf{u}(\mathbf{r}(t), \mathbf{x}(t), t)] \tag{A.2}$$

$$\frac{d\mathbf{x}}{dt} = \mathbf{V} \tag{A.3}$$

$$\frac{d\mathbf{V}}{dt} = -\frac{1}{\tau_v} \left[\mathbf{V}(t) - \frac{\mathbf{u}(\mathbf{R}_1(t), t) + \mathbf{u}(\mathbf{R}_2(t), t)}{2} \right] + \mathbf{g} = -\frac{1}{\tau_v} [\mathbf{V}(t) - \mathbf{u}_{\text{cm}}(\mathbf{R}_1(t), \mathbf{R}_2(t), t)] + \mathbf{g} \tag{A.4}$$

where \mathbf{R}_1 and \mathbf{R}_2 are the positions of the two particles. For a monodisperse suspension of particles, gravity influences pair relative motion only through the modified sampling

of the “seen” fluid relative velocity, $\Delta \mathbf{u}(\mathbf{r}(t), \mathbf{x}(t), t)$, by the settling pair. However, the center-of-mass dynamics is directly influenced by gravity, as seen in (A.4).

The governing equation for the PDF $P(\mathbf{r}, \mathbf{U}, \mathbf{x}, \mathbf{V}; t)$ is given by

$$\frac{\partial P}{\partial t} + \nabla_{\mathbf{r}} \cdot (\mathbf{U}P) + \nabla_{\mathbf{x}} \cdot (\mathbf{V}P) + \nabla_{\mathbf{U}} \cdot \left(\frac{d\mathbf{U}}{dt} P \right) + \nabla_{\mathbf{V}} \cdot \left(\frac{d\mathbf{V}}{dt} P \right) = 0 \quad (\text{A.5})$$

Using (A.2) and (A.4) in (A.5) yields

$$\begin{aligned} \frac{\partial P}{\partial t} + \nabla_{\mathbf{r}} \cdot (\mathbf{U}P) + \nabla_{\mathbf{x}} \cdot (\mathbf{V}P) - \frac{1}{\tau_v} \nabla_{\mathbf{U}} \cdot (\mathbf{U}P) + \frac{1}{\tau_v} \nabla_{\mathbf{V}} \cdot ((-\mathbf{V} + \mathbf{g}\tau_v)P) \\ + \frac{1}{\tau_v} \nabla_{\mathbf{U}} \cdot (\Delta \mathbf{u}P) + \frac{1}{\tau_v} \nabla_{\mathbf{V}} \cdot (\mathbf{u}_{\text{cm}}P) = 0 \quad (\text{A.6}) \end{aligned}$$

Averaging (A.6) over an ensemble of flow realizations yields

$$\begin{aligned} \frac{\partial \langle P \rangle}{\partial t} + \nabla_{\mathbf{r}} \cdot (\mathbf{U}\langle P \rangle) + \nabla_{\mathbf{x}} \cdot (\mathbf{V}\langle P \rangle) - \frac{1}{\tau_v} \nabla_{\mathbf{U}} \cdot (\mathbf{U}\langle P \rangle) + \frac{1}{\tau_v} \nabla_{\mathbf{V}} \cdot ((-\mathbf{V} + \mathbf{g}\tau_v)\langle P \rangle) \\ + \frac{1}{\tau_v} \nabla_{\mathbf{U}} \cdot \langle \Delta \mathbf{u}P \rangle + \frac{1}{\tau_v} \nabla_{\mathbf{V}} \cdot \langle \mathbf{u}_{\text{cm}}P \rangle = 0 \quad (\text{A.7}) \end{aligned}$$

Substituting $P = \langle P \rangle + P'$ into (A.6), and moving terms containing $\langle P \rangle$ to the RHS, we get:

$$\begin{aligned} \frac{\partial P'}{\partial t} + \nabla_{\mathbf{r}} \cdot (\mathbf{U}P') + \nabla_{\mathbf{x}} \cdot (\mathbf{V}P') - \frac{1}{\tau_v} \nabla_{\mathbf{U}} \cdot (\mathbf{U}P') + \frac{1}{\tau_v} \nabla_{\mathbf{V}} \cdot ((-\mathbf{V} + \mathbf{g}\tau_v)P') \\ + \frac{1}{\tau_v} \nabla_{\mathbf{U}} \cdot (\Delta \mathbf{u}P') + \frac{1}{\tau_v} \nabla_{\mathbf{V}} \cdot (\mathbf{u}_{\text{cm}}P') = \\ - \left[\frac{\partial \langle P \rangle}{\partial t} + \nabla_{\mathbf{r}} \cdot (\mathbf{U}\langle P \rangle) + \nabla_{\mathbf{x}} \cdot (\mathbf{V}\langle P \rangle) - \frac{1}{\tau_v} \nabla_{\mathbf{U}} \cdot (\mathbf{U}\langle P \rangle) + \frac{1}{\tau_v} \nabla_{\mathbf{V}} \cdot ((-\mathbf{V} + \mathbf{g}\tau_v)\langle P \rangle) \right. \\ \left. + \frac{1}{\tau_v} \nabla_{\mathbf{U}} \cdot (\Delta \mathbf{u}\langle P \rangle) + \frac{1}{\tau_v} \nabla_{\mathbf{V}} \cdot (\mathbf{u}_{\text{cm}}\langle P \rangle) \right] \quad (\text{A.8}) \end{aligned}$$

Subtracting (A.7) from (A.8), and making terms dimensionless with the integral length scale (L), integral time scale (τ_I), and isotropic turbulence r.m.s. fluctuating velocity (u_{rms}), yields:

$$\begin{aligned}
& \frac{\partial P'}{\partial t} + \nabla_{\mathbf{r}} \cdot (\mathbf{U}P') + \nabla_{\mathbf{x}} \cdot (\mathbf{V}P') - \frac{1}{St_I} \nabla_{\mathbf{U}} \cdot (\mathbf{U}P') + \frac{1}{St_I} \nabla_{\mathbf{V}} \cdot ((-\mathbf{V} + Sv_I \mathbf{e}_g)P') \\
& + \frac{1}{St_I} \nabla_{\mathbf{U}} \cdot (\Delta \mathbf{u}P') + \frac{1}{St_I} \nabla_{\mathbf{V}} \cdot (\mathbf{u}_{\text{cm}}P') = -\frac{1}{St_I} \nabla_{\mathbf{U}} \cdot (\Delta \mathbf{u}\langle P \rangle) \\
& - \frac{1}{St_I} \nabla_{\mathbf{V}} \cdot (\mathbf{u}_{\text{cm}}\langle P \rangle) + \frac{1}{St_I} \nabla_{\mathbf{U}} \cdot \langle \Delta \mathbf{u}P' \rangle + \frac{1}{St_I} \nabla_{\mathbf{V}} \cdot \langle \mathbf{u}_{\text{cm}}P' \rangle
\end{aligned} \tag{A.9}$$

where \mathbf{e}_g is the unit vector along the direction of gravity.

One may consider two settling regimes depending on the order of magnitude of $Sv_I = g\tau_v/u_{\text{rms}}$. The first is $Sv_I \sim St_I \gg 1$, and the second is $Sv_I \sim 1$.

A.1 $Sv_I \sim St_I \gg 1$ Regime

In this regime, the center-of-mass terminal velocity is far greater than even the large-scale fluid velocity, i.e. $g\tau_v \gg u_{\text{rms}}$. Therefore, equation (A.4) governing center-of-mass velocity \mathbf{V} essentially becomes (in dimensionless form):

$$\frac{d\mathbf{V}}{dt} = \frac{1}{St_I} (-\mathbf{V}(t) + Sv_I \mathbf{e}_g) \tag{A.10}$$

whose solution is simply $\mathbf{V}(t) = Sv_I \mathbf{e}_g$, i.e. the center of mass undergoes a ballistic motion.

We now perform perturbation analysis similar to that in Rani et al. [67].

Considering the $O(1/St_I)$ terms in (A.9), we get:

$$\frac{\partial P_1}{\partial t} + \nabla_{\mathbf{r}} \cdot (\mathbf{U}P_1) + \nabla_{\mathbf{x}} \cdot (\mathbf{V}P_1) = -\nabla_{\mathbf{U}} \cdot (\Delta \mathbf{u} \langle P \rangle) - \nabla_{\mathbf{V}} \cdot (\mathbf{u}_{\text{cm}} \langle P \rangle) \quad (\text{A.11})$$

Equation (A.11) is a Lagrangian evolution equation of P_1 in the $(\mathbf{r}, \mathbf{x}, t)$ space, with

\mathbf{U} and \mathbf{V} held fixed; (A.11) may then be written as

$$\left. \frac{dP_1}{dt} \right|_{\mathbf{U}, \mathbf{V}} = -\nabla_{\mathbf{U}} \cdot (\Delta \mathbf{u} \langle P \rangle) - \nabla_{\mathbf{V}} \cdot (\mathbf{u}_{\text{cm}} \langle P \rangle) \quad (\text{A.12})$$

From (A.12), we can write:

$$\begin{aligned} P_1 &= - \int_{-\infty}^s dt' \{ \nabla_{\mathbf{U}} \cdot [\Delta \mathbf{u}(\mathbf{r}(t'), \mathbf{x}(t'), t') \langle P \rangle(\mathbf{r}', \mathbf{U}, \mathbf{x}', \mathbf{V}; t')] + \\ &\quad \nabla_{\mathbf{V}} \cdot [\mathbf{u}_{\text{cm}}(\mathbf{R}_1(t'), \mathbf{R}_2(t'), t') \langle P \rangle(\mathbf{r}', \mathbf{U}, \mathbf{x}', \mathbf{V}; t')] \} \\ &= - \int_{-\infty}^s dt' \{ \Delta \mathbf{u}(\mathbf{r}(t'), \mathbf{x}(t'), t') \cdot \nabla_{\mathbf{U}} \langle P \rangle(t') + \\ &\quad \mathbf{u}_{\text{cm}}(\mathbf{R}_1(t'), \mathbf{R}_2(t'), t') \cdot \nabla_{\mathbf{V}} \langle P \rangle(t') \} \end{aligned} \quad (\text{A.13})$$

where $\mathbf{r}' = \mathbf{r}(t')$, $\mathbf{x}' = \mathbf{x}(t')$, and s is a characteristic variable along the Lagrangian trajectory such that $\frac{dt}{ds} = 1$, and $\frac{d\mathbf{x}'}{dt'}|_{t'=s} = \mathbf{V}$ and $\frac{d\mathbf{r}'}{dt'}|_{t'=s} = \mathbf{U}$. At the upper integration limit s , we have $\mathbf{r}(s) = \mathbf{r}(t) = \mathbf{r}$. We have also used the shorthand notation $\langle P \rangle(t') = \langle P \rangle(\mathbf{r}', \mathbf{U}, \mathbf{x}', \mathbf{V}; t')$. The integral in (A.13) can be reduced to a time integral at fixed positions with two simplifications. First, the \mathbf{r} -space convective term on the LHS of (A.11) is neglected in the asymptotic limit of $St_r \gg 1$. Second,

the pair center of mass \mathbf{x} is assumed to move only due to settling, which is valid in the limit $St_I \gg 1$. This would yield

$$\begin{aligned} \langle \Delta \mathbf{u} P' \rangle = & -\frac{1}{St_I^2} \int_{-\infty}^t dt' \{ \langle \Delta \mathbf{u}(\mathbf{r}, \mathbf{x}, t) \Delta \mathbf{u}(\mathbf{r}, \mathbf{x}_g, t') \rangle \cdot \nabla_{\mathbf{U}} \langle P \rangle(t') + \\ & \langle \Delta \mathbf{u}(\mathbf{r}, \mathbf{x}, t) \mathbf{u}_{\text{cm}}(\mathbf{R}_{1,g}(t), \mathbf{R}_{2,g}(t), t') \rangle \cdot \nabla_{\mathbf{V}} \langle P \rangle(t') \} \end{aligned} \quad (\text{A.14})$$

$$\begin{aligned} \langle \mathbf{u}_{\text{cm}} P' \rangle = & -\frac{1}{St_I^2} \int_{-\infty}^t dt' \{ \langle \mathbf{u}_{\text{cm}}(\mathbf{R}_1(t), \mathbf{R}_2(t), t) \Delta \mathbf{u}(\mathbf{r}, \mathbf{x}_g, t') \rangle \cdot \nabla_{\mathbf{U}} \langle P \rangle(t') + \\ & \langle \mathbf{u}_{\text{cm}}(\mathbf{R}_1(t), \mathbf{R}_2(t), t) \mathbf{u}_{\text{cm}}(\mathbf{R}_{1,g}(t), \mathbf{R}_{2,g}(t), t') \rangle \cdot \nabla_{\mathbf{V}} \langle P \rangle(t') \} \end{aligned} \quad (\text{A.15})$$

where the subscript g on a position vector denotes an increment of $\mathbf{g}\tau_v(t' - t)$ due to gravity. For instance, $\mathbf{x}_g = \mathbf{x} + \mathbf{g}\tau_v(t' - t)$, and $\mathbf{R}_{1,g}(t) = \mathbf{R}_1(t) + \mathbf{g}\tau_v(t' - t)$. Accordingly, the PDF $\langle P \rangle(t') = \langle P \rangle(\mathbf{r}, \mathbf{U}, \mathbf{x}_g, \mathbf{V}; t')$ after the above two simplifications. Using homogeneity, we may write $\langle P \rangle(\mathbf{r}, \mathbf{U}, \mathbf{x}_g, \mathbf{V}; t')$ as simply $\langle P \rangle(\mathbf{r}, \mathbf{U}, \mathbf{x}, \mathbf{V}; t')$. The two-time fluid velocity correlations in (A.14) and (A.15) are significant only in the time interval $t - t'$ for which the fluid eddies are correlated. Therefore, we can write $\langle P \rangle(t') \approx \langle P \rangle(t)$, since the timescales over which $\langle P \rangle$ changes are much greater than the fluid correlation timescales.

Further adopting the procedure outlined in [67], we get the following equation for the pair diffusion coefficient D_{UU} :

$$D_{UU} = \frac{1}{St_I^2} \tilde{D}_{UU} = \frac{1}{St_I^2} \int_{-\infty}^0 dt \langle \Delta \mathbf{u}(\mathbf{r}, \mathbf{x}, 0) \Delta \mathbf{u}(\mathbf{r}, \mathbf{x} + \mathbf{g}\tau_v t, t) \rangle \quad (\text{A.16})$$

Note that the effects of gravity are reflected through the shifting of the pair center-of-mass position by $\mathbf{g}\tau_v t$. In the above equation, the fluid-relative-velocity correlation inside the integral is *not* an Eulerian one-time correlation. Our aim is to convert it into one. But the approach to achieve this objective has to be different from that developed for non-settling particles in Rani et al. [67].

At this stage of the theory, the particle viscous response times are such that the conditions $St_r \gg 1$ and $St_I \gg 1$ are both satisfied. Therefore, with gravity g being an $O(1)$ quantity and $Sv_I = g\tau_v/u_{\text{rms}} \gg 1$, we can say that particle pairs settle through eddies whose size scales with separation r in times much quicker than the eddy turnover time τ_r , i.e., $r/(g\tau_v) \ll \tau_r$. The physical implication of this is that the fast-settling pairs essentially experience a frozen field of size r eddies during $[0, t]$. Thus, we may write $\Delta\mathbf{u}(\mathbf{r}, \mathbf{x}, 0) \approx \Delta\mathbf{u}(\mathbf{r}, \mathbf{x}, t)$, i.e. we now have an Eulerian one-time correlation in D_{UU} that is given by

$$D_{UU, Sv_I \gg 1} = \frac{1}{St_I^2} \tilde{D}_{UU} = \frac{1}{St_I^2} \int_{-\infty}^0 dt \langle \Delta\mathbf{u}(\mathbf{r}, \mathbf{x}, t) \Delta\mathbf{u}(\mathbf{r}, \mathbf{x} + \mathbf{g}\tau_v t, t) \rangle \quad (\text{A.17})$$

Contrast this with D_{UU} for *non-settling pairs*:

$$D_{UU, Sv_I=0} = \frac{1}{St_I^2} \tilde{D}_{UU} = \frac{1}{St_I^2} \int_{-\infty}^0 dt \langle \Delta\mathbf{u}(\mathbf{r}, \mathbf{x}, t) \Delta\mathbf{u}(\mathbf{r}, \mathbf{x} + \mathbf{W}t, t) \rangle \quad (\text{A.18})$$

where \mathbf{W} is the relative velocity between the large-scale fluid eddies advecting past the pair and the pair center of mass that is moving purely due to the effects of turbulence (i.e. no settling).

A.2 $Sv_I \sim 1$ Regime

One may want to relax the condition $Sv_I = g\tau_v/u_{\text{rms}} \gg 1$ such that $Sv_I \sim 1$, which may be achieved when $g \ll 1$. In this regime, the term containing $(-\mathbf{V} + Sv_I \mathbf{e}_g)$ on the LHS of (A.9) is anyway $O(1/St_I^2)$. Therefore, it will not contribute to the perturbation analysis. Again considering the $O(1/St_I)$ terms in (A.9), we get the same equation as for the previous regime:

$$\frac{\partial P_1}{\partial t} + \nabla_{\mathbf{r}} \cdot (\mathbf{U}P_1) + \nabla_{\mathbf{x}} \cdot (\mathbf{V}P_1) = -\nabla_{\mathbf{U}} \cdot (\Delta \mathbf{u} \langle P \rangle) - \nabla_{\mathbf{V}} \cdot (\mathbf{u}_{\text{cm}} \langle P \rangle) \quad (\text{A.19})$$

Equation (A.19) may then be written as

$$\left. \frac{dP_1}{dt} \right|_{\mathbf{U}, \mathbf{V}} = -\nabla_{\mathbf{U}} \cdot (\Delta \mathbf{u} \langle P \rangle) - \nabla_{\mathbf{V}} \cdot (\mathbf{u}_{\text{cm}} \langle P \rangle) \quad (\text{A.20})$$

Thus, even when $Sv_I \sim 1$, the only eddies through which pairs do not settle faster than their turnover times are the integral-scale ones. However, for separations $r \sim L$, the pair essentially behaves as two independent particles. The point being that even for $Sv_I \sim 1$, particles settle faster than the turnover times of most eddies. As a result, (A.17) should still be valid when $Sv_I \sim 1$.

A.3 Derivation of diffusion coefficient tensor in the settling particle pair relative velocity space

$$\begin{aligned}
\widehat{D}_{UU} &= \frac{1}{St_I^2} \int_{-\infty}^0 \langle \Delta \mathbf{u}(\mathbf{x}, \mathbf{r}, t) \Delta \mathbf{u}(\mathbf{x} + \mathbf{g}\tau_v t, \mathbf{r}, t) \rangle dt \\
&= \frac{1}{St_I^2} \int_{-\infty}^0 \left\langle \left[\mathbf{u}\left(\mathbf{x} + \frac{1}{2}\mathbf{r}, t\right) - \mathbf{u}\left(\mathbf{x} - \frac{1}{2}\mathbf{r}, t\right) \right] \right. \\
&\quad \times \left. \left[\mathbf{u}\left(\mathbf{x} + \mathbf{g}\tau_v t + \frac{1}{2}\mathbf{r}, t\right) - \mathbf{u}\left(\mathbf{x} + \mathbf{g}\tau_v t - \frac{1}{2}\mathbf{r}, t\right) \right] \right\rangle dt \\
&= \frac{1}{St_I^2} \int_{-\infty}^0 \left\langle \mathbf{u}\left(\mathbf{x} + \frac{1}{2}\mathbf{r}, t\right) \mathbf{u}\left(\mathbf{x} + \mathbf{g}\tau_v t + \frac{1}{2}\mathbf{r}, t\right) - \mathbf{u}\left(\mathbf{x} + \frac{1}{2}\mathbf{r}, t\right) \mathbf{u}\left(\mathbf{x} + \mathbf{g}\tau_v t - \frac{1}{2}\mathbf{r}, t\right) \right. \\
&\quad \left. - \mathbf{u}\left(\mathbf{x} - \frac{1}{2}\mathbf{r}, t\right) \mathbf{u}\left(\mathbf{x} + \mathbf{g}\tau_v t + \frac{1}{2}\mathbf{r}, t\right) + \mathbf{u}\left(\mathbf{x} - \frac{1}{2}\mathbf{r}, t\right) \mathbf{u}\left(\mathbf{x} + \mathbf{g}\tau_v t - \frac{1}{2}\mathbf{r}, t\right) \right\rangle dt. \tag{A.21}
\end{aligned}$$

In (A.21), there are four Eulerian two-point velocity correlation terms. Writing the two-point velocity correlation tensors in terms of the velocity spectrum tensor, $\mathbf{R}(\mathbf{k})$, we get:

$$\langle \mathbf{u}(\mathbf{x}, t) \mathbf{u}(\mathbf{x}', t) \rangle = \int \mathbf{R}(\mathbf{k}) e^{i\mathbf{k}\cdot(\mathbf{x}-\mathbf{x}')} d\mathbf{k} \tag{A.22}$$

where \mathbf{k} is the wavenumber vector. For isotropic turbulence, velocity spectrum tensor, $\mathbf{R}(\mathbf{k})$, can be written exactly as:

$$\mathbf{R}(\mathbf{k}) = \frac{E(k)}{4\pi k^2} \left(\mathbf{I} - \frac{\mathbf{k} \mathbf{k}}{k^2} \right) \tag{A.23}$$

where $k = |\mathbf{k}|$, $E(k)$ is the energy spectrum tensor, and \mathbf{I} is the identity tensor.

$$\left\langle \mathbf{u}\left(\mathbf{x} + \frac{1}{2}\mathbf{r}, t\right) \mathbf{u}\left(\mathbf{x} + \mathbf{g}\tau_v t + \frac{1}{2}\mathbf{r}, t\right) \right\rangle = \int \mathbf{R}(\mathbf{k}) e^{i\mathbf{k}\cdot\mathbf{g}\tau_v t} d\mathbf{k} \quad (\text{A.24})$$

$$\left\langle \mathbf{u}\left(\mathbf{x} + \frac{1}{2}\mathbf{r}, t\right) \mathbf{u}\left(\mathbf{x} + \mathbf{g}\tau_v t - \frac{1}{2}\mathbf{r}, t\right) \right\rangle = \int \mathbf{R}(\mathbf{k}) e^{i\mathbf{k}\cdot\mathbf{g}\tau_v t} e^{-i\mathbf{k}\cdot\mathbf{r}} d\mathbf{k} \quad (\text{A.25})$$

$$\left\langle \mathbf{u}\left(\mathbf{x} - \frac{1}{2}\mathbf{r}, t\right) \mathbf{u}\left(\mathbf{x} + \mathbf{g}\tau_v t + \frac{1}{2}\mathbf{r}, t\right) \right\rangle = \int \mathbf{R}(\mathbf{k}) e^{i\mathbf{k}\cdot\mathbf{g}\tau_v t} e^{i\mathbf{k}\cdot\mathbf{r}} d\mathbf{k} \quad (\text{A.26})$$

$$\left\langle \mathbf{u}\left(\mathbf{x} - \frac{1}{2}\mathbf{r}, t\right) \mathbf{u}\left(\mathbf{x} + \mathbf{g}\tau_v t - \frac{1}{2}\mathbf{r}, t\right) \right\rangle = \int \mathbf{R}(\mathbf{k}) e^{i\mathbf{k}\cdot\mathbf{g}\tau_v t} d\mathbf{k} \quad (\text{A.27})$$

Substituting (A.24)-(A.27) into (A.21) and simplifying, we get:

$$\widehat{\mathbf{D}}_{UU} = \frac{1}{St_I^2} \int \mathbf{R}(\mathbf{k}) (2 - e^{-i\mathbf{k}\cdot\mathbf{r}} - e^{i\mathbf{k}\cdot\mathbf{r}}) d\mathbf{k} \int_{-\infty}^0 e^{i\mathbf{k}\cdot\mathbf{g}\tau_v t} dt \quad (\text{A.28})$$

where \mathbf{k} is the wavenumber vector. The second (time) integral in (A.28) can be conveniently evaluated using the standard Fourier transforms,

$$\begin{aligned} \int_{-\infty}^0 e^{i\mathbf{k}\cdot\mathbf{g}\tau_v t} dt &= \int_{-\infty}^{\infty} H(\tau) e^{-i\mathbf{k}\cdot\mathbf{g}\tau_v \tau} d\tau, \text{ where } H \text{ is the Heaviside function} \\ &= \int_{-\infty}^{\infty} \left[\frac{1}{2} + \frac{1}{2} \text{sgn}(\tau) \right] e^{-i\mathbf{k}\cdot\mathbf{g}\tau_v \tau} d\tau, \text{ where sgn is the sign function} \\ &= \frac{1}{2} \delta\left(\frac{\mathbf{k}\cdot\mathbf{g}\tau_v}{2\pi}\right) + \frac{1}{i\mathbf{k}\cdot\mathbf{g}\tau_v}, \text{ using standard Fourier transform} \end{aligned} \quad (\text{A.29})$$

giving us:

$$\widehat{\mathbf{D}}_{UU} = \frac{1}{St_I^2} \int \mathbf{R}(\mathbf{k}) [2 - 2\cos(\mathbf{k}\cdot\mathbf{r})] \left[\frac{1}{2} \delta\left(\frac{\mathbf{k}\cdot\mathbf{g}\tau_v}{2\pi}\right) + \frac{1}{i\mathbf{k}\cdot\mathbf{g}\tau_v} \right] d\mathbf{k} \quad (\text{A.30})$$

Recognizing that $\frac{1}{i\mathbf{k}\cdot\mathbf{g}\tau_v}$ is an odd function of \mathbf{k} , the integral containing $\frac{1}{i\mathbf{k}\cdot\mathbf{g}\tau_v}$ goes to zero. This gives us:

$$\widehat{\mathbf{D}}_{UU} = \frac{1}{St_1^2} \int \mathbf{R}(\mathbf{k}) [1 - \cos(\mathbf{k} \cdot \mathbf{r})] \delta\left(\frac{\mathbf{k} \cdot \mathbf{g}\tau_v}{2\pi}\right) d\mathbf{k} \quad (\text{A.31})$$

We know

$$\int_{-\infty}^{\infty} f(x)\delta(x)dx = f(0)$$

Therefore, we want the integrand variable ‘ x ’ to be the same as the variable inside $\delta(‘x’)$. Note that $\delta\left(\frac{\mathbf{k}\cdot\mathbf{g}\tau_v}{2\pi}\right)$ is non-zero only when $\mathbf{k} \cdot \mathbf{g}\tau_v = 0$, i.e. when $\mathbf{k} \perp \mathbf{g}\tau_v$. Let $\mathbf{k} = \boldsymbol{\xi}$ satisfy this property, where $\boldsymbol{\xi} = (\xi_1, \xi_2, 0)$.

Now,

$$\begin{aligned} \frac{\mathbf{k} \cdot \mathbf{g}\tau_v}{2\pi} &= -\frac{k_3 g\tau_v}{2\pi}, \quad g = |\mathbf{g}| \\ d\left(\frac{\mathbf{k} \cdot \mathbf{g}\tau_v}{2\pi}\right) &= d\left(-\frac{k_3 g\tau_v}{2\pi}\right) \\ d(k_3) &= -\frac{2\pi}{g\tau_v} d\left(\frac{\mathbf{k} \cdot \mathbf{g}\tau_v}{2\pi}\right) \end{aligned}$$

Therefore, by plugging $d\mathbf{k} = dk_1 dk_2 dk_3 = d\xi_1 d\xi_2 \frac{2\pi}{g\tau_v} d\left(\frac{\mathbf{k}\cdot\mathbf{g}\tau_v}{2\pi}\right)$ in (A.31) we get

$$\begin{aligned} \widehat{\mathbf{D}}_{UU} &= \frac{2\pi}{St_1^2 g\tau_v} \iiint \mathbf{R}(\boldsymbol{\xi}) [1 - \cos(\boldsymbol{\xi} \cdot \mathbf{r})] \delta\left(\frac{\mathbf{k} \cdot \mathbf{g}\tau_v}{2\pi}\right) d\left(\frac{\mathbf{k} \cdot \mathbf{g}\tau_v}{2\pi}\right) d\xi_1 d\xi_2 \\ &= \frac{2\pi}{St_1^2 g\tau_v} \iint \mathbf{R}(\boldsymbol{\xi}) [1 - \cos(\boldsymbol{\xi} \cdot \mathbf{r})] d\xi_1 d\xi_2 \end{aligned} \quad (\text{A.32})$$

Let $\boldsymbol{\rho}$ is the projection of \mathbf{r} into the $\boldsymbol{\xi}$ -plane, $\rho = |\boldsymbol{\rho}|$ we can write:

$$\rho_i = (\delta_{ij} - \delta_{i3}\delta_{j3}) r_j \quad (\text{A.33})$$

$$\cos\phi = \frac{\rho_i \xi_i}{\rho \xi} = \frac{r_i \xi_i}{r \xi} \quad (\text{A.34})$$

Equation (A.32) can be rewritten in terms of ρ and by writing $R(\boldsymbol{\xi})$ in terms of the energy spectrum $E(\boldsymbol{\xi})$ as:

$$\widehat{\mathbf{D}}_{UU,ij} = \frac{2\pi}{St_I^2 g \tau_v} \int_0^\infty \xi \, d\xi \int_0^{2\pi} \frac{E(\xi)}{4\pi \xi^2} \left(\delta_{ij} - \frac{\xi_i \xi_j}{\xi^2} \right) [1 - \cos(\xi \rho \cos\phi)] \, d\phi \quad (\text{A.35})$$

Integrating $\widehat{\mathbf{D}}_{UU,ij}$ over ϕ we get:

$$\widehat{\mathbf{D}}_{UU,ij} = \frac{\pi}{St_I^2 g \tau_v} \int_0^\infty \frac{E(\xi)}{\xi} \left(\delta_{ij} - \frac{\xi_i \xi_j}{\xi^2} \right) [1 - J_0(\xi \rho)] \, d\xi \quad (\text{A.36})$$

where J_0 is the Bessel function of the first kind. We can also write $\widehat{\mathbf{D}}_{UU,ij}$ as:

$$\widehat{\mathbf{D}}_{UU,ij} = \frac{\pi}{St_I^2 g \tau_v} \int_0^\infty \frac{E(\xi)}{\xi} \left(\delta_{ij} - \frac{\xi_i \xi_j}{\xi^2} \right) [1 - J_0(\xi r \sin\theta)] \, d\xi \quad (\text{A.37})$$

where $\cos(\theta) = \mathbf{g} \cdot \mathbf{r} / (gr)$; $\theta \in [0, \pi]$. We can also write $\widehat{\mathbf{D}}_{UU}$ as:

$$\widehat{\mathbf{D}}_{UU,ij} = \lambda_1 (\delta_{ij} - \delta_{i3}\delta_{j3}) + \lambda_2 \delta_{i3}\delta_{j3} \quad (\text{A.38})$$

The expression for λ_1 can be obtained by multiplying with $(\delta_{ij} - \delta_{i3}\delta_{j3})$ on both sides of (A.38)

$$\widehat{\mathbf{D}}_{UU,ij} (\delta_{ij} - \delta_{i3}\delta_{j3}) = \lambda_1 (\delta_{ij} - \delta_{i3}\delta_{j3}) (\delta_{ij} - \delta_{i3}\delta_{j3}) + \lambda_2 \delta_{i3}\delta_{j3} (\delta_{ij} - \delta_{i3}\delta_{j3}) \quad (\text{A.39})$$

REFERENCES

- [1] J Abrahamson. Collision rates of small particles in a vigorously turbulent fluid. *Chemical Engineering Science*, 30(11):1371–1379, 1975.
- [2] K Alvelius. Random forcing of three-dimensional homogeneous turbulence. *Physics of Fluids (1994-present)*, 11(7):1880–1889, 1999.
- [3] O. Ayala, B. Rosa, and L.-P. Wang. Effects of turbulence on the geometric collision rate of sedimenting droplets. part 2. theory and parameterization. *New J. Phys.*, 10:075016, 2008.
- [4] S Balachandar and John K Eaton. Turbulent dispersed multiphase flow. *Annual Review of Fluid Mechanics*, 42:111–133, 2010.
- [5] G. K. Batchelor. *The Theory of Homogeneous Turbulence*. Cambridge University Press, Cambridge, 1953.
- [6] Colin P Bateson and Alberto Aliseda. Wind tunnel measurements of the preferential concentration of inertial droplets in homogeneous isotropic turbulence. *Experiments in fluids*, 52(6):1373–1387, 2012.
- [7] J. Bec, L. Biferale, M. Cencini, A. S. Lanotte, and F. Toschi. Intermittency in the velocity distribution of heavy particles in turbulence. *J. Fluid Mech.*, 646: 527–536, 2010.
- [8] A Bragg, DC Swailes, and R Skartlien. Drift-free kinetic equations for turbulent dispersion. *Physical Review E*, 86(5):056306, 2012.
- [9] Andrew D Bragg and Lance R Collins. New insights from comparing statistical theories for inertial particles in turbulence: I. spatial distribution of particles. *New Journal of Physics*, 16(5):055013, 2014.
- [10] Andrew D Bragg and Lance R Collins. New insights from comparing statistical theories for inertial particles in turbulence: II. relative velocities. *New Journal of Physics*, 16(5):055014, 2014.
- [11] Andrew D. Bragg, Peter J. Ireland, and Lance R. Collins. On the relationship between the non-local clustering mechanism and preferential concentration. *Journal of Fluid Mechanics*, 780:327–343, 2015.
- [12] K. A. Brucker, J. C. Isaza, T. Vaithianathan, and L. R. Collins. Efficient algorithm for simulating homogeneous turbulent shear flow without remeshing. *J. Comp. Phys.*, 225:20–32, 2007.
- [13] B. K. Brunk, D. L. Koch, and L. W. Lion. Hydrodynamic pair diffusion in isotropic random velocity fields with application to turbulent coagulation. *Phys. Fluids*, 9:2670–2691, 1997.

- [14] Jeffrey R Chasnov. Simulation of the kolmogorov inertial subrange using an improved subgrid model. *Physics of Fluids A: Fluid Dynamics (1989-1993)*, 3(1):188–200, 1991.
- [15] Shiyi Chen and Xiaowen Shan. High-resolution turbulent simulations using the connection machine-2. *Computers in Physics*, 6(6):643–646, 1992.
- [16] E. Chiang and A. Youdin. Forming planetesimals in solar and extrasolar nebulae. *Annual Reviews of Earth and Planetary Science*, 38:493–522, 2005.
- [17] Agathe Chouippe and Markus Uhlmann. Forcing homogeneous turbulence in direct numerical simulation of particulate flow with interface resolution and gravity. *Physics of Fluids (1994-present)*, 27(12):123301, 2015.
- [18] Jaehun Chun, Donald L Koch, Sarma L Rani, Aruj Ahluwalia, and Lance R Collins. Clustering of aerosol particles in isotropic turbulence. *Journal of Fluid Mechanics*, 536:219–251, 2005.
- [19] Clayton T Crowe, John D Schwarzkopf, Martin Sommerfeld, and Yutaka Tsuji. *Multiphase flows with droplets and particles*. CRC press, 2011.
- [20] IV Derevich. Statistical modeling of particles relative motion in a turbulent gas flow. *International journal of heat and mass transfer*, 49(23):4290–4304, 2006.
- [21] O. A. Druzhinin and S. Elghobashi. On the decay rate of isotropic turbulence laden with microparticles. *Phys. Fluids*, 11:602–610, 1999.
- [22] OA Druzhinin. On the two-way interaction in two-dimensional particle-laden flows: the accumulation of particles and flow modification. *Journal of Fluid Mechanics*, 297:49–76, 1995.
- [23] J. K. Eaton and J. R. Fessler. Preferential concentration of particles by turbulence. *Int. J. Multiphase Flow*, 20:169–209, 1994.
- [24] S Elghobashi. On predicting particle-laden turbulent flows. *Applied Scientific Research*, 52(4):309–329, 1994.
- [25] V. Eswaran and S. B. Pope. An examination of forcing in direct numerical simulations of turbulence. *Comput. Fluids*, 16:257–278, 1988.
- [26] Pascal Fede and Olivier Simonin. Numerical study of the subgrid fluid turbulence effects on the statistics of heavy colliding particles. *Physics of Fluids (1994-present)*, 18(4):045103, 2006.
- [27] J. Ferry, S. L. Rani, and S. Balachandar. A locally implicit improvement of the equilibrium eulerian method. *Int. J. Multiphase Flow*, 29:869–891, 2003.
- [28] Jim Ferry and S Balachandar. A fast eulerian method for disperse two-phase flow. *International journal of multiphase flow*, 27(7):1199–1226, 2001.

- [29] P. Février, O. Simonin, and D. Legendre. Particle dispersion and preferential concentration dependence on turbulent reynolds number from direct and large-eddy simulations of isotropic homogeneous turbulence. *Proceedings of the Fourth International Conference on Multiphase Flow, New Orleans, 2001*.
- [30] Crispin W. Gardiner. *Handbook of Stochastic Methods for Physics, Chemistry and the Natural Sciences*. Springer, 1990.
- [31] Mathieu Gibert, Haitao Xu, and Eberhard Bodenschatz. Where do small, weakly inertial particles go in a turbulent flow? *Journal of Fluid Mechanics*, 698:160–167, 2012.
- [32] Partha S Goswami and V Kumaran. Particle dynamics in a turbulent particle–gas suspension at high stokes number. part 1. velocity and acceleration distributions. *Journal of Fluid Mechanics*, 646:59–90, 2010.
- [33] Partha S Goswami and V Kumaran. Particle dynamics in a turbulent particle–gas suspension at high stokes number. part 2. the fluctuating-force model. *Journal of Fluid Mechanics*, 646:91–125, 2010.
- [34] P. Gualtieri, C. M. Casciola, R. Benzi, G. Amati, and R. Piva. Scaling laws and intermittency in homogeneous shear flow. *Phys. Fluids*, 14(2):583–596, 2002.
- [35] K Gustavsson and B Mehlig. Distribution of relative velocities in turbulent aerosols. *Physical Review E*, 84(4):045304, 2011.
- [36] Gary A Huber and Sangtae Kim. Weighted-ensemble brownian dynamics simulations for protein association reactions. *Biophysical journal*, 70(1):97, 1996.
- [37] KE Hyland, S McKee, and MW Reeks. Derivation of a pdf kinetic equation for the transport of particles in turbulent flows. *Journal of Physics A: Mathematical and General*, 32(34):6169, 1999.
- [38] Peter J Ireland, T Vaithianathan, Parvez S Sukheswalla, Baidurja Ray, and Lance R Collins. Highly parallel particle-laden flow solver for turbulence research. *Computers & Fluids*, 76:170–177, 2013.
- [39] Peter J Ireland, Andrew D Bragg, and Lance R Collins. The effect of reynolds number on inertial particle dynamics in isotropic turbulence. part 1. simulations without gravitational effects. *Journal of Fluid Mechanics*, 796:617–658, 2016.
- [40] Takashi Ishihara, Toshiyuki Gotoh, and Yukio Kaneda. Study of high-reynolds number isotropic turbulence by direct numerical simulation. *Annual Review of Fluid Mechanics*, 41:165–180, 2009.
- [41] Guodong Jin, Guo-Wei He, and Lian-Ping Wang. Large-eddy simulation of turbulent collision of heavy particles in isotropic turbulence. *Physics of Fluids (1994-present)*, 22(5):055106, 2010.

- [42] Jaedal Jung, Kyongmin Yeo, and Changhoon Lee. Behavior of heavy particles in isotropic turbulence. *PHYSICAL REVIEW E Phys Rev E*, 77:016307, 2008.
- [43] Robert H Kraichnan. Dynamics of nonlinear stochastic systems. *Journal of Mathematical Physics*, 2(1):124–148, 1961.
- [44] Robert H Kraichnan. Lagrangian-history closure approximation for turbulence. *Physics of Fluids (1958-1988)*, 8(4):575–598, 1965.
- [45] Robert H Kraichnan. Eulerian and lagrangian renormalization in turbulence theory. *Journal of Fluid Mechanics*, 83(2):349–374, 1977.
- [46] JGM Kuerten. Point-particle dns and les of particle-laden turbulent flow—a state-of-the-art review. *Flow, Turbulence and Combustion*, 97(3):689–713, 2016.
- [47] T. S. Lundgren. Turbulent pair dispersion and scalar diffusion. *J. Fluid Mech.*, 111:27, 1981.
- [48] Cristian Marchioli, Andrea Giusti, Maria Vittoria Salvetti, and Alfredo Soldati. Direct numerical simulation of particle wall transfer and deposition in upward turbulent pipe flow. *International journal of Multiphase flow*, 29(6):1017–1038, 2003.
- [49] F Mashayek and RVR Pandya. Analytical description of particle/droplet-laden turbulent flows. *Progress in energy and combustion science*, 29(4):329–378, 2003.
- [50] Farzad Mashayek. Direct numerical simulations of evaporating droplet dispersion in forced low mach number turbulence. *International journal of heat and mass transfer*, 41(17):2601–2617, 1998.
- [51] Martin R Maxey and James J Riley. Equation of motion for a small rigid sphere in a nonuniform flow. *Physics of Fluids (1958-1988)*, 26(4):883–889, 1983.
- [52] MR Maxey. The gravitational settling of aerosol particles in homogeneous turbulence and random flow fields. *Journal of Fluid Mechanics*, 174:441–465, 1987.
- [53] Bernhard Mehlig, Ville Uski, and Michael Wilkinson. Colliding particles in highly turbulent flows. *Physics of Fluids (1994-present)*, 19(9):098107, 2007.
- [54] Jean-Pierre Minier. On lagrangian stochastic methods for turbulent polydisperse two-phase reactive flows. *Progress in Energy and Combustion Science*, 50:1–62, 2015.
- [55] Jean-Pierre Minier and Eric Peirano. The pdf approach to turbulent polydispersed two-phase flows. *Physics Reports*, 352(1):1–214, 2001.
- [56] Matthew R Overholt and Stephen B Pope. A deterministic forcing scheme for direct numerical simulations of turbulence. *Computers & Fluids*, 27(1):11–28, 1998.

- [57] Liubin Pan and Paolo Padoan. Relative velocity of inertial particles in turbulent flows. *Journal of Fluid Mechanics*, 661:73–107, 2010.
- [58] Liubin Pan and Paolo Padoan. Turbulence-induced relative velocity of dust particles. i. identical particles. *The Astrophysical Journal*, 776:1–37, 2013.
- [59] Liubin Pan and Paolo Padoan. Turbulence-induced relative velocity of dust particles. ii. the bidisperse case. *The Astrophysical Journal*, 791:1–20, 2014.
- [60] Liubin Pan and Paolo Padoan. Turbulence-induced relative velocity of dust particles. iii. the probability distribution. *The Astrophysical Journal*, 792:1–24, 2014.
- [61] Liubin Pan and Paolo Padoan. Turbulence-induced relative velocity of dust particles. iv. the collision kernel. *The Astrophysical Journal*, 797:1–18, 2014.
- [62] Liubin Pan and Paolo Padoan. Turbulence-induced relative velocity of dust particles. v. testing previous models. *The Astrophysical Journal*, 812:1–21, 2015.
- [63] Liubin Pan, Paolo Padoan, John Scalo, Alexei G Kritsuk, and Michael L Norman. Turbulent clustering of protoplanetary dust and planetesimal formation. *The Astrophysical Journal*, 740(1):6, 2011.
- [64] S. B. Pope. *Turbulent Flows*. Cambridge University Press, New York, 2000.
- [65] Jacek Pozorski and Jean-Pierre Minier. Probability density function modeling of dispersed two-phase turbulent flows. *Physical Review E*, 59(1):855–863, 1999.
- [66] Sarma L Rani and S Balachandar. Evaluation of the equilibrium eulerian approach for the evolution of particle concentration in isotropic turbulence. *International journal of multiphase flow*, 29(12):1793–1816, 2003.
- [67] Sarma L Rani, Rohit Dhariwal, and Donald L Koch. A stochastic model for the relative motion of high stokes number particles in isotropic turbulence. *Journal of Fluid Mechanics*, 756:870–902, 2014.
- [68] Baidurja Ray and Lance R Collins. Preferential concentration and relative velocity statistics of inertial particles in navier–stokes turbulence with and without filtering. *Journal of Fluid Mechanics*, 680:488–510, 2011.
- [69] Walter C Reade and Lance R Collins. Effect of preferential concentration on turbulent collision rates. *Physics of Fluids (1994-present)*, 12(10):2530–2540, 2000.
- [70] M. W. Reeks. On the continuum equations for dispersed particles in nonuniform flows. *Physics of Fluids A*, 4:1290–1303, 1992.
- [71] M Wi Reeks. Eulerian direct interaction applied to the statistical motion of particles in a turbulent fluid. *Journal of Fluid Mechanics*, 97(03):569–590, 1980.

- [72] Michael W Reeks. On probability density function equations for particle dispersion in a uniform shear flow. *Journal of Fluid Mechanics*, 522:263–302, 2005.
- [73] MW Reeks. On a kinetic equation for the transport of particles in turbulent flows. *Physics of Fluids A: Fluid Dynamics (1989-1993)*, 3(3):446–456, 1991.
- [74] B Rosa, H Parishani, O Ayala, and L-P Wang. Effects of forcing time scale on the simulated turbulent flows and turbulent collision statistics of inertial particles. *Physics of Fluids (1994-present)*, 27(1):015105, 2015.
- [75] Bogdan Rosa, Hossein Parishani, Orlando Ayala, Wojciech W Grabowski, and Lian-Ping Wang. Kinematic and dynamic collision statistics of cloud droplets from high-resolution simulations. *New Journal of Physics*, 15(4):045032, 2013.
- [76] Juan PLC Salazar, Jeremy De Jong, Lujie Cao, Scott H Woodward, Hui Meng, and Lance R Collins. Experimental and numerical investigation of inertial particle clustering in isotropic turbulence. *Journal of Fluid Mechanics*, 600:245–256, 2008.
- [77] Ewe Wei Saw. *Studies of spatial clustering of inertial particles in turbulence*. PhD thesis, Michigan Technological University, 2008.
- [78] Ewe Wei Saw, Raymond A Shaw, Sathyanarayana Ayyalasomayajula, Patrick Y Chuang, and Armann Gylfason. Inertial clustering of particles in high-reynolds-number turbulence. *Physical review letters*, 100(21):214501, 2008.
- [79] Ewe-Wei Saw, Raymond A Shaw, Juan PLC Salazar, and Lance R Collins. Spatial clustering of polydisperse inertial particles in turbulence: Ii. comparing simulation with experiment. *New Journal of Physics*, 14(10):105031, 2012.
- [80] Brian Sawford. Turbulent relative dispersion. *Annual review of fluid mechanics*, 33(1):289–317, 2001.
- [81] K Sengupta, B Shotorban, GB Jacobs, and F Mashayek. Spectral-based simulations of particle-laden turbulent flows. *International Journal of Multiphase Flow*, 35(9):811–826, 2009.
- [82] Raymond A Shaw. Particle-turbulence interactions in atmospheric clouds. *Annual Review of Fluid Mechanics*, 35(1):183–227, 2003.
- [83] Babak Shotorban and S Balachandar. A eulerian model for large-eddy simulation of concentration of particles with small stokes numbers. *Physics of Fluids*, 19:118107, 2007.
- [84] Babak Shotorban and Farzad Mashayek. Modeling subgrid-scale effects on particles by approximate deconvolution. *Physics of Fluids (1994-present)*, 17(8):081701, 2005.

- [85] Babak Shotorban and Farzad Mashayek. A stochastic model for particle motion in large-eddy simulation. *Journal of Turbulence*, (7):N18, 2006.
- [86] Eric D Siggia and GS Patterson. Intermittency effects in a numerical simulation of stationary three-dimensional turbulence. *Journal of Fluid Mechanics*, 86(03): 567–592, 1978.
- [87] O Simonin, E Deutsch, and JP Minier. Eulerian prediction of the fluid/particle correlated motion in turbulent two-phase flows. In *Advances in Turbulence IV*, pages 275–283. Springer, 1993.
- [88] Kyle D Squires and John K Eaton. Particle response and turbulence modification in isotropic turbulence. *Physics of Fluids A: Fluid Dynamics (1989-1993)*, 2(7):1191–1203, 1990.
- [89] Kyle D Squires and John K Eaton. Preferential concentration of particles by turbulence. *Physics of Fluids A: Fluid Dynamics (1989-1993)*, 3(5):1169–1178, 1991.
- [90] Neal P Sullivan, Shankar Mahalingam, and Robert M Kerr. Deterministic forcing of homogeneous, isotropic turbulence. *Physics of Fluids (1994-present)*, 6(4):1612–1614, 1994.
- [91] Shivshankar Sundaram and Lance R Collins. Collision statistics in an isotropic particle-laden turbulent suspension. part 1. direct numerical simulations. *Journal of Fluid Mechanics*, 335:75–109, 1997.
- [92] David C Swailes and Kirsty FF Darbyshire. A generalized fokker-planck equation for particle transport in random media. *Physica A: Statistical Mechanics and its Applications*, 242(1):38–48, 1997.
- [93] Sudheer Tenneti and Shankar Subramaniam. Particle-resolved direct numerical simulation for gas-solid flow model development. *Annual Review of Fluid Mechanics*, 46:199–230, 2014.
- [94] Lian-Ping Wang and Martin R Maxey. Settling velocity and concentration distribution of heavy particles in homogeneous isotropic turbulence. *Journal of Fluid Mechanics*, 256:27–68, 1993.
- [95] Lian-Ping Wang and Anthony S Wexler. Statistical mechanical description and modelling of turbulent collision of inertial particles. *Journal of Fluid Mechanics*, 415:117–153, 2000.
- [96] Lian-Ping Wang, Shiyi Chen, James G Brasseur, and John C Wyngaard. Examination of hypotheses in the kolmogorov refined turbulence theory through high-resolution simulations. part 1. velocity field. *Journal of Fluid Mechanics*, 309:113–156, 1996.

- [97] Lian-Ping Wang, Anthony S Wexler, and Yong Zhou. Statistical mechanical descriptions of turbulent coagulation. *Physics of Fluids (1994-present)*, 10(10):2647–2651, 1998.
- [98] A Witkowska, D Juvé, and JG Brasseur. Numerical study of noise from isotropic turbulence. *Journal of Computational Acoustics*, 5(03):317–336, 1997.
- [99] P. K. Yeung and S. B. Pope. Lagrangian statistics from direct numerical simulations of isotropic turbulence. *J. Fluid Mech.*, 207:536, 1989.
- [100] L. I. Zaichik and V. M. Alipchenkov. Pair dispersion and preferential concentration of particles in isotropic turbulence. *Phys. Fluids*, 15:1776–1787, 2003.
- [101] L. I. Zaichik, O. Simonin, and V. M. Alipchenkov. Collision rates of bidisperse inertial particles in isotropic turbulence. *Phys. Fluids*, 18:035110, 2006.
- [102] L. I. Zaichik, O. Simonin, and V. M. Alipchenkov. Collision rates of bidisperse inertial particles in isotropic turbulence. *Phys. Fluids*, 18:035110, 2006.
- [103] Leonid I Zaichik and Vladimir M Alipchenkov. Refinement of the probability density function model for preferential concentration of aerosol particles in isotropic turbulence. *Physics of Fluids (1994-present)*, 19(11):113308, 2007.
- [104] Leonid I Zaichik and Vladimir M Alipchenkov. Statistical models for predicting pair dispersion and particle clustering in isotropic turbulence and their applications. *New Journal of Physics*, 11(10):103018, 2009.
- [105] Leonid I Zaichik, Olivier Simonin, and Vladimir M Alipchenkov. Two statistical models for predicting collision rates of inertial particles in homogeneous isotropic turbulence. *Physics of Fluids (1994-present)*, 15(10):2995–3005, 2003.
- [106] LI Zaichik. A statistical model of particle transport and heat transfer in turbulent shear flows. *Physics of Fluids (1994-present)*, 11(6):1521–1534, 1999.